Università degli Studi di Cagliari

DOTTORATO DI RICERCA

Scienze e Tecnologie Chimiche

Ciclo XXXI

TITOLO TESI

Design of spinel ferrite-based nanoheterostructures synthesized by solvothermal approaches

Settore/i scientifico disciplinari di afferenza

CHIM/02

CHIM/03

Presentata da:	Marco Sanna Angotzi
Coordinatore Dottorato	Prof. Stefano Enzo
Tutor	Prof.ssa Carla Cannas Prof.ssa Anna Musinu

Esame finale anno accademico 2018-2019

To Daniel

I will always remember you

as a mentor of work and life

Acknowledgments

First and foremost, I want to thank my supervisor Prof. Carla Cannas for the continuous support of my Ph.D. study, for her motivation, enthusiasm, and knowledge. My sincere thanks also go to my second supervisor Prof. Anna Musinu, who has always guided me with her expertise and encouragement.

A very special thank goes to Prof. Daniel Nižňanský, for his enormous scientific and human contribution during my Ph.D. path. His untimely demise profoundly affected me, but I will always remember him as a genuine, smiling, and honest person.

Great acknowledgments go to all my colleagues and friends, in particular, Ph.D. Valentina Mameli, Ph.D. Claudio Cara, Ph.D. Andrea Ardu, Mirko Antonio Vacca, and Fausto Secci.

Stefania Orgiu, Luca Cappai, Marianna Gerina, and Stefano Lonis are gratefully acknowledged for their contribution to the Ph.D. work.

Moreover, a sincere thank goes to Prof. Huolin Xin from the Brookhaven National Laboratory, Prof. Jana Vejpravova from the Charles University of Prague, and Ph.D. Claudio Sangregorio from Consiglio Nazionale delle Ricerche, for having welcomed me in their labs and helped me with their vast support and expertise.

Prof. Stefano Enzo is gratefully acknowledged as head of the Ph.D. board and for all the helpful suggestions during my work.

I also want to thank all the people who have helped me in the research activity, especially Ph.D. Anton Repko from the Charles University of Prague, Dominika Zákutná and Prof. Sabrina Disch from the University of Cologne, and Prof. Antonella Rossi and Prof. Marzia Fantauzzi from University of Cagliari.

Last but not least, I want to thank my family and Laura for their unconditional support in both difficult and happy situations.

Contents

List of Figures

List of Tables

List of Abbreviations

AC	Alternate Current
AFM	Antiferromagnetic
$(BH)_{max}$	Maximum Energy Product
CMC	Critical Micellar Concentration
CME	Chiral Magnetic Effect
CP	Co-Precipitation
CTAB	Cetyl TrimethylAmmonium Bromide
DC	Direct Current
DLS	Dynamic Light Scattering
DMSA	Dimercaptosuccinic Acid
DMSO	Dimethyl Sulfoxide
EDX	Energy Dispersive X-ray Spectroscopy
EELS	Electron Energy Loss Spectroscopy
FC	Field Cooled
FiM	Ferrimagnetic
FM	Ferromagnetic
FT-IR	Fourier Transform – Infrared Spectroscopy
HDD	Hard Drive Disk
HRSTEM	High-Resolution Scanning Transmission Electron Microscopy
HRTEM	High-Resolution Transmission Electron Microscopy
HT	Hydrothermal
ICP-OES	Inductive Coupled Plasma – Optical Emission Spectrometer
LT	Low Temperature
MFH	Magnetic Fluid Hyperthermia
MNHs	Magnetic Nanoheterostructures
MT	Magnetic Tape
MUA	Mercapto Undecanoic Acid
NPs	Nanoparticles
MRI	Magnetic Resonance Imaging
NHs	Nanoheterostructures
PDF	Powder Diffraction Files
PEG	Poly Ethylene Glycol
PEG-TMS	Poly Ethylene Glycol Trimethoxysilane
PRP	Peer-Reviewed Paper
PVP	PolyVinylPyrrolidone
RT	Room Temperature
SAR	Specific Absorption Rate
SERS	Surface Enhanced Raman Spectroscopy

SLP	Specific Loss Power
SPM	Superparamagnetic
ST	Solvothermal
STEM	Scanning Transmission Electron Microscopy
TEM	Transmission Electron Microscopy
TGA	ThermoGravimetric Analysis
TD	Thermal Decomposition
XPS	X-ray Photoelectron Spectroscopy
XRD	X-ray Diffraction
ZFC	Zero Field Cooled

Introduction

Spinel ferrite nanoparticles (NPs) are a class of magnetic materials widely studied, due to their properties and stability. Spinel ferrite-based heterostructures can combine in a single material novel properties and functionalities, opening a new horizon of applications, including catalysis, magnetic recording, and biomedicine. In particular, magnetically hard and soft spinel ferrites can be engineered in a core-shell architecture, allowing the magnetic coupling between the different phases and the optimization of the magnetic properties (saturation magnetization, magnetic anisotropy, *etc.*). Again, by connecting noble metals with spinel ferrite, it is possible to prepare multicomponent heterostructures in the form of dimers, oligomers, or flower-like structures that can display both the optical (localized surface plasmon resonance) and magnetic effects. A crucial aspect to be considered is the synthesis methodology able to produce highly crystalline with low size dispersity and to finely tune size and shape of the NPs.

In this thesis, the solvothermal method was proposed to synthesize a different kind of spinel ferrite-based nanoheterostructures. The first system consists of hard-soft magnetically-coupled spinel ferrite core-shell heterostructures, that find application in magnetic fluid hyperthermia, thanks to the possibility to release heat under the application of an external alternate magnetic field. The second system combines the localized surface plasmonic resonance effect of silver NPs with hard or soft magnetic spinel ferrite NPs in flower-like heterostructured nanocrystals, that might be employed in different research areas, such as catalysis (homogenous catalysis with magnetic recovery or with the application of an AC magnetic field to generate heat), surface-enhanced Raman scattering and hyperthermic therapy by combined AC magnetic field and photothermal exposures.

In detail, the first chapter of this thesis will deal with a general overview of spinel ferrite nanoparticles and their heterostructures, synthesis methods, and applications, with a particular focus on the solvothermal method and the magnetic fluid hyperthermia. The second chapter will cover the solvothermal synthesis and characterization of various samples of cobalt ferrite, manganese ferrite, and spinel iron oxide (magnetite/maghemite), along with the hyperthermic properties of the cobalt ferrite series. The third chapter will be dedicated to (i) the design of spinel ferrite-based core-shell heterostructures, made up of the hard-cobalt ferrite core and soft manganese ferrite or spinel iron oxide shell, or *vice-versa*; (ii) their structural, compositional, morphological, and magnetic characterization also at the nanoscale; (iii) the hyperthermic properties of the cobalt ferrite-based core-

shell nanoparticles. The fourth chapter will concern itself with the comparison between the core-shell systems with cobalt-manganese mixed ferrites (as chemical mixtures) and mixtures of cobalt ferrite and manganese ferrite (as physical mixtures). Finally, to join optical and magnetic properties, the fifth chapter will put forward a synthetic strategy to obtain flower-like silver-spinel ferrite nanoheterostructures by using the solvothermal method and will include the characterization of these samples.

1 *Spinel ferrite nanoparticles and heterostructures*

Abstract

Nanostructured spinel ferrites are one of the most studied classes of magnetic materials, due to the possibility of finely tuning the magnetic properties by changing chemical composition, size, and shape, or by engineering heterostructures. Indeed, spinel ferrite-based nanoheterostructures, thanks to their multifunctionalities, may be employed in a wide range of applications, from catalysis to biomedicine and magnetic recording. Herein, a general discussion about nanomaterials, properties, and implementation of spinel ferrite nanoparticles and their heterostructures is presented.

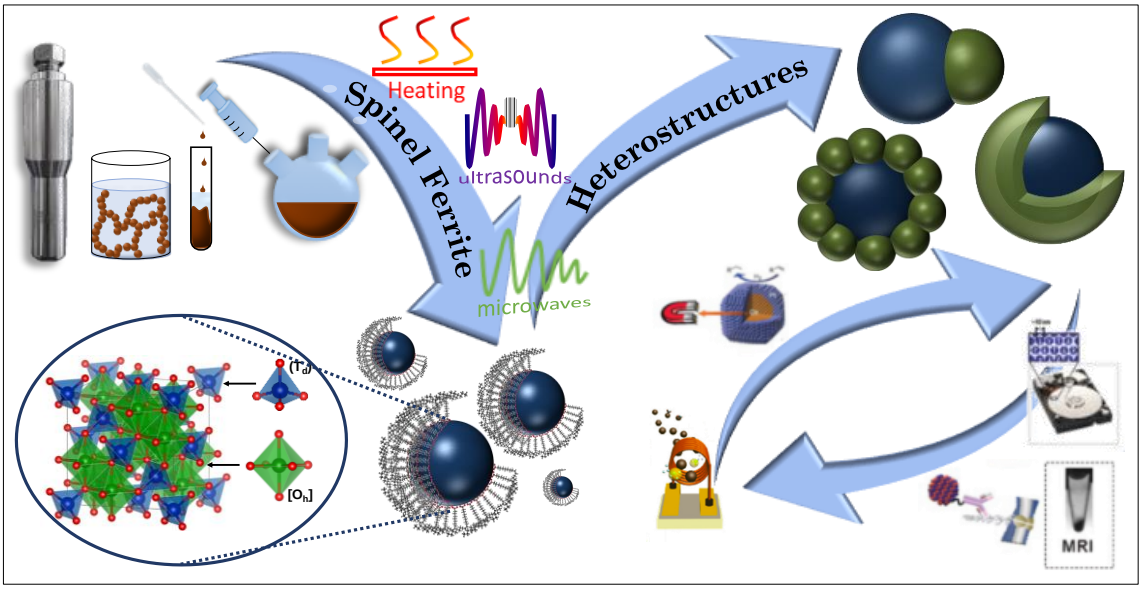

1.1 Nanomaterials

In ISO/TS 80004, a nanomaterial is defined as a "material with any external dimension in the nanoscale or having internal structure or surface structure in the nanoscale", with nanoscale defined as the "length range approximately from 1 nm to 100 nm". This includes both nano-objects, which are discrete pieces of material, and nanostructured materials, which feature internal or surface structure on the nanoscale. A nanomaterial may be a member of both these categories.

Nanomaterials show unique physical and chemical properties with respect to their bulk counterparts because of the high surface/volume ratio and the occurrence of quantum effects.[1]

Nanomaterials can be classified according to how many of their dimensions fall in the nanoscale, and we can have nanoparticles (3D), nanofibers, with nanotubes being hollow and nanorods solid (2D), and nanoplates (1D).

1.2 Spinel Ferrites

Among the magnetic nanostructured materials, cubic (spinel) ferrites having formula $M^{II}Fe_2O_4$ (where M^{II} = Fe, Co, Mn, Ni, Zn, *etc.*) have attracted the interest of many research fields, due to possibility to tune their magnetic and chemical properties, and their wide range of applications, such as biomedicine[2–18], environmental remediation[19–21], sensors,[22–26] data storage[27–30], and catalysis[31–43]. Indeed, since 1950, about 7000 peer-reviewed papers (prp) have been published in different subject area having “spinel ferrite” as the keyword, according to the database Scopus® (Figure 1). The timeline of the prp on spinel ferrite (Figure 1b) is characterized by a sharp increase by the beginning of the 21st century. The analysis of these data reveals that in the 20th century the research fields mainly focused on spinel ferrites were Physics & Astronomy (893 prp), Materials Science (838 prp), Engineering (507 prp) and Chemistry (295 prp). Since 2001, a different trend can be highlighted with an increased number of studies published in the Materials Science area (+10%) which turned out to be the principal subject of investigations. This may be an index of the fact that since the 1950’s there has been considerable interest towards the basic physical properties of bulk spinel ferrites, such as their crystalline structure and their magnetic behavior. Over the last two decades, thanks to the discovery of the novel properties of nanomaterials[44–58] and the development of more efficient synthetic strategies able to finely tune these properties ,[59–63] more applicative studies in the field of Materials Science have been published.

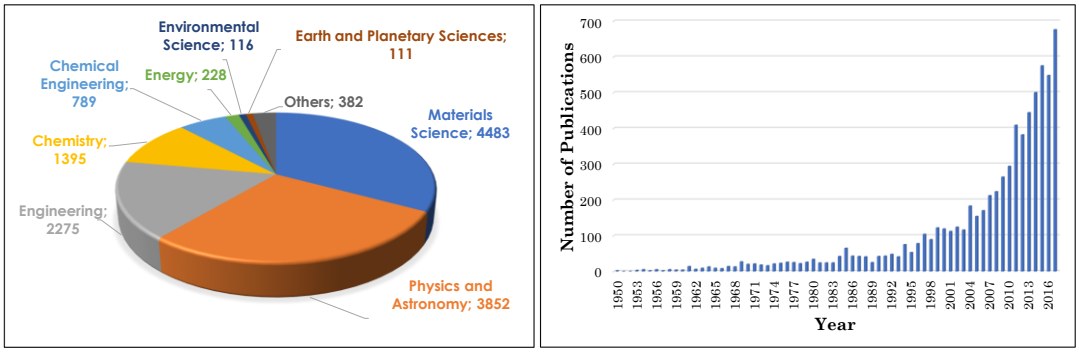

Figure 1. Number of peer-reviewed papers published in different subject areas (a) and their time frame (b) in the period 1950-2017 according to Scopus®.

1.2.1 Structure

The physical properties of spinel ferrites are strongly related to their crystalline structure. In detail, spinel ferrites, with formula $M^{II}Fe_2O_4$, feature a face-centered cubic (fcc) structure in which the oxygen atoms are cubic close-packed (Figure 2). Metallic cations are located within two types of interstitial sites, associated with two different coordination of metallic ions to oxygens: tetrahedral, referred as T_d (A) sites, and octahedral, referred as O_h [B] sites. When the (A)-sites are occupied by M^{II} cations and the [B]-sites by Fe^{III} cations, the structure is referred to as normal spinel, $(M^{II})[Fe^{III}]O_4$. However, if the (A)-sites are entirely occupied by Fe^{III} and the [B]-sites are held by both M^{II} and Fe^{III}, then the structure is referred to as inverse spinel, $(Fe^{III})[M^{II}, Fe^{III}]O_4$. Partially inverse structures may exist in agreement with the general formula $\left(Me^{II}_{\delta}Fe^{III}_{1-\delta}\right)\left[Me^{II}_{1-\delta}Fe^{III}_{1+\delta}\right]O_4$, where 1-$\delta$ is the so-called inversion degree (γ), which is equal to 1 for a normal spinel and 0 for an inverse one.[1,64,65]

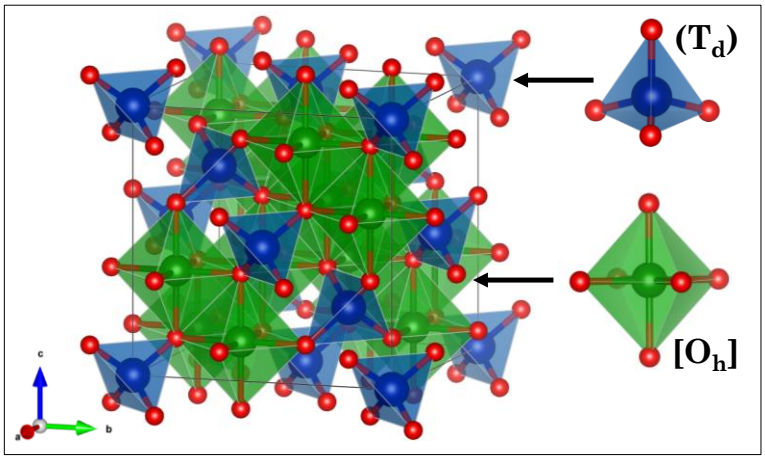

Figure 2. Schematic representation of spinel structure having tetrahedral (blue) and octahedral (green) interstitial sites, drawn with the software VESTA.[66,67]

Superexchange interactions between atomic magnetic moments in A- and B-sites lead to a ferromagnetic (FM) order between the ions located in each site type, respectively, giving rise to two magnetic sublattices. On the other hand, interactions between magnetic ions in the A and B sites induce antiferromagnetic order and are generally higher than the AA and BB

interactions. The dominant AB interactions then induce a non-compensated antiferromagnetic order (ferrimagnetic, FiM) between the A and B sublattices.[68] Hence, it is clear that the magnetic properties of spinel oxides can be controlled through the chemical composition and the crystalline structure of the materials. Indeed, by adjusting the chemical identity of Me^{II} and the relative position of the cations in the structure (inversion degree) the magnetic configuration of $Me^{II}Fe_2O_4$ can be chemically engineered to provide a wide range of magnetic behaviours .[69–71] Moreover, even small changes in the cationic distribution of the compounds with the same chemical composition can result in substantial changes in the magnetic moments.[72]
Regarding the effect of the chemical composition, cations having different single-ion anisotropy will affect the overall behaviour of the spinel ferrite, giving rise of hard ferrite, as $CoFe_2O_4$, and soft ferrites as $MnFe_2O_4$, Fe_3O_4, *etc.* (Table 1).

Table 1. Structural and magnetic properties of some spinel ferrites:[70] *a* (cell parameter), structure, Curie temperature (T_c, Néel temperature in case of zinc ferrite, T_N), saturation magnetization (M_s), magnetic moment for unit cell (μ_{UC}), anisotropy constant (K), and magnetic behaviour.

Material	a (pm)	Structure	T_c (K)	M_s (Am^2/kg)	μ_{UC} (μ_B)	K (J/m^3)	Magnetic Behaviour
$CoFe_2O_4$	839	$(Fe^{III})[Co^{II}Fe^{III}]O_4$	790	85	24	$2.9 \cdot 10^5$	Hard
Fe_3O_4	840	$(Fe^{II})[Fe^{II}Fe^{III}]O_4$	860	92	32	$-1.3 \cdot 10^4$	Soft
$NiFe_2O_4$	834	$(Fe^{III})[Ni^{II}Fe^{III}]O_4$	865	61	16	$-7 \cdot 10^3$	Soft
γ-Fe_2O_3	834	$(Fe^{III})[Fe^{III}_{5/3}\square_{1/3}]O_4$	985	88	26.6	$-5 \cdot 10^3$	Soft
$MnFe_2O_4$	852	$(Fe^{III})[Mn^{II}Fe^{III}]O_4$	575	100	40	$-3 \cdot 10^3$	Soft
$MgFe_2O_4$	836	$(Fe^{III})[Mg^{II}Fe^{III}]O_4$	713	40	0	$-3 \cdot 10^3$	Soft
$ZnFe_2O_4$	844	$(Zn^{II})[Fe^{III}_2]O_4$	T_N=9	-	80	-	-

1.2.2 Nanomagnetism

Beyond the strong dependence of the magnetic behaviour of spinel ferrites from their structure and chemical composition, great influences are also exerted size and shape of the nanomaterial.[70] Indeed, bulk materials are organized in small magnetic regions, called magnetic domains, in which the magnetic moments are oriented in the same direction. Magnetic domains are separated by domain walls, where the magnetic moments gradually rotate from one domain to another. Below a critical dimension (Figure 3), a multi-domain structure is no longer energetically favourable, but instead, a mono-domain structure is established, with each particle constituting a single domain, called superspin, and presenting very high coercivity.[73,74]

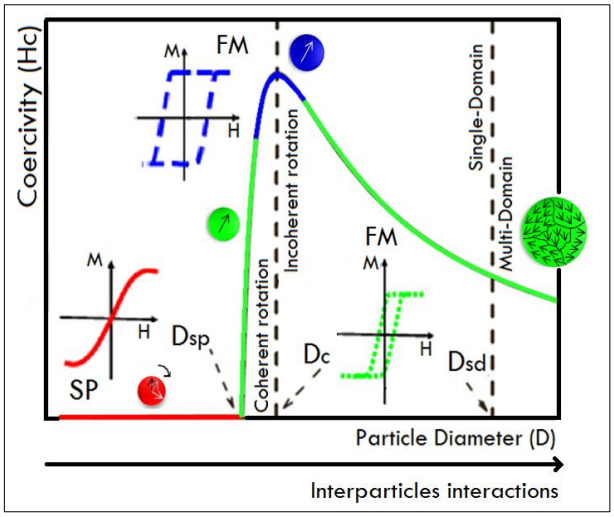

Figure 3. Variation of the coercive field with nanoparticle size.

The critical radius is given by Eq. 1

$$r_{sd} \approx 9\frac{\sqrt{A \cdot K_u}}{\mu_0 {M_s}^2} \qquad \textbf{Eq. 1}$$

Where A and K_u are the exchange and uniaxial anisotropy constants respectively, μ_0 the vacuum permeability and M_s the saturation magnetization. Therefore, the radius depends on the properties of the material, *e.g.* about 160 nm for $CoFe_2O_4$, 38 nm for Fe_3O_4, and 30 nm for γ-Fe_2O_3.[70,75]

As shown in Figure 3, another critical dimension is present, below which the coercivity of a ferro(i)magnetic materials falls to zero. This phenomenon is analogous to paramagnetism but involves superspins and it is therefore called superparamagnetism. This is caused by the magnetization reversal process (relaxation), that was firstly proposed by Néel in 1949[76] and further developed by Brown in 1963.[76] At any finite temperature, thermal activation can overcome the anisotropy energy barrier leading to the reversal of the particle moment (Figure 4).

When the thermal energy (K_BT) is higher than the energy barrier ($\Delta E_B = KV$, where K is the anisotropy constant and V the particle volume), the magnetization flips and the nanoparticles show superparamagnetic (SPM) behaviour (unblocked state). On the contrary, if the energy barrier is higher than the thermal energy, the magnetization remains in an energy minimum, and the material show ferro(i)magnetic behaviour (blocked state). For nanomaterials, the anisotropy depends on many factors, such as chemical composition (magnetocrystalline anisotropy), shape (shape anisotropy), the surface on volume ratio (surface anisotropy).

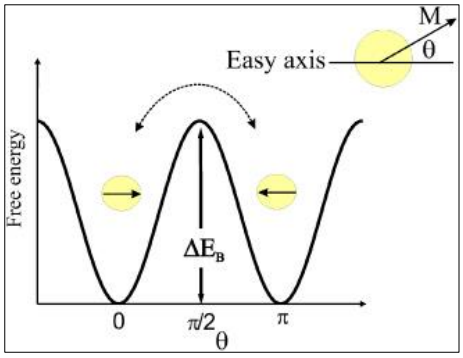

Figure 4. Schematic picture of the free energy of a single-domain particle with uniaxial anisotropy as a function of magnetization direction. E_B is the energy barrier hindering the free rotation of the magnetization and θ is the angle between the magnetization M and the easy axis. Republished with permission from ref. 73 © IOP Publishing. All right reserved.

The rate of the magnetization flipping is described by Eq. 2:

$$\tau \approx \tau_0 e^{\frac{\Delta E_B}{K_B T}} \qquad \textbf{Eq. 2}$$

Where K_B is the Boltzmann constant and τ_0 is the characteristic relaxation time (10^{-9}-10^{-11} s). The observation of magnetic properties of single-domain particles (*i.e.* blocked or unblocked behaviour) strongly depends on the experimental measuring time (τ_m) of the technique used to observe the relaxation. If $\tau << \tau_m$, the relaxation during the experiment is so fast that only a time average of the magnetization is observed, and the particles will appear superparamagnetic. On the contrary, if $\tau >> \tau_m$, the relaxation is so slow that only static properties are seen, as in a large ordered magnetic crystal (blocked state). The blocking temperature (T_B) is defined as the temperature at which the relaxation time is equal to the experimental measuring time. From the definition of T_B, Eq. 2 can be rewritten as:

$$\tau_m \approx \tau_0 e^{\frac{\Delta E_B}{K_B T_B}} \qquad \textbf{Eq. 3}$$

1.3 Synthesis methods

As seen so far, the magnetic properties of spinel ferrite nanoparticles can be governed by controlling of the energy barrier and therefore by tuning volume (particle size and their distribution) and anisotropy (structure, chemical composition, shape, surface effect, and magnetic coupling). For this reason, different strategies have been proposed in the literature able to tune these properties finely.

The synthesis methods can be classified according to the adopted approach (physical or chemical) and the specific phase in which the synthesis is carried out (gas, liquid, or solid). Liquid-phase chemical approaches are the most used in the literature, due to their distinctive advantages, such as the possibility to obtain a large quantity of product also in the form of colloidal dispersions. Moreover, when compared with physical, vapour-, or solid-phase chemical approaches, they are straightforward, versatile, and economical. Table 2 summarises advantages and disadvantages for the most important chemical methods.[77]

Table 2. Advantages and disadvantages of the chemical methods for the synthesis of nanostructured spinel ferrites.

Media	Method	Advantages	Disadvantages	Ref.
Aqueous	Coprecipitation	High yield Scalability Low cost Eco-friendly Low temperature Ease	Difficulties in particle size, shape and size distribution control Poor crystallinity	78–122
	Aqueous Sol-gel	High yield Scalability Low cost Eco-friendly	Difficulties in finding metal precursors The high reactivity of metal precursors Many parameters to be controlled Low crystallinity The necessity of post-synthesis treatments Difficulties in particle size, shape and size distribution control	123–155
	Hydrothermal	Low cost Eco-friendly Repeatable Low temperature Ease Good crystallinity	Difficulties in particle size, shape and size distribution control Difficulties in the comprehension of the mechanism Special experimental apparatus Long reaction time	156–199
Non-aqueous	Surfactant-assisted thermal decomposition	High yield High crystallinity Shape and size control Low dispersity	High quantities of high-boiling and toxic organic solvents Expensive High temperature Difficulties in the comprehension of the mechanism	59–63,200–262
	Nonaqueous Sol-gel	Fairly good size control Good crystallinity Versatility Ease High yield	The necessity of post-synthesis treatments to lower the dispersity	263–271
	Solvothermal	Low-boiling organic solvents Repeatability Mild temperature High crystallinity Size control Low dispersity	Difficulties in the comprehension of the mechanism Special experimental apparatus Long reaction time	263–265,272–302
	Microemulsion	Low temperature Hydrophobic and hydrophilic NPs Size control	Low yield Poor crystallinity Difficulties in producing large particles Environmental and economic issues in waste disposal	81,210,303–329
	Polyol	High crystallinity Wide temperature range Versatility Size control	High temperature Expensive Low dispersity	330–362
Methods employing alternative/additional energy source	Microwave-assisted	Fast reaction time Scalability Repeatability Low temperature Uniform and efficient heating	Low yield Expensive Special experimental apparatus	117,158,161,163,164,176,266–271,275,295,330,332,355,359
	Sonochemical	Fast reaction time High crystallinity Ease in producing anisometric particles Good control over the composition	Low yield Difficulties in shape control Special experimental apparatus	335,363–384

1.3.1 Aqueous phase synthesis

The development of synthesis methods to be conducted in aqueous phases represents a significant goal due to the possibility to produce hydrophilic NPs in a one-pot process, commonly required for different applications, such as biomedicine or in environmental remediation. Moreover, the use of water as solvent should ensure an environmentally friendly and low-cost synthetic route.

1.3.1.1 Coprecipitation

Among the different chemical methods, the precipitation is one of the oldest and most well-established. Usually, the metal precursors, such as a metallic salt, are dissolved in an aqueous medium leading to hydroxylated aquo- or oxocomplexes. When a precipitating agent is added, usually a base as NaOH, KOH, or ammonia solution, an insoluble solid precipitates. Indeed, the complexes condense *via* two mechanisms involving nucleophilic substitution: olation for hydroxylated aquocomplexes, or oxolation for hydroxylated oxocomplexes.
The first mechanism is a one-step mechanism that proceeds through the direct elimination of a water molecule while in the oxolation an intermediate step takes place because no water molecules are present in the coordination sphere of the metal (Figure 5).

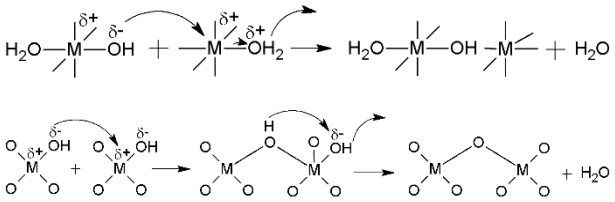

Figure 5. Mechanisms of olation (top) and oxolation (bottom) reactions for the precipitation of ferrite nanoparticles.

The reaction is controlled by pH, size, charge, and electronegativity of the metal cations. In particular, only neutral complexes lead to the formation of a solid phase. For this reason, a base is usually added into the acidic solution of the metallic salt. At pH ≥ 3, iron oxohydroxides phases precipitate immediately usually forming poorly-crystalline phases such as the 2-line ferrihydrite. Then, these phases evolve by aging towards more stable crystalline phases, as magnetite or maghemite.[385] Large quantities of the final product can be obtained inexpensively by scaling-up merely the process. Being water the primary solvent used for the syntheses, this method represents an environmentally friendly choice. However, the major drawbacks are poor control over the size and the shape of the final particles leading to large particle size distributions, due to the dependence of the

method only on kinetic factors and on a high number of parameters that needs to be monitored.[3] To sort out this issues, besides the classical coprecipitation strategies, other strategies were developed with the addition of stabilising and surfactant agents able to control the nucleation and the growth of the particles.[81,90,97,100,107,115,116]

1.3.1.2 Aqueous sol-gel

Aqueous sol-gel chemistry has been successfully adopted to synthesize different bulk metal oxide phases. The process at the basis of this method can be described as an inorganic polymerization through hydrolysis and condensation reactions involving the transformation of an aqueous solution of a metal precursor, *i.e.* metal salts (nitrate, chloride, sulfates, …) or metal alkoxides, into a solid network. The aqueous solution is firstly converted by hydrolysis reactions into a sol, which is a colloidal dispersion; this latter then forms a crosslinked inorganic network enclosing a liquid phase, *i.e.* a gel, thanks to condensation reactions. Once the liquid phase is removed (under hypercritical or ambient conditions to form aerogels or xerogels, respectively), a solid phase is obtained. Concerning the metal precursors, metal alkoxides are generally preferred over inorganic salts which can produce a broad spectrum of species of unpredictable reactivity or whose anionic counterpart can persist in the final product. Metal alkoxides are converted in metal oxide phases through hydrolysis (Eq. 4), producing the metal hydroxide *via* the nucleophilic attack of a water molecule, and condensation reactions, oxolation (Eq. 5) or alkoxolation (Eq. 6). The side products are alcohols or water.[386]

Hydrolysis reactions

$$\equiv M - OR + H_2O \rightarrow \equiv M - OH + ROH \qquad \textbf{Eq. 4}$$

Condensation reactions

$$\equiv M - OH + OH - M \equiv\rightarrow \equiv M - O - M \equiv + H_2O \text{ (oxolation)} \qquad \textbf{Eq. 5}$$

$$\equiv M - OR + OH - M \equiv\rightarrow \equiv M - O - M \equiv + ROH \text{ (alkoxolation)} \qquad \textbf{Eq. 6}$$

It is worth noting that silicon, titanium, aluminium, and zirconium alkoxides are commercially available at a low price, but others are difficult to synthesize, such as Mn, Fe, Co, Ni, Cu, Zn *etc*. Also, their chemical reactivity and the reaction rates can be somewhat variable.[386] The chemical reactivity of alkoxides depends on the electronegativity, the charge and the coordination number of the metal, the steric hindrance of the alkoxy group, the molecular structure of the metal alkoxide, the amount and the modality of the addition of water in the reaction mixture, the polarity, the dipole moment and the pH of the solvent.[386,387] Generally, transition-metal alkoxides are more reactive in comparison with silicon alkoxides, due to their lower electronegativity

(which makes them more susceptible towards hydrolysis and condensation reactions) and their tendency to form stable coordination compounds or to form oligomers *via* alkoxy bridging or other associations (*e.g.* alcohol association).[387] For instance, the hydrolysis rate constant for $Ti(OR)_4$ at pH 7 is more than five orders of magnitude higher than that for $Si(OR)_4$ (10^{-3} $M^{-1}\cdot s^{-1}$ against $5\cdot10^{-9}$ $M^{-1}\cdot s^{-1}$), whereas the condensation rates constants are 10^{-4} $M^{-1}\cdot s^{-1}$ and 30 $M^{-1}\cdot s^{-1}$ for $Si(OEt)_4$ and $Ti(OEt)_4$, respectively.[387,388] All the above-cited factors related to the reactivity of the metal alkoxide contribute to making difficult the control of the sol-gel processes in aqueous media, especially for the synthesis of ferrite NPs.[386] Furthermore, when nanoscaled products are requested, this synthetic approach is not appropriate for many reasons: (i) high reactivity of the metal precursors with water; (ii) water acts as both a ligand and a solvent for the metal centres; (iii) many parameters are involved in the reaction and, therefore, ought to be controlled; (iv) due to the high reaction rates, the so obtained products are generally amorphous, leading to the necessity of post-synthesis treatments that are hardly compatible with a good control of size and shape.

However, two different strategies have been developed to obtain nanostructured spinel ferrites.

The first consists in the use of aqueous sol-gel to build a silica network as the matrix hosting the metal salt precursor, which then can be thermally decomposed to produce spinel ferrite NPs (nanocompositing). The textural properties of the silica matrix affect the final features of the spinel ferrite.[137–142,144,145,148,151,152]

The second strategy makes use of metal precursors, such as metal nitrates or chlorides, and coordinating agents, such as citric acid[127,129,130,135,146,149] and glycine[131–134,136], that can induce sol-gel transitions through polymerisation (carboxylate sol-gel). When metal nitrates are used as precursors in the presence for example of citric acid or glycine, an autocatalytic redox reaction can occur inducing a self-combustion reaction that leads directly to the nanosized spinel ferrite.[150]

1.3.2 Non-aqueous phase synthesis

As described so far, the use of water as the solvent, despite ensuring more eco-friendly and low-cost methods, does not allow a satisfactory control on size, size distribution, and shape of the final particles. Indeed, the crucial point is represented by the complicated control of the nucleation and the growth of the particles in water-based syntheses, even in the presence of suitable stabilizing/surfactant molecules. Organic-soluble surfactants (oleic acid, oleylamine, *etc*) or organic solvents (benzyl alcohol, alcohols, oleylamine, *etc*), acting as both solvent and surfactant, can adsorb and desorb at the surface of the nuclei and guarantee a controlled growth process. Moreover,

non-aqueous media allow the use of a broader range of precursors, including organometallic compounds (*e.g.* metal carbonyls) and organic complexes (*e.g.* metal acetylacetonates, acetates).

The production of spinel ferrite NPs featuring a narrow size distribution, and therefore controlled physical properties, has been the most crucial challenge in the development of the synthesis methods. The study by La Mer and Dinegar[389] has demonstrated that this condition can be reached if a single, rapid nucleation event takes place, followed by a slower and controlled growth of the nuclei. The nucleation and growth steps must be temporally discrete events. The precursor concentration must be higher than a given nucleation threshold (supersaturated solution) to generate similarly-sized nuclei at the same time. The precursor concentration then drops considerably preventing other nucleation events and leading to the growth of particles with a narrow size distribution ($\sigma < 10\%$).[2,3,386] The condition described so far can be achieved by two different approaches: (i) hot-injection; (ii) heat-up.

In the hot-injection method, the room-temperature precursors' solution is rapidly injected into the hot reaction mixture containing the solvent eventually together with the surfactants. The fast injection of the precursor induces a high degree of supersaturation, resulting in a short burst of nucleation. During the nucleation process, the precursor concentration in the solution decreases abruptly, followed by a diffusion-controlled growth with the absence of any further nucleation event. As shown in the LaMer diagram in Figure 6, the hot-injection process is a particular case of this model, letting alone the first stage in which the monomer accumulation occurs.

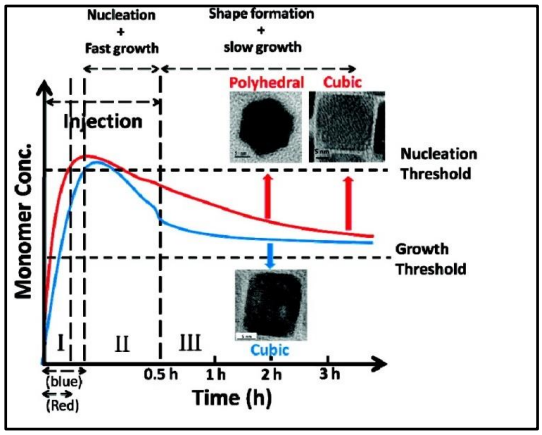

Figure 6. The LaMer diagram. Reprinted with permission from [390]. Copyright (2011) American Chemical Society.

Conversely, in the heat-up processes, all the reactants (precursors, surfactants, and solvent) are mixed at a certain temperature and heated up to induce the nucleation process of the nanocrystals at a certain reaction temperature. Then, further heating results in the growth of the nuclei. This process follows quite well the LaMer model, with the accumulation of the monomer in the first stage, the burst nucleation in the second and the size

focusing in the third (Figure 6). By using both the hot-injection and heat-up approaches it is possible to obtain highly crystalline products with very low dispersity and high yields.[391]

1.3.2.1 Surfactant-assisted thermal decomposition

Surfactant assisted-thermal decomposition methods are probably the most employed synthetic strategies for the preparation of spinel ferrites. Commonly, this approach involves the decomposition at high temperatures and in high-boiling solvents of metal carboxylates or metal carbonyls, in the presence of molecules such as oleylamine and oleic acid. In particular, when carboxylates are used, free radicals are formed, as shown in the Eq. 7 and Eq. 8:[204,244]

$$M - OOCR \rightarrow M^{\cdot} + RCOO^{\cdot} \quad \textbf{Eq. 7}$$

$$M - OOCR \rightarrow MO^{\cdot} + RC^{\cdot}O \quad \textbf{Eq. 8}$$

These radical species can recombine, decompose into smaller molecules, or react with other metal carboxylate molecules to propagate the decomposition reaction.

Since the development of the method, tremendous efforts have been spent on the synthesis of spinel ferrite nanocrystals and nowadays there are many examples of different systems, sizes, shapes, and synthesis procedures. Despite the differences, similar results are obtained by these methods in terms of the quality of the product. Indeed, it has to be highlighted that surfactant-assisted thermal decomposition permits the production of highly crystalline NPs with narrow size distribution and definite shape. Nevertheless, the drawbacks of the methods are related to the use of toxic, high-boiling organic solvents. Ensuring precisely the same experimental conditions each time appears challenging and therefore the technique may lack repeatability; high temperatures are necessary and might be considered expensive in comparison with those conducted in aqueous media or at lower temperatures.

By the end of the 1990s, both the hot-injection and heat-up approaches had emerged as reasonable solutions to produce uniformly sized spinel ferrite through the surfactant-assisted thermal decomposition method. In particular, Rockenberger, Scher, and Alivisatos[60] in 1999 proposed a hot-injection method for the synthesis of maghemite NPs. The rapid injection of the Cupferron complex (where Cup: N-nitrosophenylhydroxylamine, $C_6H_5N(NO)O^-$) was performed at high temperature (250 °C, 300 °C) but then the system was kept at lower temperature (200 °C, 225 °C) for 30 minutes. The size of the particles was modulated according to the reaction temperature: the higher the temperature the larger the particles were, with

5.2±1.5 nm particles when the precursor was injected at 250 °C and 6.7±1.4 nm at 300 °C.

Hyeon et al. in 2001[63] reported for the first time the synthesis of 13 nm γ-Fe_2O_3 NPs by a heat-up process. The synthesis consists in the oxidative thermal decomposition of the iron pentacarbonyl in the presence of surfactant through two heating steps, one for the nucleation with the injection of the complex at 100 °C and one for the growth, raising the temperature to reflux. This work also reported an alternative method in which the production of maghemite NPs with sizes ranging between 4 and 16 nm go through the oxidation of iron NPs, prepared by the aging of iron-oleate complexes. The tuning of the particle size was in this case achieved by using different metal precursor/surfactant ratios until 11 nm, whereas larger particles were obtained by aging the 11 nm particles in the presence of iron-oleate complexes (seed-mediated growth). Both the methods permitted to obtain NPs with narrow size distributions. In further studies, some authors delved into this study enlightening the possibility of: (i) a 1 nm tuning of the particle size of magnetite NPs between 6 and 13 nm [233]; (ii) producing larger particles with sizes > 15 nm[232]; (iii) producing other nanosized spinel ferrite, such as $CoFe_2O_4$ with sizes from 4 to 9 nm[59] and $MnFe_2O_4$ with sizes between 5 and 13 nm.[215]

Between 2002 and 2004, Sun and co-workers revised the heat-up process developing a versatile strategy for the synthesis of spinel ferrite NPs with different sizes and composition. In 2002, they proposed a one heating step strategy heating the reaction mixture (Fe^{III} acetylacetonate, oleic acid, oleylamine, 1,2-hexadecandiol in phenyl ether) directly to reflux. 4-16 nm magnetite/maghemite NPs were obtained by combining this method with the seed-mediated growth.[62] In 2004, the authors added an intermediate heating step at 200 °C before heating up to reflux.

1.3.2.2 Non-aqueous sol-gel

To overcome the intrinsic limits of aqueous sol-gel approaches (paragraph 1.3.1.2), these have also been developed in organic solvents in the absence of water. In aqueous sol-gel processes, the oxygen for the formation of the oxidic compound is supplied by water molecules. In non-aqueous systems, where intrinsically no water is present, the oxygen needed for the nanoparticle formation is provided by the solvent (ethers, alcohols, ketones or aldehydes) or by the organic constituent of the precursor (alkoxides or acetylacetonates). Metal oxides can be formed by different pathways: alkyl halide elimination (Eq. 9), ether elimination (Eq. 10), condensation of carboxylate groups (ester and amide eliminations, Eq. 11), C-C coupling of benzylic alcohols and alkoxide molecules (Eq. 12) and aldol/ketimine condensation (Eq. 13).

Alkyl halide elimination

$$\equiv M - X + R - O - M \equiv \rightarrow \equiv M - O - M \equiv + R - X \quad \textbf{Eq. 9}$$

Ether elimination

$$\equiv M - OR + RO - M \equiv \rightarrow \equiv M - O - M \equiv + R - O - R \quad \textbf{Eq. 10}$$

Ester elimination

$$\equiv M - OOCR' + R - O - M \equiv \rightarrow \equiv M - O - M \equiv + R - OOCR' \quad \textbf{Eq. 11}$$

C-C bond formation between benzylic alcohols and alkoxides

$$2 \equiv M - O - CH(CH_3)_2 + PhCH_2OH \xrightarrow{-iPrOH} \equiv M - O - M \equiv + PhCH_2CH_2CH(OH)CH_3 \quad \textbf{Eq. 12}$$

Aldol condensation

$$2 \equiv M - OR + 2O = C(CH_3)_2 \xrightarrow{-ROH} \equiv M - O - M \equiv + CH_3C(O)CH = C(CH_3)_2 \quad \textbf{Eq. 13}$$

Details on formation mechanisms are described elsewhere.[386,392,393]
Although this method has been successfully adopted for the synthesis of different nanostructured metal oxides,[386] the synthesis of spinel iron oxides by these mechanisms is, to the best of our knowledge, yet to be developed. Indeed, sometimes the term “non-aqueous sol-gel” is used to describe non-aqueous methods which are not based on the sol-gel chemistry but instead the formation of the oxide goes through the thermal decomposition of iron precursors. A few valuable examples are obtained when sol-gel methods are employed in solvothermal condition[263–265] or under external heating with microwaves,[266–269] to provide the necessary energy to obtain crystalline products. This will be described in paragraph 1.3.4.

1.3.2.3 Microemulsion

A microemulsion is defined by IUPAC as a “dispersion made of water, oil, and surfactant(s) that is an isotropic and thermodynamically stable system with dispersed domain diameter varying approximately from 1 to 100 nm, usually 10 to 50 nm”.[394] The domains in which the dispersed liquid is organized are stabilised by an interfacial film of surface active molecules (surfactants), named micelles. Indeed, above the critical micelle concentration (CMC), surfactants self-assemble to form spherical aggregates with the hydrocarbon chain directed toward the inside or the outside of the aggregates, depending on the nature of the continuous phase, *i.e.* water or oil. Microemulsion methods can be therefore based on normal micelles oil-in-water (o/w) or reverse micelles water-in-oil (w/o) depending on the nature of the dispersed and the continuous phases. Microemulsions have a dynamic structure wherein the micelles of the dispersed phase are diffusing through the continuous phase and colliding with each other. These inelastic collisions, named 'sticky collisions', consist in the coalescence and the temporarily merging of the micelles into each other. This is followed by their

fragmentation to form separate droplets. To produce inorganic NPs, generally, two microemulsions are mixed, one with the inorganic precursor and the other with a precipitating agent, that cause the production of the nanocrystals after the collisions. The final precipitated product, *i.e.* the nanoparticles, is therefore confined to the interior of the micelle (nanoreactor), that determines its size and shape.[314,327]

This method has several advantages, such as the use of low reaction temperature, the possibility to obtain hydrophilic and hydrophobic NPs depending on the type of the micelles and to tune their size by changing the surfactants, co-surfactants and their concentration. In contrast, the main drawbacks are the poor crystallinity due to the mild temperatures and the surfactant instability at high annealing temperatures, and the low reaction yields, due to the necessity to work with diluted systems.

Despite these issues, many examples of the use of microemulsions for the synthesis of spinel ferrites nanoparticles are available in the literature, in particular about magnetite[81,322], maghemite[313], cobalt ferrite[210,323–329], nickel ferrite[303–306,322], manganese ferrite[307–311], zinc ferrite[312] and mixed ferrites[314–321].

1.3.2.4 Polyol

Polyol methods are versatile hydrolytic sol-gel chemical processes (as anticipated in paragraph 1.3.1.2) that involve the use of polyols as solvents, because of their interesting properties, such as the ability of dissolving inorganic compounds, the high dielectric constant, the relatively high boiling point, which ensures a wide range of operating temperature (160-350 °C). Moreover, the low electric potential permits them to act as the reducing agent and as the stabilizer for the particle growth, preventing interparticle interaction. The general procedure is facile: typically, an inorganic compound (*e.g.* chlorides, nitrates, acetates, acetylacetonates) is suspended into liquid polyol together with a hydrolysis agent (water), then stirred and heated. During the reaction, the metal precursor becomes soluble in the diol and forms an intermediate, which undergoes hydrolysis, and nucleates to form the NPs. The hydrolysis of the inorganic intermediate is governed by the hydrolysis ratio, *i.e.* the water/total cations molar ratio, where the water is normally present as an impurity inside the polyol and is enough to cause the reaction. Nevertheless, a proper amount of distilled water may be added to reach some particular reaction conditions. The choice of the polyol is an important point since it determines the solubility of the inorganic precursors and the reaction temperature, that governs the size and crystallinity of the final product, acting as the capping agent (when no other surfactants are employed).[3,395,396]

The possibility to obtain hydrophilic NPs, the high crystallinity and low dispersity of the products can be considered the main advantages of this method. Different parameters can be controlled to tune composition, size, dispersity, crystallinity of the products. The type of metal precursors, inorganic salts[333,335,336,339,342,343,345–348,352–354,356,358,359] or organics[337,338,340–342,344,347,349–351,353,358,361,369], the metal cations ratio[334,339–341,350,352,360,361,372] and concentration[333] play a fundamental role on the composition and size of the NPs.

Polyol methods have been employed for the synthesis of a wide range of nanosized spinel ferrite, as Fe_3O_4,[331,333,336,337,342,347–349,358] γ-Fe_2O_3,[344,347,351] $CoFe_2O_4$,[343,346,347,353,358] $ZnFe_2O_4$,[343,347,357] $NiFe_2O_4$,[343,347,358,362] $CuFe_2O_4$,[345,347,354] $MnFe_2O_4$,[343,347] and mixed ferrites.[334,339,340,350,352,356,360,361,372]

Some authors adopt bases, such as sodium hydroxide, acetate or citrate, to favour the hydrolysis and the precipitation of the oxides.[277,333,339,353,358]

1.3.3 Solvothermal methods

Solvothermal processes are referred to syntheses performed in a sealed vessel called autoclave at high temperature and consequent autogenous pressure.[397–399] When the employed solvent is water, the method is called hydrothermal (paragraph 1.3.3.1); while, when organic solvents or a mixture of solvents (including water) are used, it is referred to as "solvothermal method" (paragraph 1.3.3.2).[400] Generally, reactants and solvents are placed inside an autoclave, sealed, placed into an oven (pre-heated or at room temperature) and treated for a certain time at a certain temperature (100-500 °C).[115,166,167,169,173–175] The solvents also have the function of the pressure-inducing medium, in which the solubility of the reactants is pressure-, temperature-dependent. The reaction rates, as well the diffusivity of the reactants, is favoured by the high temperature. Parameters such as pressure, temperature, reaction time, and the precursor-product system can be tuned to maintain high nucleation rates and to control the nanoparticles growth.[397,398] The pressure can be controlled either by changing the temperature (externally) or by varying the ratio between the filled and empty volumes (internally).[199]

General advantages are the low cost, easiness of the procedure, repeatability and lower temperature compared to room pressure procedures. On the contrary, these methods present difficulties when studying the mechanism of the reaction is needed. To overcome these issues, new types of autoclaves have been designed, that allow to monitor temperature and pressure, add reagents, collect a sample and stir the reactant mixture (Figure 7).

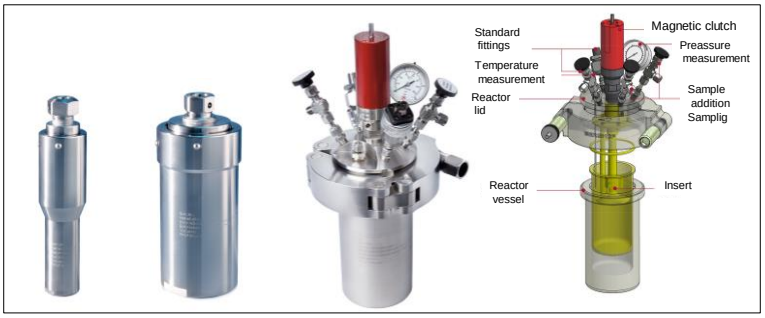

Figure 7. Example of standard autoclaves from Berghof having different capacities (left) and autoclave with various accessories (right). Printed with permission from Berghof Products + Instruments GmbH.

1.3.3.1 Hydrothermal

Hydrothermal methods have been adopted to synthesize different kinds of spinel ferrites, such as iron oxide (*i.e.* magnetite or maghemite),[156,157,168,179,190,195–197] cobalt ferrite,[175,177,191] nickel ferrite,[160,166,167,173] zinc ferrite[169] and mixed ferrites[159,165,174,192]. The process is environmentally friendly and versatile since it does not involve any organic solvents or post-treatments such as calcination. To tune composition, shape and size of the products, different parameters can be modified, such as type and concentration of precursors,[170,177] temperature[163,198,199] and time of the reaction,[163,179] reactant concentration,[173] pH[166,172,173,179,199] and additives[157,160,168,171,193]. Among the additives, some authors adopted surfactants such as polyethylene glycol (PEG)[159,162,165,171,192], Cetyl trimethylammonium bromide (CTAB)[160], octadecylamine[177] to achieve a better shape and size control.

It is worth noting that hydrothermal approaches are often adopted, besides as synthesis method, as crystal growth treatments, improving the crystallinity.

Recently, hydrothermal processes have been associated with dielectric heating to maximise reaction yields and simplify the operation procedures, giving rise to the so-called microwave-hydrothermal method.[158,161,163,164,176]

The hydrothermal method has also been employed to synthesize spinel ferrite NPs in continuous flow reactors.[178,180–189]

Fast heating, due to the contact of the flowing solutions with supercritical water, and short residence times in the reactor (5-30 s) are typical of this method. Due to low control over particle size, shape, and size distribution, only a few papers are reported in the literature on spinel ferrite NPs and few types of systems. Nevertheless, these routes present several advantages such as high scalability, ultrafast synthesis, high crystallinity of products, and therefore they are interesting for an application that does not require specific size and shape. Indeed, supercritical fluids provide homogeneous single-phase reaction media combining the advantages of both liquids (density and solvation capabilities) and gases (high diffusivity, low viscosity, and zero

surface tension). The control of the chemical reaction, and therefore of the materials characteristics (size, structure, composition), is accomplished by choosing specific operating parameters among pressure, temperature, residence time, precursor nature and concentration. Additionally, the choice of the supercritical solvent is of primary importance.

1.3.3.2 Solvothermal

The necessity to gain better control over nanoparticles' nucleation and growth rate, as well as their particle size and shape, has led to the use of surfactants and other solvents other than water: this is known as a solvothermal method. Despite being more expensive and contemplating the use of somewhat toxic and/or hazardous solvents, this method makes a plethora of new reaction condition feasible, by allowing the use of various organometallic precursors, surfactants, and solvents of different polarity, critic temperature, the resulting autogenous pressure, and, in some cases, to lower the reaction rate with respect to pure water (*e.g.* hydrolysis and condensation reactions).[288,290,291,294] All these parameters that can be controlled make solvothermal methods a versatile strategy for the synthesis of different spinel ferrite NPs with desired size and low dispersity (Table 3).

Wang et al.[290] were one of the first researchers who exploited the feasibility of the solvothermal method in the obtainment of spinel ferrite NPs. Indeed, they synthesized $CoFe_2O_4$, $MnFe_2O_4$, $MgFe_2O_4$, $ZnFe_2O_4$, Fe_3O_4 starting from their corresponding inorganic salts through a liquid-solid-solution (LSS) phase transfer and separation process in solvothermal condition, by using sodium linoleate, linoleic acid, and ethanol.[290] A phase transfer process of the metal ions, based on ion exchange, takes place spontaneously across the interface between the sodium linoleate and the water-ethanol solution, thus forming the metal linoleate. Then, at a certain temperature, the nucleation of the linoleic acid-capped magnetic NPs occurs, which separate from the liquid phase because of their weight and the incompatibility between the hydrophobic surfaces and their hydrophilic surroundings. Since then, this process is widely used for the synthesis of spinel ferrite NPs.[276,279,296]

Starting from the method developed by Wang and co-workers, Repko et al.[289,291,293] prepared magnetite and cobalt ferrite NPs by a one-step[289,293] (*in-situ* oleate formation) and two-step[291] (*ex-situ* oleate formation) processes. In the two-step approach, the preparation of cobalt-iron oleate solution is followed by its hydrolysis under the solvothermal condition to generate NPs with sizes in the range 6-11 nm (σ = 15-23 %). The *ex-situ* precursor preparation ensures to obtain higher purity of the precursors and products, higher batch yield and uniform size and shape when compared to the one-step approach.

Table 3. Various examples of spinel ferrite nanoparticles prepared by solvothermal treatment.

System	Precursor	Solvents	Additive	Temperature (°C)	Size (nm)	Mechanism	Ref
Fe_3O_4 $CoFe_2O_4$ $MgFe_2O_4$ $MnFe_2O_4$ $ZnFe_2O_4$	Oleates	Ethanol/ water	Sodium Linoleate	120-180	4-11	LSS	[290]
$CoFe_2O_4$ $MnFe_2O_4$	Nitrates	Toluene	Sodium Oleate	180	8	LSS	[296]
$CoFe_2O_4$	Chlorides	Ethanol /water	Sodium Oleate, oleylamine	180	6	LSS	[276]
$CoFe_2O_4$	Nitrates	Ethanol/ water	Sodium hydroxide, Oleic acid	180	6	LSS	[279]
Fe_3O_4	Isopropoxide	Ethanol/ water	Oleylamine Oleic acid	140-220	4-9	Sol-Gel	[294]
Fe_3O_4	Acetylacetonates	Octanol	Octylamine	240	4-6	Sol-Gel	[273]
$CoFe_2O_4$	Oleates	Pentanol Toluene Octanol	Water	180-220	5-12	Sol-Gel	[288,291,293]
Fe_3O_4 $CoFe_2O_4$ $MnFe_2O_4$ $NiFe_2O_4$	Acetylacetonates	Benzyl Alcohol	-	175-200	5-16	Sol-Gel	[263–265]
$Ni_xCo_{1-x}Fe_2O_4$	Chloride Nitrates Acetylacetonates	Octanol	Sodium Dodecyl Sulfate	240	11	Sol-Gel	[278]
Fe_3O_4	Acetylacetonates	Benzyl Ether	Oleylamine	200	4	TD	[274]
$CoFe_2O_4$	Acetylacetonates	Acetophe none	-	120-200	3-11	TD	[285,302]
Fe_3O_4	Chloride	Ethylene Glycol	PVP/Citrate	220	10-50	Polyol	[280]
Fe_3O_4	Chloride	Ethylene Glycol	Oleylamine 1,3-diaminopropane Sodium acetate	200	93	Polyol	[272]
$CoFe_2O_4$	Nitrates	Ethylene Glycol	-	160	3	Polyol	[284]
$CoFe_2O_4$	Chloride Acetylacetonates	Ethylene Glycol	Sodium acetate Water, PVP	180	10-200	Polyol	[287]
$MnFe_2O_4$	Chlorides	Triethyle ne Glycol	Benzylamine	200	10	Polyol	[281,286]
$MnFe_2O_4$	Chlorides	Ethylene Glycol	Hexamethylene tetramine	100-160	25	Polyol	[277]
$NiFe_2O_4$	Chloride	Ethylene Glycol	Sodium Acetate	180	12	Polyol	[283]
$ZnFe_2O_4$	Nitrates	Ethylene Glycol	Potassium Hydroxide	160-290	4-19	Polyol	[275]
$Zn_xCo_{1-x}Fe_2O_4$	Nitrates Chlorides	Ethylene Glycol	PEG Sodium Acetate	200	10-16	Polyol	[282]

The authors also studied the temperature and solvent polarity influences on particle size by preparing different cobalt ferrite NPs in various mixtures of organic solvents (ethanol, 1-pentanol, 1-octanol, toluene). It was found that higher polarity of the solvent and higher temperature lead to larger particles. The metal oleates are hydrolysed and the growing particles precipitate into the aqueous phase after reaching a critical diameter, which can be controlled by the polarity of the organic phase.

A sol-gel process in solvothermal condition has been investigated by Cara et al.[294] who prepared magnetite NPs starting from Fe^{III} isopropoxide as iron oxide precursor, oleylamine and oleic acid as surfactants, ethanol as solvent and water vapour as hydrolysis agent. To control and reduce the hydrolysis rate, an external compartment of the autoclave was adopted to host the hydrolysis agent (azeotropic ethanol). The amounts of oleylamine, oleic acid, and the reaction temperature were found to be the key parameters to generate different crystallographic phases and to tune crystallite, particle sizes, and size distribution. In particular, the authors found linear dependences between the reaction temperature (140-220 °C) and the crystallite (4-9 nm) and particle (7-12 nm) sizes.

Pinna et al., in 2005, developed a non-hydrolytic sol-gel approach in solvothermal condition, named "benzyl alcohol route", for the preparation of magnetite nanocrystals with tunable sizes between 8 and 25 nm depending on the reaction temperature and postreaction selection. Fe^{III} acetylacetonate was dissolved in benzyl alcohol and treated in an autoclave between 175 and 200 °C, without the use of any additives. Indeed, the benzyl alcohol is considered to act both as a solvent and a ligand.[263] This method produced highly crystalline NPs if compared with other non-aqueous sol-gel methods.

The growth process of spinel iron oxide NPs by a non-aqueous sol-gel method was monitored by Masthoff et al. in 2014.[264] The synthesis was carried out by using Fe(acac)3 as the precursor and benzyl alcohol as the solvent. The synthesis was performed in a 1.5 L polyclave Büchi reactor at 200 °C for 23 h. By XRD and TEM analyses, it was found that at the beginning the particles initially consist of a crystalline core and an amorphous shell, as the process continues the particles are converted in single crystalline particles. Moreover, the spectroscopic analyses (XPS and ^{57}Fe Mössbauer spectroscopy) showed mostly the formation of maghemite. The variation in the reaction time permitted to vary the particle size from 4-10 nm (5 h) to 10-16 nm (23 h).

Yáñez-Vilar et al.[265] prepared different spinel ferrite NPs (manganese, cobalt and nickel ferrite) through aldol condensation of metal acetylacetonates in benzyl alcohol. In this multi-step process, firstly benzyl alcohol reacts with one carbonyl group of the acetylacetonate ligand, followed by the formation of benzyl acetate which coordinates the Fe centre. Secondly, the enolate reacts with the coordinated benzyl alkoxide, releasing 4-phenyl-2-butanone. The

particle formation starts when the Fe-bound hydroxyl group binds another Fe centre.[393] Hexanol has also been proposed as an alternative to benzyl alcohol because it enhances the solvolysis of the Fe-acetylacetonate species, rendering the nucleation step faster than the growth and producing smaller NPs. This effect has been ascribed to the higher Lewis basicity of hexanol with respect to benzyl alcohol.

Another method that is widely employed in solvothermal condition is the polyol method. Indeed, cobalt ferrite,[284] manganese ferrite,[281,286] nickel ferrite,[283] zinc ferrite,[275] magnetite[280] have been successfully prepared to start from metal chlorides or nitrates, in ethylene glycol, triethylene glycol or propanediol. Generally, an electrostatic stabilizer is added to prevent nanoparticle agglomeration, such as sodium acetate,[282,283] ammonium acetate,[280] potassium hydroxide[275,286] or potassium acetate.[283] Furthermore, other additives can be employed, as benzylamine,[281] PEG,[282] polyvinylpyrrolidone (PVP) or citrate.[280]

Magnetite and cobalt ferrite NPs were also prepared in solvothermal condition by thermal decomposition of metal acetylacetonates in benzyl ether, acetophenone, 1-octanol.[273,274,285]

It is worth noting that, although the solvothermal methods have been demonstrated to be efficient on the size tuning of spinel ferrite NPs, a shape control has not been studied so far on these systems. Nonetheless, this goal has been achieved for other nanostructured metal oxides, such as TiO_2,[401] and therefore it seems realistic to expect that differently-shaped spinel ferrite NPs can also be obtained by proper changes in critical parameters (*e.g.* the precursor/surfactant molar ratio).

In the same way of hydrothermal treatments, solvothermal methods can also be microwave-assisted, to add external heating to the reaction and thus decrease reaction time and temperature (paragraph 1.3.4.1).

Solvothermal methods have been used to prepare spinel ferrite NPs in a continuous flow reactor using supercritical organic solvents.[297–301] For instance, Pascu *et al.*[299] synthesised spinel iron oxide and manganese ferrite NPs with size <10 nm in supercritical ethanol. Among the solvents employed in flow reactors, ethanol might be advantageous for several reasons. For instance, the supercritical coordinates of ethanol (pc = 6.39 MPa and T_{sc} = 243 °C) are much lower than those of water (pc = 22.1 MPa and T_{sc} = 374 °C), lowering energy consumption. Ethanol is also preferable over methanol, being non-toxic and obtainable from bio-resources. Nanomaterials synthesized in supercritical ethanol can also be easily collected and the solvent can be recycled.

1.3.4 Methods employing alternative/additional energy source

1.3.4.1 Microwaves

So far, microwave heating has been widely used in organic chemistry and is now opening new opportunities also in the synthesis of inorganic nanomaterials.[402] It permits to lower the reaction times and temperature, and to improve yield and reproducibility. The microwave region goes from 0.3 GHz to 300 GHz. Microwave radiation of proper frequency affects molecular rotations, leading to absorption of energy, generation of heat and consequently to an increase in temperature. The energies involved are not sufficient to break bonds and to lead to direct variations of the chemical structures, that, on the contrary, can be affected by the high temperatures reached during the heating. The oscillating electric field associated with the microwaves, interferes with those generated by dipoles or ions in a material whose motions continuously attempt to follow the microwave electric field. To be efficient, the microwave frequency should be comparable to that of dipolar and ionic movements. The most used frequency is 2.45 GHz, that corresponds to an energy of $1 \cdot 10^{-5}$ eV or 1 $J \cdot mol^{-1}$. Microwave heating is a volumetric or bulk effect. Indeed, the specimen is heated to a certain penetration depth, defined as the depth at which the initial power has dropped to 50% of its original value and inversely depends on the parameter tanδ, defined as:

$$tan\delta = \frac{\varepsilon''}{\varepsilon'} \qquad \text{Eq. 14}$$

Where ε'' is the dielectric loss and ε' is the permittivity. Consequently, high loss materials (with high ε") have low penetration depth, such as metallic objects.[398]

Microwave heating is finding increasing applications in nanomaterial synthesis in combination with other methods, such as hydro/solvothermal,[158,161,163,164,176,275] polyol,[330,332,355,359] *etc*. The advantages of the use of microwaves are several: fast reaction time, repeatability and scalability of the process, uniform and efficient heating at low temperature. However, the process requires special equipment.

1.3.4.2 Sonochemical

Sonochemical or ultrasonic cavitation is an alternative chemistry route also employed for the synthesis of spinel ferrite nanomaterials. [335,363–384] Ultrasonic irradiation provides exceptionally high local temperatures (5000 K) and pressures (20 MPa) in liquids combined with rapid cooling rate (10^{10} $K \cdot s^{-1}$). Furthermore, it can induce exceptional morphological changes in the synthesis of metal oxides, leading to fast reactions, uniform size distributions and high phase purity.[335] The procedure is described as a sonochemical-

assisted co-precipitation. For example, to prepare MFe_2O_4 NPs (M = Mn^{II}, Zn^{II}, Co^{II}, Ni^{II}, Cu^{II}, Fe^{II}), the inorganic salts (chloride, sulfate, acetate, *etc.*) are dissolved into water (or other solvents), then sonicated by using an ultrasonic processor for a particular time (from 15 min to hours), while a base (NaOH, KOH, NH_4OH, *etc.*) is injected into the reaction mixture after starting the sonication. After that, the as-formed NPs can be washed and collected. The intense ultrasonic waves produce the formation of bubbles in the reaction mixture (cavitation) that leads to the generation of H_2O_2. Indeed, during expansion of the cavitation bubble, large amounts of water vapour evaporates into the bubble and diffuses to the core of it. During the ensuing compression phase, the bubble contracts and the vapour starts spreading back to gas-liquid interface. During final moments of the collapse, the bubble wall velocity becomes extremely high, and all the vapour that entered the bubble cannot escape (or diffuse back to the bubble wall and condenses). This water vapour is entrapped in the bubble and is subjected to extreme temperature and pressure and undergoes dissociation to generate radicals:[380]

$$H_2O \rightarrow H^{\cdot} + OH^{\cdot} \qquad \textbf{Eq. 15}$$

The hydroxyl radicals generated by the bubble can recombine to yield hydrogen peroxide that leads to oxidation of hydroxide to oxides, like magnetite (Eq. 19) or other ferrites (Eq. 20):[374]

$$OH^{\cdot} + OH^{\cdot} \rightarrow H_2O_2 \qquad \textbf{Eq. 16}$$
$$H_2O + H^{\cdot} \rightarrow OH^{\cdot} + H_2 \qquad \textbf{Eq. 17}$$
$$2Fe^{II} + H_2O_2 \rightarrow 2Fe^{III} + 2OH^{-} \qquad \textbf{Eq. 18}$$
$$Fe^{II} + 2Fe^{III} + 8OH^{-} \rightarrow Fe_3O_4 + 4H_2O \qquad \textbf{Eq. 19}$$
$$M^{II} + 2Fe^{III} + 8OH^{-} \rightarrow MFe_2O_4 + 4H_2O \qquad \textbf{Eq. 20}$$

Compared with the conventional co-precipitation method, the sonochemical-assisted co-precipitation approach can ensure lower size distribution, faster reaction time, and higher crystallinity. The main parameters that can be modulated are the type of the solvent, the precipitating agent, the feeding rate, the amplitude and time of the ultrasound, and the possibility to insufflate gas.

1.4 Heterostructures

A heterostructure is an all-solid-state multicomponent crystal, distinguished by a spatially controlled distribution of its composition and structure and made of chemically and/or structurally different materials, which are welded together *via* direct solid-state chemically bonded heterointerface, called heterojunction, to form individually distinguishable, solution free-standing multifunctional hybrid nanoplatform.[403,404]

Nanoheterostructures (NHs) can be engineered with various structural and topological diversities, thus exhibit novel properties and functionalities, opening a new horizon of applications.

Generally, NHs can be distinguished in: (i) core-shell architectures, where one component is arranged in concentric or eccentric onion-like, (ii) heterodimers, in which the secondary domains are asymmetrically placed in space through small heterojunctions, leaving a fraction of the surface of each material accessible, and (iii) other geometries, such as hollow boxes, multi-core-shells, yolk-shells, *etc* (Figure 8).

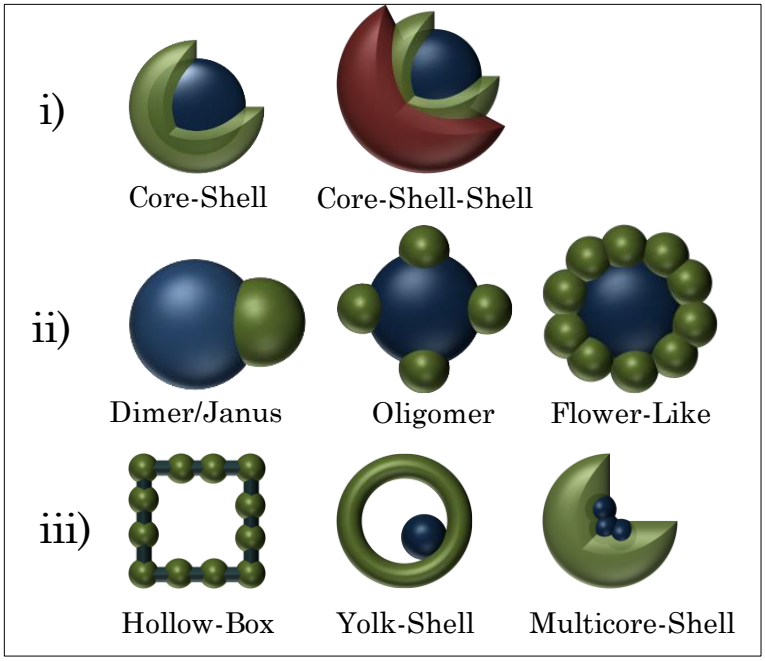

Figure 8. Examples of different heterostructured nanocrystal architectures.

It is essential to distinguish NHs from colloidal nanocomposites, that are constructed by weak interactions (electrostatic or van der Waals) or by linking bifunctional molecules between the building blocks. On the contrary, NHs feature attached domains that grow crystalline, allowing the lattices to have precise crystallographic and spatial relationships.

In this context, spinel ferrite-based heterostructures represent a class of magnetic heterostructured nanocrystals (MNHs) widely studied and with applications in various fields, thanks to the opportunity to tailor their

different properties. In the next paragraph, the most employed synthesis method for spinel ferrite-based heterostructured nanocrystals and their applications will be discussed.

1.4.1 Synthesis methods

Various methods are employed for the synthesis of spinel ferrite-based NHs, summarized in Table 4.

Table 4. Spinel ferrite-based nanoheterostructures prepared by different methods. HT: Hydrothermal. CP: Co-precipitation. TD: Thermal Decomposition.

System	Coupling	Architecture	Synthesis	Seed	Ref
$NiFe_2O_4$@$CoFe_2O_4$	FiM-FiM	Core-Shell	Seeded-Growth (HT)	$NiFe_2O_4$	405
$CoFe_2O_4$@$NiFe_2O_4$	FiM-FiM	Core-Shell	Seeded-Growth (HT)	$CoFe_2O_4$	405,406
$CoFe_2O_4$@γ-Fe_2O_3	FiM-FiM	Core-Shell	Seeded-Growth (CP)	$CoFe_2O_4$	407
$MnFe_2O_4$@γ-Fe_2O_3	FiM-FiM	Core-Shell	Seeded-Growth (CP)	$MnFe_2O_4$	407
$ZnFe_2O_4$@γ-Fe_2O_3	FiM-FiM	Core-Shell	Seeded-Growth (CP)	$ZnFe_2O_4$	408
$CoFe_2O_4$@$MnFe_2O_4$	FiM-FiM	Core-Shell	Seeded-Growth (TD)	$CoFe_2O_4$	243,409–415
$CoFe_2O_4$@Fe_3O_4	FiM-FiM	Core-Shell	Seeded-Growth (TD)	$CoFe_2O_4$	409
$CoFe_2O_4$@$ZnFe_2O_4$	FiM-FiM	Core-Shell	Seeded-Growth (TD)	$CoFe_2O_4$	225
Fe_3O_4@$CoFe_2O_4$	FiM-FiM	Core-Shell	Seeded-Growth (TD)	Fe_3O_4	409,416–418
Fe_3O_4@$MnFe_2O_4$	FiM-FiM	Core-Shell	Seeded-Growth (TD)	Fe_3O_4	416
Fe_3O_4@ $Mn_xZn_{1-x}Fe_2O_4$	FiM-FiM	Core-Shell	Seeded-Growth (TD)	Fe_3O_4	419
Fe_3O_4@$Mn_xFe_{3-x}O_4$	FiM-FiM	Core-Shell	Seeded-Growth (TD)	Fe_3O_4	420–422
$MnFe_2O_4$@$CoFe_2O_4$	FiM-FiM	Core-Shell	Seeded-Growth (TD)	$MnFe_2O_4$	409,412,415
$Zn_{0.4}Co_{0.6}Fe_2O_4$@ $Zn_{0.4}Mn_{0.6}Fe_2O_4$	FiM-FiM	Core-Shell	Seeded-Growth (TD)	$Zn_{0.4}Co_{0.6}Fe_2O_4$	409
$Zn_xCo_{1-x}Fe_2O_4$@ $MnFe_2O_4$	FiM-FiM	Core-Shell	Seeded-Growth (TD)	$Zn_xCo_{1-x}Fe_2O_4$	413
$ZnFe_2O_4$@$CoFe_2O_4$	FiM-FiM	Core-Shell	Seeded-Growth (TD)	$ZnFe_2O_4$	225,423
$MnFe_2O_4$@$CoFe_2O_4$@ $NiFe_2O_4$	FiM-FiM	Core-Shell-Shell	Seeded-Growth (TD)	$MnFe_2O_4$	208
Mn_3O_4@Fe_3O_4	FiM-FiM	Flower	Seeded-Growth (TD)	Mn_3O_4	424,425
Fe_3O_4@Mn_3O_4	FiM-FiM	Core-Shell	Seeded-Growth (TD)	Fe_3O_4	424
FePt@Fe_3O_4	FM-FiM	Core-Shell	Seeded-Growth (TD)	FePt	426
Fe_3O_4@CoO	FiM-AFM	Core-Shell	Seeded-Growth (TD)	Fe_3O_4	427
$CoFe_2O_4$@MnO	FiM-AFM	Core-Shell	Seeded-Growth (TD)	$CoFe_2O_4$	428
CoO@Fe_3O_4	AFM-FiM	Core-Shell	Seeded-Growth (TD)	CoO	429
FeO@Fe_3O_4@MnO	AFM-FiM	Core-Shell-Shell	Seeded-Growth (TD)	FeO@Fe_3O_4	430
Fe_3O_4@Ag	FiM-DM	Flower	Seeded-Growth (TD)	Fe_3O_4	431
Fe_3O_4@Au	FiM-DM	Core-Shell	Seeded-Growth (TD)	Fe_3O_4	432,433
Au@Fe_3O_4	DM-FiM	Janus/Flower	Seeded-Growth (TD)	Au	434–436
Ag@Fe_3O_4	DM-FiM	Janus	Seeded-Growth (TD)	Ag	436–440
Pt@Fe_3O_4	DM-FiM	Janus	Seeded-Growth (TD)	Pt	436
Pd@Fe_3O_4	DM-FiM	Janus	Seeded-Growth (TD)	Pd	436
γ-Fe_2O_3@Au	FiM-DM	Flower	Surface Reduction	γ-Fe_2O_3	441–448
$CoFe_2O_4$@Au	FiM-DM	Flower	Surface Reduction	$CoFe_2O_4$	449–451
$CoFe_2O_4$@Ag	FiM-DM	Flower	Surface Reduction	$CoFe_2O_4$	452
Fe_3O_4@Ag	FiM-DM	Flower	Surface Reduction	Fe_3O_4	448,453

Table 4. Continue.

System	Coupling	Architecture	Synthesis	Seed	Ref
$Au@Fe_3O_4$	DM-FiM	Core-Shell	Surface Oxidation	Au@Fe	454,455
$Au@Fe_3O_4$	DM-FiM	Flower	Surface Oxidation	Au@Fe	434,455–464
$Pt@Fe_3O_4$	DM-FiM	Flower	Surface Oxidation	Pt@Fe	462
$Ag@Fe_3O_4$	DM-FiM	Janus/Core-Shell	Surface Oxidation	Ag@Fe	465,466
$FeO@Fe_3O_4$	AFM-FiM	Core-Shell	Surface Oxidation	FeO	430,467–469
$Co_xFe_{1-x}O@Co_yFe_{3-y}O_4$	AFM-FiM	Core-Shell	Surface Oxidation	$Co_xFe_{1-x}O$	454,470–472
$Fe_3O_4@\gamma\text{-}Fe_2O_3$	FiM-FiM	Core-Shell	Surface Oxidation	Fe_3O_4	473
v	FiM-FiM	Flower	Cation Exchange	Fe_3O_4	474
$Au@CoFe_2O_4$	DM-FiM	Flower	Cation Exchange	$Au@Fe_3O_4$	454
$Co_xFe_{1-x}O_4@CoFe_2O_4$	AFM-FiM	Core-Shell	Cation Exchange	$FeO@CoFe_2O_4$	454
$Mn_3O_4@\gamma\text{-}Fe_2O_3$	FiM-FiM	Hollow-Box	Galvanic Replacement	Mn_3O_4	475
$Fe_3O_4@CoFe_2O_4$	FiM-FiM	Core-Shell	Superlattice Annealing	Fe_3O_4+Co	476
$Ag@Fe_3O_4$	DM-FiM	Flower	One Pot (TD)	-	477
$Ag@Fe_3O_4$	DM-FiM	Flower	One Pot (HT)	-	478
$Ag@Fe_3O_4$	DM-FiM	Flower	One Pot (ST)	-	479

1.4.1.1 Seed-mediated growth

The most employed method is the seed-mediated growth, that consists in the treatment at high temperature of the pre-formed germs for accommodating secondary monodomains of different materials upon heterogeneous nucleation of the respective precursors. The final type of the NHs depends on the sign of the total Gibbs free surface energy change function, ΔG_s (Figure 9 and Eq. 21).

$$\Delta G_S = \gamma_1 - \gamma_2 + \gamma_{1,2} \qquad \textbf{Eq. 21}$$

Where γ_1 and γ_2 are the solid/solution interfacial energies of the bare surfaces of the substrate and of the second material through which the heterojunction will be attained, and $\gamma_{1,2}$ is the solid/solid interfacial energy associated with the formed heterointerface.

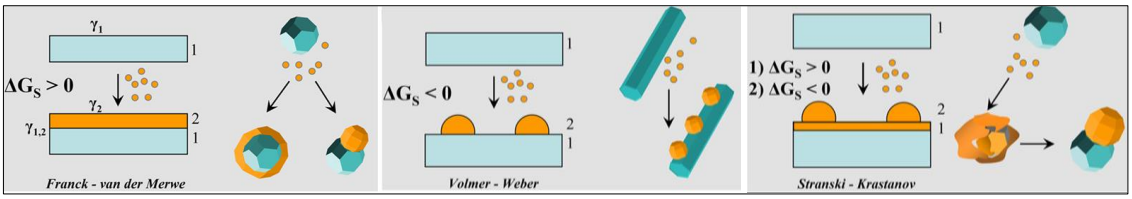

Figure 9. Comparative sketches illustrating possible heterogeneous deposition modes for a secondary material (referred to as "2") that is deposited from the respective molecular precursor on a preformed seed substrate of a different material (referred to as "1"). Adapted with permission from ref. 403. Copyright (2016) Scarfiello, Nobile, and Cozzoli.

This route can lead to the creation of chemical bonds between dissimilar materials and can allow the formation of epitaxial heterointerfaces between the crystalline components. Nevertheless, if the structural dissimilarities of

the different materials do not permit to overcome the energy barrier, different heterogeneous nucleation might happen (Figure 9), or standalone homogeneous nucleation of the second phase.
The method has been successfully applied to produce NHs with dimer (or janus-like),[434–436] flower-like,[424,431,434–436] core-shell,[225,243,405–414,416,419,422,424,426–429,432,433] and core-multishell[208,430] architecture.
Core-shell architectures are preferentially produced when the crystal system of the two components is the same (*e.g.* cubic) and the cell parameters are similar, as when both seeds and shell are isostructural spinel ferrites. In this case, a controllable epitaxial growth is expected, and a core-shell architecture should be obtained. Generally, the method is conducted under thermal decomposition conditions, *i.e.* at high temperature with high-boiling organic solvents and organic complexes precursors (oleates, acetates, acetylacetonates, *etc.*), described in paragraph 1.3.2.1.[208,225,243,409–424] Nevertheless, there are various examples of core-shell NHs obtained by seed-mediated growth through co-precipitation[407,408] or hydrothermal[405,406] syntheses.
Another type of coupling has also been dealt with, such as between the ferrimagnetic spinel ferrites and antiferromagnetic metal oxides.[427–430] For example, by using spinel ferrite as seeds, it is possible to grow a manganese oxide shell[428,430] or a cobalt oxide[427] shell using manganese acetate or cobalt stearate, respectively. Interestingly, Troitiño *et al.*,[429] prepared $CoO@Fe_3O_4$ core-shell nanocubes using CoO nanoparticles as seeds and Fe^{II} acetate as shell precursor, while generally this kind AFM-FiM core-shell NHs are prepared by surface oxidation, as described later.
Spinel ferrite nanoparticles have also been decorated with noble metals, to form janus of flower-like NHs, starting from the spinel ferrite[431–433] or the noble metal[434–439] as seed material. Regarding the first case, gold or silver domains can be formed on magnetite surface using Au^{III} acetate[432,444] or Ag oleate,[431] respectively. On the contrary, spinel ferrite is grown on noble metal seeds using Fe^{III} acetylacetonate or Fe^{III} oleate.

1.4.1.2 Surface Treatment

One of the most straightforward route to fabricate NHs arises from the surface treatment of nanoparticles[430,441–454,467–473] of already formed core-shell nanoparticles[430,434,454,455,457–463,465,466] to obtain heterostructures with different physicochemical properties. Surface treatments can be distinguished into reduction or oxidation, to form noble metal[441–453] of metal oxide[430,434,454,455,457–463,465–473] domains, respectively. The main advantages of the method are the easiness and the inexpensiveness but suffer from the lack of possible combinations and the poor crystallinity of the shell structure and interphase.

For instance, $CoFe_2O_4$-Au flower-like NHs are prepared through sonochemical reduction of $HAuCl_4$ on the cobalt ferrite surface functionalized with DMSA molecules,[449] whereas silver nitrate is employed to be reduced on the spinel ferrite surface to form silver domains.[448,452,453]
Surface oxidation is useful to produce spinel ferrite-noble metal NHs, through the first step of thermal decomposition of $Fe(CO)_5$ on the noble metal (Au/Ag) seeds to produce metallic iron, followed by air oxidation to produce magnetite or maghemite.[434,454–466]
Another important use of surface oxidation is to create metal oxide-spinel ferrite NHs, starting from metal oxide nanoparticles[430,454,467–472] or core-shell with metal oxide shell.[430] In this case, FeO[430,467–469] or $Co_xFe_{1-x}O$[454,470–472] nanoparticles are prepared *via* thermal decomposition of metal oleates. In details, at high temperature the initial reduction of Fe^{III} ions to Fe^{II} occurs due to the breakup of the oleate chain, forming FeO (or $Co_xFe_{1-x}O$). Then, the surface treatment involves a topotaxial transformation of the particle surface through oxidation that leads to Fe_3O_4 (or $Co_yFe_{3-y}O_4$) shell.
Furthermore, surface oxidation may be employed to create maghemite shell in magnetite nanoparticles.[473]

1.4.1.3 Post-synthetic Substitution Reaction

Galvanic replacement and cation exchange reaction represent two versatile and straightforward tools to achieve NHs with shape and composition not easily accomplishable by other methods.[454,474,475] On the contrary, a restricted number of combinations are possible in terms of variety of phases and architectures.
Galvanic reactions are based on electrochemical processes that involve the oxidation of one cation by another cation in solution with higher reduction potential. While galvanic replacement often shows substantial morphology changes (it is used to produce hollow NHs), cation exchange permits to preserves the anionic sublattice and does not modify the nanocrystal shape. For example, Pinna *et al.*,[475] prepared γ-Fe_2O_3 nanocages *via* Mn_3O_4@γ-Fe_2O_3 hollow boxes starting from Mn_3O_4 nanocrystals through galvanic replacement. Mn_3O_4 nanocrystals were placed in the solution together with Fe^{II} perchlorate. The galvanic reaction began with the surface dissolution of Mn_3O_4 and precipitation of γ-Fe_2O_3 on the outermost shell of Mn_3O_4. As the reaction progresses, the electrons released from Fe^{II} migrate inward and reduce the octahedral Mn^{III} in the interior, leading at the end to γ-Fe_2O_3 nanocages.
Cation exchange processes have been applied on metal oxide species to replace the divalent cation and change physicochemical properties without creating or modifying the crystal structure. For instance, Zuddas *et al.*,[474] substituted Mn^{II} in magnetite nanoparticles, creating Fe_3O_4@$Mn_xFe_{3-x}O_4$

core-shell NHs, while Sytnyk and co-workers[454] studied the cation exchange in already formed core-shell nanoparticles. Indeed, they prepared $Au@Fe_3O_4$ and $FeO@CoFe_2O_4$ NHs and performed cation exchange reactions with Co^{II} cations. In both cases Co^{II} substituted Fe^{II}, modifying the shell in the first example (forming $Au@CoFe_2O_4$), and the core in the second one (forming $Co_xFe_{1-x}O@CoFe_2O_4$).

1.4.1.4 Other methods

Less conventional approaches have also been reported in the literature for the synthesis of spinel ferrite based NHs. For instance, magnetite nanoparticles can self-assemble together with Co nanoparticles, giving rise to bi-modal superlattices that, after annealing, can produce $Fe_3O_4@CoFe_2O_4$ core-shell nanoparticles.[476] Other examples are the one-pot reactions between silver and iron oxide precursors to produce flower-like HCNs.[477–479] Thanks to the same crystal system (cubic), the formation of the heterostructure takes place, but it is difficult to avoid the homogeneous nucleation of the component.

1.5 Applications

Spinel ferrites find use in many fields. Here, a brief description of the most important ones is given.

1.5.1 Recording Media

Ferro(i)magnetic (F(i)M) NPs, when magnetized, can retain magnetization (remanent magnetization, M_r) after the removal of the external magnetic field. Therefore, F(i)M NPs can be employed as recording media for magnetic data storage or permanent magnet component to store magnetic energy. Generally, the smaller the ferromagnetic NPs, the higher the recording areal density, but since they must be in the blocked state, there should be a balance between the NPs size and their thermal stability. The energy barrier required should be at least 60 times higher than the thermal energy for commercial NPs.[480] The set-up for magnetic recording are two: hard disk drive (HDD) and magnetic tape (MT) recording.

HDD recording consists of three components: an assembly of ferromagnetic NPs, a write-head, and a read-head. In the writing process, the write-head converts the flux current that carries the digital information into an external flux field.[481] The flux field changes the magnetization direction of a small area of the recording medium under the write-head, reserving what is recorded on the film as one bit. The read-head is made of a giant magnetoresistance sensor and can translate the recorded magnetic bit information back to digitized electric signals. Currently, the magnetic recording medium in a HDD is based on the thin film assembly of ~8.5 nm nanomagnets of CoCrPt made from the sputtering method, which can support recording densities over 750 $Gb \cdot in^{-2}$,[480] but also cobalt ferrite nanoparticles are employed.[482,483]

MT recording is similar to HDD, but it has different configuration. Magnetically softer NPs, such as γ-Fe_2O_3 and FeCo- based NPs, are selected as the standard recording media. But because of the small K, the NPs have to be made in a needle shape to obtain large shape anisotropy, with much larger dimensions than those used in HDD. This leads to a smaller areal density in the magnetic tape media than that in HDD. Since magnetic tape has a larger surface area, the overall storage capacity of a magnetic tape device is comparable to the HDD. With its much lower cost, the magnetic tape recording is playing an important role in big data storage.[484]

Antiferromagnetic-ferro(i)magnetic coupled NHs exhibit exchange bias phenomena,[485–487] that results in a shifted hysteresis loop and increased coercivity, as well as higher blocking temperature and improved thermal stability with respect to the single components, and find progressively extensive use as read-heads in high density magnetic storage disks.[419,428,429,467–469,471]

1.5.2 Permanent Magnets

Spinel ferrite nanoparticles are used as building blocks of a permanent magnet for magnetic energy storage applications. Magnetic NPs require high coercive field and remanent magnetization, to obtain high maximum energy product $(BH)_{max}$, that corresponds to the area of the largest rectangle inside the second quadrant of the B−H hysteresis loop. The higher the $(BH)_{max}$, the smaller the magnet needed for a given energy storage/output in magnetic devices. Hard-soft materials ideally combines the desirable properties of the hard (high H_c) and soft (large M_s) counterparts and are widely studied as high energy storing materials for permanent magnets.[422,424,470]

1.5.3 Catalysis

Thanks to their surface/volume ratio, spinel ferrite NPs are excellent heterogeneous catalysts for chemical reactions. Indeed, spinel iron oxides are used in a significant number of reactions such as the synthesis of styrene, photocatalytic production of hydrogen and oxygen, removal of carbon monoxide, catalytic conversion of methane in aromatic compounds, thermal decomposition of ammonium perchlorate as well as in water treatment, catalytic decomposition of hydrogen peroxide, fuel cells and in the production of biodiesel.[488–492]

Again, spinel iron oxide NPs are employed, dispersed in silica mesostructures, as sorbents for the removal of heavy metals, pollutants, *etc.*[488,493] For instance, mesostructured silica-based maghemite NPs have been recently applied, thanks to their high efficiency and regenerability, for sulfur compounds removal in desulfidation processes at mid temperature.[494,495] The involved reaction is:

$$Fe_2O_3 + 3H_2S \rightarrow Fe_2S_3 + 3H_2O \qquad \textbf{Eq. 22}$$

Being that Fe_2S_3 is a thermodynamically unstable phase, it easily converts to pyrite (FeS_2) and Fe_3S_4 or pyrite, pyrrhotite (FeS_x), and sulfur:

$$2Fe_2S_3 \rightarrow FeS_2 + Fe_3S_4 \qquad \textbf{Eq. 23}$$

$$Fe_2S_3 \rightarrow \alpha FeS_2 + \beta FeS_x + \gamma S \qquad \textbf{Eq. 24}$$

Where α, β, and γ are the relative molar amounts. The regeneration process conducted at mid-temperature (500 °C) permits to re-obtain iron oxide through the following reaction:

$$4FeS + 3O_2 \rightarrow 2Fe_2O_3 + \frac{1}{2}S_8 \qquad \textbf{Eq. 25}$$

Spinel ferrite NPs can also be used as supports to anchor homogeneous catalysts, to stabilize and to recycle them for long-term use. Their insoluble nature and strong response to an external magnetic field, spinel ferrite NPs can be an ideal platform on which a catalyst can be anchored and recycled by magnetic separation, eliminating the necessity of filtration. For example, Ag decorated spinel ferrite nanoparticles are employed for water purification purposes.

Gold-spinel ferrite NHs are employed as catalysts for various reactions, such as 4-nitrophenol reduction,[435,446] CO oxidation,[464] and H_2O_2 reduction.[456]

Silver-spinel ferrite NHs are instead used for the reduction of Rhodamine B in the presence of $NaBH_4$[496] or methyl orange,[452] for purification of dye effluents.

1.5.4 Magnetic Separation

Magnetic separation is a process used to separate magnetic materials from those that are less or non-magnetic. Magnetic forces pull the magnetic NPs, while frictional, gravitational and inertial forces pull the others. Specifically, in a magnetic separator, a stainless steel column is packed with a stainless steel wool, placed between two poles of an electromagnet producing magnetic field from 0 to several T. When a magnetic field is applied during the process, the wool dehomogenizes the magnetic field resulting in large field gradients around the wool that attract and trap magnetic particles. The attraction of the NPs highly depends on the generation of the magnetic field gradients as well as the size and magnetization of the particles.[497,498] Magnetic separation is the key of different applications such as cell separation, drug delivery, waste management in the mining industry, or water purification. For instance, the main problem of conventional drug delivery is the inability to target a specific site, therefore large doses are used to reach the desired location, which can cause toxic effect or non-target organs. Magnetic guidance and separation could then be used to target specific sites, reducing the side effects of conventional drug delivery and increasing the concentration of drugs at the desired locations.

1.5.5 Biomedical Applications

Spinel ferrite NPs, especially in the superparamagnetic state, have been extensively studied for their biomedical applications, among them drug delivery, magnetic resonance imaging (MRI), and magnetic fluid hyperthermia (MFH). To be applied in this field, NPs must satisfy some specific requirements, such as non-toxicity, negligible remanent magnetization, good morphological and structural properties, chemical and colloidal stability, *etc.*[5,9,499–506]

1.5.5.1 Magnetic Resonance Imaging

Due to the superparamagnetic behaviour and high magnetic moments in an external magnetic field, these NPs stabilized in biological environments can respond quickly to an external magnetic field, generating a secondary field around each NP and interfering with the proton nuclear spin relaxation. Such NPs can serve as sensitive magnetic probes (contrast agents) in magnetic resonance imaging (MRI). MRI is an imaging technique that measures the difference of proton nuclear magnetic resonance of water molecules around solid tissue and its surrounding biological solution. In a strong permanent magnetic field, the proton nuclear spins can be split into low-energy (along the magnetic field) and high-energy (against the magnetic field) states. When a secondary electromagnetic radio frequency pulse is applied at the resonance frequency (also called Larmor frequency), the low-energy spins can absorb the radio frequency energy, and as a result, the spin direction can be switched from the low-energy state to the higher energy state. Once the pulse is turned off, the excited spins tend to relax to their original low-energy state, generating two simultaneous and independent relaxation processes: longitudinal (T_1) relaxation process and transverse (T_2) relaxation process. The T_1 process allows the spins to "realign" along the permanent magnetic field direction, releasing the absorbed RF energy into the surrounding; the method is also called spin-lattice relaxation. The T_1 relaxation time is referred to as the time required for the longitudinal magnetization value to recover approximately 63% of its original value. The T_2 process causes the decay of transverse magnetization due to the random spin-spin interaction/ dephasing; this process is also called spin-spin relaxation. The T_2 relaxation time is determined by the time it takes for the transverse magnetization to decay to 37% of its original value. The efficiency of a contrast agent is usually expressed by its relaxivity r_i (i = 1, 2), which is defined by the change in relaxation rate $\Delta(1/T_i)$ after the introduction of a contrast agent. Its unit is $mM^{-1}\cdot s^{-1}$. The larger the r_i, the better the MRI sensitivity. MRI contrast agents are used to enhance the proton relaxation rates to improve the MRI sensitivity. The most common T_1 enhancement agents are complexes based on Gd^{III} with seven unpaired electrons.[507] Superparamagnetic spinel ferrite NPs are also studied T_1 contrast agents, [508–511] but thanks to the high magnetization values, they can significantly shorten the T_2 relaxation time of the nearby protons, reducing the proton signal intensity and darkening the T_2-weighted MR images, and are therefore mostly employed as T_2 contrast agents.[512–515]

1.5.5.2 Magnetic Fluid Hyperthermia

Under an alternate magnetic field, magnetic NPs can convert the magnetic energy into thermal energy. As cancer cells are more sensitive to heat than the normal ones, the heat generated from the NPs around the cancerous area can inhibit the cancer growth or even destroy these cancer cells.[499,500,502,503] This physical approach for cancer therapy is referred to as magnetic fluid hyperthermia (MFH).

The heat can be generated by the nanoparticles through hysteresis losses (for multi-domain or blocked single-domain ferro(i)magnetic NPs), or relaxation losses (for superparamagnetic NPs). According to the linear response theory,[516,517] the heat released by a superparamagnetic nanoparticle depends on the out-of-phase component (χ'') of the magnetic susceptibility (Eq. 26).

$$P = \mu_0 \pi \chi'' f H_0^2 \qquad \textbf{Eq. 26}$$

Where P is the power loss ($W \cdot m^3$), μ_0 is the permeability in free space ($4\pi \cdot 10^{-7}$ $T \cdot m \cdot A^{-1}$), f the frequency (s^{-1}), and H_0 the amplitude ($A \cdot m^{-1}$) of the applied magnetic field. χ'' is expressed in Eq. 27.

$$\chi'' = \frac{\omega\tau}{1 + (\omega\tau)^2}\chi_0 \qquad \textbf{Eq. 27}$$

ω is the angular frequency ($2\pi f$), τ the effective relaxation time (s, Eq. 31), and χ_0 the actual susceptibility, expressed in Eq. 28.

$$\chi_0 = \chi_i \frac{3}{\xi}(coth\xi - \frac{1}{\xi}) \qquad \textbf{Eq. 28}$$

χ_i is the susceptibility calculation parameter (Eq. 29) and ξ the Langevin parameter (Eq. 30).

$$\chi_i = \frac{\mu_0 \phi M_d^2 V_m}{3 k_B T} \qquad \textbf{Eq. 29}$$

$$\xi = \frac{\mu_0 M_d H_0 V_m}{k_B T} \qquad \textbf{Eq. 30}$$

ϕ is the NPs' volume fraction, M_d the domain magnetization of the NPs ($A \cdot m^{-1}$), V_m the NPs' volume (m^3), k_B the Boltzmann constant ($1.380 \cdot 10^{-23}$ $J \cdot K^{-1}$), T the temperature (K).

$$\tau = \frac{\tau_N \tau_B}{\tau_N + \tau_B} \qquad \textbf{Eq. 31}$$

τ_N is the Néel relaxation time (Eq. 32), while τ_B is the Brown relaxation time (Eq. 33) and are associated to the vector magnetization reversal inside and through physical rotation of the particle, respectively.

$$\tau_N = \tau_0 e^{\frac{KV_m}{k_B T}} \quad \text{Eq. 32}$$

$$\tau_B = \frac{3\eta V_H}{k_B T} \quad \text{Eq. 33}$$

τ_0 is the characteristic relaxation time (10^{-9}-10^{-11} s), K the magnetic anisotropy constant (J·m^3), η the viscosity of the solution (Pa·s), and V_H the hydrodynamic volume of the NPs (m^3). These equations are valid only for a monodisperse system. Eq. 34 reports the description of the heat released per volume unit from a log-normal distributed NPs system.[517]

$$\overline{P} = \int_0^\infty P\, g(R) dR \quad \text{Eq. 34}$$

$$g(R) = \frac{1}{\sqrt{2\pi}\sigma R} exp\left[\frac{-(lnR/R_0)^2}{2\sigma^2}\right] \quad \text{Eq. 35}$$

Where Eq. 35 is the log-normal function. The linear response theory is valid only for superparamagnetic nanoparticles, but frequently real samples, especially those in the SPM-F(i)M edge, present both relaxation and hysteresis losses.[518]

The theory reveals that the power heat strongly depends on the frequency and amplitude of the applied field. However, for clinical applications, it is not possible to exceed a threshold of the product $f \cdot H_0$, due to side effects in the patients as the generation of eddy currents (Eq. 36). Eddy currents are produced in conductive materials by the alternate magnetic field due to the Faraday's law of induction.

$$P_{eddy} \sim \pi a \sqrt{\left(\frac{\pi f \mu}{\sigma_{FM}}\right)} H_0^2 L \quad \text{Eq. 36}$$

Where a is the radius and L the length of the particle, μ e is the magnetic permeability, and σ_{FM} is the conductivity of the ferromagnetic material.[519] The threshold should be equal to $5 \cdot 10^9$ A·m^{-1}·s^{-1} for a loop diameter of 30 cm and one hour of treatment.[520]

The linear response theory for superparamagnetic nanoparticles reveals that, besides the external parameters f and H_0, the released heat depends on parameters internal at the nanoparticle, that is saturation magnetization, anisotropy, and volume (magnetic and hydrodynamic). The dependence of the heat release with these parameters is reported in Figure 10.

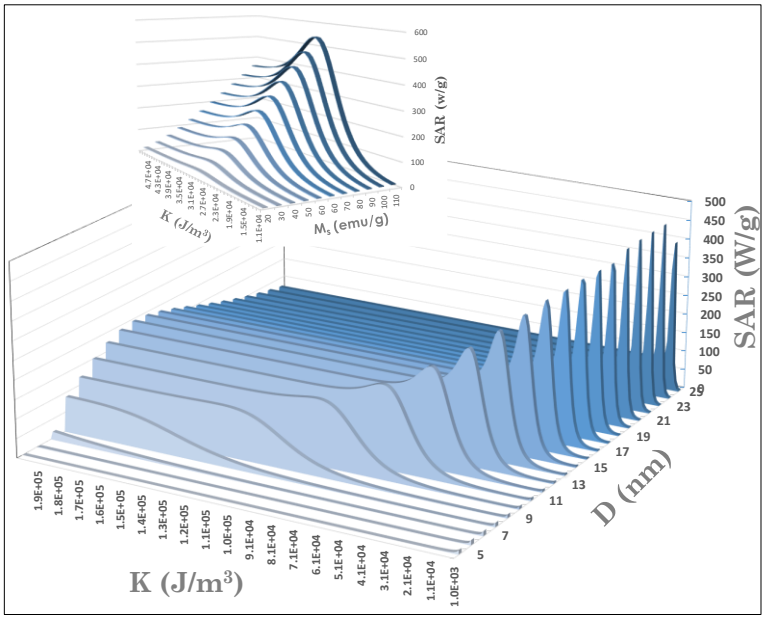

Figure 10. Simulated plot of SAR based on nanoparticle size (*D*) and magnetic anisotropy (*K*) at a saturation magnetization M_s = 80 Am²/kg. Inset: simulated plot of SAR based in *Ms* and *K* for 13 nm nanoparticle. Simulation is based on the linear response theory.

The other parameters used for the simulation besides *D*, *K*, and M_s are reported in Table 5.

Table 5. Parameters used for the SAR simulation.

Parameter	*f* (Hz)	H_0 (A/m)	ρ (g/m³)	T (K)	φ	τ_0 (s)	η (Pa·s)	V_H
Value	183000	17000	$5.3 \cdot 10^6$	303.15	0.00064	10^{-9}	0.000894	6 nm increase to D

Generally, the heat released is expressed in term specific absorption rate (SAR) or specific loss power (SLP), that have the unit of power per unit mass (W/g):

$$SAR = SLP = \frac{P}{\varrho\phi} \qquad \textbf{Eq. 37}$$

Where ρ is the NPs density ($g \cdot m^3$). As shown in Figure 10, SAR has a maximum for a specific value of D and K. Indeed, the anisotropy constant affects the Néel relaxation time, while *D* affects both the Nèel (in terms of magnetic volume) and Brown (in terms of hydrodynamic volume) relaxation times. The maximum is located between $1\text{-}7 \cdot 10^4$ $J \cdot m^3$ for what concerns the magnetic anisotropy and 20 nm for nanoparticle diameter, even if shows high value in a wide range between 6 and 25 nm. The inset of Figure 10 shows the dependence of SAR with the saturation magnetization for a 13 nm nanoparticle having *K* between $1 \cdot 10^3$ and $2 \cdot 10^5$ J m^3 and it is clear that the higher the saturation magnetization, the higher the SAR. Therefore, it is imperative to finely tune these parameters by choosing an adequate material

and synthesis method. The dependence of the total relaxation time on the Brown and Néel ones is reported in Figure 11.

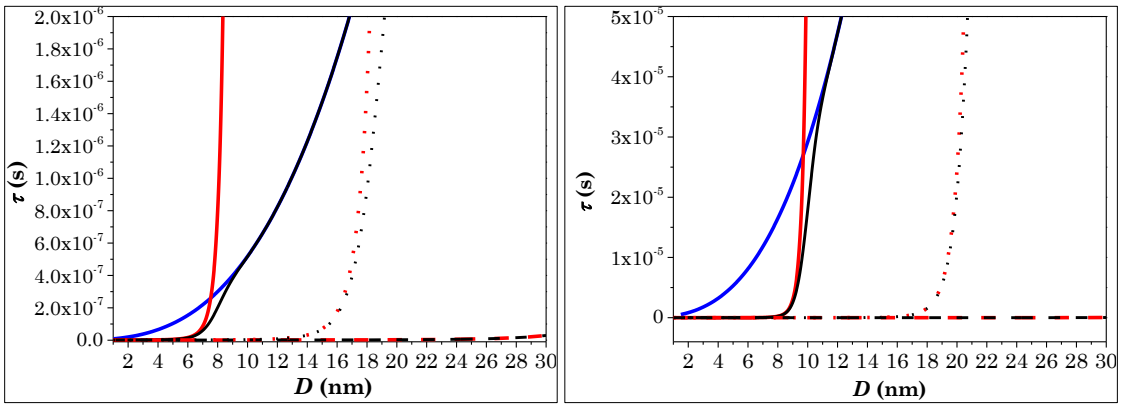

Figure 11. Left side: entire relaxation time (black line), Nèel relaxation time (red line), and Brown relaxation time constant (blue line) versus particle diameter calculated for different anisotropy constant: $1{\cdot}10^5$ (solid), $1{\cdot}10^4$ (dot), and $1{\cdot}10^3$ (dash) J m^{-3}. Right side: calculation assuming the hydrodynamic volume of 4 aggregated particles.

The plot shows that the shorter time constant tends to dominate in determining the effective relaxation time for any given size of the particle, intended as the inorganic diameter (Eq. 31). Generally, the higher the anisotropy constant of the system, the faster the Néel relaxation time rise with increasing the particle size. Therefore, for $K = 1{\cdot}10^5$ J·m^{-3} (Figure 11, left side, solid lines), τ mainly depends on τ_N up to a particle size of 6 nm and on τ_B beyond 9 nm, while for $K = 1{\cdot}10^4$ J·m^{-3} and $1{\cdot}10^3$ J·m^{-3} τ_N dominates up to 16 and 30 nm, respectively (Figure 11, left side, dot and dash lines). Interestingly, often more than one particle contributes to the Brown relaxation time, due to particle aggregation. As can be seen in Figure 11, right side, when 4 particles aggregates, τ_B grows more quickly with the particle size and the critical diameter for the dependence of the total τ with τ_N is shifted at higher values, that is 9 nm for $K = 1{\cdot}10^5$ J·m^{-3} and 20 nm for $K = 1{\cdot}10^4$ J·m^{-3}.
It should be highlighted that the linear response theory is valid only for superparamagnetic nanoparticles. Indeed, when NPs size is approaching the superparamagnetic limit, hysteresis losses start to be significant. Experimentally, SAR values are obtained by the following equation:

$$SAR = \frac{\sum_i m_i C_i}{m_{NPs}} \frac{\Delta T}{\Delta t} \qquad \text{Eq. 38}$$

Where m_i and C_i are mass and specific heat of the i^{th} species composing the sample, m_{NPs} is the total NPs mass and ΔT is the temperature increase in the interval Δt during which the AC field is applied.[521]
15 nm iron oxide with an aminosilane coating (NanoTherm™) developed by MagForce® Nanotechnologies GmbH is the only heat mediator approved for human application by the European regulatory.[522] Many efforts have been spent over the last decade on magnetic fluid hyperthermia treatment, and

different magnetic materials have been proposed, especially spinel ferrite nanoparticles.[10,13,18,409,516,523–537]

In the literature, various systems have been proposed as heat mediator for MFH treatments, such as metallic NPs,[538–542] magnetosomes,[543–545] spinel iron oxide NPs,[10,13,18,409,516,523–531,533–537] manganese ferrite NPs,[409,534] cobalt ferrite NPs,[10,409,534,546–550] substituted-ferrite NPs,[551–553] and hard-soft spinel ferrite NPs.[246,409,412–418,423,554–556]

The latter system has attracted great attention thanks to the possibility to finely tune size, saturation magnetization, and magnetic anisotropy with the magnetic coupling between a hard and a soft ferrimagnetic phase.

2 *Oleate-Capped $M^{II}Fe_2O_4$ (M^{II} = Co^{II}, Mn^{II}, Fe^{II}) Nanoparticles: Synthesis and Characterization*

Abstract

A solvothermal method was explored to synthesize spinel iron oxide (γ-Fe_2O_3/Fe_3O_4), cobalt ferrite ($CoFe_2O_4$) and manganese ferrite ($MnFe_2O_4$) of different sizes. All samples were characterized from the compositional, structural, morphological and magnetic point of view. The method permitted to obtain single spinel phases and to finely tune the size of the product by modifying synthetic parameters such as temperature, organic solvent polarity, and precursor concentration. The heating abilities of the cobalt ferrite nanoparticles were also tested.

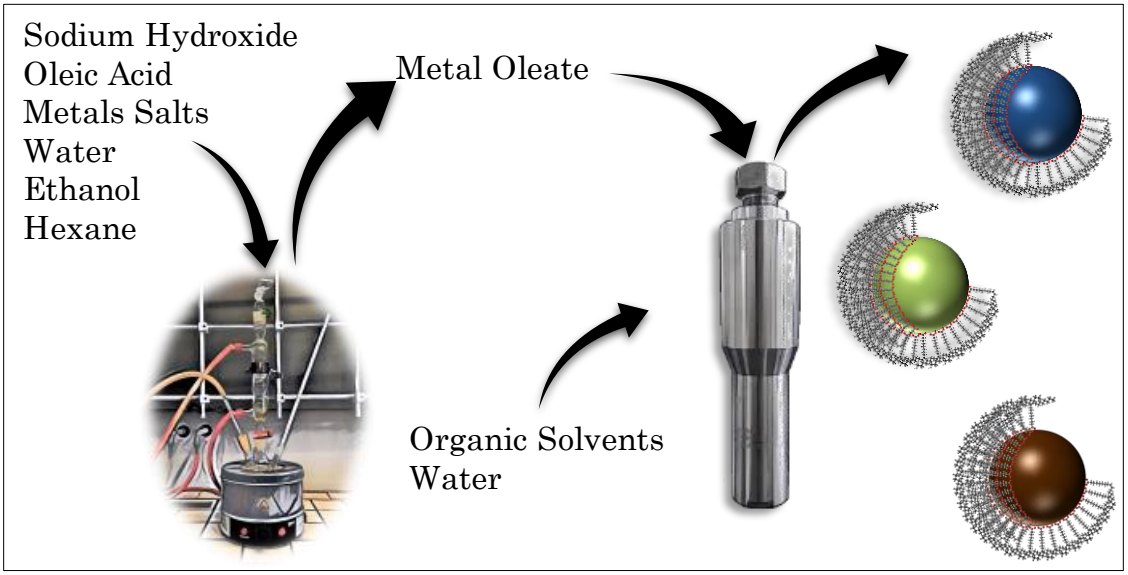

2.1 Introduction

Spinel ferrite nanoparticles represent a multipurpose material utilized in a wide range of application, from catalysis to biomedicine.[505,557–559] Indeed, the physical and chemical properties can be easily modulated by changing size, shape, divalent cations, capping agent, *etc*., and it is, therefore, necessary to use a very versatile synthetic strategy to design the material with the desired features properly.

Among the spinel ferrites, cobalt ferrite deserves particular attention, being the only magnetically hard one, with a magnetocrystalline anisotropy constant for bulk materials equal to $2.9 \cdot 10^5$ J·m^{-3}. On the contrary, manganese ferrite and spinel iron oxide (magnetite/maghemite) are magnetically soft (two orders of magnitude lower compared to cobalt ferrite), with low magnetocrystalline anisotropy constant (Table 1), but very high saturation magnetization (88-100 Am^2·kg^{-1}). Furthermore, maghemite and magnetite are biocompatible (U.S. Food and Drug Administration approved)[560] and low-cost. For these reasons, spinel iron oxide, cobalt, and manganese ferrites are the most studied spinel ferrite materials. Among the numerous synthetic approaches present in the literature, one of the most adopted is the surfactant-assisted thermal decomposition of organic complexes or organometallic compounds, due to the excellent size and shape control. Nevertheless, as anticipated in paragraph 1.3.3, the main drawback of this method are the high number of parameters to be controlled and the consequent difficulty in repeating the synthesis under the same experimental conditions, the complexity of the experimental equipment (vacuum or inert gas atmospheres, reliable temperature and pressure controllers), and the high amount and toxicity of the solvents and precursors. In the last decade, solvothermal methods have drawn particular attention, due to high repeatability, size control, high crystallinity and low dispersity of the products, the use of low boiling organic solvents and mild temperatures.

In this chapter, cobalt ferrite, manganese ferrite, and spinel iron oxide nanoparticles are synthesized *via* a solvothermal method and characterized by the compositional, structural, magnetic and morphological point of view. Emphasis is given to the dependency of the chemical and physical properties over the size of the nanoparticles. The cobalt ferrite samples were also tested as heat mediators for magnetic fluid hyperthermia.

2.2 Synthesis

The synthesis of $CoFe_2O_4$, $MnFe_2O_4$ and γ-Fe_2O_3/Fe_3O_4 was performed following the procedure set up by A. Repko *et al.*,[561] through solvothermal hydrolysis of mixed metal oleates previously prepared. Two samples of cobalt ferrite were prepared to replace oleic acid with palmitic or stearic acid.

2.2.1 Metal Oleate Synthesis

The mixed M^{II}-Fe^{III} oleates (M^{II} = Co^{II}, Mn^{II}) were used as metal precursors for the synthesis of $CoFe_2O_4$ or $MnFe_2O_4$, respectively, while a mixture of Fe^{II}-oleate and Fe^{III}-oleate, prepared separately, was used to synthesize γ-Fe_2O_3/Fe_3O_4 nanoparticles. The molar ratios among the reactants are given in Table 6 for the different metal oleates.

Table 6. Synthesis condition for the different metal oleates.

Metals Oleate	Inorganic salts	Oleic acid	NaOH	Ethanol	Water	Hexane
Co^{II}-Fe^{III}	$Fe(NO_3)_3$: 16 mmol $Co(NO_3)_2$: 8 mmol	65 mmol	66 mmol	20 mL	20 mL	20 mL
Mn^{II}-Fe^{III}	$Fe(NO_3)_3$: 16 mmol $Mn(NO_3)_2$: 8 mmol	65 mmol	66 mmol	20 mL	20 mL	20 mL
Fe^{II}	$FeCl_2$: 24 mmol	60 mmol	54 mmol	20 mL	20 mL	20 mL
Fe^{III}	$Fe(NO_3)_3$: 21 mmol	66 mmol	64 mmol	20 mL	20 mL	20 mL

A sodium oleate solution was prepared in a 250 mL round-bottom flask by dissolving sodium hydroxide in 10 mL of distilled water and adding 20 mL of ethanol together with the oleic acid. Then, the iron(III) nitrate and Me(II) nitrate (M^{II} = Co^{II}, Mn^{II}) or only iron(II) chloride or iron(III) nitrate were dissolved in 10 mL of distilled water. This was then added into the sodium oleate solution and mechanically stirred to obtain the M^{II}-Fe^{III} oleate, the Fe^{II}-oleate, or the Fe^{III}-oleate. After the addition, the formation of the metals oleate complexes made the solution black and viscous. The successive addition of 20 mL of hexane led to a liquid biphasic system, the upper phase is the metals oleate containing organic phase while the lower is the water phase. This mixture was boiled under reflux for 60 min to complete the formation of metal oleates. The as-described procedure was carried out under an inert atmosphere in the case of the Fe^{II} oleate synthesis. Then, the system was left to cool down to room temperature. The aqueous phase was removed with a Pasteur pipette, while 20 mL of water, 5 mL of ethanol and 5 mL of hexane were added into the organic phase. The mixture was boiled under reflux for 30 min. This washing step was performed twice. Finally, the aqueous phase was removed entirely and 15 mL of 1-pentanol were added into the flask. The mixture was heated for about 30 min to induce the complete evaporation of hexane. The obtained product as a viscous black

liquid (dark red for the Fe^{III}-oleate) was transferred into a 40 mL glass vial with the help of 5 mL of 1-pentanol. The composition of the product, *i.e.* the final amount of pentanol and consequently the concentration of metals oleate was estimated from its weight, assuming quantitative yield from metals salts.

2.2.2 Solvothermal Synthesis of Spinel Ferrite Nanoparticles

$CoFe_2O_4$, $MnFe_2O_4$ and γ-Fe_2O_3/Fe_3O_4 were prepared by solvothermal hydrolysis of mixed Co^{II}-Fe^{III}-, Mn^{II}-Fe^{III}-, and Fe^{II}-oleate and Fe^{III}-oleate respectively, in a mixture of organic solvents and water. A summary of the synthesis conditions for each sample is reported in Table 7.

Table 7. Synthesis condition for spinel ferrite nanoparticles.

Label	System	n Oleate (mmol)[a]	1-pentanol (mL)	Octanol (mL)	Toluene (mL)	Distilled water (mL)	Temperature (°C)
CoA	$CoFe_2O_4$	6	20	-	-	10	180
CoB	$CoFe_2O_4$	6	10	10	-	5	180
CoC	$CoFe_2O_4$	6	10	10	-	5	220
CoD	$CoFe_2O_4$	6	10	-	10	5	220
CoE	$CoFe_2O_4$	3	10	-	10	5	220
CoF	$CoFe_2O_4$	2.75	10	-	10	5	220
CoG	$CoFe_2O_4$	2*	10	-	10	5	220
MnA	$MnFe_2O_4$	6	10	10	-	5	220
MnB	$MnFe_2O_4$	6	10	-	10	5	220
MnC	$MnFe_2O_4$	3	10	-	10	5	220
MnD	$MnFe_2O_4$	2*	10	-	10	5	220
MnE	$MnFe_2O_4$	*	10	-	10	5	220
FeA	γ-Fe_2O_3/Fe_3O_4	6	10	10	-	5	220
FeB	γ-Fe_2O_3/Fe_3O_4	6	10	-	10	5	220
FeC	γ-Fe_2O_3/Fe_3O_4	3	10	-	10	5	220
FeD	α-Fe_2O_3	2*	10	-	10	5	220
FeE	γ-Fe_2O_3/Fe_3O_4	*	10	-	10	5	220

***With the presence of 25 mg of seeds.**

The metal oleates were prepared separately, to avoid the formation of by-products and reduce size-dispersion of the products.[561,562] The formation mechanism of the nanoparticles has been already described by Repko *et al.*[561,562] In solvothermal conditions, water hydrolyses the oleate and the formation of nanoparticles takes place upon nucleation and growth in the organic phase until they reach a critical diameter, which bring them to precipitate. At the end of the treatment a black precipitate is found at the bottom of the teflon liner, with two liquid phases being present, an aqueous and an organic one. The aqueous phase is always colourless indicating, as expected, that no particles are present in it. On the contrary, the colour of the organic phase becomes gradually darker with the decrease of solvent polarity due to the presence of hydrophobic oleate-capped nanoparticles with a size

below the critical diameter necessary to precipitate. The appropriate amount of metal oleates in 1-pentanol was transferred into a 50 mL teflon liner and a further amount of a mixture of other solvents (octanol or toluene) was added to reach a total volume of 20 mL, as described in Table 7. Then, 10 or 5 mL of water, depending on the reaction temperature, were added. The solvents and their relative ratios were chosen according to the study by Repko *et al.*[561] to prepare particles of different sizes. The liner-free space was flushed with nitrogen and was enclosed in a stainless-steel autoclave (Berghof DAB-2), briefly shaken and put vertically into a pre-heated (180° or 220 °C) oven. The reaction time was 10 hours. After the heat treatment, the autoclave was left to cool down to room temperature, and the as-prepared magnetic nanoparticles were magnetically separated from the supernatant that was then discarded. A purification process was carried out twice as follows. First, the particles were dispersed in 10 mL of hexane (with the help of sonication), then 10 mL of ethanol were used to wash and precipitate the nanoparticles that were finally separated by a magnet. At the end of this step, the nanoparticles were dispersed in 5 mL of hexane and centrifuged at 3000 rpm for 5 min. The supernatant, which is the desired product in this case, was collected and the precipitate was discarded (~2%). The nanoparticles concentration was estimated by sampling an aliquot of the colloidal dispersion, drying it and weighing it. It is worthy of note that solvent polarity (by using 1-octanol or toluene together with 1-pentanol), reaction temperature (180 °C or 220 °C), and precursor concentration play the leading role in the nanoparticle's growth and their final size.

Three replicas of the CoG, MnC and FeC samples were performed to test the repeatability of the method.

The CoG, MnD, and FeD samples were obtained by a post-synthesis solvothermal treatment of an aliquot of the CoF, MnC, and FeC samples, by adding 2 mmol of metal oleate precursor (seed-mediated growth). Around 25 mg of the nanoparticles were dispersed in 10 mL of toluene and added to the teflon liner together with 2 mmol of metal oleate, 10 mL of 1-pentanol- and 5 mL of water. Finally, the liner was enclosed into the autoclave and treated at 220 °C for 10 hours. After the heat treatment, the washing steps were performed in the same as previously described.

The sample MnE and FeE were obtained by a post-synthesis solvothermal treatment, with no addition of any metal oleate precursor, of the sample MnC and FeC, respectively. The procedure was the same as described above for CoG, MnD, and FeD.

2.2.3 Post-synthesis surface treatments

The hydrophobic nanoparticles where converted into hydrophilic one by intercalation process with cetyltrimethylammonium bromide (CTAB,

($C_{16}H_{33}$)N(CH_3)$_3$Br) or by exchange ligand with polyethylene glycol trimethoxysilane (PEG-TMS).[563,564]

In the intercalation procedure, around 13.6 mg of inorganic sample were dispersed with 1 mL of toluene, which was slowly added under stirring to a 4 mL water solution of 0.1 g of CTAB. The dispersion was stirred for 1 hour at room temperature until it became murky-brown, due to the CTAB molecules that intercalate the capping agent stabilizing the magnetic oil droplets leading to the formation of an oil-in-water microemulsion.[565] Subsequent, the mixture was heated for another hour at 60 °C to form a limpid black-coloured dispersion. The evaporation of the volatile organic solvent by mild heating drives CTAB molecules to directly interact with the magnetic nanoparticles surface ligands through hydrophobic interactions. The CTAB alkyl chains and the nanoparticles surface ligands intercalate into each other, rendering the CTAB cationic headgroup (quaternary amine) facing outward and the magnetic nanoparticles-CTAB complex water-soluble.[566,567]

In the exchange ligand procedure, around 6 mg of inorganic particles where dispersed in 30 mL of hexane containing 0.01% (v/v) acetic acid. Then, 0.5% (v/v) of PEG-TMS was added into the mixture and let under stirring in a rotor for 72 hours, during which the particles sedimented. The black-brown precipitate was separated using a magnet and washed three times with hexane to remove all silanes in excess. The product was re-dispersed in distilled water.

The concentration of the colloidal dispersions was 3.4–4.0 $mg \cdot mL^{-1}$ for all the samples.

2.3 Characterization

2.3.1 Powder X-Ray Diffraction (XRD)

Powder X-ray diffraction patterns have been measured for all samples to study their structure (Figure 12).

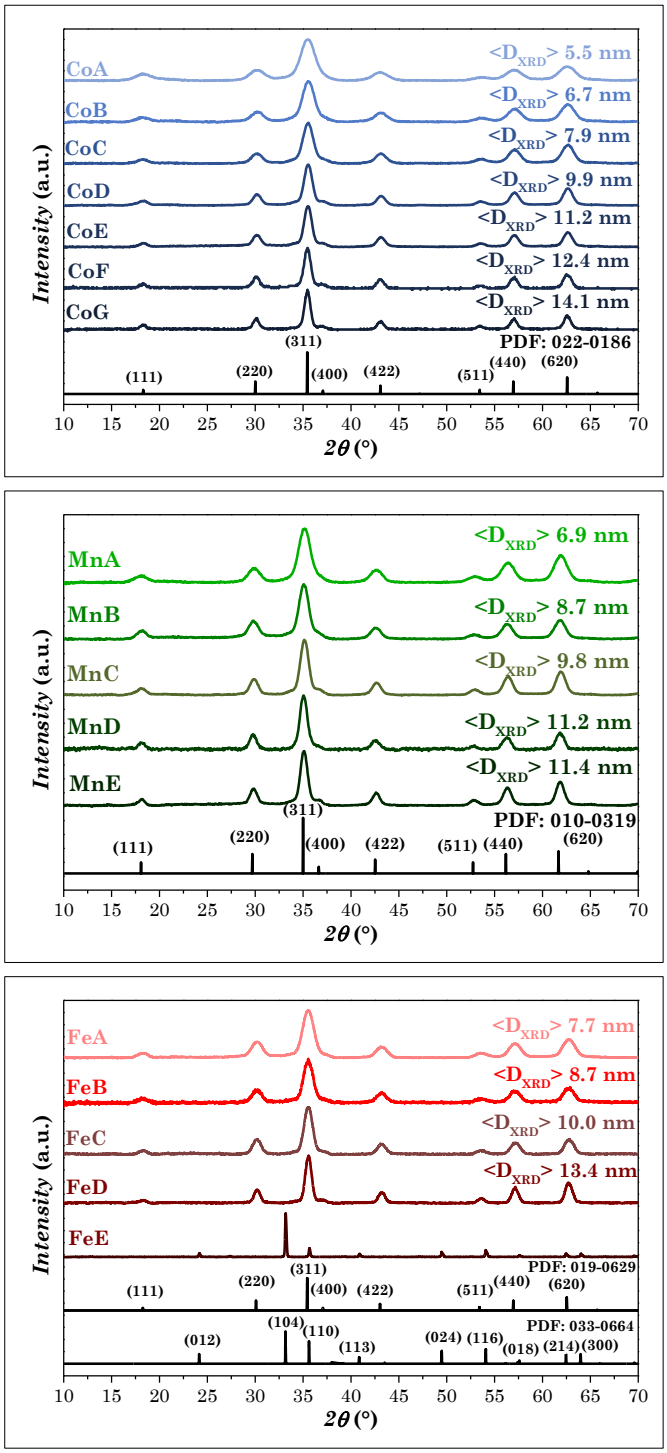

Figure 12. XRD Patterns of cobalt ferrite, manganese ferrite, and spinel iron oxide nanoparticles.

All patterns show diffraction peaks ascribable only to nanostructured spinel ferrites except for the sample FeE, which consists of hematite. The cell

parameters, a, reported in Table 8, are in good agreement with the value for cobalt ferrite and manganese ferrite in the literature (8.3919 Å, PDF Card: 022-1086 and 8.4990 Å, PDF Card: 010-0319, respectively). Spinel iron oxide samples feature a cell parameter of about 8.37(1) Å, which is between the value of maghemite (8.3515 Å, PDF Card: 039-1346) and magnetite (8.3960 Å, PDF Card: 019-0629), but closer to this latter with no size-dependence. These results suggest the co-presence of these two crystalline phases but also a low-extent of oxidation of divalent iron ions. From the profile analyses, the average crystallite sizes have been estimated and are reported in Table 8.

Table 8. Cell parameter (a), mean crystallite ($\langle D_{XRD} \rangle$) and particle ($\langle D_{TEM} \rangle$) size, particle size dispersity (σ), the weight percentage of the organic phase, and M^{II}:Fe^{III} ratio determined by ICP-OES of the samples.

Sample	a (Å)	$\langle D_{XRD} \rangle$ (nm)	$\langle D_{TEM} \rangle$ (nm)	σ $\langle D_{TEM} \rangle$ (%)	Organic phase (%)	M^{II}:Fe^{III}
CoA	8.39(1)	5.5(2)	5.4	17	24	0.49
CoB	8.38(1)	6.7(1)	7.1	14	20	0.45
CoC	8.38(1)	7.9(2)	8.5	14	18	0.55
CoD	8.38(1)	9.9(5)	11.1	13	15	0.47
CoE	8.39(1)	11.2(4)	12.3	12	12	0.45
CoF	8.38(1)	12.8(5)	13.3	13	10	0.48
CoG	8.40(1)	14.1(9)	17.3	14	8	0.52
MnA	8.47(1)	6.9(4)	7.8	14	21	0.43
MnB	8.48(1)	8.7(3)	9.8	14	18	0.38
MnC	8.47(1)	9.8(3)	10.8	13	15	0.50
MnD	8.49(1)	11.2(4)	13.8	14	9	-
MnE	8.48(1)	11.4(8)	12.3	14	Uncapped	0.40
FeA	8.38(1)	7.7(4)	8.4	13	12	-
FeB	8.38(1)	8.7(3)	9.3	12	11	-
FeC	8.37(1)	10.1(1)	10.0	11	9	-
FeD	8.37(1)	13.4(3)	14.4	10	6	-
FeE*	-	Micrometric	Micrometric	-	Uncapped	-

***Hematite**

The sample CoA, having a crystallite size of 5.5 nm, was obtained using 6 mmol of mixed Co^{II}-Fe^{III}-oleate, 20 mL of 1-pentanol and 10 mL of water as solvents, at 180 °C. The sample CoB was obtained instead by using as organic solvents 10 mL pentanol and 10 mL of octanol, and the resulting crystallite size was 6.7 nm. The increased crystallite size with respect to CoA can be related to the decreased polarity of the solvents. The particles nucleate and grow in the organic media until they reach a critical diameter, after which they sediment at the bottom of the water phase. The stability in the organic phase is governed by the solvent polarity (the less polar the solvent, the larger the critical diameter), as well as the temperature and the precursor concentration.[288,293,561] Indeed, larger crystallite size was obtained for sample CoC (7.9 nm), synthesized at the same experimental condition of CoB but a higher temperature (220 °C). The sample CoD was obtained by further decreasing the organic solvent polarity with respect to CoC, by replacing

octanol with toluene, and the resulting crystallite size was 9.9 nm. Finally, CoE and CoF were prepared by reducing the precursor concentration from 6 mmol (for CoD) to 3 (CoE) and 2.75 (CoF), giving rise to crystallite sizes of 11.2 and 12.8 nm for CoE and CoF, respectively.

Manganese ferrite and spinel iron oxide nanoparticles were synthesized under the same synthetic conditions of CoC, CoD, and CoE because smaller particles of these soft phases usually do not show suitable properties. In detail, MnA and FeA, as well as CoC, were prepared at 220 °C, starting from 6 mmol of metal oleates, 10 mL of pentanol, 10 mL of octanol and 5 mL of water, and led to a crystallite size of 6.9, 7.7 and 7.9 nm for MnA, FeA and CoC, respectively. The samples MnB and FeB, as well CoD, were obtained replacing octanol with toluene, that increased the crystallite size to 8.7 nm for both MnB and FeB and 9.9 for CoD. Finally, the decrease of the oleate precursor from 6 to 3 mmol in MnC, FeC, and CoE resulted in a crystallite size of 9.8, 10.1 and 11.1 nm, respectively. From this comparison, it seems that cobalt ferrite tends to crystallise under the same experimental conditions giving rise to larger particles in comparison with the other spinel ferrites, probably due to the higher stability of cobalt ferrite phase.

In the light of these results, size-tuning can be achieved by means of a direct approach for both systems which consists of: (i) increasing the reaction temperature; (ii) decreasing the solvent polarity: the lower the polarity of the solvent the higher the stability of the forming nanoparticles and therefore the higher the precipitation critical size; (iii) decreasing the metal oleate concentration, probably due to the formation of a lower number of nuclei that can grow more with respect to those formed in concentrated reaction systems in agreement with the La Mer & Dinegar model.[389] To obtain larger particles, a step further in the synthesis of larger particles passes through post-synthesis treatment of preformed seeds in the presence or absence of further metal precursors. Following the first approach, a net increase in the crystallite and particle sizes was obtained for the CoG and FeD samples, while just a slight growth is observed for the crystallite size of the manganese ferrite sample (MnD, from 10 nm to 11 nm). The absence of metal oleates in the post-synthesis solvothermal treatment (second approach) led to produce hematite instead of spinel ferrite in the FeE sample, in the form of micrometric particles, while in the MnE sample the spinel phase was preserved and a 1 nm increase in the crystallite size with respect to the MnC sample was obtained.

2.3.2 Transmission Electron Microscopy (TEM and HRTEM)

TEM and HRTEM measurements were carried out to study the morphology, the crystallinity, and the particle size of the samples. TEM bright field images of the samples (Figure 13) show well-separated spheroidal nanoparticles with particle size similar to crystallite size, suggesting a high crystallinity of the particles (Table 8), and are characterised by narrow unimodal particle size distributions, with a dispersity in a 10-17 % range, except for MnD, MnE, and FeE. Sample MnD is characterized by different anisotropic shapes having a particle size of 13.8 nm. The remarkable difference between the crystallite and particle sizes for this sample can be justified by the assumption of spheroidal shape in the use of the Scherrer equation for analysing the XRD patterns. MnE shows agglomeration phenomena, due to the removal of the capping agent from the particle surface. The TEM images of the FeE sample, made by micrometric hematite as indicated by the XRD pattern, show the presence of anisotropic shapes of the microparticles, suggesting that also in this case agglomeration phenomena have taken place. Some attempts aimed to preserve the spinel ferrite phase in the case of iron oxide were performed, changing the amount of water, reaction time and temperature. However, the optimisation of the experimental conditions, even though it is responsible for the stabilisation of the spinel ferrite with a slight growth of the seeds, did not lead to a stable colloidal dispersion due to the removal of the capping molecules probably caused by dissolution of the oleates in the solvent mixture. HRTEM images of the samples show highly crystalline particles with no evidence of defects. As an example, in Figure 13 are reported the images of samples CoE, MnC, and FeC. The interlayer distances confirmed the presence of the spinel oxide phase, in agreement with the XRD data. In the light of these results, the addition of new metal precursors as in the first approach (based on the seed-mediated growth) led to stable and larger nanoparticles of the desired crystalline phase and therefore it is the most promising one to grow preformed particles. Indeed, the high homogeneity of the particles is well demonstrated for samples CoF and FeD from the formation of superlattices in the TEM grids when the dispersity is low enough as soon as the solvent evaporates, as shown in Figure 14.

It is already known that generally solvothermal methods benefit of good repeatability, being the reaction carried out under strictly controlled experimental conditions. Replicas of the CoE, MnC and FeC samples were prepared. Figure 15 reports the XRD and TEM characterization of the samples. All samples show the same microstructural and morphological features with very similar crystallite and particle size and same spheroidal shape of the particles. This study, therefore, clearly proves that the solvothermal method guarantees high repeatability in the synthesis of size-tailored nanoparticles for different spinel ferrites.

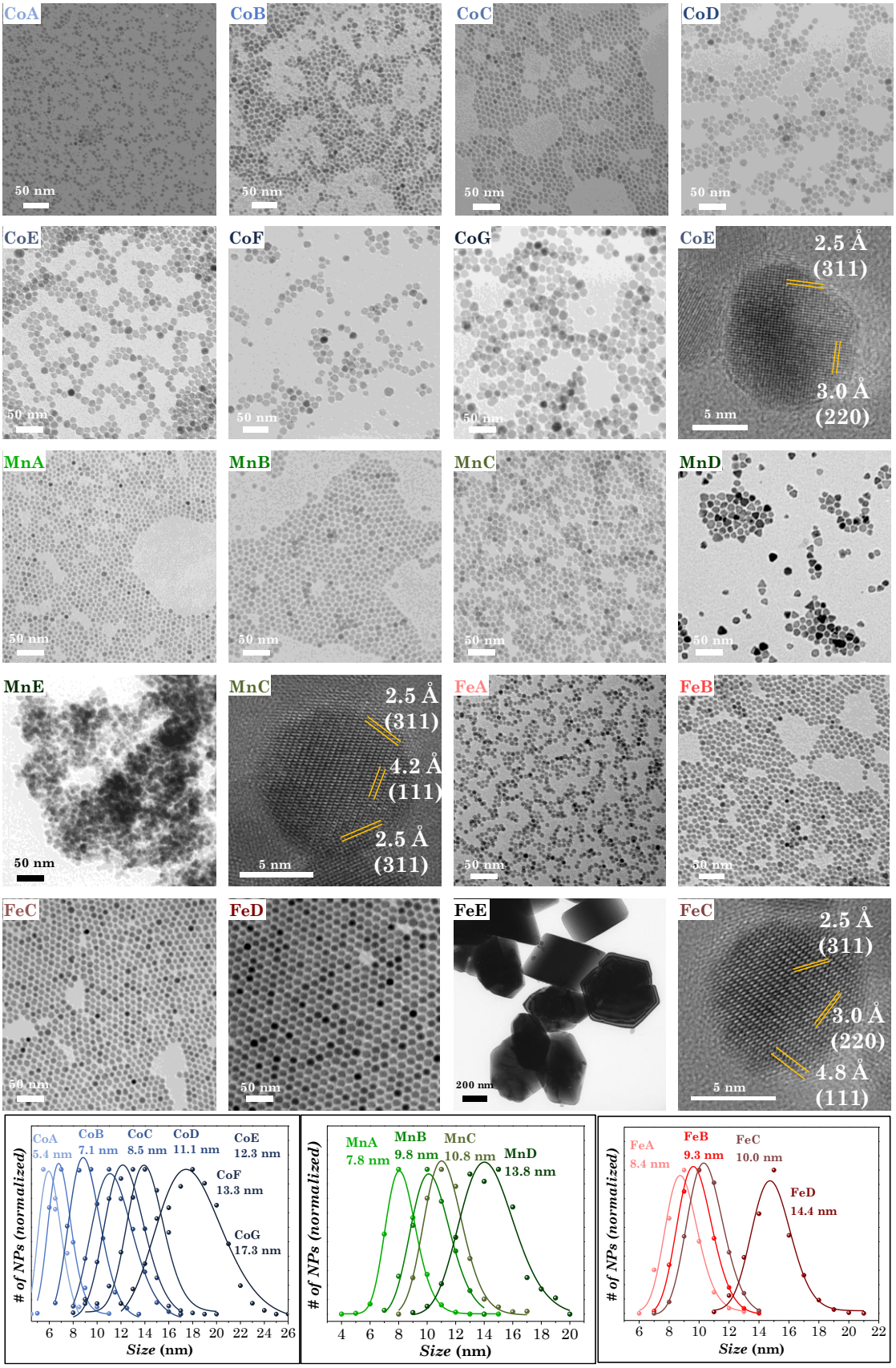

Figure 13. TEM Bright Field, HRTEM images, and particle size distributions of cobalt ferrite, manganese ferrite, and spinel iron oxide NPs.

.

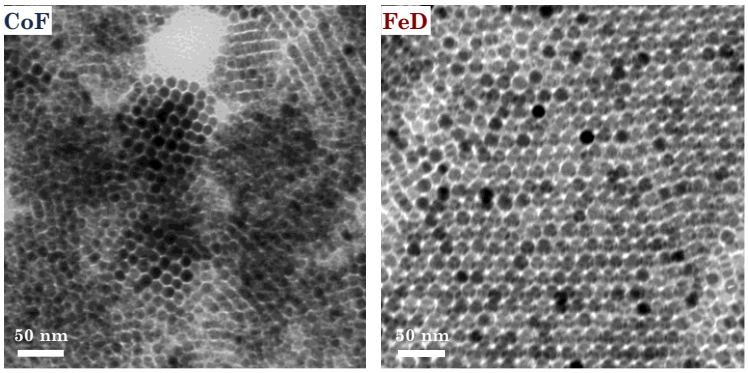

Figure 14. TEM images of superlattices of samples CoF and FeC@Fe.

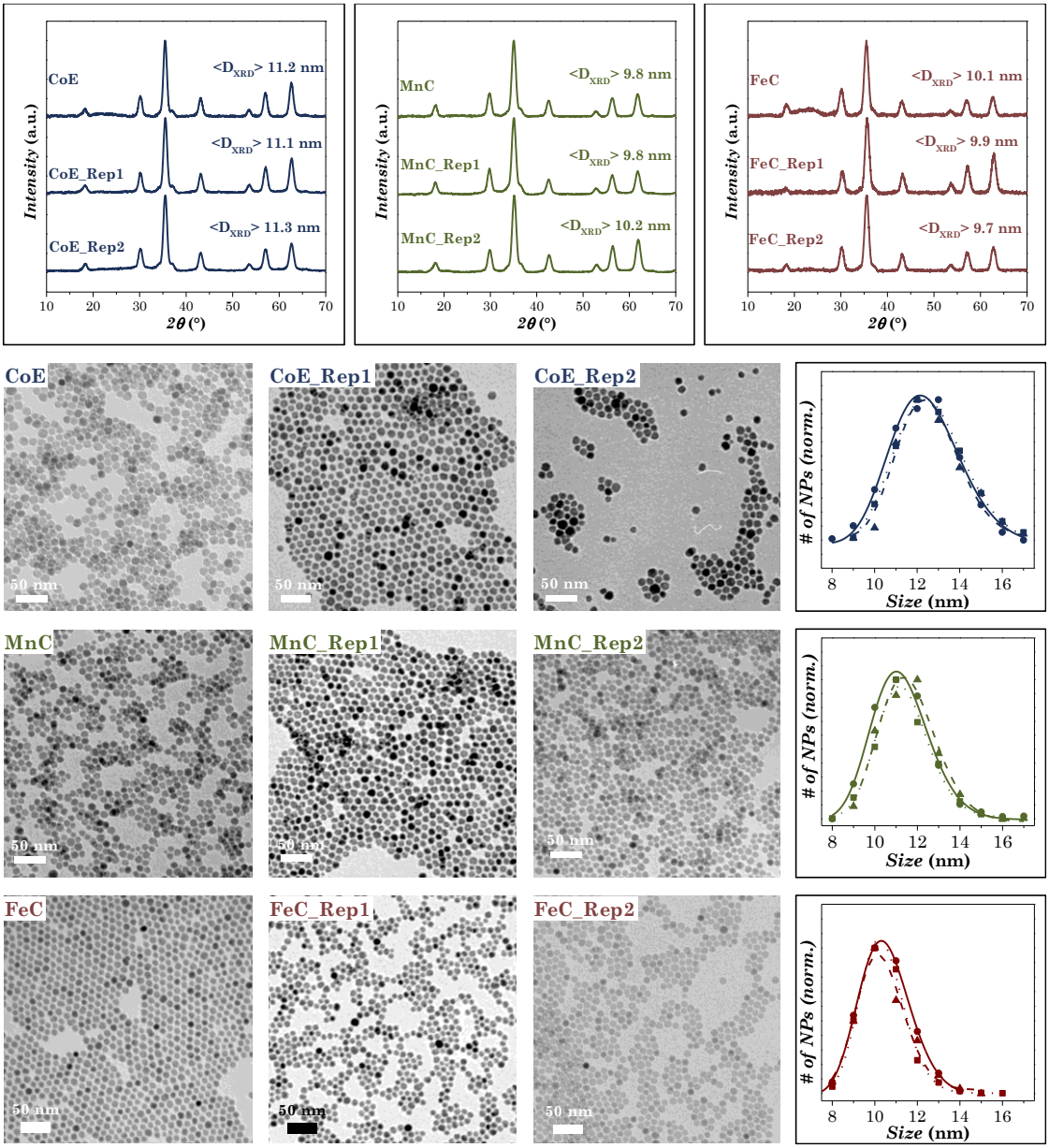

Figure 15. XRD patterns, TEM bright field images and particle size distribution of the sample CoE, MnC, and FeC and their two replicas.

2.3.3 Inductive Coupled Plasma-Optic Emission Spectroscopy (ICP-OES)

Composition of cobalt ferrite and manganese ferrite samples has been evaluated through ICP-OES. The M^{II}:Fe^{III} molar ratio are reported in Table 8. While cobalt ferrite nanoparticles always show an almost stoichiometric formula (Co^{II}:Fe^{III} = 0.5), manganese ferrite ones present a deficit in manganese. These results highlight the importance of determining the actual chemical composition in studies which correlate physical and chemical properties. Spinel iron oxide nanoparticles' composition cannot be studied by ICP, since iron cannot be related to oxygen content. Furthermore, it is known that magnetite nanoparticles, where both Fe^{II} and Fe^{III} is present, are highly susceptible to oxidation, leading to maghemite, which is formed only by Fe^{III}. In this context, we found that the optimal ratio between Fe^{II}-oleate and Fe^{III}-oleate to synthesize spinel iron oxide nanoparticles is 2:1, in disagreement with the theoretical magnetite ratio 1:2. Indeed, higher Fe^{III}-oleate content would have led to hematite. In the same way, the sample FeD was synthesized using only Fe^{II}-oleate as shell precursor. Among the techniques that can be used for the discerning of magnetite and maghemite (e.g. ^{57}Fe Mössbauer spectroscopy, Raman spectroscopy, XPS, X-rays absorption),[568,569] ^{57}Fe Mössbauer spectroscopy was chosen and it will be discussed later.

2.3.4 Energy-Dispersive X-ray Spectroscopy in Scanning/ Transmission Electron Microscopy Mode (STEM-EDX)

STEM-EDX mapping of Fe, Co, and Mn elements was carried out on some selected samples, and the results for samples CoC, MnC, and FeC are shown in Figure 16.

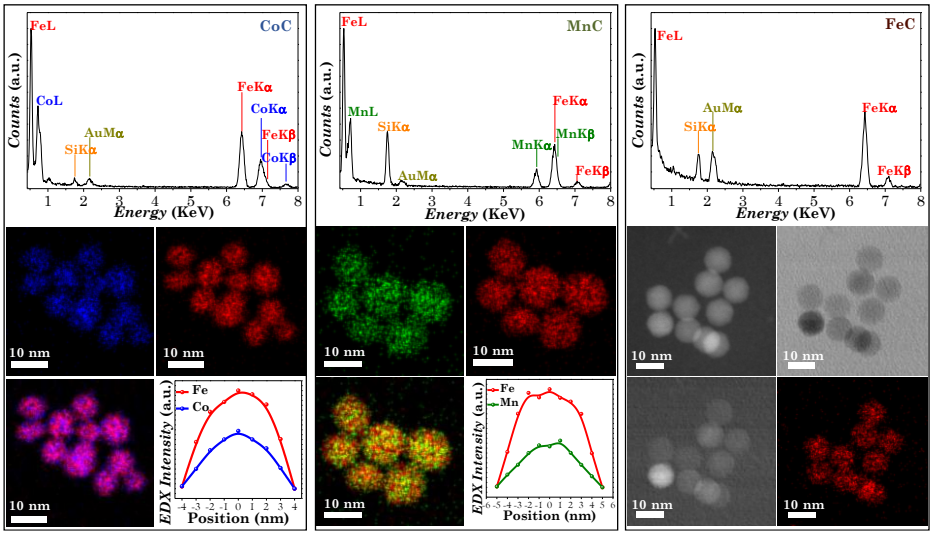

Figure 16. EDX spectra, chemical mapping of the nanoparticles, and line profile across the samples for CoC and MnC. EDX spectra, Dark Field, Bright Field, HAADF, and chemical mapping for FeC. The Si and Au emission lines are associated with the detector and the TEM grid, respectively. The signal at about 1 and 8 keV may be ascribable to the *L* and *Ka* lines of the Cu present in the TEM grid.

EDX spectra show the main X-ray emission lines of manganese, iron, and cobalt present in the nanoparticles, that is the *L* lines at about 0.6-0.9 KeV and *Kα* and *Kβ* lines at about 5.9-7.7 KeV. Chemical mapping images (Figure 16, bottom) show a homogeneous distribution of Co (or Mn) and/or Fe throughout the particles, also confirmed by the line profile obtained as average for different sections all over the particle.

2.3.5 Thermogravimetric Analysis (TGA) and Fourier Transform-Infrared Spectroscopy (FT-IR)

The capping by oleate molecules was demonstrated through FT-IR (Figure 17) and TGA (Figure 18). FT-IR spectra show the main vibrational modes associated with the oleate molecules linked at the surface of the nanoparticles, as the COO- vibrational modes (ν_{as} (COO^-), ν_s (COO^-)) and those related to the hydrocarbon chain.[553,563,570] The sample MnE does not show any capping covering in agreement with the TEM image, in which the particles appeared agglomerated. The complete assignment for all the samples is reported in Table 9 and Table 10.

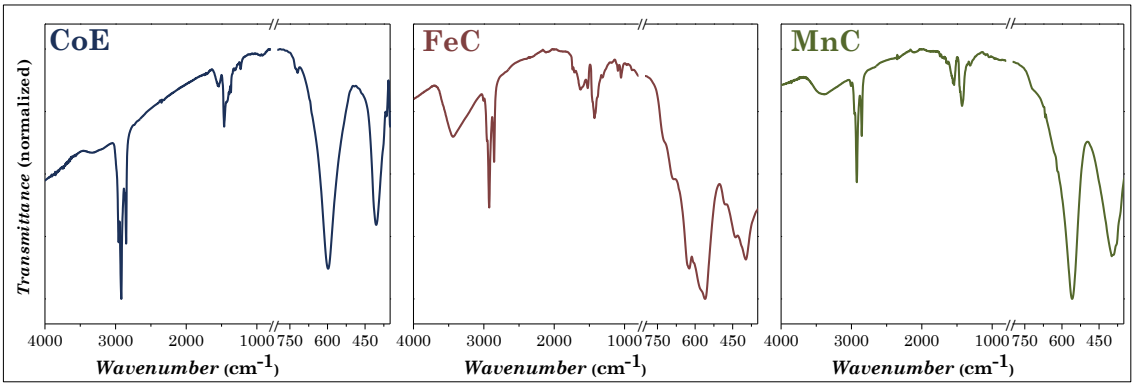

Figure 17. FT-IR spectra of CoE, FeC, and MnC samples.

Table 9. Assignment of FT-IR bands of cobalt ferrite samples.

Wavenumber (cm^{-1})							Vibration mode
CoA	**CoB**	**CoC**	**CoD**	**CoE**	**CoF**	**CoG**	
3006	3007	3007	3007	-	3004	3008	**CH=CH stretching**
2954	2956	2957	2956	2956	2955	2958	**C-H asymmetric stretching (CH_3)**
2922	2924	2924	2924	2919	2922	2925	**C-H asymmetric stretching (CH_2)**
2871	2873	2872	2872	2873	2870	2873	**C-H symmetric stretching (CH_3)**
2850	2854	2854	2853	2851	2853	2854	**C-H symmetric stretching (CH_2)**
1550	1552	1550	1552	1547	1545	1557	**COO^- asymmetric stretching**
1417	1425	1427	1425	1463	1429	1422	**COO^- symmetric stretching**
721	723	721	721	723	719	722	**CH_2 wagging**
596	594	594	593	598	593	585	**M-O stretching of T_d and O_h sites**
409	407	404	399	405	404	393	**M-O stretching of O_h sites**

Table 10. Assignment of FT-IR bands of manganese ferrite and spinel iron oxide samples.

Wavenumber (cm^{-1})									Vibration mode
MnA	**MnB**	**MnC**	**MnD**	**MnE**	**FeA**	**FeB**	**FeC**	**FeD**	
3004	3005	3008	3007	3014	3005	3005	-	-	**CH=CH stretching**
2953	2955	2958	2955	2956	2954	2954	2957	2958	**C-H asymmetric stretching (CH_3)**
2921	2923	2925	29222	2922	2924	2924	2922	2925	**C-H asymmetric stretching (CH_2)**
-	2872	2871	2874	2872	2870	2872	2873	2874	**C-H symmetric stretching (CH_3)**
2850	2852	2854	2853	2850	2854	2854	2858	2858	**C-H symmetric stretching (CH_2)**
1544	1547	1550	1543	-	1525	1524	1573	1596	**COO^- asymmetric stretching**
1427	1427	1429	1427	-	1429	1427	1415	1458	**COO^- symmetric stretching**
724	719	721	721	-	725	725	721	723	**CH_2 wagging**
-	-	-	-	-	688	689	-	682	**Fe-O stretching**
-	-	-	-	-	624	624	619	-	**Fe-O stretching**
573	554	559	547	569	577	580	580	582	**M-O stretching of T_d and O_h sites**
-	-	-	-	-	560	559	567	567	**Fe-O stretching**
-	-	-	-	-	480	482	-	-	**Fe-O stretching**
-	-	-	-	-	440	439	437	-	**Fe-O stretching**
427	389	395	384	-	400	397	395	397	**Metal-O stretching of O_h sites**

TGA curves, recorded under an oxygen atmosphere, are shown in Figure 18 (three samples as an example), while the weight losses percentages obtained all the samples are reported in Table 8.

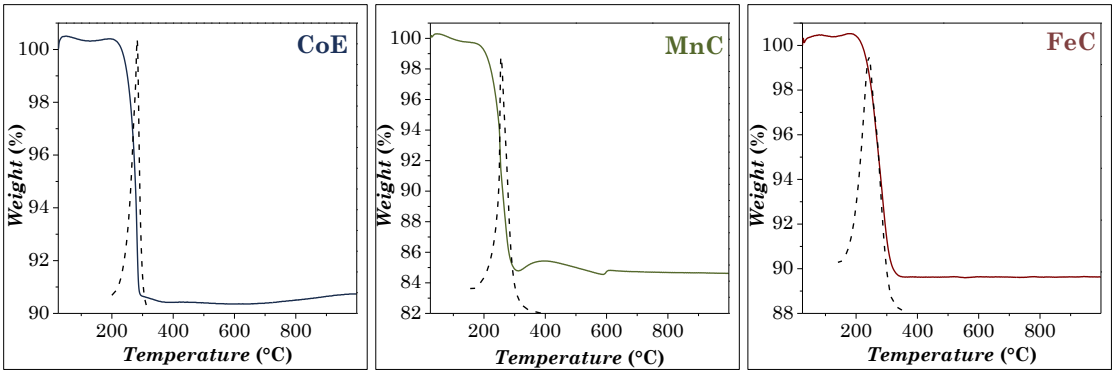

Figure 18. TGA curves of samples CoE, MnC, and FeC acquired under oxygen flux.

The curves show a weight loss occurring between 200 and 300 °C, associated with the decomposition of the oleate molecules capping the nanoparticles' surface. A decrease of the organic content with the increase of NPs size was observed for all samples. Indeed, as the size of the particles increases, the surface/volume ratio decreases, leading to a lower number of organic molecules able to cap the surface. The weight percentages correspond to a monolayer of oleate molecules surrounding the nanoparticle surface. An example of the computation for the sample CoA is given. Considering a particle diameter of 5.4 nm ($<D_{TEM}>$) and a spheroidal shape for the NPs, a

surface area of 92 nm^2 is obtained. A 24% w/w of organic capping corresponds to ~$5.1 \cdot 10^{20}$ oleate molecules. Considering the *bulk*-$CoFe_2O_4$ density of 5.3 g/cm^3 and the volume of a single spheroidal nanoparticle (82 nm^3), a 76% w/w of inorganic phase corresponds to a number of spinel ferrite nanoparticles of $1.7 \cdot 10^{18}$. The number of capping molecules per particle, obtained as the ratio between the number of oleate molecules and the total number of nanoparticles, is about 295 molecules of oleate/nanoparticle. Finally, the nanoparticle surface area (92 nm^2) over the number of molecules provides a surface area occupied by each oleate molecules of 31 $Å^2$/molecule. This value is in good agreement with those reported by other authors for oleic acid-coated spinel iron oxides nanoparticles and suggests the presence of a close-packed monolayer of the capping agent.[571–573] The same computation was performed for all the samples and the results are shown in Table 11, considering the density for *bulk*-$MnFe_2O_4$ and *bulk*-spinel iron oxide of 5.0 and 5.1 g/cm^3 respectively.

Table 11. Computation of capping molecule packing on the nanoparticle surface.

Sample	$\langle D_{TEM} \rangle$ (nm)	A_{NP} (nm^2)	V_{NP} (nm^3)	m_{NP} (g)	#NPs	m_{Ol} (g)	n_{Ol} (mmol)	#Ol	#Ol/NP	A_{Ol} ($Å^2$)
CoA	5.4	92	82	$4.4 \cdot 10^{-19}$	$1.7 \cdot 10^{18}$	0.24	0.85	$5.1 \cdot 10^{20}$	295	31
CoB	7.1	158	187	$9.9 \cdot 10^{-19}$	$8.7 \cdot 10^{17}$	0.20	0.71	$4.3 \cdot 10^{20}$	531	30
CoC	8.5	227	322	$1.7 \cdot 10^{-18}$	$4.8 \cdot 10^{17}$	0.18	0.64	$3.9 \cdot 10^{20}$	800	28
CoD	11.1	387	716	$3.8 \cdot 10^{-18}$	$2.2 \cdot 10^{17}$	0.15	0.53	$3.2 \cdot 10^{20}$	1433	27
CoE	12.3	457	974	$5.2 \cdot 10^{-18}$	$1.7 \cdot 10^{17}$	0.12	0.43	$2.6 \cdot 10^{20}$	1507	32
CoF	13.3	556	1232	$6.5 \cdot 10^{-18}$	$1.4 \cdot 10^{17}$	0.10	0.36	$2.1 \cdot 10^{20}$	1552	36
CoG	17.3	940	2711	$1.4 \cdot 10^{-17}$	$6.4 \cdot 10^{16}$	0.08	0.28	$1.7 \cdot 10^{20}$	2673	35
MnA	7.8	191	248	$1.2 \cdot 10^{-18}$	$6.4 \cdot 10^{17}$	0.21	0.75	$4.5 \cdot 10^{20}$	707	27
MnB	9.8	302	493	$2.5 \cdot 10^{-18}$	$3.3 \cdot 10^{17}$	0.18	0.64	$3.9 \cdot 10^{20}$	1157	26
MnC	10.8	366	660	$3.3 \cdot 10^{-18}$	$2.6 \cdot 10^{17}$	0.15	0.53	$3.2 \cdot 10^{20}$	1245	29
MnD	13.8	598	1376	$6.9 \cdot 10^{-18}$	$1.3 \cdot 10^{-17}$	0.09	0.32	$1.9 \cdot 10^{-20}$	1456	41
FeA	8.4	222	310	$1.6 \cdot 10^{-18}$	$5.6 \cdot 10^{17}$	0.12	0.43	$2.6 \cdot 10^{20}$	462	48
FeB	9.3	273	421	$2.1 \cdot 10^{-18}$	$4.1 \cdot 10^{17}$	0.11	0.89	$2.4 \cdot 10^{20}$	568	48
FeC	10.0	314	524	$2.7 \cdot 10^{-18}$	$3.4 \cdot 10^{17}$	0.09	0.32	$1.9 \cdot 10^{20}$	565	56
FeD	14.4	651	1563	$8.0 \cdot 10^{-18}$	$1.2 \cdot 10^{17}$	0.06	0.21	$1.3 \cdot 10^{20}$	1089	60

2.3.6 ^{57}Fe Mössbauer Spectroscopy

2.3.6.1 Room-Temperature ^{57}Fe Mössbauer Spectroscopy

Room temperature (RT) ^{57}Fe Mössbauer measurements were carried out for all samples (Figure 19) to gather information on the structural and the magnetic properties of the spinel ferrite nanoparticles, as shown in Table 12.

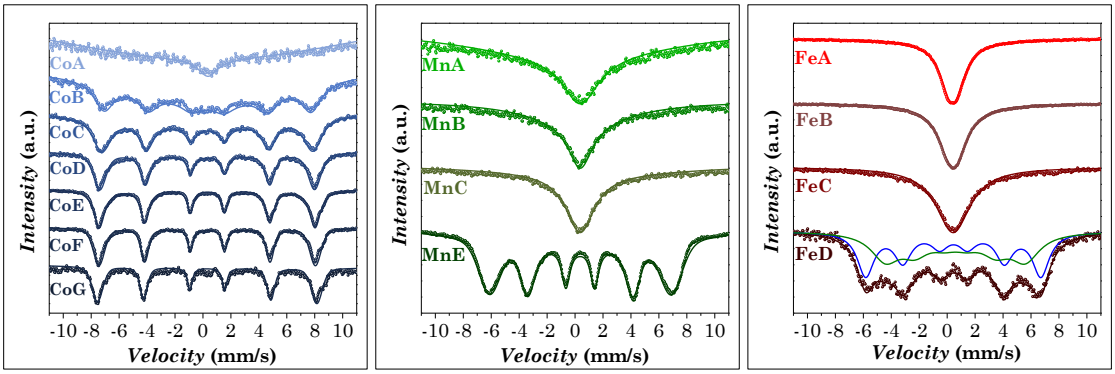

Figure 19. RT ^{57}Fe Mössbauer spectra of all samples.

Table 12. RT ^{57}Fe Mössbauer parameters of the samples: values of the isomer shift (δ), hyperfine field (B_{hf}), and full width at half-maximum (FWHM) of the components.

Sample	$<D_{XRD}>$ (nm)	Signal	δ (mm/s)	B_{hf} (T)	FWHM (mm/s)
CoA	5.5(2)	Singlet	0.20(1)	-	12(1)
CoB	6.7(1)	B-Sextet	0.34(1)	46.1(1)	1.7(1)
CoC	7.9(2)	B-Sextet	0.32(1)	46.9(1)	0.8(2)
CoD	9.9(5)	B-Sextet	0.31(1)	47.8(1)	0.6(1)
CoE	11.2(4)	B-Sextet	0.31(1)	48.0(1)	0.4(1)
CoF	12.8(5)	B-Sextet	0.31(1)	48.5(1)	0.4(1)
CoG	14.1(9)	B-Sextet	0.30(1)	48.7(1)	0.4(1)
MnA	6.9(4)	Singlet	0.39(1)	-	3.1(1)
MnB	8.7(3)	Singlet	0.38(1)	-	2.1(1)
MnC	9.8(3)	Singlet	0.37(1)	-	2.8(1)
MnE	11.4(8)	B-Sextet	0.37(1)	40.4(1)	0.6(1)
FeA	7.7(4)	Singlet	0.38(1)	-	2.0(1)
FeB	8.7(3)	Singlet	0.42(1)	-	2.3(1)
FeC	10.1(1)	Singlet	0.43(1)	-	3.0(1)
FeD	13.4(3)	B-Sextet	0.45(1)	39.9(1)	1.4(1)
		B-Sextet	0.59(1)	31.1(1)	2.5(1)

All cobalt ferrite RT ^{57}Fe Mössbauer spectra but CoA were fitted with one broad sextet, deriving from the overlapping at room temperature accounting for Fe^{III} in the octahedral and tetrahedral sites of cobalt ferrite in the blocked state, and one broad singlet ascribed to NPs with the relaxation time close to the measurement time scale (not reported in the table). Even though in some cases the fitting by using two sextets gave better results in terms of accuracy of the fitting, they did not provide physically acceptable hyperfine parameters. Indeed, according to the literature, octahedral sites differ from tetrahedral ones by: i) higher isomer shift values, due to the lower covalent character;[574] ii) higher full-width at half maximum (FWHM), because of two non-equivalent octahedral sites;[575] iii) lower hyperfine field values at room temperature.[576] Since not always these physical limits were respected, the fitting by using only one broad sextet to follow the correlation between crystallite size and hyperfine parameters was preferred. CoA shows a singlet

in place of a sextet related to the particles in the superparamagnetic state. All the others cobalt ferrite samples were fitted by using.
The quadrupole splitting values for all samples were almost zero, indicating a cubic symmetry. The isomer shift values (δ) of all samples are in the 0.28-0.41 mm/s range typical for Fe^{III}.[577]
Hyperfine field values gradually increase along with the increase crystallite sizes of cobalt ferrite samples, as shown in Figure 20.

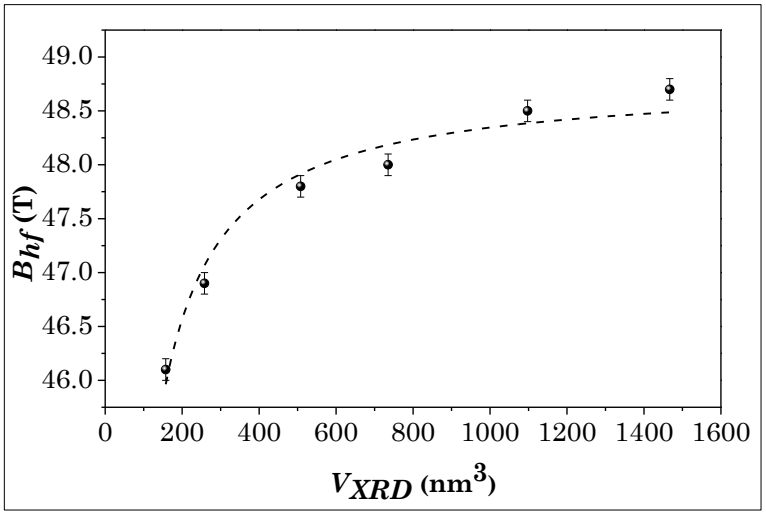

Figure 20. Evolution of B_{hf} as a function of crystallite sizes of cobalt ferrite nanoparticle.

The data reported in Figure 20 were fitted by using the Eq. 39, obtained from CME model:[578–580]

$$B_{hf} = B_0\left(1 - \frac{K_b T}{2KV}\right) \qquad \textbf{Eq. 39}$$

Where B_0 is the saturation hyperfine field, K_b the Boltzmann constant, T the temperature, K the anisotropy constant, and V the magnetic volume of the particles. Even though the anisotropy is size-dependent and increases with increasing the size, the fitted curve produced satisfactory results as indicated by the adjusted R^2 equal to 0.96. All manganese ferrite RT ^{57}Fe Mössbauer spectra but MnE show a sharp singlet, associated with particles in the superparamagnetic state. MnE spectrum presents a sextet, indicating that the nanoparticles are in the blocked state. The larger crystallite size that is necessary for manganese ferrite (~11 nm) to be in the blocked state, compared to cobalt ferrite (~7 nm), is explained by the different magnetocrystalline anisotropy of the two phases, that is $3 \cdot 10^3$ J/m^3 for *bulk*-$MnFe_2O_4$ and $2.9 \cdot 10^5$ J/m^3 for *bulk*-$CoFe_2O_4$.[70] This is also evident when CoE and MnE are compared. They both have similar crystallite size, but the hyperfine field value of the cobalt ferrite sample is 7.6 T higher than that of the manganese ferrite one. Indeed, as reported in Eq. 39, hyperfine field strongly depends on anisotropy constant.

As for manganese ferrite nanoparticles, all RT ^{57}Fe Mössbauer spectra but FeD present a sharp singlet, associated with particles in the superparamagnetic state. Sample FeD was fitted with two broad sextets, ascribed to nanoparticles just above the blocking temperature. The isomer shift values of these samples, especially in the case of FeD, are slightly higher compared to cobalt and manganese ferrites, due to the presence of Fe^{II}, suggesting its incomplete oxidation into Fe^{III}, that together with the XRD data suggest the copresence of maghemite and magnetite.

2.3.6.2 Low-Temperature ^{57}Fe Mössbauer spectroscopy

Low-temperature (LT) ^{57}Fe Mössbauer measurements in the absence and the presence of magnetic field (6T) were carried out on the CoA, CoB, CoB, MnA, and FeC samples, to assess site occupancy and spin canting phenomena. As an example, Figure 21 reports the spectra of the samples CoA, MnA, and FeC, while in Table 13 the Mössbauer parameters are listed.

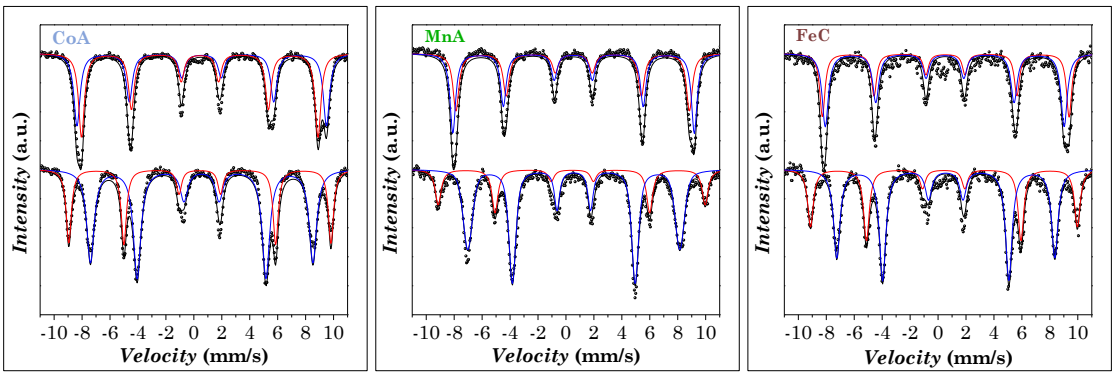

Figure 21. LT ^{57}Fe Mössbauer spectra in the absence (top) and the presence (bottom) of magnetic field (6T) of samples CoA, MnA, and FeC.

Table 13. LT (4 K) ^{57}Fe Mössbauer parameters obtained in the absence and with external magnetic field (6T) of the samples: values of the isomer shift (δ), effective field at 0T ($B_{eff}^{0T} = B_{hf}$) and 6T (B_{eff}^{6T}), relative area (A), canting angles (α), inversion degree (γ), and chemical formula calculated from site occupancy corrected by ICP-OES data.

Sample	Signal	Site	δ (mm/s)	B_{eff}^{0T} (T)	B_{eff}^{6T} (T)	A (%)	α (°)	γ	Formula
CoA	Sextet	T_d	0.43(1)	52.6(1)	58.3(1)	34%	19	0.67	$(Co_{0.31}Fe_{0.69})[Co_{0.67}Fe_{1.32}]O_4$
	Sextet	O_h	0.56(1)	55.4(1)	49.4(1)	66%	0		
CoB	Sextet	T_d	0.37(1)	51.2(1)	56.9(1)	35%	19	0.65	$(Co_{0.27}Fe_{0.72})[Co_{0.65}Fe_{1.33}]O_4$
	Sextet	O_h	0.49(1)	54.1(1)	48.2(1)	65%	10		
CoC	Sextet	T_d	0.37(1)	51.2(1)	56.7(1)	35%	25	0.74	$(Co_{0.33}Fe_{0.68})[Co_{0.74}Fe_{1.27}]O_4$
	Sextet	O_h	0.49(1)	54.4(1)	48.4(1)	65%	0		
MnA	Sextet	T_d	0.43(1)	54.3(1)	59.3(1)	26%	35	0.43	$(Mn_{0.43}Fe_{0.53})[Mn_{0.43}Fe_{1.54}]O_4$
	Sextet	O_h	0.56(1)	52.8(1)	47.1(1)	74%	17		
FeC	Sextet	T_d	0.41(1)	53.5(1)	59.3(1)	36%	16	-	$(Fe_1)[Fe_{1.75}]O_4$
	Sextet	O_h	0.55(1)	54.1(1)	48.5(1)	63%	20		

Without the external magnetic field, the spectra show the overlapping of two sextets associated with the octahedral and tetrahedral sites of the spinel

structure. The in-field measurements allow to split these two subspectra and to calculate the occupancy in the two sublattices.
For instance, from the relative areas of the two sextets in the in-field spectrum of CoA, it is found that 34% of iron cations are located in tetrahedral position and 66% in octahedral positions. Taking into account these results the inversion degree (percentage of bivalent cations in octahedral position) is 0.67 and the formula can be written as $(Co_{0.31}Fe_{0.69})[Co_{0.67}Fe_{1.32}]O_4$, in agreement with the random Co^{II} site occupancy in cobalt ferrite nanoparticles.[553,561,581–585] Similar results were found for the sample CoA and CoC, whose inversion degrees are equal to 0.65 and 0.74, respectively.
On the contrary, Mn^{II} has the preference for tetrahedral sites,[586] and in fact, the inversion degree of the MnA sample is equal to 0.50, which corresponds to the formula $(Mn_{0.43}Fe_{0.53})[Mn_{0.43}Fe_{1.54}]O_4$.
Concerning the sample FeC, from the relative sextets area, 36% of iron is located in the tetrahedral sites and 64% in the octahedral ones, corresponding to a ratio Fe(O_h)/Fe(T_d) of 1.75. Considering the theoretical bulk ratios for maghemite (1.67) and magnetite (2),[70] it is possible to conclude that the structure of the samples is probably more oriented towards maghemite, but not wholly oxidized, as also supposed from the RT Mössbauer data.
By using Eq. 55, it is also possible to calculate the canting angles. For example, the values for the octahedral and tetrahedral sites of CoA are 0° and 19°, respectively. Within the experimental error, we can consider that the magnetic moments of both sublattices are not canted, being the angles calculated from the cosine's equation (Eq. 55). Therefore, small changes in the cosθ lead to significant changes in the angles' values. Similar results were found for the other samples, whose canting angle values for octahedral and tetrahedral sites are reported in Table 13. The sample MnA present a canting angle in tetrahedral sites equal to 35%, slightly higher compared to the others, suggesting an influence of the manganese preferential occupancy for T_d sites.

2.3.7 X-ray Photoelectron Spectroscopy (XPS)

In collaboration with the group of surface, electrochemical, and corrosion analysis of the University of Cagliari and ETH Zurich (Prof. A. Rossi and PhD. M. Fantauzzi), X-ray photoelectron spectroscopy measurements were performed at ETH Zurich on CoA and CoB samples, to gather information on Fe/Co ratios, oxidation state, and inversion degree by using a different approach. Survey spectra of the samples are shown in Figure 22, and exhibit only the presence of the carbon signal in addition to the Co, Fe, and O photoelectron along with X-ray induced Auger electron peaks. There is no overlap of Auger with photoelectron signals, due to the use of the Mg *Ka* radiation.

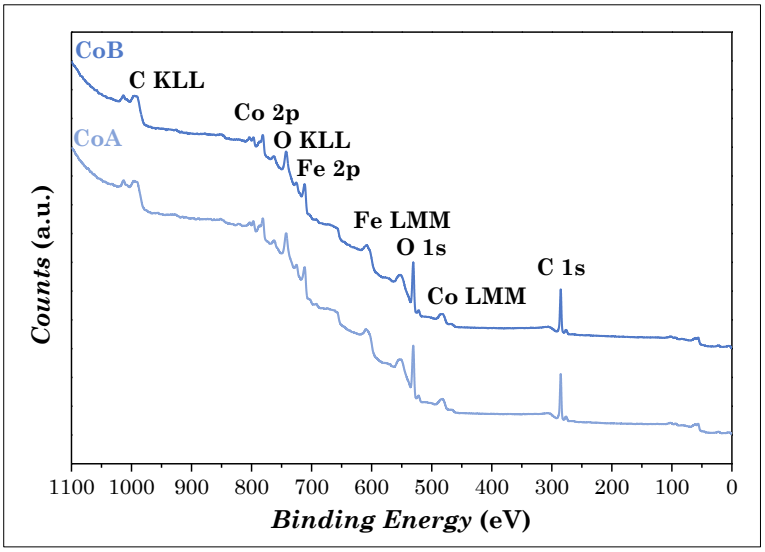

Figure 22. Survey spectra of CoA and CoB.

The presence of oleate capping the NPs' surface significantly reduces the sampling depth. For a pure cobalt ferrite sample, the sampling depth can be estimated using the formula:

$$D = 3\lambda cos\theta \qquad \text{Eq. 40}$$

Where θ is the emission angle (0°) and λ is the inelastic mean free path for inorganic compounds according to Seah and Dench.[587] The inelastic mean free path for electron with $KE > 150$ eV can be estimated using the formula

$$\lambda = B\sqrt{KE} \qquad \text{Eq. 41}$$

Where $B = 0.096$ for inorganic compounds and E is the kinetic energy of the electron.[587] In the case of Fe2p electron moving through a pure inorganic compound the sampling depth is estimated to be about 6.7 nm. However, because of the presence of an organic layer with a thickness of 1 nm, the sampling depth is reduced, and can be calculated by the formula:

$$D = 3\lambda cos\theta \cdot \frac{e^{-t}}{\lambda_c cos\theta} \qquad \text{Eq. 42}$$

Where t is the thickness of the organic layer and λ_c the inelastic mean free path for organic materials.[587] The sampling depth for a Fe2p electron is thus reduced to about 4.1 nm that, due to the random orientation, permit to obtain information on the bulk and not only the surface for the samples CoA and CoB.

2.3.7.1 Cationic Ratio

Cationic ratio was determined from both $2p_{1/2}$ and $2p_{3/2}$ peaks of the elements, after subtraction of a Tougaard background. This background subtraction

was chosen because it is less sensitive to the binding energy range selected for the signal area determination.[588] The Co:Fe ratio resulted to be 0.56 for CoA and 0.53 for CoB, slightly higher than those determined from ICP-OES measurements but in agreement within the XPS experimental error and indicating the obtainment of almost stoichiometric cobalt ferrite NPs.

2.3.7.2 Chemical State

To evaluate the chemical state of Fe and Co, the $2p_{3/2}$ peaks were analysed. The fitting method, called multiple splitting approach, was firstly developed by Gupta and Sen,[589,590] who predicted the energy separation of the multiple components of 2p peaks from 36 ions belonging to the 3d-block transition metals using Hartree-Fock free ion method and taking into account the electrostatic interactions, the spin-orbit coupling between the 2p hole and the unpaired 3d electrons and crystal field interactions. This approach was applied to several systems by other authors[591–593] and it is nowadays a fully consolidated method. The spectra are reported in Figure 23 and the fitting results in Table 14. The binding energy values were typical for Fe^{III} and Co^{II}, and no evidence of Fe^{II} and Co^{III} were found, in agreement with the ^{57}Fe Mössbauer spectroscopy data that revealed the exclusive presence of Fe^{III}.

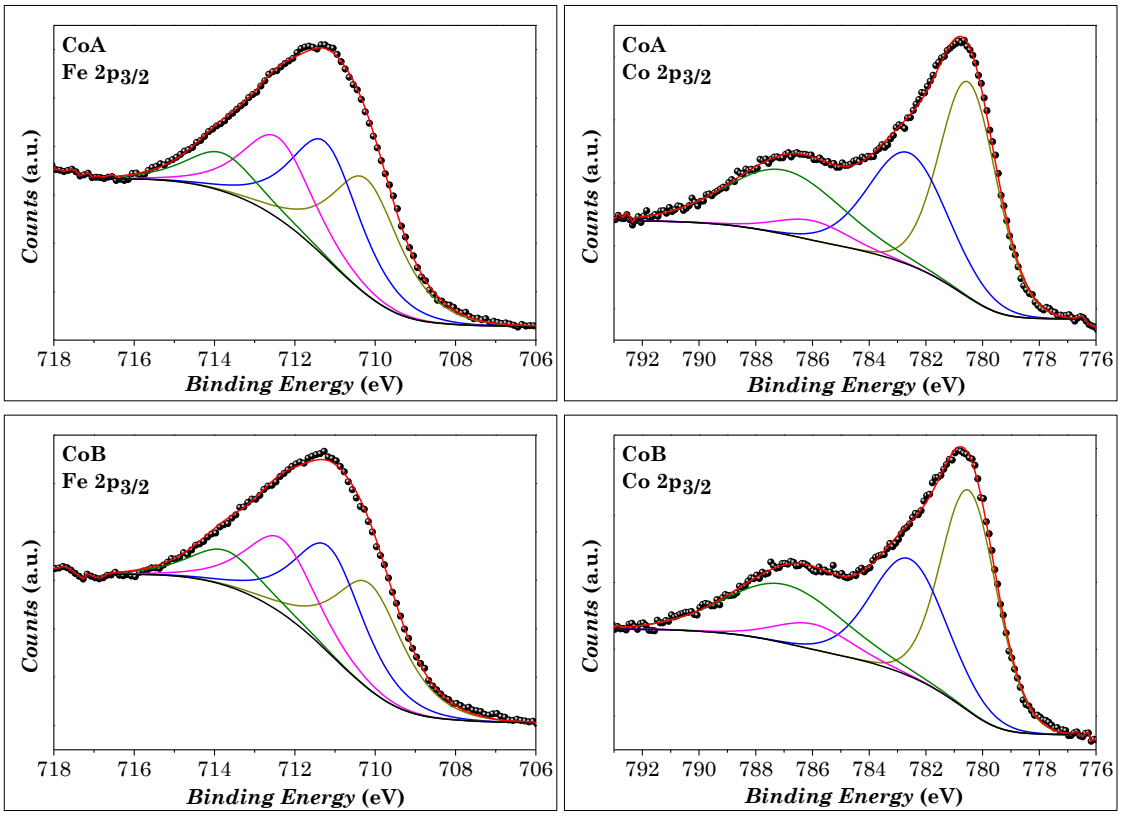

Figure 23. Fe and Co 2p3/2 peaks of CoA and CoB samples fitted by multiplet splitting approach.

Table 14. Curve fitting parameters for multiplet splitting approach on Fe $2p_{3/2}$ and Co $2p_{3/2}$: binding energy (BE) and full width at half maximum (FWHM) of the different components.

Sample	Signal	I		II		III		IV	
		BE (ev)	FWHM (eV)	BE (ev)	FWHM (eV)	BE (ev)	FWHM (eV)	BE (ev)	FWHM (eV)
CoA	Fe $2p_{3/2}$	710.2(1)	2.0(1)	711.2(1)	2.0(1)	712.4(1)	2.0(1)	713.8(1)	2.0(1)
	Co $2p_{3/2}$	780.5(1)	2.4(1)	782.6(1)	3.3(1)	786.0(1)	3.0(1)	787.0(1)	4.8(1)
CoB	Fe $2p_{3/2}$	710.1(1)	2.0(1)	711.1(1)	2.0(1)	712.3(1)	2.0(1)	713.7(1)	2.0(1)
	Co $2p_{3/2}$	780.5(1)	2.3(1)	782.6(1)	3.1(1)	786.0(1)	3.1(1)	787.0(1)	4.9(1)

2.3.7.3 Inversion Degree

The determination of the site occupancy of cations in the tetrahedral and the octahedral sublattices and the inversion degree, was conducted by fitting the $2p_{3/2}$ peak for Fe and $2p_{1/2}$ and $2p_{3/2}$ peaks for Co, according to reported procedures.[594–597] The spectra are indicated in Figure 24 and the results of the fitting process in Table 15.

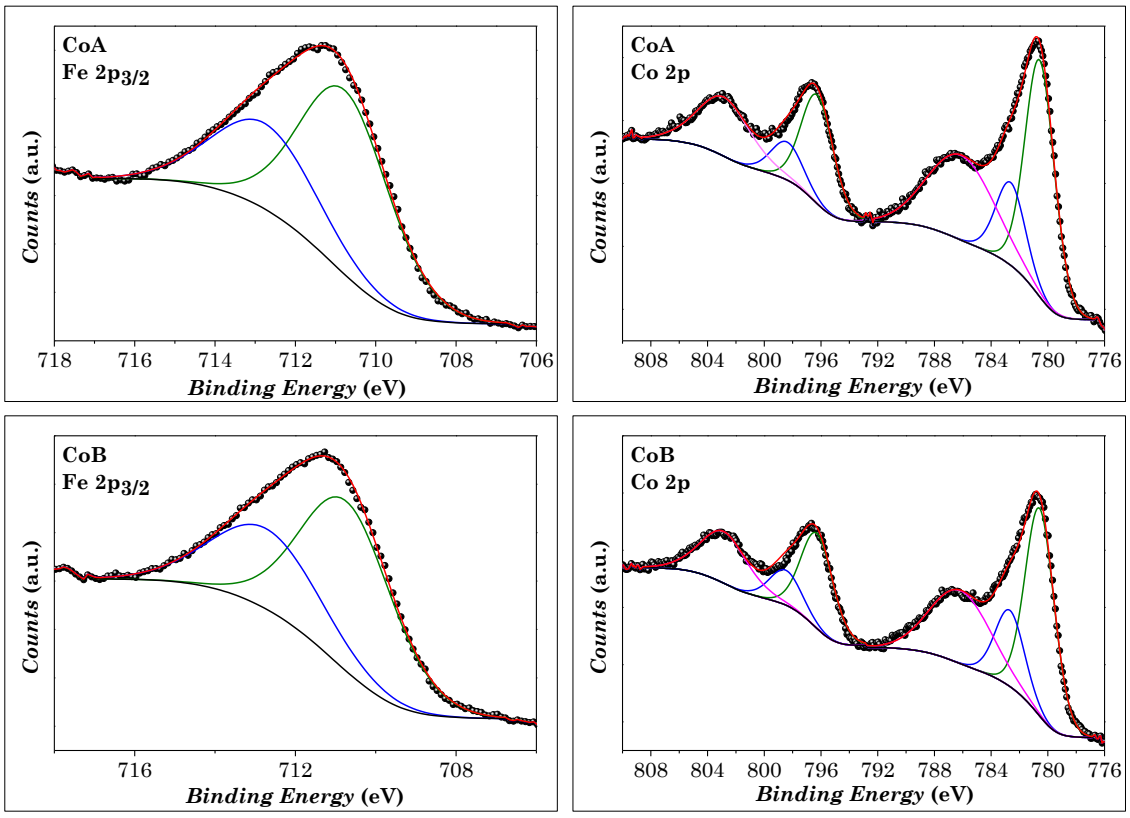

Figure 24. Fe and Co 2p peaks of CoA and CoB samples fitted by cation distribution approach. O_h sites are green, T_d blue, satellite magenta.

The lower value of binding energy is ascribable to the metal located in the octahedral positions, taking into account the effective charge on cations and the polarizability of oxygen. The inversion degrees found for both samples were found to be around 0.7 calculated from signals of both iron and cobalt, in good agreement with the values obtained from Mössbauer spectroscopy (0.67 and 0.65 for CoA and CoB, respectively).

Table 15. Curve fitting parameters for cation distribution approach on Fe2p$_{3/2}$ and Co2p$_{1/2}$ and 2p$_{3/2}$: binding energy (*BE*), full width at half maximum (FWHM), relative amount, inversion degree (γ), and inversion degree corrected by ICP-OES data. Co 2p$_{1/2}$ peaks are shifted by 16 eV toward higher binding energy.

Sample	Signal	BE (eV)	FWHM (eV)	Assignment	Relative Amount (%)	γ	γ (Corr.)
CoA	Fe 2p3/2	710.8(1)	2.7(1)	Fe in O_h	65	0.70	0.69
		712.8(1)	3.2(1)	Fe in T_d	35		
	Co 2p3/2	780.6(1)	2.4(1)	Fe in O_h	74	0.74	0.73
		782.6(1)	2.4(1)	Fe in T_d	26		
		786.4(1)	5.5(1)	Satellite	-		
CoB	Fe 2p3/2	710.7(1)	2.7(1)	Fe in O_h	64	0.72	0.67
		712.7(1)	2.7(1)	Fe in T_d	36		
	Co 2p3/2	780.6(1)	2.4(1)	Fe in O_h	73	0.73	0.67
		782.7(1)	2.4(1)	Fe in T_d	27		
		786.4(1)	5.5(1)	Satellite	-		

2.3.8 DC Magnetometry

DC magnetometry measurements were carried out on some selected samples (CoA, CoB, CoC, MnB, FeD). The magnetization isotherms and the ZFC-FC curves of the samples are reported in Figure 25, while the magnetic parameters in Table 16.

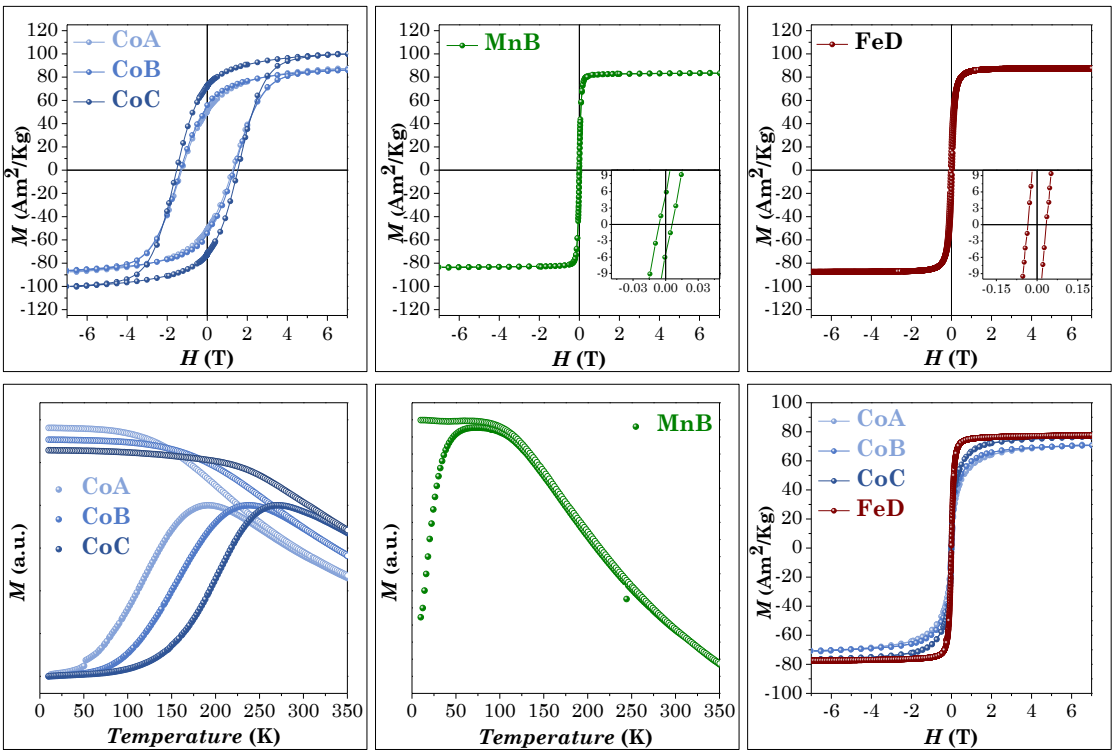

Figure 25. Magnetization isotherms recorded at 10 K (top); ZFC (full circles) and FC (empty circles) curves recorded at 10 mT (bottom); magnetization isotherms recorded at 300 K (bottom right) of CoA, CoB, CoB, MnB, and FeD samples.

Table 16. Basic parameters determined from the ZFC curves and magnetization isotherms. T_{max}, T_{diff}, T_b correspond to the maximum and furcation point of the ZFC curve (2%), and distribution of blocking temperatures respectively; H_c^{10}, H_K^{10} (2%), M_7^{10}, M_s^{10}, M_s^{300}, and M_r^{10} correspond to the coercivity, anisotropy field, magnetization at 7 T, saturation magnetization values at 10 K and 300 K, and remanent magnetization, respectively. Errors are about 5%.

Sample	T_{max} (K)	T_{diff} (K)	T_b (K)	H_c^{10} (T)	H_K^{10} (T)	M_7^{10} (Am²/kg)	M_s^{10} (Am²/kg)	M_r^{10} (Am²/kg)	M_r/M_s	M_s^{300} (Am²/kg)
CoA	195	270	126	1.28	4.2	90	97	53	0.55	73
CoB	241	266	163	1.32	3.8	90	96	58	0.62	74
CoC	274	313	206	1.54	4.1	92	100	67	0.67	77
MnB	79	81	18	0.01	0.01	83	83	6	0.07	-
FeD	-	-	-	0.34	0.34	87	87	20	0.23	78

Magnetization isotherms of all samples show no hysteretic behaviour at 300 K, typical for particles in the superparamagnetic state. A large hysteresis is instead present at 10 K for cobalt ferrite samples, and a tiny one for manganese ferrite and spinel iron oxide, indicating the soft magnetic behaviour of these phases. Coercive field increases with increases the particle size, in agreement with the Stoner-Wohlfarth model,[598] while the saturation magnetization is constant within the experimental error. Saturation magnetization of manganese ferrite and spinel iron oxide samples is equal to the magnetization at 7 T, while the estimated saturation magnetization is higher than the 7 T value in cobalt ferrite samples. This behaviour is related to the hard magnetic nature of cobalt ferrite, making the sample more difficult to saturate.[599] The reduced remanent magnetization (M_r/M_s) increases with the size of cobalt ferrite, going from 0.55 for CoA to 0.67 for CoC. The values are far from those expected for pure cubic anisotropy (0.83 for bulk cobalt ferrite)[600] and suggest that the cobalt ferrite samples have mixed cubic-uniaxial anisotropy with the first component becoming more dominant with the increase of the particles' size.

ZFC-FC curves show a furcation at a specific temperature (T_{diff}), with a maximum on the ZFC curve (T_{max}), that are proportional to the blocking temperature of the largest particles and the mean value, respectively. T_b is the blocking temperature calculated with the first derivative of the difference curve (M_{FC}-M_{ZFC}) as the temperature at which 50% of the nanoparticles are in the superparamagnetic state.[601,602] Both T_{max} and T_b increases with the size of cobalt ferrite, as predicted by the Stoner-Wohlfarth model,[598] and are in a good agreement with the previously reported values for cobalt ferrite of similar size.[235,562,603,604] An increase of interparticle interaction with the size of the particles is observed in the FC curves, as demonstrated by the temperature independent behaviour (curves flatness), kept for higher temperatures. The manganese ferrite sample (MnB) features lower T_{max}, T_{diff}, and T_b values compared to cobalt ferrite samples, due its soft magnetic behaviour.

2.3.9 AC Magnetometry

AC magnetometry was used to measure the temperature dependence of the in-phase (χ') and out-of-phase (χ'') component of the magnetic susceptibility at different frequencies (0.1-1000 Hz) for the cobalt ferrite samples CoA, CoB, and CoC (Figure 26).

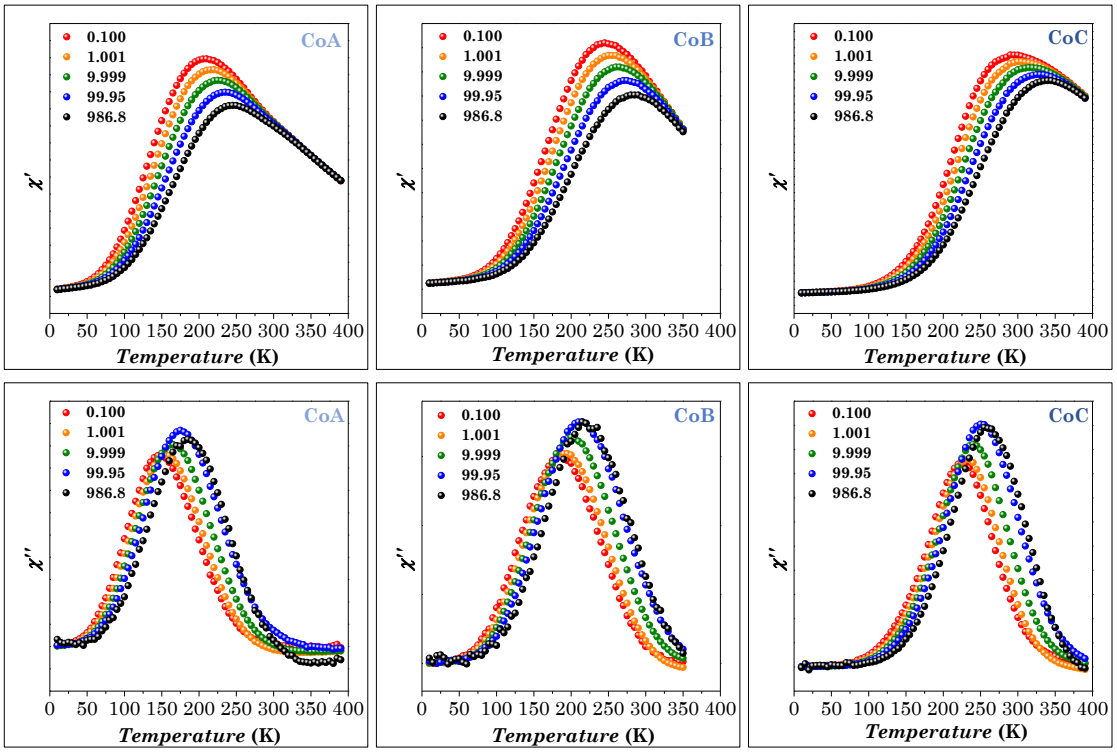

Figure 26. AC susceptibility measurements of the s CoA, CoB, and CoC samples. The in-phase (χ') component of the magnetic susceptibility is displayed in the upper part and the out-of-phase (χ'') in the bottom part.

T_{max} values show a shift towards higher frequencies, and it is, therefore, possible to estimate the Néel relaxation time, by using the Vogel-Fulcher model:[605]

$$\tau_N = \tau_0 e^{\left(\frac{E_b}{T-T_0}\right)} \qquad \text{Eq. 43}$$

Where τ_0 is the characteristic relaxation time, E_b the energy barrier against magnetization reversal, T the absolute temperature, and T_0 the temperature value accounting for the strength of magnetic interactions. The results are reported in Figure 27.

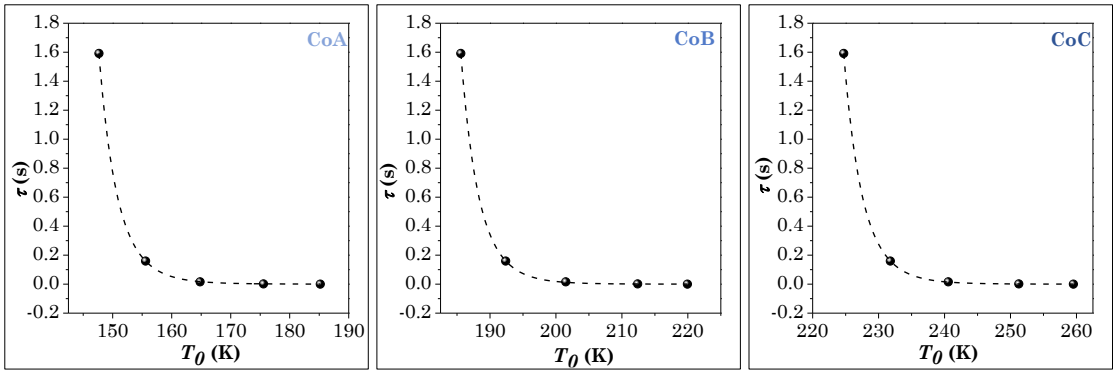

Figure 27. Curve fitting for the estimation of Néel relaxation time at 300 K, τ_N, by the Vogel-Fulcher model.

Table 17. Parameters obtained from the curve fitting by the Vogel-Fulcher model for T = 300 K. τ_0 is the characteristic relaxation time, E_b is the energy barrier against the magnetisation reversal, T_0 is the temperature value accounting for the strength of magnetic interactions, τ_N is the Néel relaxation time.

Sample	τ_0 (s)	E_b (K)	T_0 (K)	τ_N (s)
CoA	$9.4 \cdot 10^{-13}$	2499	59	$3 \cdot 10^{-8}$
CoB	$6.2 \cdot 10^{-13}$	2222	108	$6 \cdot 10^{-8}$
CoC	$1.5 \cdot 10^{-13}$	2555	140	$1 \cdot 10^{-6}$

The Néel relaxation times are equal to $3 \cdot 10^{-8}$, $6 \cdot 10^{-8}$, and $1 \cdot 10^{-6}$ s for CoA, CoB, and CoC, respectively. These results are in line with the increase of the particles' size of the nanoparticles.

2.4 Heat Release

In the light of these results, cobalt ferrite samples are the most promising materials, in terms of magnetic properties, and they were tested as heat mediator for magnetic thermal induction. Indeed, thanks to their hard magnetic behaviour, cobalt ferrite NPs present hyperthermic properties at smaller size compared to soft magnetic NPs. In detail, some selected cobalt ferrite samples were tested by recording heating curves under a magnetic field of 183 kHz and 17 kA·m^{-1}. The hydrophobic nanoparticles were made hydrophilic by an intercalation process with CTAB as described in paragraph 2.2.3. The concentration of the colloidal dispersion was 3.4 mg·mL^{-1}. The presence of CTAB molecules was verified by FT-IR, as shown in Figure 28.

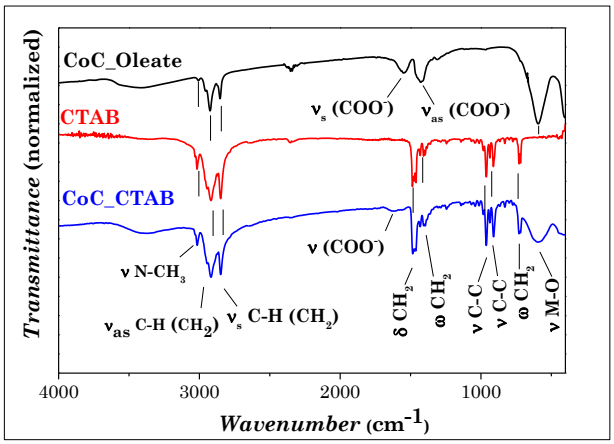

Figure 28. FT-IR spectra of CTAB, CoC_CTAB, and CoC_Oleate samples.

The FT-IR spectrum of CoC after the intercalation process (CoC_CTAB, Figure 28), shows the main vibration M-O mode at 594 cm^{-1}, the bands at 2945, 2917, 2870, and 2850 cm^{-1} associated to the different modes of the hydrocarbon chain (present in both oleate and CTAB), and the bands typical of CTAB in the region 1500-500 cm^{-1} besides the peak at 3015 cm^{-1} related to the N-CH_3 mode. The presence of the oleic acid molecules bonded to the nanoparticle surface is confirmed by the band at around 1550 cm^{-1}, associated with the carboxylate stretching mode.[606] The heating curves of the samples are reported in Figure 29.

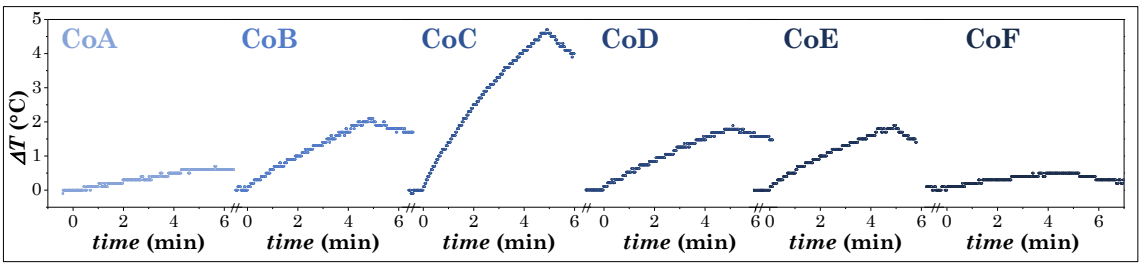

Figure 29. Heating curves obtained on aqueous colloidal dispersions (C_{inorg} = 3.4 mg/mL) of the cobalt ferrite samples at 30 °C and under a magnetic field of f = 183 kHz and H_0 = 17 kA/m.

Table 18. SAR and ILP values normalized for the oxide phase of the water dispersion of CTAB-cobalt ferrite samples.

Sample	$\langle D_{XRD} \rangle$ (nm)	$\langle D_{TEM} \rangle$ (nm)	$\sigma \langle D_{TEM} \rangle$ (%)	SAR (W/g_{ox})	ILP ($nH \cdot m^2 \cdot kg_{ox}^{-1}$)
CoA	5.5(2)	5.4	17	0*	0*
CoB	6.7(1)	7.1	14	21(1)	0.39(2)
CoC	7.9(2)	8.5	14	32(2)	0.60(4)
CoD	9.9(5)	11.1	13	19(3)	0.36(6)
CoE	11.2(4)	12.3	12	18(2)	0.33(2)
CoF	12.8(5)	13.3	13	0*	0*

***This has to be intended as negligible heat release**

Sample CoA does not heat up, due to the small size. On the contrary, all other samples show an increase in the temperature after the application of the alternate magnetic field. The heat released increases until CoC sample and then decreases up to CoF, which does not heat up again. These results are in agreement with other studies on cobalt ferrite nanoparticles that show a first increase in the heat release and a subsequent decrease after reaching a maximum at about 8-9 nm (Figure 30).[409]

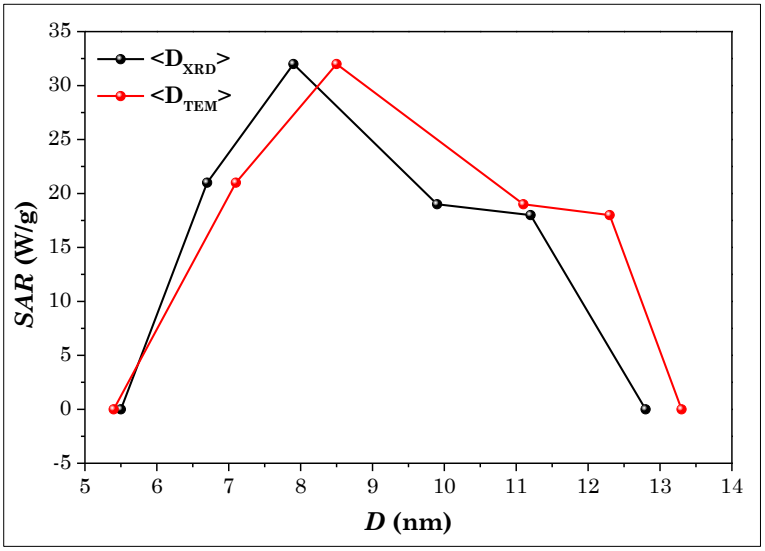

Figure 30. Evolution of SAR values with cobalt ferrite sizes.

The maximum SAR value reached is 32 W/g_{ox}, but for a better comparison with the literature it is useful to employ a parameter named Intrinsic Loss Power (ILP, $nH \cdot m^2 \cdot kg_{ox}^{-1}$), defined in Eq. 44:

$$ILP = \frac{SAR}{f \cdot H_0^2} \qquad \textbf{Eq. 44}$$

This formula arises from the observation that SAR increases linearly with the frequency quadratically with the amplitude.[607] It is valid under certain conditions as frequency values of up to several MHz, crystallite polydispersity of more than 0.1. Furthermore, a comparison among ILP values is possible only if similar environmental thermodynamic losses are involved.[608]

ILP values of cobalt ferrite nanoparticles are in line with those obtained by other authors for cobalt ferrite of similar particle size.[409,534] The initial increase of SAR is predicted by the linear response theory (paragraph 1.5.5.2) and agrees with the rise of nanoparticles size (Table 8) and Nèel relaxation times (Table 17) of the samples. Indeed, the maximum heat release is reached when the NPs relaxation time matches the inverse of the applied frequency. In our case, this value is 183 kHz, so $8.7 \cdot 10^{-7}$ s, therefore the $1 \cdot 10^{-6}$ s of sample CoC is more effective than those of CoA and CoB. However, the total relaxation time depends both on the Néel and Brown relaxation times, therefore DLS analyses were carried out on the aqueous dispersions to calculate the τ_B from the diffusion coefficient D_T, substituting the hydrodynamic volume of Eq. 33 with the diffusion coefficient (Eq. 46), through the Stokes-Einstein equation (Eq. 45):

$$R_H = \frac{K_B T}{6\pi\eta D_T} \qquad \textbf{Eq. 45}$$

$$\tau_B = \frac{1}{54}\frac{(K_B T)^2}{\pi^2 \eta^2 D_T^3} \qquad \textbf{Eq. 46}$$

The results are reported in Table 19:

Table 19. Diffusion coefficient calculated by DLS measurements and Brown relaxation time of the samples.

Sample	D_T (μm²/s)	τ_B (s)
CoA	1.76	$9 \cdot 10^{-3}$
CoB	4.92	$4 \cdot 10^{-4}$
CoC	5.53	$3 \cdot 10^{-4}$

The Brown relaxation time are in the order of 10^{-4} s, 2-3 orders of magnitude higher than Néel relaxation times and therefore not influencing the total relaxation time of the systems (Eq. 31). As discussed in paragraph 1.5.5.2, for materials with high magnetic anisotropy as cobalt ferrite nanoparticles, the Brown relaxation time should be significant beyond a value of particle size diameter of 8-9 nm. The high τ_B values found for cobalt ferrite samples suggest that the particles tend to agglomerate, as already observed.[553]

2.4.1 Ligand Exchange

To overcome the toxicity problem of the CTAB coating and to understand if the organic coating plays a role in the heat released by the samples, a different coating procedure were carried out by exchanging the original oleate capping agent with polyethylene glycol trialkoxysilane (PEG-TMS), as described in paragraph 2.2.3. This molecule was chosen for its numerous advantages, such as the colloidal, chemical and physical stability, surface

stabilisation, the possibility to functionalize for further conjunction, and the decrease of steric hindrance that reduces the clearance process by reticuloendothelial system organs.[609]

The exchange ligand process were done on a replica of CoC, named CoC_Rep, as it features the highest SAR value (Table 18). The replacement of the molecules as capping agent was confirmed by FT-IR analyses, as reported in Figure 31.

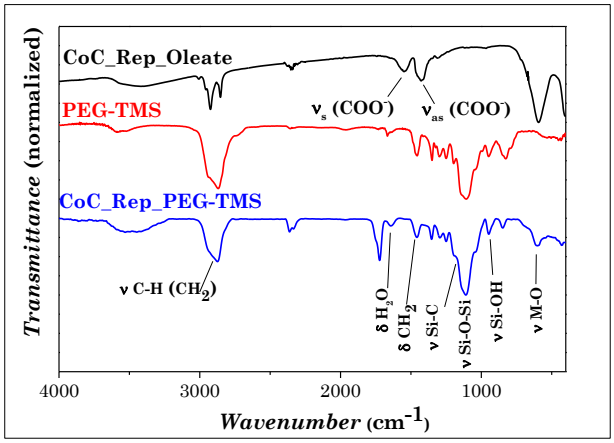

Figure 31. FT-IR spectra of PEG-TMS, CoC_Rep_PEG-TMS, and CoC_Rep_Oleate.

FT-IR spectrum of cobalt ferrite sample CoC after exchange ligand process (CoC_PEG-TMS) shows the M-O vibrational stretching mode at 600 cm^{-1}, shifted when compared to the original 594 cm^{-1} found for the sample with oleic acid as capping agent (Table 9), due to the formation of M-O-Si bond.[610] The characteristic bands of PEG-TMS in the region 1000-1100 cm^{-1} are evident in the cobalt ferrite sample, especially the Si-C, Si-O-Si, and Si-OH stretching modes at 1197, 1109, and 945 cm^{-1}, respectively.

The sample was tested as heat-mediator and the heating curves are reported in Figure 32 and the resulting SAR values in Table 20.

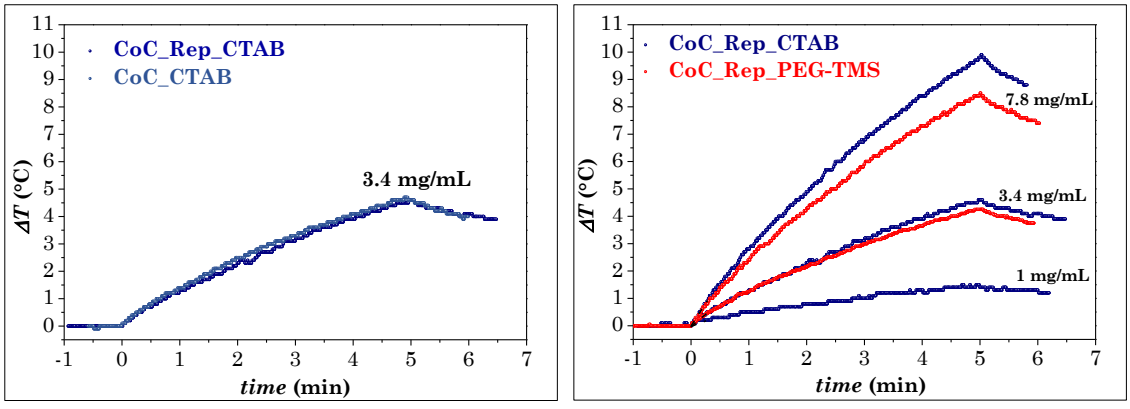

Figure 32. Left: heating curves obtained on aqueous colloidal dispersions at 3.4 mg/mL of CTAB coated CoC and CoC_Rep. Right: and heating curves obtained on aqueous colloidal dispersions of PEG-TMS coated and CTAB coated CoC_Rep sample at various concentration. All curves are obtained at an initial temperature of 30 °C and under a magnetic field of *f*=183 kHz and H_0 = 17 kA/m.

The heating curves were obtained at various concentrations for the sample CoC_Rep, to assess the SAR dependence on the concentration. Even though the final temperature of the curves is slightly different, the SAR values are equal within the experimental error for CoC and CoC_Rep, at different concentrations and different coating molecules (CTAB and PEG-TMS), except for the curve measured at 1 mg/mL where it is not possible to calculate the derivative dT/dt. The nature of the coating might influence the hydrodynamic diameter and therefore the Brown relaxation times, leading to different SAR values. Nonetheless, the Brown relaxation times estimated from DLS measurements are equal to $3 \cdot 10^{-4}$ and $2 \cdot 10^{-4}$ for CTAB and PEG-TMS coating, respectively, being both higher and negligible with respect to the Néel relaxation time. These results highlight the reliability and the repeatability of the measurements, as well as the strong dependence of the SAR on the inorganic part of the nanoparticles, in these experimental conditions.

Table 20. SAR and ILP values normalized for the oxide phase of the water dispersion of CTAB- and PEG-TMS CoC and CoC_Rep samples.

Sample	Ligand	Concentration (mg/mL)	$\langle D_{XRD} \rangle$ (nm)	SAR (W/g_{ox})	ILP (ILP ($nH \cdot m^2 \cdot kg_{ox}^{-1}$))
CoC	CTAB	3.4	7.9(2)	32(2)	0.60(4)
CoC_Rep	CTAB	3.4	7.7(7)	31(1)	0.58(1)
CoC_Rep	CTAB	7.8	7.7(7)	30(1)	0.57(1)
CoC_Rep	CTAB	1	7.7(7)	-	-
CoC_Rep	PEG-TMS	7.8	7.7(7)	32(1)	0.60(2)
CoC_Rep	PEG-TMS	3.4	7.7(7)	32(2)	0.60(4)

More experiments and comparisons focusing on different systems and particle size are needed to have a complete overview of the topic, however, the PEG-TMS coating offers numerous advantages over the CTAB in terms of toxicity, functionalisation for further conjugation, surface stabilization and a decrease of steric hindrance.[609] Nevertheless, the intercalation process with CTAB should be regarded as a good compromise for laboratory-scale studies, due to its simplicity, stability, and low-cost, and for these reasons, it has been chosen to prepare the aqueous colloidal dispersions for magnetic fluid hyperthermia tests.

2.5 Conclusions and Perspectives

Various samples of cobalt ferrite, manganese ferrite, and spinel iron oxide nanoparticles with different sizes were prepared through an oleate-based solvothermal synthesis. For all samples but MnD, MnE, and FeE, XRD, TEM, HRTEM, STEM-EDX, TGA, and FT-IR show spinel phase, spherical shape, unimodal size distribution with low dispersity, high crystallinity, and a monolayer of oleate capping molecules. Larger particle size were achieved by varying reaction temperature, solvent polarity, precursor concentration, and using the seed-mediated growth method. While cobalt ferrite samples resulted to be stoichiometric, a deficit of manganese was found in manganese ferrites. LT ^{57}Fe Mössbauer spectroscopy allowed to calculate the inversion degree, that correspond to 0.7 and 0.5 for $CoFe_2O_4$ and $MnFe_2O_4$ respectively, the absence of spin canting phenomena, and the partial oxidation of magnetite samples into maghemite. XPS confirmed the inversion degree values of cobalt ferrite, as well as the stoichiometric Co:Fe ratio and the absence of Fe^{II} and Co^{III}. RT Mössbauer and DC Magnetometry revealed the hard-magnetic properties of cobalt ferrite samples with respect to manganese ferrite and spinel iron oxide. AC magnetometry permitted to calculate the Néel relaxation times for the cobalt ferrite samples, that increases with crystallite and particle sizes. Finally, cobalt ferrite samples were tested as heat mediators for magnetic fluid hyperthermia, showing an increase of the heat released up to 32 W/g_{ox} for the sample CoC (~8 nm) and then a decrease until 0 W/g_{ox} for sample CoF (~13 nm). The toxicity of CTAB molecules was addressed by changing the coating with PEG-TMS through exchange ligand procedure. The same results obtained, concerning SAR response, with respect to CTAB coating represent an interesting strategy to be further explored. To maximize the performances, it could be interesting to further tune the magnetic properties through magnetic coupling between a hard and soft ferrimagnetic phase. Furthermore, starting with the hard cobalt ferrite phase, it is important to cover it with a crystalline non-toxic or biocompatible shell, to prevent the eventual cobalt release. A uniform coating could be in principle achievable with isostructural phases with similar cell parameters. Therefore, manganese ferrite and spinel iron oxide are the best candidates for this purpose.

3 *Spinel Ferrite-Based Core-Shell Nanostructures: Synthesis and Characterization*

Abstract

The oleate-based solvothermal method described in chapter 2 for the synthesis of single spinel ferrite NPs was also exploited in a seed-mediated growth approach to produce core-shell nanoheterostructures. Indeed, magnetic coupling between hard and soft ferrimagnetic phases permits the tuning of the magnetic properties and the optimization of the SAR response. In detail, cobalt ferrite and manganese ferrite nanoparticles (CoA, CoB, CoC, and MnC) were coated with isostructural spinel ferrites like maghemite/magnetite, $MnFe_2O_4$ and $CoFe_2O_4$ to create different heterostructures. The conventional study of the structure, morphology and composition (ICP-OES, XRD, TEM, RT and LT ^{57}Fe Mössbauer, TGA, FT-IR, DC and AC magnetometry) was combined with advanced techniques to provide details on the interface at the nanoscale level. Clear evidences of the heterostructure formation were obtained by mapping the nanoparticles' chemical composition by electron energy loss spectroscopy (EELS) and energy-dispersive X-ray spectroscopy (EDX) in the scanning transmission electron microscopy mode (STEM). In addition, chemical-sensitive electron tomography in STEM-EDX mode was applied to obtain detailed 3D images with a sub-nanometer spatial resolution. The cobalt ferrite-based nanostructures were tested as heat mediator for magnetic thermal induction.

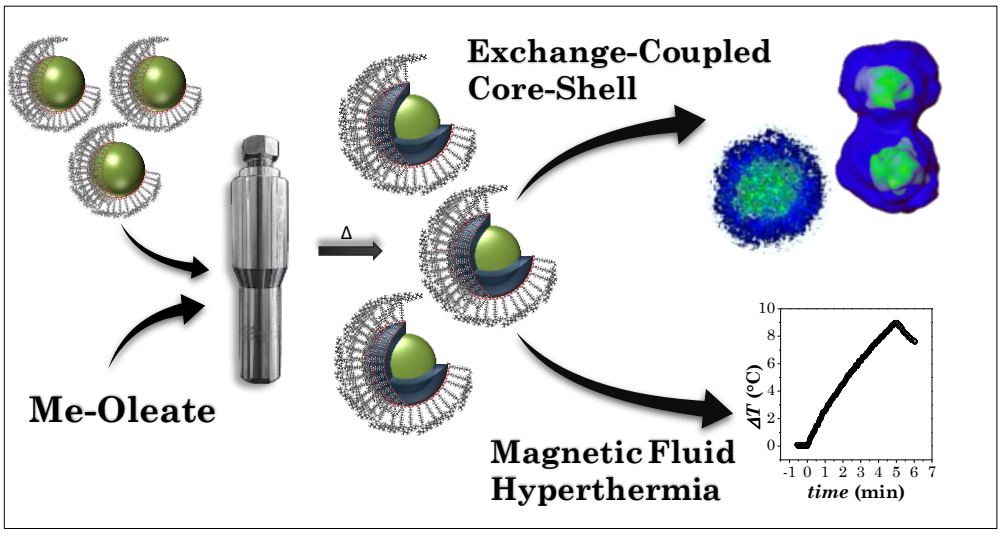

3.1 Introduction

In recent years, magnetic nanoparticles featuring a core-shell architecture have been studied increasingly to combine the physical and chemical properties of the different components to obtain multifunctional materials with a wide range of applications or to improve their performances.[505,557–559] In this framework, bi-magnetic core-shell nanoparticles play a fundamental role because of the interactions arising from the interface of antiferromagnetic (AF), ferromagnetic (FM) and ferrimagnetic (FiM) phases. Since the discovery of the exchange bias phenomena by Meiklejohn and Bean,[611] who prepared Co/CoO core-shell nanoparticles by surface treatment, FM(or FiM)/AFM and AFM/FM(or FiM) couplings have been extensively studied.[612–615] On the contrary, although the combination of magnetically hard and soft FM/FiM phases is of great interest for different applications (magnetic recording, permanent magnets, microwave absorption, biomedicine), these systems have been understudied, probably due to the difficulties in preparing such materials with respect to oxidized metals.[505] In this context, examples of ideal crystalline phases to study this type of magnetic interaction are provided by spinel ferrites ($M^{II}Fe_2O_4$, M^{II} = Fe^{II}, Co^{II}, Mn^{II}, Ni^{II}, *etc.*) which may exhibit hard or soft magnetic nature depending on the type of divalent ion[505,549,553,616] and can be easily prepared in a variety of methods.[386,570,616–619] As already seen, cobalt ferrite, with a high magnetocrystalline anisotropy, shows a hard-magnetic behaviour, while the isostructural manganese ferrite and spinel iron oxides (magnetite and maghemite) are magnetically soft phases. Appropriate engineering, in terms of type of architecture, shell thickness, core size, *etc.*, of hard-soft nanoheterostructures makes possible a fine tuning of the magnetic properties of the materials such as anisotropy and magnetization, that are crucial in many applications, including magnetic thermal induction (paragraph 1.5.5.2) Furthermore, another advantage of using isostructural phases is the possibility of an epitaxial growth of the shell around pre-existing seeds, with the so-called seed-mediated growth method.[243,409,620,621] This two-step synthetic strategy represents a versatile approach to achieve well-defined heterostructures with controllable interfaces by changing size, shape, composition, and structure of the core and the precursors of the shell.

Some studies have been carried out on various spinel ferrite materials with the aim of optimizing SAR performances.[202,409,413,415–418,554–556,622–624] Among the most efficient platforms, bimagnetic core-shell nanostructures, proposed by Cheon and co-workers,[409,623] exhibit surprisingly high SAR values compared to their single-phase counterparts, although obtained for organic colloidal dispersions under an AC field with frequency f = 500 kHz and amplitude H_0 = 37.3 kA/m.

Thus mastering the design and the preparation of advanced coupled bimagnetic core–shell NPs with specific properties is one of the ultimate goals in the research area of magnetic NPs.[405,625] In this context, it is essential to acquire a deep understanding of the underlying physical principles giving rise to the desired properties.

In this chapter, a seed-mediated growth approach in solvothermal conditions has been developed to synthesize core-shell nanoheterostructures made up of hard magnetic ($CoFe_2O_4$) and soft (magnetite Fe_3O_4/maghemite γ-Fe_2O_3 or $MnFe_2O_4$) phase featuring the same spinel structure, similar cell parameter, and phase-contrast imaging. Clear evidences of the effective obtainment of the core-shell structure were found by combining conventional techniques such as powder X-ray diffraction (XRD), transmission electron microscopy (TEM), induced coupled-plasma (ICP), room and low temperature ^{57}Fe Mössbauer spectroscopy, DC and AC magnetometry, with more advanced approaches (STEM-EELS, STEM-EDX, and STEM-EDX tomography) to map the chemical composition at the nanoscale. The heating ability of the aqueous colloidal dispersions of cobalt ferrite-based core-shell NHs is discussed based on an in-depth investigation of their magnetic behaviour, structure, and composition.

3.2 Synthesis: Seed-Mediated Growth

The synthesis of spinel ferrite-based core-shell nanoparticles through seed-mediated growth in solvothermal condition of mixed metal oleates is reported in ref. [288].

The CoA, CoB, CoC, and MnC nanoparticles were used as seeds to produce core-shell nanostructures employing a second solvothermal treatment in the presence of the shell metal precursors (seed-mediated growth, Table 21). In particular, for CoA and CoB, two core-shell samples were prepared with a shell of spinel iron oxide and manganese ferrite, indicated as Cox@Fe and Cox@Mn (where x = A, B), respectively. Moreover, for CoC, two core-shell of different thickness were prepared from both manganese ferrite and spinel iron oxide. This samples were labelled as CoC@Mn1 and CoC@Mn2 (or CoC@Fe1 and CoC@Fe2). Finally, two core-shell samples with a shell of cobalt ferrite and spinel iron oxide were prepared for sample MnC, labelled as MnC@Co and MnC@Fe respectively.

Different attempts (not reported) were carried out to achieve the best experimental conditions, concerning ratio seeds/shell precursor, solvent, concentration of the precursors, allowing the production of larger nanoparticles with a narrow size distribution. Therefore, in this chapter is reported a selection of the best samples obtained, regarding size dispersion, for the selected experimental conditions. For example, we found out that 1-octanol is not a suitable solvent because it leads to a high dispersity of the product. This might be ascribed to the polarity of the solvent that causes colloidal instability in the seed nanoparticles' dispersion. Being toluene an excellent solvent to disperse nanoparticles, it was chosen instead of 1-octanol. We used a mixture of M^{II}-Fe^{III} oleates (M^{II} = Co^{II}or Mn^{II}, in ratio M^{II}:Fe^{III} = 1:2) to create a shell of cobalt or manganese ferrite, whereas Fe^{II}-oleate was the chosen precursor to build up a shell of spinel iron oxide. Indeed, in these experimental conditions, the use of Fe^{III} or a mixture of Fe^{II} and Fe^{III}-oleates leads to the formation of hematite (see chapter 2). The amount of hexane dispersion containing the desired quantity of particles (seeds) was added into a teflon liner. The particles were precipitated by adding ethanol in a 1:1 volume ratio with the hexane dispersion and separated with the aid of a magnet while pouring away the supernatant. Then, the particles were dissolved in 10 mL of toluene (with the help of sonication) and 10 mL of a 1-pentanol solution of metals oleate were added. Finally, after the addition of 5 mL of distilled water, the liner was enclosed into the autoclave and treated at 220 °C for 10 hours. After the heat treatment, the purification steps were the same used for the seeds. Table 21 summarises the synthesis conditions for the core-shell nanostructures.

Table 21. Synthesis condition for the core-shell nanoparticles.

Sample	Seeds (mg)	n Oleate (mmol)[a]	1-pentanol (mL)	Toluene (mL)	Water (mL)	Temperature (°C)	Reaction time (h)
CoA@Mn	105	1.3	10	10	5	220	10
CoA@Fe	50	2.5	10	10	5	220	10
CoB@Mn	50	1	10	10	5	220	10
CoB@Fe	50	1	10	10	5	220	10
CoC@Mn1	50	2.5	10	10	5	220	10
CoC@Mn2	50	1.5	10	10	5	220	10
CoC@Fe1	50	4	10	10	5	220	10
CoC@Fe2	50	2	10	10	5	220	10
MnC@Co	25	1	10	10	5	220	10
MnC@Fe	25	1	10	10	5	220	10

[a]Referred to Mn^{II}-Fe^{III} oleates (manganese ferrite shell), Co^{II}-Fe^{III} Oleates (cobalt ferrite shell) or Fe^{II} oleate (spinel iron oxide shell)

3.3 Characterization

3.3.1 Powder X-ray Diffraction (XRD)

XRD patterns of the core-shell systems (Figure 33) show the typical reflections of a spinel phase. From the profile analysis, the average crystallite sizes were estimated and are reported in Table 22.

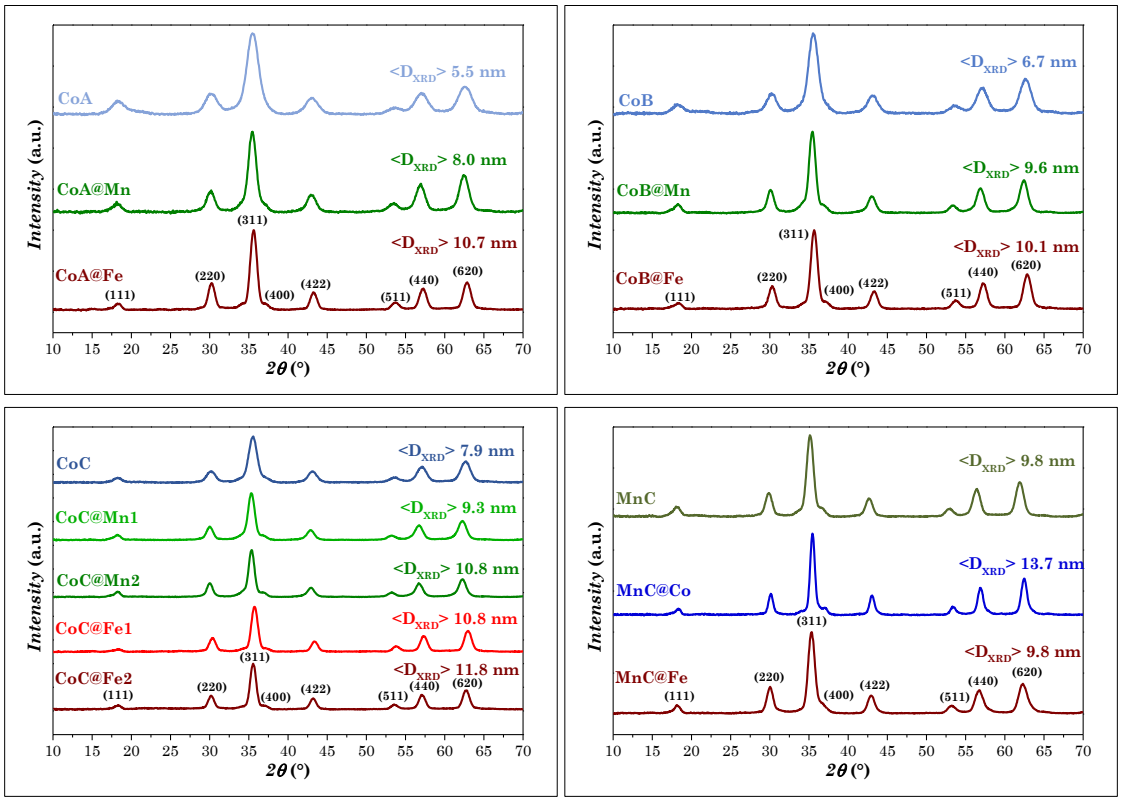

Figure 33. XRD patterns of core-shell samples with respective cores.

Table 22. Cell parameter (a), mean crystallite (<D_{XRD}>) and particle (<D_{TEM}>) size, particle size dispersity (σ), organic phase weight percentage, and M^{II}:Fe^{III} ratio determined by ICP of the core-shell samples and respective core.

Sample	a (Å)	<D_{XRD}> (nm)	<D_{TEM}> (nm)	σ <D_{TEM}> (%)	Organic phase (%)	M^{II}:Fe^{III}[a]
CoA	8.39(1)	5.5(2)	5.4	17	24	0.49
CoA@Mn	8.40(2)	8.0(2)	9.4	11	21	0.41
CoA@Fe	8.36(1)	10.7(3)	10.5	11	11	-
CoB	8.38(1)	6.7(1)	7.1	14	20	0.45
CoB@Mn	8.41(1)	9.6(4)	12.7	12	12	0.43
CoB@Fe	8.35(1)	10.1(3)	12.2	13	10	-
CoC	8.38(1)	7.9(2)	8.5	14	18	0.55
CoC@Mn1	8.43(1)	9.3(6)	12.6	13	12	0.41
CoC@Mn2	8.43(1)	10.8(8)	14.4	11	9	0.45
CoC@Fe1	8.34(1)	10.8(2)	11.1	13	11	-
CoC@Fe2	8.38(1)	11.8(6)	12.1	13	10	-
MnC	8.47(1)	9.8(3)	10.8	13	15	0.50
MnC@Co	8.40(1)	13.7(8)	17.9	11	8	0.64
MnC@Fe	8.42(1)	9.8(8)	12.8	13	9	-

[a]referred to the shell fraction in case of core-shell samples

A slight variation of the lattice parameter was observed for some core-shell systems. An increase of the lattice parameter is found in the case of manganese ferrite-covered cobalt ferrite samples, in agreement with the higher value of cell parameter for manganese ferrite than that of cobalt ferrite. Conversely, a decrease of the lattice parameter was detected when the shell is made of spinel iron oxide. The core-shell samples MnC@Co and MnC@Fe underwent a reduction of the lattice parameter due to the presence of cobalt ferrite and spinel iron oxide, respectively. Concerning the crystallite size obtained from the experimental profile, all the core-shell samples showed higher values compared to the cores (Table 22), suggesting that a growth process took place, except for the sample MnC@Fe, where the crystallite size was identical to the one found for the core. This can be explained with the formation of an amorphous shell of spinel iron oxide around the pre-formed core or a partial dissolution of the core surface.

3.3.2 Inductive Coupled Plasma-Optic Emission Spectroscopy (ICP-OES)

ICP analyses were carried out on both core and core-shell systems. Taking into account the M^{II}:Fe^{III} molar ratio found in the cores (paragraph 2.3.3), it was possible to roughly estimate the M^{II}:Fe^{III} molar ratio in the shell, in the case of cobalt or manganese ferrite coating. Indeed, CoA@Mn, CoB@Mn, CoC@Mn1, CoC@Mn2, and Mn1@Co samples showed a M^{II}:Fe^{III} molar ratio in the shell equal to 0.48, 0.43, 0.41, 0.45, and 0.64, respectively, indicating the formation of quasi-stoichiometric spinel ferrite shell. The empirical formulas are reported in Table 22.

3.3.3 Transmission Electron Microscopy (TEM and HRTEM/HRSTEM)

The TEM Bright Field images of the core-shell samples, reported in Figure 34, show spherical particles with unimodal size distribution and mean particle size higher than the core, suggesting that the growth of new phase around the pre-existing seeds forming a core-shell heterostructure occurred, instead of the nucleation of new particles. This is also supported by the significant decrease of the dispersity with respect to the original core.
A careful study using high-resolution microscopy (HRTEM, Figure 35 and HRSTEM, Figure 36) was conducted on all the samples, showing highly crystalline particles with no evidence of any amorphous part or heterojunctions. The interlayer distances confirmed the presence of the spinel oxide phase in agreement with the XRD data. The core-shell samples showed no lattice mismatch, suggesting an epitaxial coating on the respective cores.

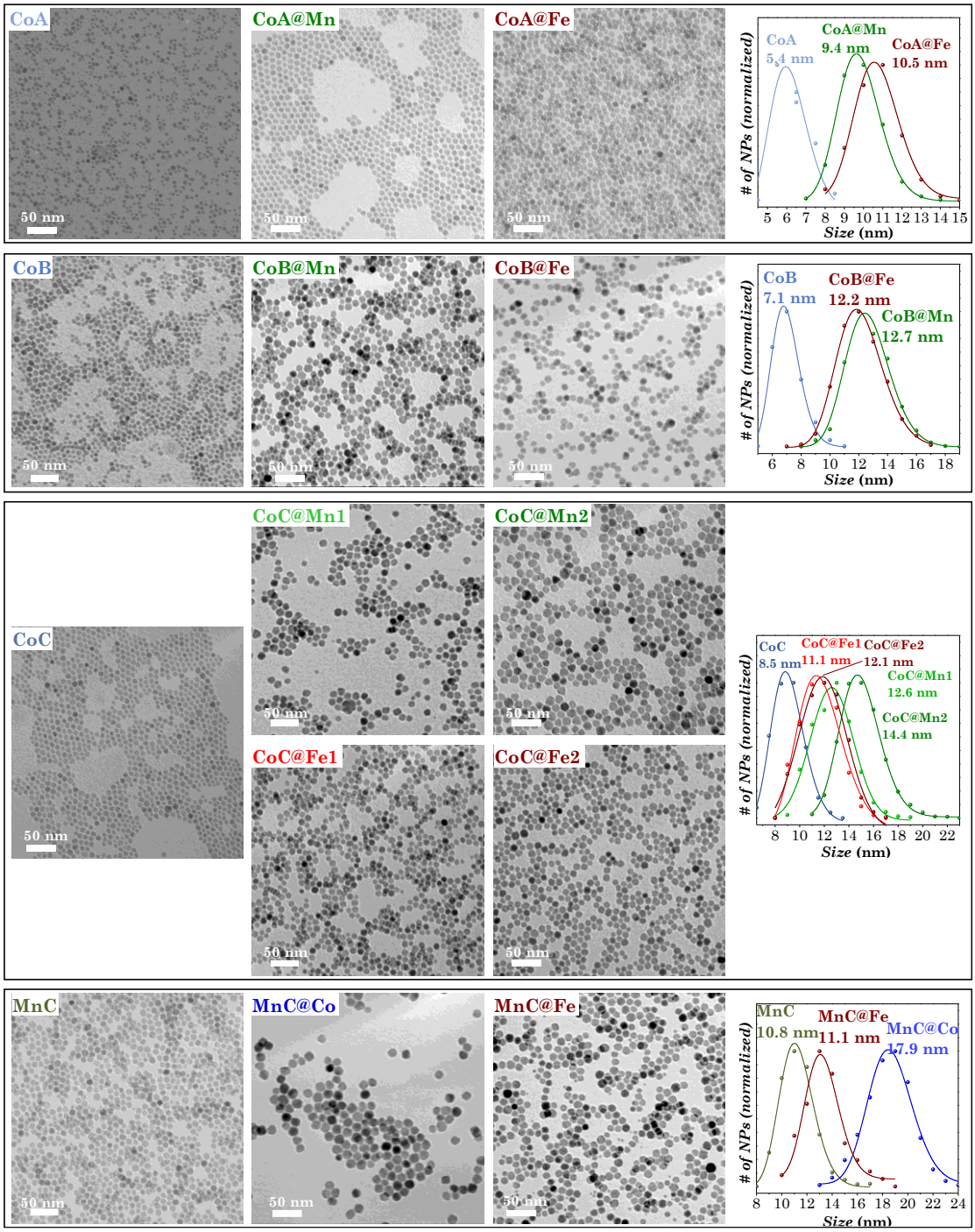

Figure 34. TEM Bright Field images and particle size distributions of core-shell samples and respective cores

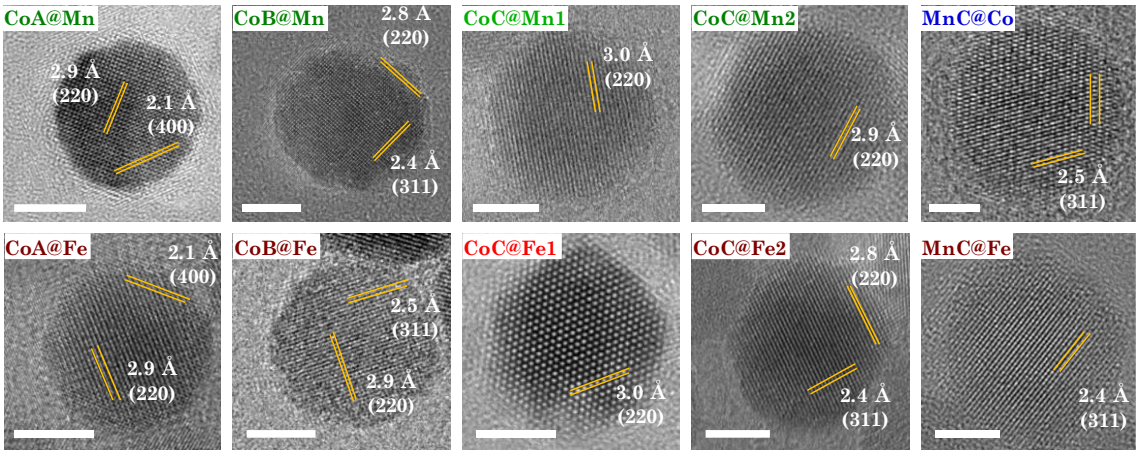

Figure 35. HRTEM images of core-shell samples.

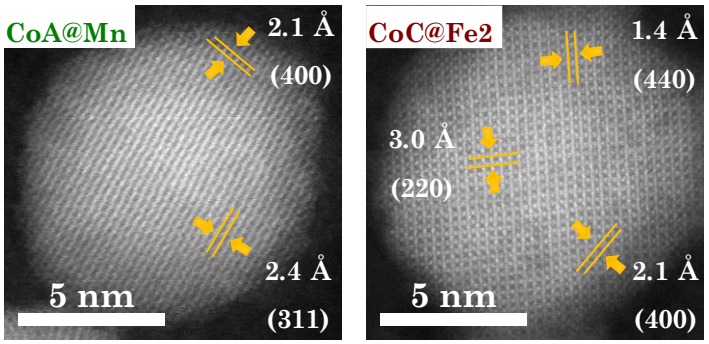

Figure 36. HRSTEM images of CoA@Mn and CoC@Fe2 samples.

Unfortunately, due to the very similar phase-contrast imaging, even high-resolution microscopy could not distinguish the core from the shell.

3.3.4 Thermogravimetric Analysis (TGA) and Fourier Transform-Infrared Spectroscopy (FT-IR)

The capping by oleate molecules was demonstrated by FT-IR (Figure 37) and TGA (Figure 38), as for the single cores (paragraph 2.3.5). Complete assignment of FT-IR bands is reported in Table 23. The Me-O stretching bands are shifted to lower wavenumbers when cobalt ferrite nanoparticles are covered with a shell of manganese ferrite or spinel iron oxide, while they are shifted at higher value when manganese ferrite is covered by cobalt ferrite. The shift is in agreement with the theoretical values for cobalt ferrite (575 cm^{-1}), manganese ferrite (550 cm^{-1}), and maghemite (580 cm^{-1}).[626,627] The core-shell samples covered by spinel iron oxide show, in the region between 700-350 cm^{-1}, show the typical bands of maghemite, suggesting that the oxidation of Fe^{II} to Fe^{III} occurred.

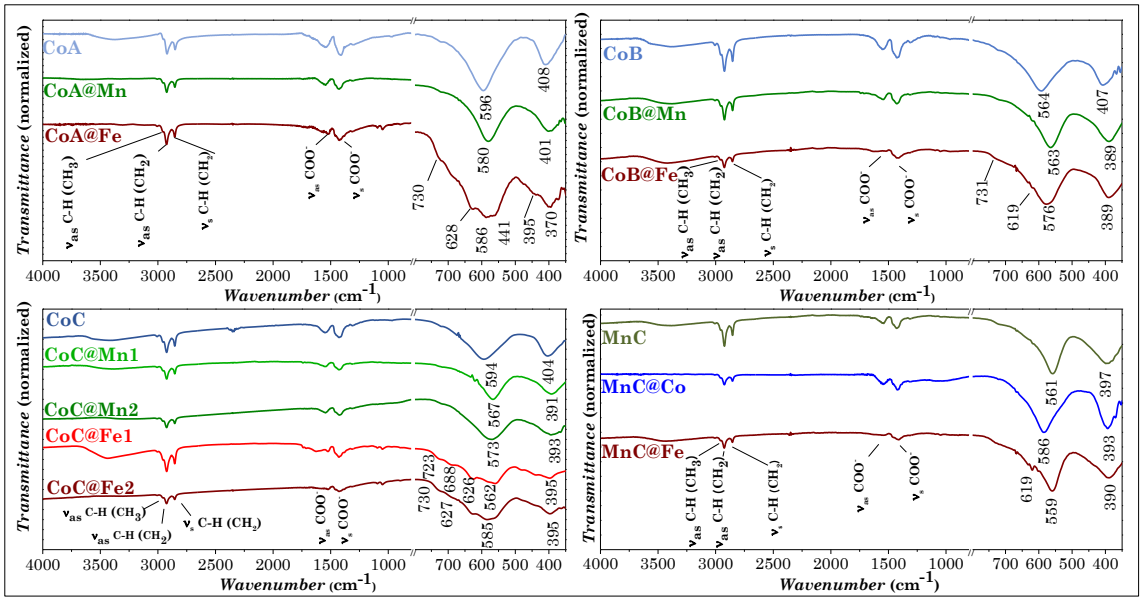

Figure 37. FT-IR spectra of CoA, CoA@Mn, and CoA@Fe.

Table 23. Assignment of FT-IR bands of core-shell samples.

Wavenumber (cm^{-1})										Vibration mode
CoA@		CoB@		CoC@				MnC@		
Mn	Fe	Mn	Fe	Mn1	Mn2	Fe1	Fe2	Co	Fe	
3007	3008	3005	3007	3008	3006	3006	3008	3008	3007	CH=CH stretching
2957	2956	2954	2958	2956	2958	2954	2958	2958	2956	C-H asymmetric stretching (CH_3)
2924	2926	2923	2925	2924	2925	2924	2926	2925	2925	C-H asymmetric stretching (CH_2)
2874	2874	2870	-	2872	2874	2871	2874	2874	2874	C-H symmetric stretching (CH_3)
2854	2854	2853	2854	2854	2854	2852	2854	2852	2854	C-H symmetric stretching (CH_2)
1550	1550	1546	1520	1549	1545	1550	1550	1548	1549	COO^- asymmetric stretching
1429	1427	1427	1419	1427	1425	1422	1429	1421	1415	COO^- symmetric stretching
721	721	719	731	717	721	723	730	-	-	CH_2 wagging
-	688	-	-	-	-	688	-	-	-	Fe-O stretching
-	628	-	619	-	-	626	627	-	619	Fe-O stretching
596	586	563	576	567	573	584	585	586	559	Metal-O stretching of T_d and O_h sites
-	441	-	-	-	-	562	-	-	-	Fe-O stretching
409	399	389	389	391	393	395	395	393	390	Metal-O stretching of O_h sites
-	370	-	-	-	-	-	-	-	-	Fe-O stretching

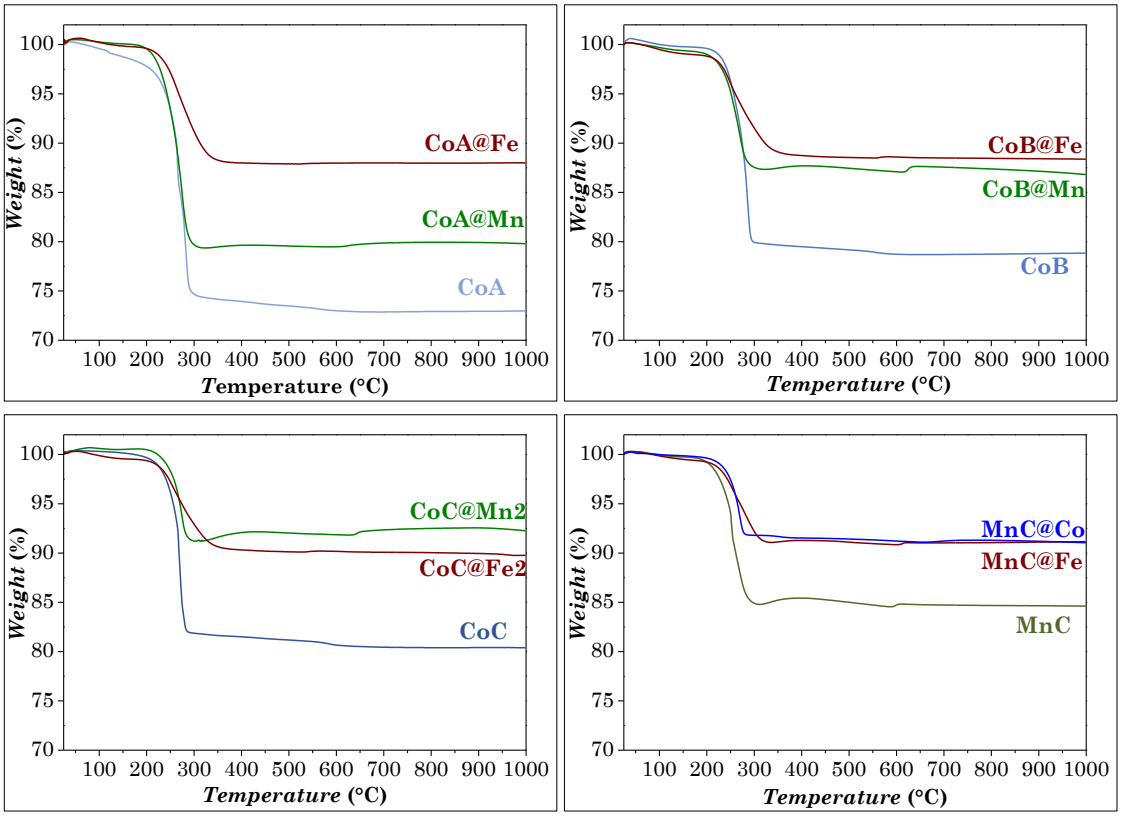

Figure 38. TGA curves of core-shell samples and respective cores obtained in oxygen atmosphere.

As described in paragraph 2.3.5,[55] the weight loss percentages obtained from the TGA curves were used to estimate the surface area occupied by oleate molecules. The computations are reported in Table 24 and the values are in the range 22-42 Å²/molecule, in good agreement with those reported by other authors for oleic acid-coated spinel iron oxides nanoparticles and suggests the presence of a close-packed monolayer of the capping agent.[571–573]

Table 24. Computation of capping molecule packing on the core-shell nanoparticle surface.

Sample	$\langle D_{TEM} \rangle$ (nm)	A_{NP} (nm²)	V_{NP} (nm³)	m_{NP} (g)	#NPs	m_{Ol} (g)	n_{Ol} (mmol)	#Ol	#Ol/NP	A_{Ol} (Å²)
CoA@Mn	9.4	278	435	$2.2 \cdot 10^{-18}$	$3.6 \cdot 10^{17}$	0.21	0.75	$4.5 \cdot 10^{20}$	1261	22
CoA@Fe	10.5	346	606	$3.1 \cdot 10^{-18}$	$2.9 \cdot 10^{17}$	0.11	0.39	$2.4 \cdot 10^{20}$	817	42
CoB@Mn	12.7	507	1073	$5.5 \cdot 10^{-18}$	$1.6 \cdot 10^{17}$	0.12	0.43	$2.6 \cdot 10^{20}$	1596	32
CoB@Fe	12.2	468	951	$4.8 \cdot 10^{-18}$	$1.9 \cdot 10^{17}$	0.1	0.36	$2.1 \cdot 10^{20}$	1153	41
CoC@Mn1	12.6	499	1047	$5.3 \cdot 10^{-18}$	$1.6 \cdot 10^{17}$	0.12	0.43	$2.6 \cdot 10^{20}$	1558	32
CoC@Mn2	14.4	651	1563	$8.0 \cdot 10^{-18}$	$1.1 \cdot 10^{17}$	0.09	0.32	$1.9 \cdot 10^{20}$	1687	39
CoC@Fe1	11.1	387	716	$3.7 \cdot 10^{-18}$	$2.4 \cdot 10^{17}$	0.11	0.39	$2.4 \cdot 10^{20}$	966	40
CoC@Fe2	12.1	460	928	$4.7 \cdot 10^{-18}$	$1.9 \cdot 10^{17}$	0.1	0.36	$2.1 \cdot 10^{20}$	1125	41
MnC@Co	17.9	1007	3003	$1.5 \cdot 10^{-17}$	$6.0 \cdot 10^{16}$	0.08	0.28	$1.7 \cdot 10^{20}$	2849	35
MnC@Fe	12.8	515	1098	$5.6 \cdot 10^{-18}$	$1.6 \cdot 10^{17}$	0.11	0.39	$2.4 \cdot 10^{20}$	1481	35

3.3.5 ^{57}Fe Mössbauer Spectroscopy

RT and LT, in the absence and the presence of an external magnetic field, were performed to investigate the structure and the magnetic properties of the samples.

3.3.5.1 Room-Temperature ^{57}Fe Mössbauer Spectroscopy

RT ^{57}Fe Mössbauer spectra are reported in Figure 39, while the hyperfine parameters are shown in Table 25.

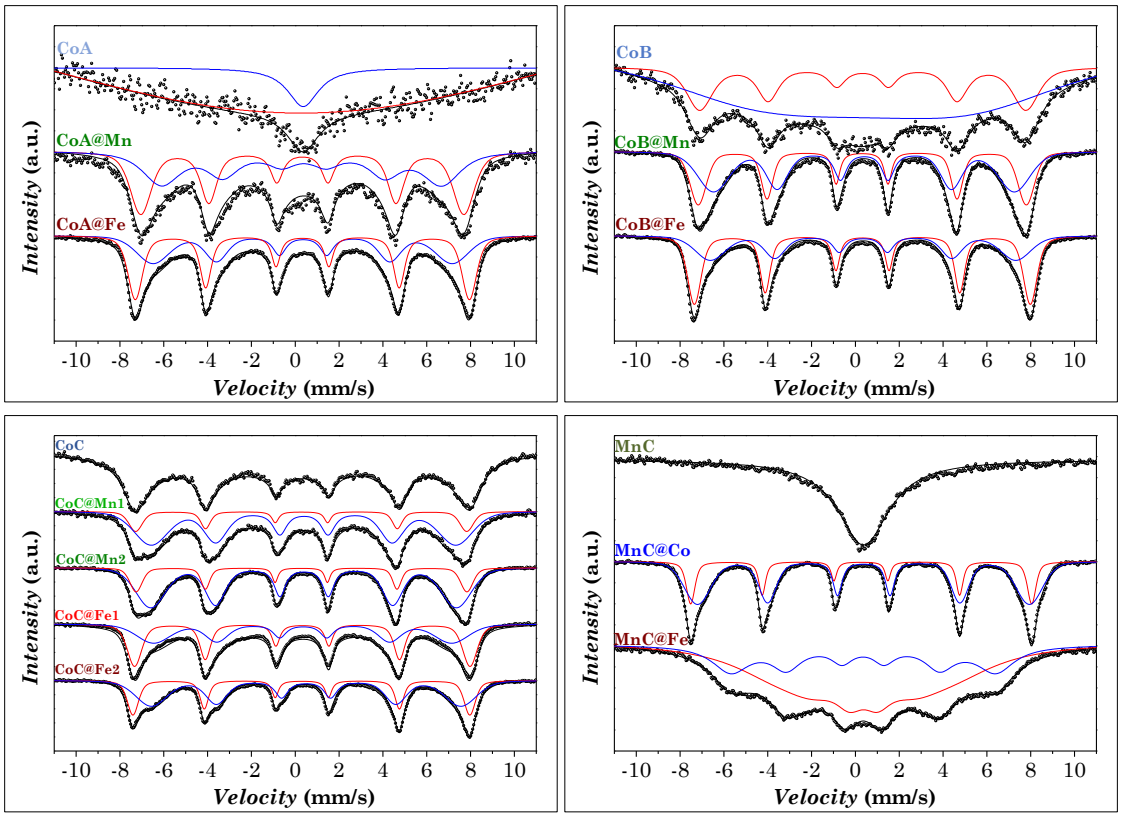

Figure 39. RT ^{57}Fe Mössbauer spectra of core-shell samples and respective cores.

The spectra of core-shell samples were fitted with two sextets, due to the appearance of two contributions that can be due to two different spinel phases ($CoFe_2O_4$ and $MnFe_2O_4$ or maghemite/magnetite) or to two different sublattices (octahedral and tetrahedral) in a spinel phase due to the formation of a single coherent structural domain, as observed by HRTEM (Figure 36). As already discussed in paragraph 2.3.6.1, octahedral sites differ from tetrahedral ones by different features: i) higher isomer shift values;[574] ii) higher full-width at half maximum (FWHM);[575] iii) lower hyperfine field values at room temperature.[576] Nevertheless, because of the strong overlap of signals at room temperature it is difficult to obtain unambiguous conclusions on structural phase and iron position in octahedral and tetrahedral sites. The discussion of Mössbauer spectra will be therefore mainly focused on the evolution of magnetic properties manifested by the hyperfine field.

Table 25. RT ^{57}Fe Mössbauer parameters of core-shell samples and respective cores: values of the isomer shift (δ), hyperfine field (B_{hf}), and full width at half-maximum (FWHM) of the components.

Sample	$<D_{XRD}>$ (nm)	Signal	δ (mm/s)	B_{hf} (T)	FWHM (mm/s)
CoA	5.5(2)	**Singlet**	0.2(1)	-	12(1)
		Singlet	0.44(6)	-	1.1 (2)
CoA@Mn	8.0(2)	**Sextet**	0.32(1)	45.8(1)	0.7(2)
		Sextet	0.34(2)	39.7(2)	1.6(5)
CoA@Fe	10.7(3)	**Sextet**	0.32(1)	47.3(1)	0.5(1)
		Sextet	0.35(1)	42.4(2)	0.6(1)
CoB	6.7(1)	**Sextet**	0.34(1)	46.1(1)	1.7(1)
CoB@Mn	9.6(4)	**Sextet**	0.31(1)	46.5(1)	0.4(1)
		Sextet	0.40(1)	42.7(1)	0.6(1)
CoB@Fe	10.1(3)	**Sextet**	0.32(1)	47.6(1)	0.4(1)
		Sextet	0.36(1)	43.3(1)	0.6(1)
CoC	7.9(2)	**Sextet**	0.32(1)	46.9(1)	0.9(2)
CoC@Mn1	9.3(6)	**Sextet**	0.28(1)	46.9(1)	0.3(1)
		Sextet	0.39(1)	43.2(1)	0.7(1)
CoC@Mn2	10.8(8)	**Sextet**	0.28(1)	46.9(1)	0.3(1)
		Sextet	0.39(1)	43.4(1)	0.6(1)
CoC@Fe1	10.8(2)	**Sextet**	0.32(1)	47.6(1)	0.4(1)
		Sextet	0.35(1)	42.3/	0.6(1)
CoC@Fe2	11.8(6)	**Sextet**	0.29(1)	47.8(1)	0.3(1)
		Sextet	0.50(1)	43.9(1)	0.6(1)
MnC	9.8(3)	**Singlet**	0.37(1)	-	2.8(1)
MnC@Co	13.7(8)	**Sextet**	0.26(1)	48.3(1)	0.3(1)
		Sextet	0.37(2)	47.1(1)	0.4(2)
MnC@Fe	9.8(8)	**Sextet**	0.39(1)	24.8(1)	1.0(1)
		Sextet	0.35(2)	37.5(2)	1.0(2)

The isomer shift values for all the samples but CoC@Fe2 are in the range of Fe^{III} (0.28-0.40 mm/s), whereas CoC@Fe2 presents a higher isomer shift for one sextet (δ = 0.50 mm/s), due to the presence of Fe^{II}, suggesting incomplete oxidation to Fe^{III}. The different behaviour from to the other spinel iron oxide covered core-shell systems is probably due to the larger nanoparticle size that leads to a lower degree of oxidation of magnetite to maghemite. Nevertheless, since iron is present in both the core and the shell, the evaluation of the amount of Fe^{II} and Fe^{III} in our samples is not trivial and the occurrence of Fe^{II} in the other spinel iron oxide coated core-shell NPs cannot be wholly excluded. The hyperfine field values can be affected by the nature of the coating (manganese ferrite or spinel iron oxide) and the thickness of the shell (and consequently the final crystallite size). For instance, in this study, the core-shell samples with spinel iron oxide coating showed hyperfine field values higher than those for manganese ferrite shell, due to the higher anisotropy constant of spinel iron oxide. Nonetheless, crystallite size affects the hyperfine field values, for instance for CoC@Fe1 and CoC@Fe2, where the higher hyperfine field values were found for the larger sample (CoC@Fe2).

The sample MnC@Co showed the highest hyperfine field values for both sextets, due to the large crystallite size and the presence of cobalt ferrite in the shell, which accounts for 78% of the total nanoparticle volume. On the contrary, the sample MnC@Fe shows two collapsed sextets, due to the presence of nanoparticles in the edge between the superparamagnetic and the blocked state, which present the lowest hyperfine field values for both signals, being manganese ferrite and maghemite/magnetite two magnetically soft phases compared to cobalt ferrite.

3.3.5.2 Low-Temperature ^{57}Fe Mössbauer Spectroscopy

LT ^{57}Fe Mössbauer with external magnetic field (6T) spectra are reported in Figure 40, while the hyperfine parameters are shown in Table 26.

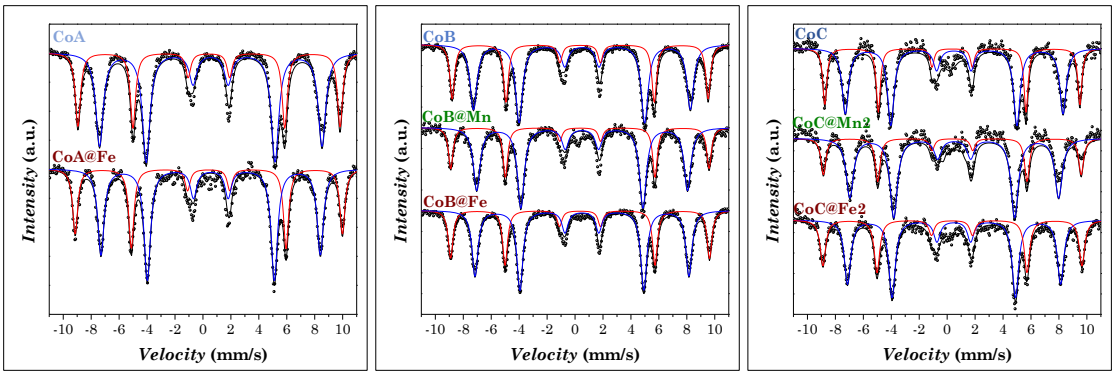

Figure 40. LT ^{57}Fe Mössbauer spectra of core-shell samples and respective cores measured with the presence of external magnetic field of 6T. Octahedral sites are represented in blue, tetrahedral in red.

Table 26. Low Temperature (4 K) ^{57}Fe Mössbauer parameters of the samples recorded under an external magnetic field (6T): values of the isomer shift (δ), effective field at 0T ($B_{eff}^{0T} = B_{hf}$) and 6T (B_{eff}^{6T}), relative area (A), canting angles (α), inversion degree (γ) of the core or the shell (in case on core-shell NPs), and chemical formula calculated from site occupancy corrected by ICP-OES data.

Sample	Signal	Site	δ (mm/s)	B_{eff}^{0T} (T)	B_{eff}^{6T} (T)	A (%)	α (°)	γ	Formula
CoA	Sextet	T_d	0.43(1)	52.6(1)	58.3(1)	34%	19	0.67	$(Co_{0.31}Fe_{0.69})[Co_{0.67}Fe_{1.32}]O_4$
	Sextet	O_h	0.56(1)	55.4(1)	49.4(1)	66%	0		
CoA@Fe	Sextet	T_d	0.41(1)	53.0(1)	59.4(1)	37%	0	-	$@(Fe_1)[Fe_{1.65}]O_4$
	Sextet	O_h	0.56(1)	55.1(1)	48.8(1)	63%	0		
CoB	Sextet	T_d	0.37(1)	51.2(1)	56.9(1)	35%	19	0.65	$(Co_{0.27}Fe_{0.72})[Co_{0.65}Fe_{1.33}]O_4$
	Sextet	O_h	0.49(1)	54.4(1)	48.2(1)	65%	10		
CoB@Fe	Sextet	T_d	0.36(1)	51.5(1)	57.5(1)	36%	0	-	$@(Fe_1)[Fe_{1.71}]O_4$
	Sextet	O_h	0.49(1)	53.5(1)	47.5(1)	64%	0		
CoB@Mn	Sextet	T_d	0.36(1)	51.1(1)	57.4(1)	30%	0	0.44	$@(Mn_{0.48}Fe_{0.50})[Mn_{0.44}Fe_{1.55}]O_4$
	Sextet	O_h	0.50(1)	52.5(1)	46.9(1)	70%	20		
CoC	Sextet	T_d	0.37(1)	51.2(1)	56.7(1)	35%	25	0.74	$(Co_{0.33}Fe_{0.68})[Co_{0.74}Fe_{1.27}]O_4$
	Sextet	O_h	0.49(1)	54.4(1)	48.4(1)	65%	0		
CoC@Fe2	Sextet	T_d	0.36(1)	51.2(1)	57.6(1)	36%	0	-	$@(Fe_1)[Fe_{1.74}]O_4$
	Sextet	O_h	0.48(1)	53.2(1)	47.4(1)	64%	14		
CoC@Mn2	Sextet	T_d	0.37(1)	51.2(1)	57.3(1)	27%	0	0.46	$@(Mn_{0.43}Fe_{0.55})[Mn_{0.46}Fe_{1.52}]O_4$
	Sextet	O_h	0.51(1)	52.6(1)	46.4(1)	73%	0		

As for the pure core (paragraph 3.3.5.2) in the absence of the external magnetic field, the spectra show the overlapping of two sextets associated with the octahedral and tetrahedral sites of the spinel structure. The in-field measurements allow to split these two subspectra and to calculate the occupancy in the two sublattices, reported in Table 26.
The isomer shift values are in the range typical for Fe^{III} measured at 4 K and are equal to the values of the corresponding core. Consequently, the presence of a maghemite shell can be supposed in the case of the spinel iron oxide coated core-shell, suggesting that oxidation of the original magnetite took place. For the sample CoA@Fe, it was found from related area that 37% of Fe cations are located in tetrahedral positions and 63% in octahedral positions. The comparison of these data with the core ones allowed to estimate the cation distribution of the shell. Taking into account the iron fraction in the core calculated from ICP-OES measurements (0.10) and the site occupancy of the core, we can estimate the amount of Fe in the shell, which corresponds to 38% and 62% for tetrahedral and octahedral sites respectively. Consequently, the ratio Fe(O_h)/Fe(T_d) is 1.65. This result is in agreement with the theoretical maghemite ratio, which value is 1.67, while for stoichiometric magnetite is 2.[70] The same behaviour is revealed in the samples CoB@Fe and CoC@Fe2, whose Fe(O_h)/Fe(T_d) ratios are equal to 1.71 and 1.74, respectively. The increased Fe(O_h)/Fe(T_d) ratio with the NPs size is in line with the RT Mössbauer data the suggested a lower degree of oxidation for the larger sample, CoC@Fe2.
By using the same procedure, Fe content in CoB@Mn shell was estimated and the inversion degree was found equal to 0.46. Consequently, the formula of the shell can be written as $(Mn_{0.43}Fe_{0.55})[Mn_{0.46}Fe_{1.52}]O_4$. A similar behaviour was observed for sample CoC@Mn, with an inversion degree of 0.44. This result is in good agreement with the theoretical value of inversion degree for nanosized manganese ferrite,[586] also found in the sample MnA (Table 13). The chemical formula of the different samples with site occupancies are reported in Table 26.
Canting angles were calculated, as for the cores (paragraph 2.3.6.2), and no spin canting was revealed (Table 26) supporting the evidence from HRTEM data for a homogeneous epitaxial growth of the shell around the core with a formation of a single crystalline domain (Figure 36).
The sample CoB@Fe was measured at different magnetic field (from 1 to 6 T) to get information on the spin saturation process (Figure 41).

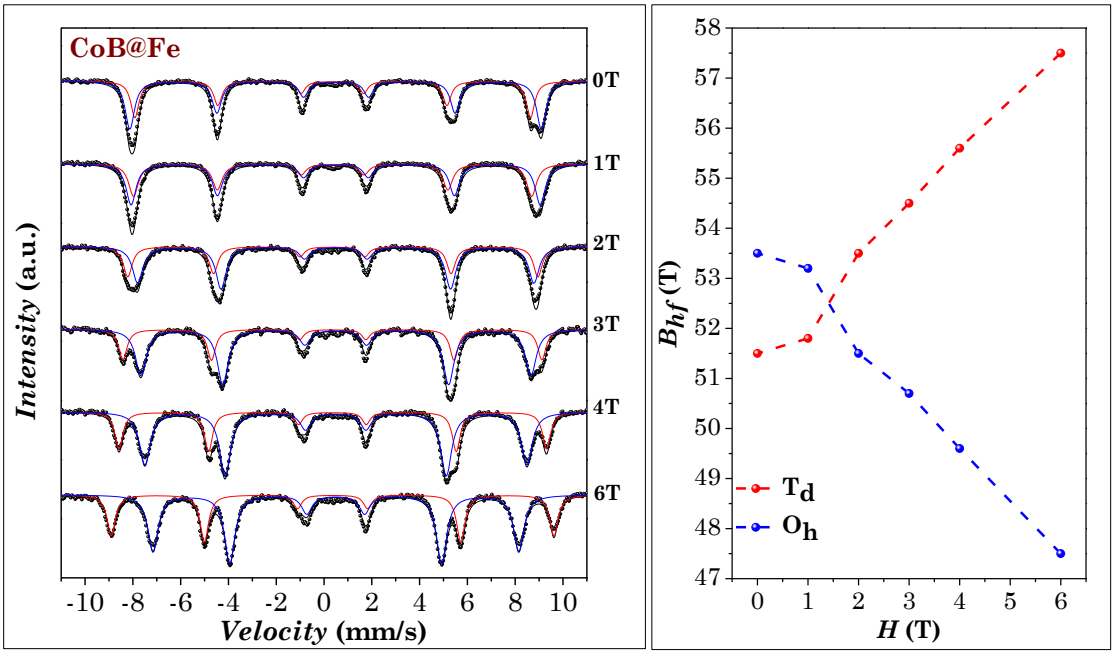

Figure 41. LT ^{57}Fe Mössbauer spectra of CoB@Fe sample measured with an external magnetic field from 1 to 6T (left); Evolution of B_{hf} as a function of the external field (right). Octahedral sites are represented in blue, tetrahedral in red.

Even with the external magnetic field of 1 T, the splitting of the two sextets was observed. From the right panel of Figure 41 right, it can be noticed that, at 0 T, the octahedral sites have larger hyperfine field than tetrahedral ones, while at 6 T an inversion occurred. This is due to the antiparallel direction of octahedral hyperfine field with respect to the external applied field (Figure 72). The increase of the hyperfine field in the tetrahedral sites (or decrease in octahedral sites), when 1 T of external field is applied, is equal to 0.3 T. When 2 T of external magnetic field is applied, the B_{hf} changes of 1.5 T for T_d and 1.7 for O_h sites, while it changes of about 1 T for all the subsequent increase of external magnetic field up to 6 T. The different behaviour observed below and above 2 T is probably caused by the unsaturated magnetic moment, that requires a field of such strength to be saturated, as it can be revealed from the field-dependence of the magnetization at low temperature (Figure 48).

3.3.6 Electron Energy Loss Spectroscopy (STEM-EELS), Energy-Dispersive X-ray Spectroscopy (STEM-EDX), and 3D-Tomography in Scanning/Transmission Mode

It is worth noting that to have a direct and unambiguous proof of the formation of core-shell heterostructures, chemical mapping at the nanoscale is mandatory.[628–630] Consequently, STEM-EDX, STEM-EDX tomography, and STEM-EELS mapping of Fe, Co and Mn were carried out. In the literature, only EELS[208,405,409,422,623] is generally performed for chemical mapping at the nanoscale and there are no examples of the combined use of the two techniques. Thanks to the recent technological progresses in the field of energy-dispersive X-ray spectroscopy, in particular in the development of

ultrasensitive detectors (Super-X™ detector with multiple silicon drift detectors),[631–633] high-quality EDX maps[634,635] and a detailed comparison between EDX and EELS are here presented in order to support our findings about the actual obtainment of a core-shell heterostructure.

Figure 42 shows, as an example, the comparison between STEM-EDX and STEM-EELS chemical mapping with the corresponding line profiles of CoA-based core-shell NPs. Other chemical mapping images for core-shell nanoparticles having cobalt ferrite and manganese ferrite as core are shown in Figure 43 and Figure 44, respectively.

Both STEM-EDX and EELS chemical mapping of the core-shell samples unambiguously indicate the formation of a core-shell heterostructure with the same spatial resolution. Considering the extensive and established use of the electron energy loss spectroscopy, this comparison reveals that also the energy-dispersive x-ray spectroscopy can also be employed as a powerful approach to investigate core-shell heterostructures with sub-nanometer spatial resolution.[634]

The single particle line profile calculated from EDX and EELS data reveals that the amount of M^{II} (Co^{II} or Mn^{II}) in the shell gradually decreases up to the interface. This behaviour, already observed,[208,409] can be explained by technical or chemical effects. First of all, the chemical mapping was performed in transmission mode, so on 2D projections of spheroidal nanoparticles. Only ideal objects, such as perfect spheres with an ideal core-shell structure, lead to not-overlapped core and shell compositional profiles (Figure 45).

On the contrary, for real samples, shape imperfections of the three-dimensional particle will result in a misrepresented one-dimensional profile, being the average of several sections all over the particle (360°). Concerning the chemical effect, it is known that the high temperature and acid condition[408,636] can induce a partial dissolution of the nanoparticles. Hence, during the seed-mediated growth treatment, a slight dissolution of the core surface might occur, leading to a mixed chemical composition in the interface. However, in our case, *i.e.* mild temperature (220 °C) and non-acid condition, the dissolution phenomena can be considered limited.

These results allowed to visualize the core-shell heterostructure, pointing out 3D details: a sharp interface, the spheroidal shape of the particle and homogenous coating of the shell around the well-centred core, *i.e.* with a uniform shell thickness.

The shell thickness was calculated from the chemical maps and are reported in Table 27.

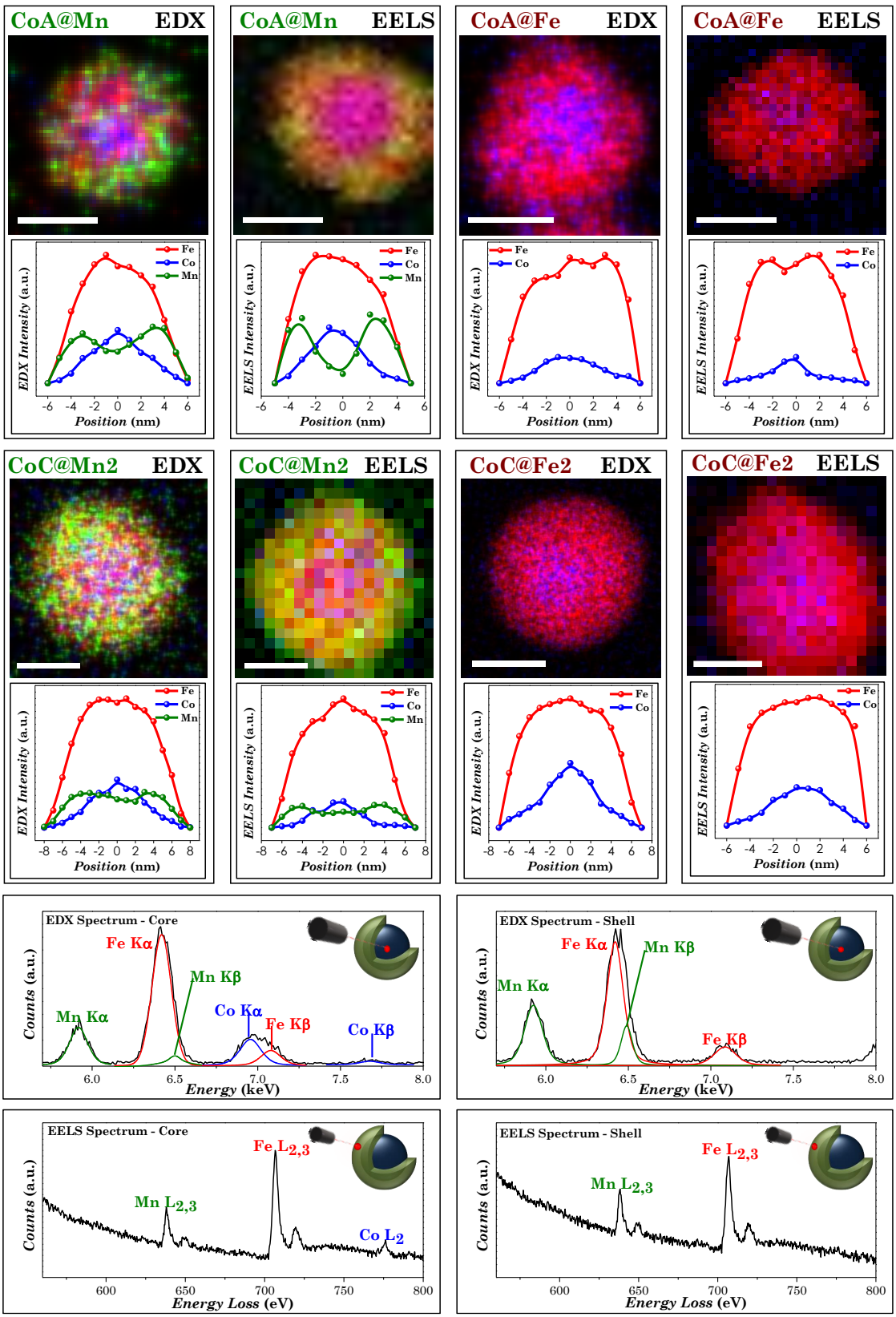

Figure 42. STEM-EDX and STEM-EELS chemical mapping on top of the line profile across the samples. Cobalt is represented in blue, manganese in green, iron in red. Scale bar is 5 nm. Bottom: example of EDX and EELS spectra of CoC@Mn2 recorded at the centre of the particle (core) and the edge (shell).

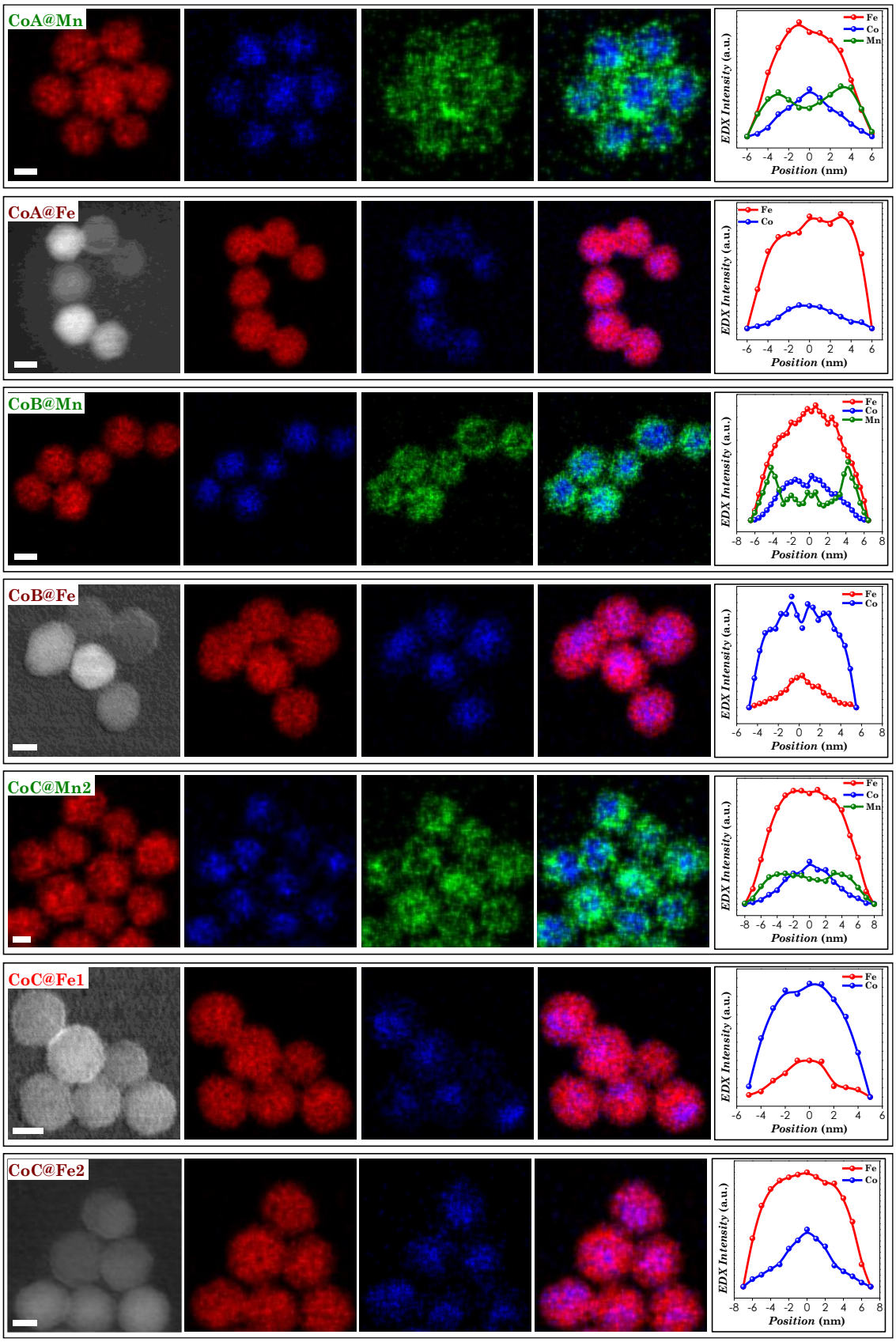

Figure 43. STEM-EDX chemical mapping of cobalt ferrite-based core-shell nanoparticles, line profile across the samples, and HAADF images. Cobalt is represented in blue, manganese in green, iron in red. Scale bar is 5 nm.

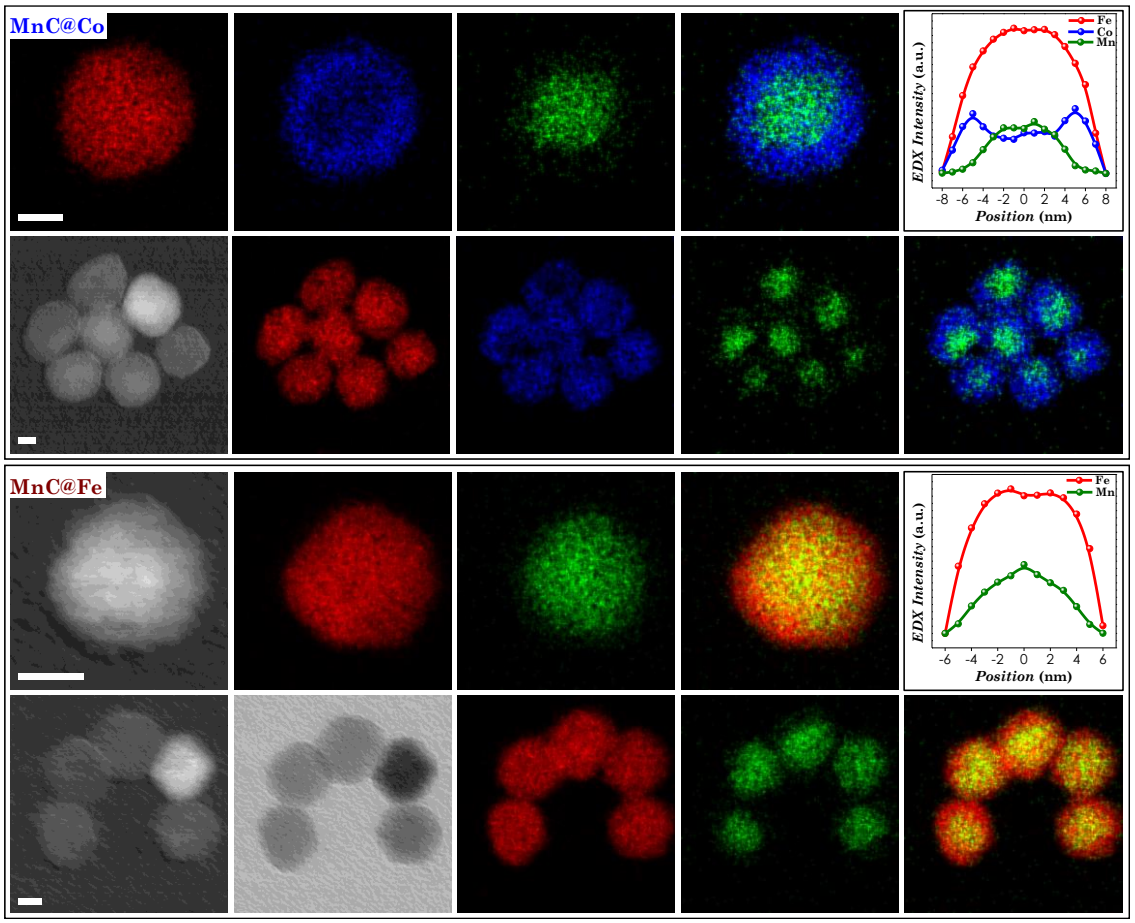

Figure 44. STEM-EDX chemical mapping of manganese ferrite-based core-shell nanoparticles, line profile across the samples, and HAADF images. Cobalt is represented in blue, manganese in green, iron in red. Scale bar is 5 nm.

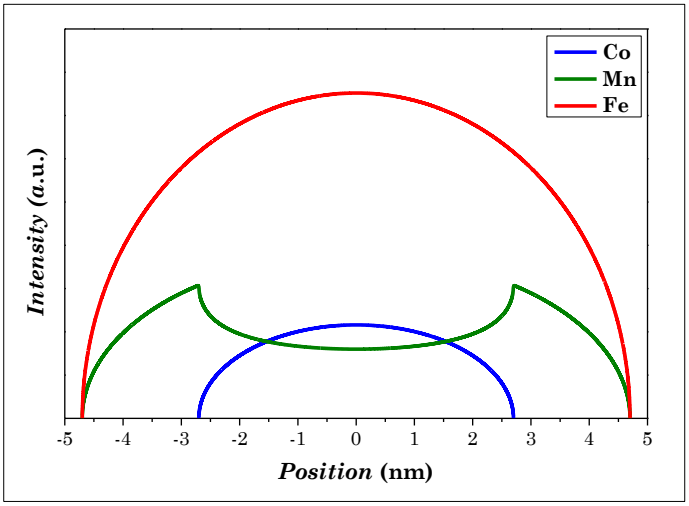

Figure 45. Ideal compositional profile of a 9.4 nm core-shell nanoparticles having a 5.4 nm cobalt ferrite core and 2 nm manganese ferrite shell thickness.

Being aware of the projection limits (2D images and 1D line profiles), STEM-EDX tomography were performed on the CoC@Fe2 sample. The three-dimensional reconstruction of the Co and Fe distributions are shown in Figure 46.

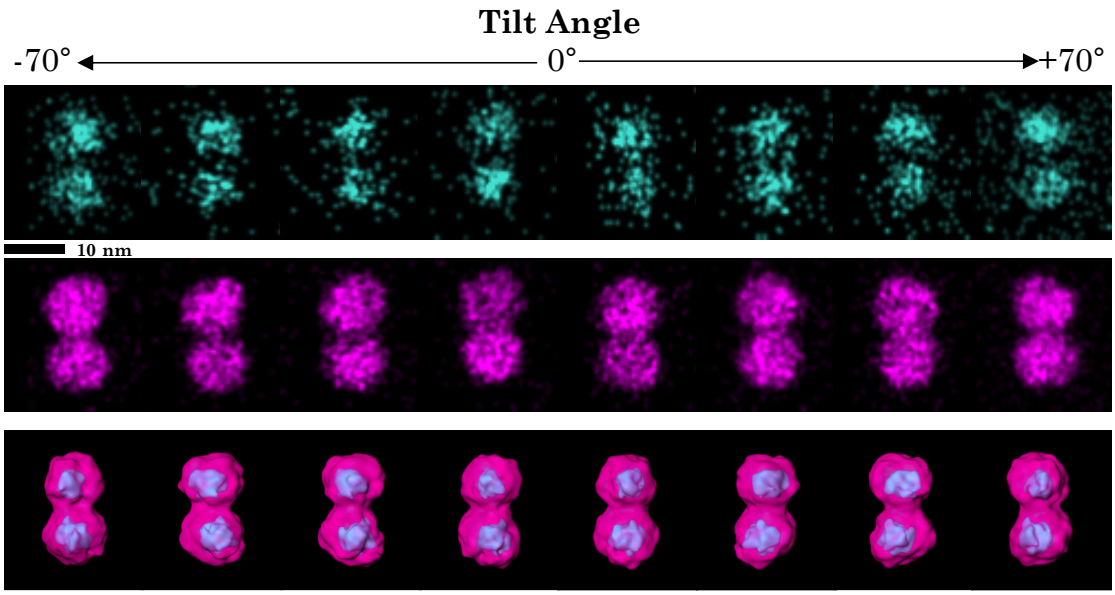

Figure 46. STEM-EDX tomography of the CoC@Fe2 sample. Top two rows show the projected distribution of Co and Fe mapped by STEM-EDX and the third row shows the isosurface rendition of the 3D distributions of Co and Fe in two touching CoC@Fe2 particles.

Table 27. Shell thickness calculated from TEM (<Δ_{TEM}>), STEM-EDX (<D_{EDX}>), and STEM-EELS (<D_{EELS}>).

Sample	Shell Thickness		
	<Δ_{TEM}> (nm)	<D_{EDX}> (nm)	<D_{EELS}> (nm)
CoA@Mn	2.3	2.2	1.9
CoA@Fe	2.5	2.9	3.0
CoB@Mn	2.8	2.0	-
CoB@Fe	2.6	2.5	-
CoC@Mn1	2.1	-	-
CoC@Mn2	3.0	3.1	3.1
CoC@Fe1	1.3	1.8	-
CoC@Fe2	2.1	2.6	2.5
MnC@Co	3.5	4.5	-
MnC@Fe	1.0	1.6	-

Δ_{TEM} has been calculated as difference between <D_{TEM}> of core-shell and core NPs. D_{EDX} and D_{EELS} have been calculated directly from chemical mapping images.

The values correspond quite well to the ones calculated by conventional TEM as difference between core and core-shell diameters and are between 2-3 nm. By the above findings, thanks to the nanoscale chemical mapping, the achievement of core-shell heterostructures was proven.

3.3.7 DC Magnetometry

DC magnetometry measurements, *i.e.* Zero Field Cooled and Field Cooled protocols (ZFC-FC, Figure 47)) and magnetization isotherms at 300 and 10 K (Figure 48) were carried out on the core-shell nanoparticles having cobalt ferrite as core, to study the magnetic coupling between the hard and the soft ferrimagnetic phases. In the previous chapters, the core-shell architecture of the heterostructure and the physical contact between the two phases were

demonstrated, but an in-depth study of the magnetic coupling is required. Some magnetic features of the field- and temperature-dependent magnetization evidenced in the samples can be an indication of the effective magnetic coupling phenomena between the two ferrimagnetic phases in hard-core/soft-shell systems: (i) the presence of a single-phase like hysteretic behaviour (Figure 48); (ii) the decrease of coercive field with respect to the respective cores (Figure 48; Table 28); (iii) the presence of a single maximum in ZFC-FC curves shifted toward higher temperatures (Figure 47); (iv) the increase of the magnetic diameter *(<D_{MAG}>;* Table 29).

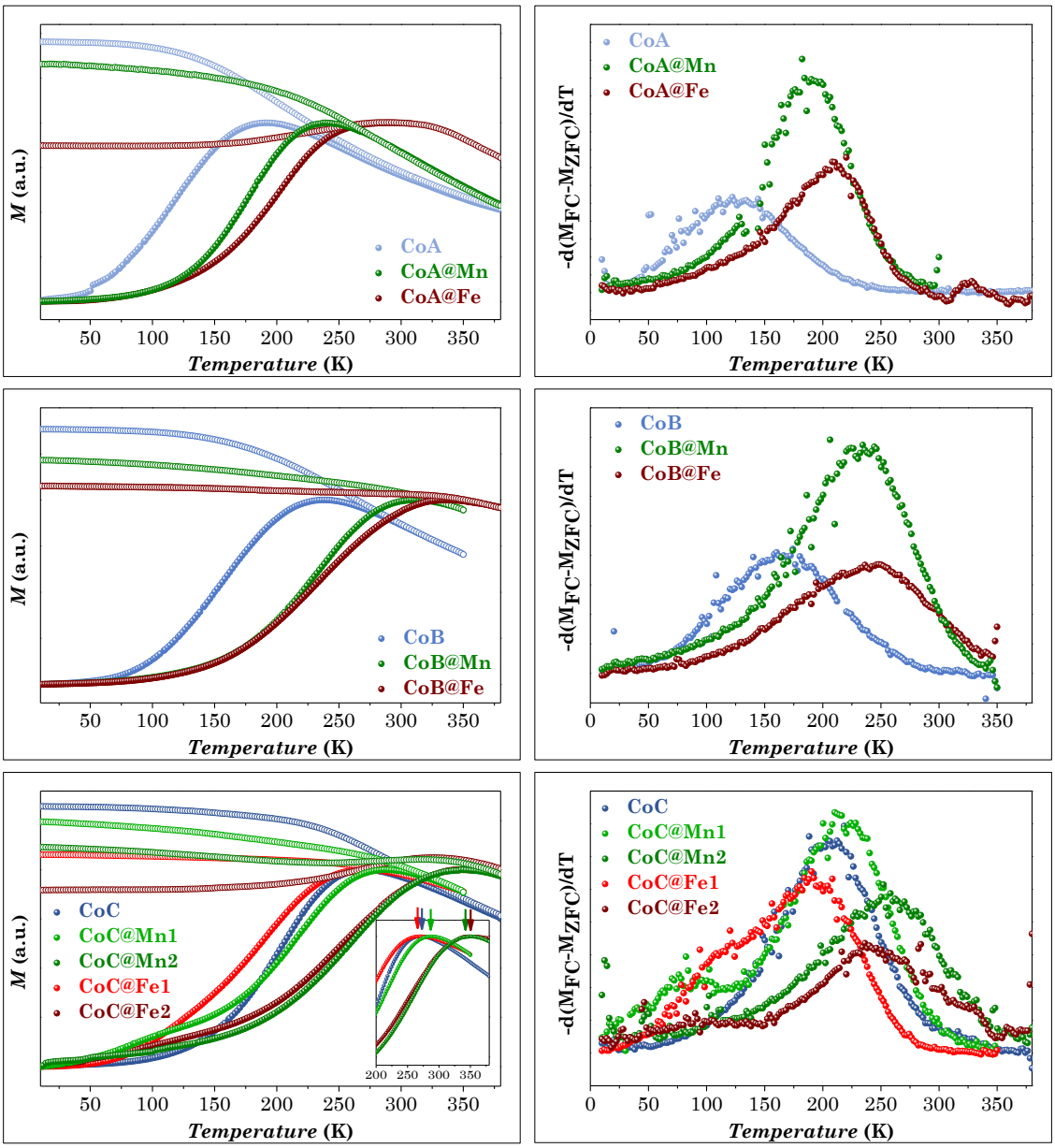

Figure 47. ZFC (full circles) and FC (empty circles) curves, normalized for the magnetization at T_{max} of the ZFC curve, of core-shell samples and respective cores recorded at low external magnetic field (10 mT) (left); anisotropy energy barrier distributions estimated by the first derivative $-d(M_{FC}-M_{ZFC})/dT$ (right).

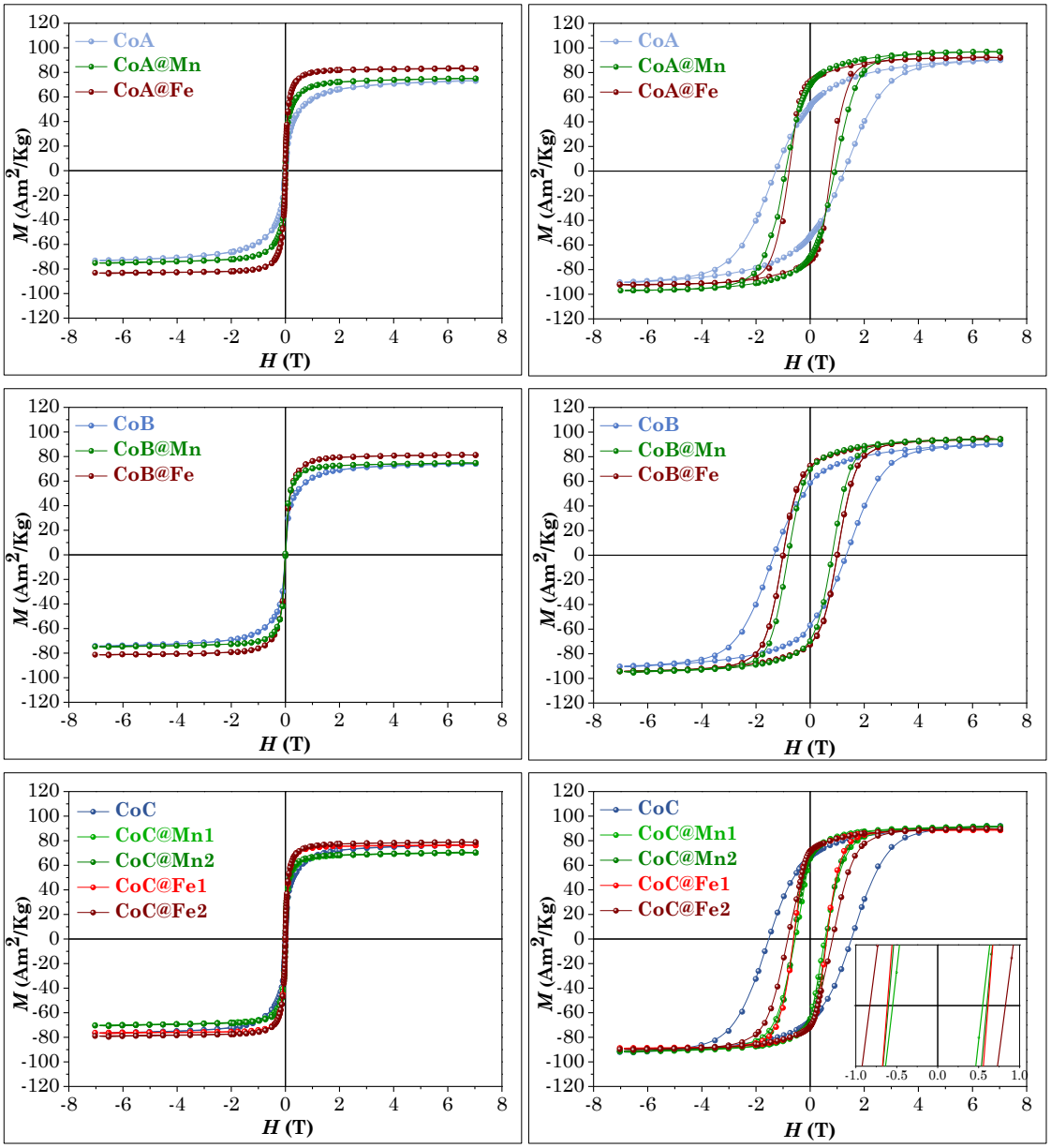

Figure 48. Magnetization isotherms of core-shell samples and respective cores recorded at 300 K (left side) and 10 K (right side).

ZFC curves (Figure 47) of core-shell samples show a single maximum (T_{max}), associated with single particle population, also confirmed by a single energy barrier distribution ($-d(M_{FC}-M_{ZFC})/dT$)[637] centred at a certain temperature (T_b), for all samples but CoC@Mn1, CoC@Fe1, and CoC@Fe2. Both T_{max} and T_b values increase in the core-shell samples compared to the cores, due to the increased particle volume. The difference T_{diff} - T_{max} is generally lower in the core-shell samples than in the cores, suggesting a decrease in the energy barrier distribution dispersity, because of the homogeneous growth on the shells around the seeds that induces a narrower size distribution. Furthermore, core-shell samples show higher interparticle interactions than cobalt ferrite (paragraph 2.3.8), as evidenced by the flatness of the FC curves. In particular, spinel iron oxide coated core-shells have a more pronounced FC flatness behaviour, with the occurrence in some cases (CoA@Fe, CoC@Mn2,

and CoC@Fe2) of a maximum, typical of high interacting systems (*e.g.* superspin glass).[73,638,639] It is worth nothing that only in the CoC set, the samples CoC@Mn1, CoC@Fe1, and CoC@Fe2 show different features in the ZFC-FC and $-d(M_{FC}-M_{ZFC})/dT$ curves: (i) the ZFC curves display a first increase in the magnetization in the region up to 150-180 K and then a sharper increase until the T_{max} is reached; (ii) the energy barrier distribution reveals a shoulder at temperatures lower than T_b (<150 K). Moreover, the CoC@Fe1 presents a shift of T_b towards lower temperature if compared to that of CoC. Different size-, composition-, and structure-related reasons can be responsible for such behaviour. Concerning the size, a polymodal distribution in the particle size or the shell thickness can cause polymodal energy barrier distribution. Inhomogeneities in the chemical composition of the shell or the entire particle can also lead to a polymodal distribution in the anisotropy. Furthermore, structurally disordered shell (at the surface or in thickness as the whole) or interface may be responsible for spin frustration, magnetic disorder, and eventually frozen spins with different temperature responses. Among these features, TEM analysis revealed a monomodal particle size distribution with a decrease of the dispersity in the core-shell NPs if compared to the cores, suggesting that this factor is not the main responsible for the evidenced unusual features. Conversely, the shell thickness distribution, as well as the core size distribution of the core-shell systems, could not be calculated due the representativeness of the nanoscale chemical mapping analysis, and therefore their variability may not be excluded and can give different energy barriers. Regarding structure-related reasons, both HRTEM and LT ^{57}Fe Mössbauer spectroscopy did not reveal structural disorder or spin canting phenomena. However, the co-presence of magnetite and maghemite detected for iron oxide coated core-shell NPs (paragraph 3.3.5) may induce spin frustration due to the presence of vacancies (typical in maghemite) and therefore different temperature responses of magnetic spins. The slight shift of T_b towards lower temperature recorded only for the sample CoC@Fe1 may be due to a partial dissolution of the cobalt ferrite core during the seed-mediated growth treatment. Compositional or structural/magnetic inhomogeneities should be further investigated, for instance, by neutron scattering techniques (SANS), by in-field ^{57}Fe Mössbauer spectroscopy at various temperature, and by DC magnetometry experiments *ad hoc* designed for the study of the interparticle interactions (isothermal remanent magnetization (IRM), direct current demagnetization (DCD), Henkel plot) and super spin glasses (memory experiments).[640]

Table 28. Basic parameters determined from the ZFC curves and magnetization isotherms. T_{max}, T_{diff}, T_b correspond to the maximum, furcation point of the ZFC curve (2%), and blocking temperatures; H_c^{10}, H_K^{10} (2%), M_7^{10}, M_s^{10}, M_s^{300}, and M_r^{10} correspond to the coercivity, anisotropy field, magnetization at 7 T, saturation magnetization values at 10 K and 300 K, and remanent magnetization, respectively.

Sample	T_{max} (K)	T_{diff} (K)	T_b (K)	H_c^{10} (T)	H_K^{10} (T)	M_7^{10} (Am²/kg)	M_s^{10} (Am²/kg)	M_r^{10} (Am²/kg)	M_r/M_s	M_s^{300} (Am²/kg)
CoA	195(3)	270(9)	126(2)	1.28(1)	4.2(1)	90(3)	97(3)	53(2)	0.55	73(2)
CoA@Mn	246(3)	275(3)	185(5)	0.92(1)	2.6(1)	97(4)	97(4)	67(2)	0.72	75(2)
CoA@Fe	294(1)	262(3)	199(3)	0.76(1)	2.0(1)	92(1)	93(1)	72(2)	0.78	83(3)
CoB	241(3)	266(3)	163(2)	1.32(2)	3.8(1)	90(4)	96(5)	58(3)	0.62	74(3)
CoB@Mn	314(3)	312(3)	233(2)	0.81(1)	2.3(1)	94(3)	96(5)	74(3)	0.73	75(3)
CoB@Fe	337(3)	333(3)	237(4)	1.02(1)	2.5(2)	94(3)	96(5)	72(3)	0.76	81(2)
CoC	274(3)	313(3)	206(2)	1.54(1)	4.1(1)	92(1)	100(5)	67(1)	0.67	77(1)
CoC@Mn1	292(2)	295(1)	216(1)	0.56(2)	2.5(1)	92(1)	94(2)	66(2)	0.69	70(1)
CoC@Mn2	348(3)	>380	251(5)	0.60(1)	1.9(1)	91(2)	93(3)	67(1)	0.72	71(1)
CoC@Fe1	278(5)	270(5)	190(1)	0.60(1)	1.8(1)	89(3)	89(3)	71(2)	0.79	77(3)
CoC@Fe2	352(4)	>380	246(4)	0.83(1)	2.6(1)	90(2)	90(2)	71(1)	0.79	79(2)

M vs H curves (Figure 48) display a superparamagnetic behaviour at 300 K with generally higher saturation magnetization (M_s) values for the core-shell samples with respect to the cores, in agreement with the literature for similar systems.[415,416,624] In all cases, the highest saturation magnetization is reached for spinel iron oxide coated core-shell nanoparticles. *M vs H* curves at 300 K have been analysed by MINORIM software (Figure 49),[641] that use a non-regularized inversion method, to calculate the median magnetic moment of the NPs and estimate the magnetic diameter (<D_{MAG}>) through the Eq. 47:

$$D_{MAG} = \sqrt[3]{\frac{6\mu_m a^3}{\mu_{uc}\pi}} \qquad \textbf{Eq. 47}$$

Where μ_m, a, and μ_{uc} are the median magnetic moment, the lattice parameter, and the magnetic moment of the unit cell (calculated assuming site occupancy estimated from LT ^{57}Fe Mössbauer spectroscopy), respectively (Table 29).

Table 29. Cell parameter (a). median magnetic moment (μ_m), magnetic moment of the unit cell (μ_{uc}), and magnetic diameter of the core-shell NPs.

Sample	a (Å)	μ_m ($\mu_B \cdot 10^3$)	μ_{uc} ($\mu_B \cdot 10^3$)	<D_{MAG}> (nm)
CoA	8.39(1)	3.1(2)	33.8	4.7(2)
CoA@Mn	8.40(2)	9.8(2)	37.9	6.6(2)
CoA@Fe	8.36(1)	10.6(2)	26.9	7.6(2)
CoB	8.38(1)	3.8(2)	33.5	5.0(2)
CoB@Mn	8.41(1)	10.9(2)	38.5	6.9(2)
CoB@Fe	8.35(1)	8.5(2)	30.5	6.7(4)
CoC	8.38(1)	5.2(2)	33.4	5.6(2)
CoC@Mn1	8.43(1)	10.1(2)	38.3	6.7(2)
CoC@Mn2	8.43(1)	17.6(2)	37.7	8.1(3)
CoC@Fe1	8.34(1)	10.6(2)	29.4	7.4(2)
CoC@Fe2	8.38(1)	17.6(2)	29.6	8.7(4)

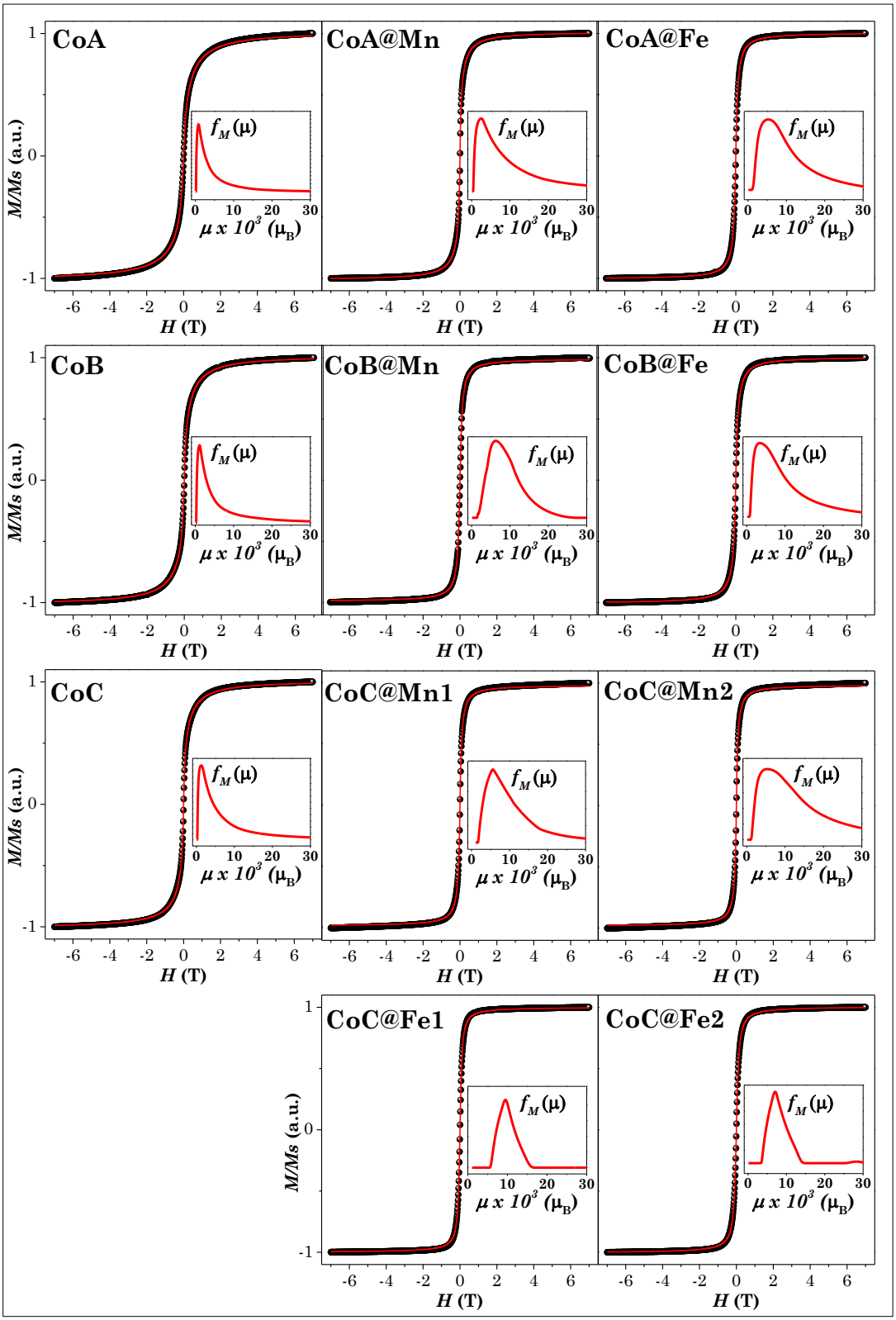

Figure 49. ***M vs H*** **refinement of core and core-shell NPs by using MINORIM. In the insets, the resulting magnetic moment distributions for individual refinements are shown.**

At 10 K all samples show a single-hysteretic behaviour with coercive field of core-shell samples lower than the respective cobalt ferrite cores, due to the effective magnetic coupling between the hard and the soft phases (Table

28).[409,505] While hard cobalt ferrite exhibits very high coercive field, due to its high anisotropy constant, manganese ferrite and spinel iron oxide show no coercivity at 10 K, but when coupled, the coercive field is intermediate because of the magnetic coupling between hard and soft materials and they do not reveal the two independent reversal of the magnetization of the two spinel ferrites. Theoretically, this double-magnet behaviour is observable in the presence of (i) mixture of hard and soft phases not coupled, *i.e.* physical mixtures (Figure 50, discussed in paragraph 4.4), or (ii) "spring magnet" core-shell NPs, where the soft phase shell thickness is double the width of the domain walls of the hard phase, and therefore the soft layer nucleates the reversal at fields lower than those of the hard layer.[83] In our case, due to the low thickness of the magnetically soft shell (well below the critical double of the bulk domain wall thickness), the two phases are expected to be rigidly coupled and reverse at the same nucleation field, as an uniform single magnet:[83] Certainly, also mixed ferrites ($Co_xM^{II}_{1-x}Fe_2O_4$, where M^{II}: Mn^{II}, Fe^{II}) are responsible for a "single-magnet behaviour", nevertheless, chemical mapping at the nanoscale revealed the presence of well-defined core-shell interface for all samples, excluding this scenario. Furthermore, the comparison between the core-shell samples and chemically mixed Co-Mn ferrites (having similar Co/Mn ratios and crystallite and particle sizes, Figure 50, discussed in paragraph 4.4), confirms the different magnetic behaviour.

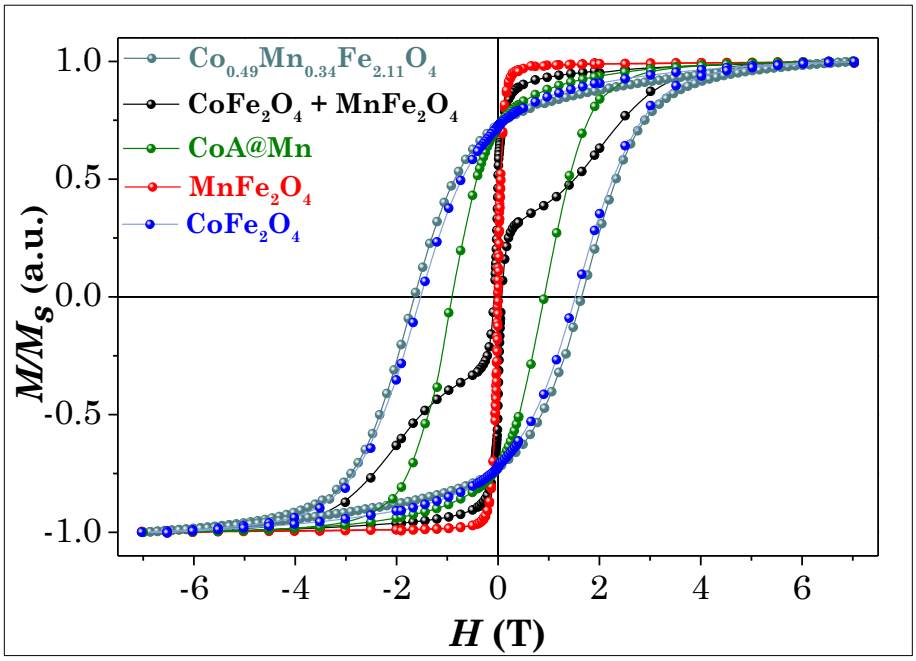

Figure 50. Magnetization isotherms of the core-shell sample CoA@Mn, cobalt ferrite, manganese ferrite, and physical and chemical mixtures of cobalt and manganese ferrites recorded at 10 K.

Saturation magnetization values at 10 K do not change much among all samples, and they are in the range 90-100 $Am^2 \cdot kg^{-1}$. On the contrary, reduced remanent magnetization (M_r/M_s) is around 0.7 for manganese ferrite coated core-shells and 0.8 for spinel iron oxide ones, suggesting a higher tendency

towards cubic anisotropy. Anisotropy field H_K is about 4 T for cobalt ferrite samples and in the range 1.8-2.6 T for the core-shell samples, due to the soft magnetic features of the shell

In the literature, effective anisotropy constants are calculated in different ways, summarized below:

$$K_1 = \frac{H_c M_s}{0.96\left(1 - \left(\frac{T}{T_b}\right)^{0.77}\right)} \qquad \textbf{Eq. 48}^{642}$$

$$K_2 = \frac{H_K M_s}{2} \qquad \textbf{Eq. 49}^{643}$$

$$K_3 = \frac{25 K_B T_b}{V} \qquad \textbf{Eq. 50}^{583}$$

Eq. 48 and Eq. 49 depend on saturation magnetization and coercive field or anisotropy field, respectively, and give an approximated value of anisotropy constant assuming collinear orientation with respect to the magnetic field. Eq. 50 derives from the energy barrier equation and it depends on blocking temperature (T_b) estimated from $-d(M_{FC}-M_{ZFC})/dT$ curves and particle volume. It gives a more complete estimation of effective anisotropy constant since it contains all different contributions given by magnetocrystalline, shape, and surface anisotropy but it is strongly affected by the size determination. Indeed, anisotropy constant K_3 was calculated by using $<D_{MAG}>$, $<D_{XRD}>$, and $<D_{TEM}>$ values. The results are reported in Table 30.

Table 30. Anisotropy constant calculated by using Eq. 48, Eq. 49, and Eq. 50 with $<D_{MAG}>$, $<D_{XRD}>$, and $<D_{XRD}>$ values.

Sample	$<D_{MAG}>$ (nm)	$<D_{XRD}>$ (nm)	$<D_{TEM}>$ (nm)	$K_1 \cdot 10^4$ (J/m³)	$K_2 \cdot 10^4$ (J/m³)	$K_3\_D_{MAG} \cdot 10^4$ (J/m³)	$K_3\_D_{XRD} \cdot 10^4$ (J/m³)	$K_3\_D_{TEM} \cdot 10^4$ (J/m³)
CoA	4.7	5.5	5.4	75	100	8.9	5.5	5.9
CoA@Mn	6.6	8.0	9.4	52	63	4.7	2.6	1.6
CoA@Fe	7.6	10.7	10.5	41	40	3.3	1.2	1.3
CoB	5.0	6.7	7.1	75	91	9.6	4.0	3.3
CoB@Mn	6.9	9.6	12.7	44	55	5.8	1.7	1.0
CoB@Fe	6.7	10.1	12.2	56	60	5.9	1.7	1.0
CoC	5.6	7.9	8.5	89	100	8.6	3.1	2.5
CoC@Mn1	6.7	9.3	12.6	30	59	5.3	2.0	0.8
CoC@Mn2	8.1	10.8	14.4	32	44	3.5	1.5	0.6
CoC@Fe1	7.4	10.8	11.1	31	40	3.4	1.1	1.0
CoC@Fe2	8.7	11.8	12.1	43	59	2.7	1.1	1.0

K_1 and K_2 values are in the order of 10^5 J·m^{-3} and are comparable, while K_3 values are one or two order of magnitude lower, due to the different model adopted for the estimation. Nevertheless, the trend in the core-shell systems

is comparable in all cases. Indeed, core-shell samples have generally lower anisotropy constant values compared with the respective cores.

3.3.8 AC Magnetometry

AC magnetometry was used to measure the temperature dependence of the in-phase (χ') and out-of-phase (χ'') component of the magnetic susceptibility at different frequencies (0.1-10000 Hz) for the cobalt ferrite-based core shell samples (Figure 51) and the Néel relaxation time estimated by the Vogel-Fulcher equation (Eq. 43) is reported in Table 31. The Néel relaxation times of core-shell samples is slower than those of the respective cores, due to the increased particle volume that dominates the overall decrease of effective anisotropy. The calculated Brown relaxation times (Eq. 46, Table 31) resulted to be always slower than τ_N, and therefore not influencing the total relaxation time of the system. As already evidenced by $-d(M_{FC}-M_{ZFC})/dT$ curves, the samples CoC@Mn1, CoC@Fe1 and CoC@Fe2 show different contributions in the χ' and χ'' susceptibilities, which are frequency dependent. These features can be justified in the light of the phenomena described in the previous paragraph.

Table 31. Parameters obtained from the curve fitting by the Vogel-Fulcher model for T = 300 K. τ_0 is the characteristic relaxation time, E_b is the energy barrier against the magnetisation reversal, T_0 is the temperature value accounting for the strength of magnetic interactions, τ_N is the Néel relaxation times. Brown relaxation times (τ_B) are also reported.

Sample	τ_0 (s)	E_b (K)	T_0 (K)	τ_N (s)	τ_B (s)
CoA	$9 \cdot 10^{-13}$	2499	59	$3 \cdot 10^{-8}$	$9 \cdot 10^{-3}$
CoA@Mn	$2 \cdot 10^{-14}$	2999	115	$2 \cdot 10^{-7}$	$4 \cdot 10^{3}$
CoA@Fe	$2 \cdot 10^{-11}$	2510	137	$1 \cdot 10^{-5}$	$1 \cdot 10^{-3}$
CoB	$6 \cdot 10^{-13}$	2222	108	$6 \cdot 10^{-8}$	$4 \cdot 10^{-4}$
CoB@Mn	$2 \cdot 10^{-11}$	2566	157	$1 \cdot 10^{-3}$	$2 \cdot 10^{-2}$
CoB@Fe	$2 \cdot 10^{-10}$	2464	157	$5 \cdot 10^{-3}$	$8 \cdot 10^{-2}$
CoC	$2 \cdot 10^{-13}$	2555	140	$1 \cdot 10^{-6}$	$3 \cdot 10^{-4}$
CoC@Mn1	$2 \cdot 10^{-13}$	2570	161	$2 \cdot 10^{-5}$	$4 \cdot 10^{-4}$
CoC@Mn2	$2 \cdot 10^{-12}$	2583	176	$2 \cdot 10^{-3}$	$3 \cdot 10^{-2}$
CoC@Fe1	$5 \cdot 10^{-12}$	1923	146	$1 \cdot 10^{-6}$	$2 \cdot 10^{-3}$
CoC@Fe2	$5 \cdot 10^{-10}$	1915	173	$2 \cdot 10^{-3}$	$6 \cdot 10^{-2}$

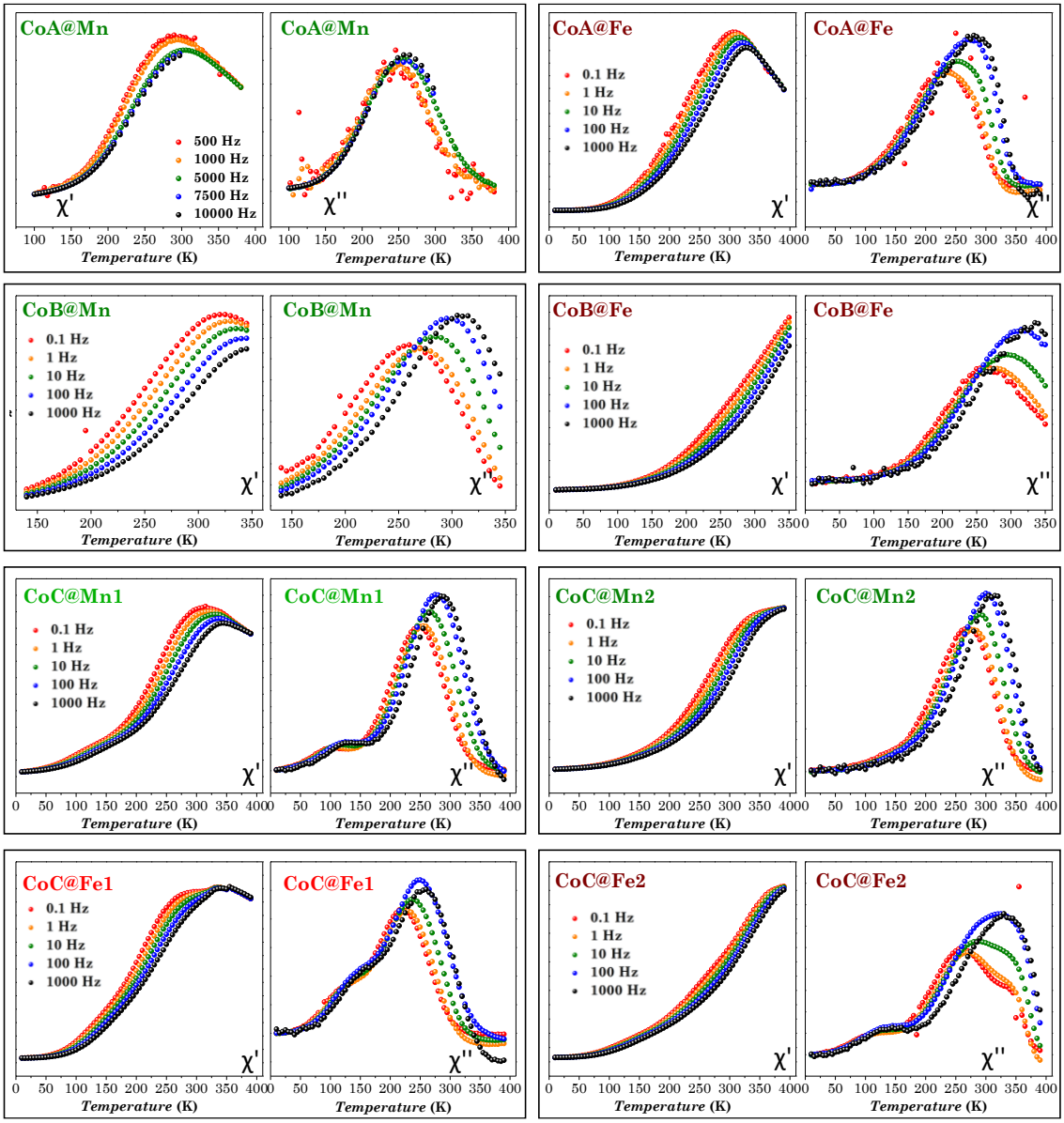

Figure 51. AC susceptibility measurements of the core-shell samples.

3.4 Heat release

All cobalt ferrite-based core-shell NPs were tested to determine the heating abilities of their aqueous colloidal dispersions under mild experimental conditions (*i.e.* external magnetic field with frequency f = 183 kHz and amplitude H_0 = 17 kA·m^{-2}). As for the cores, the hydrophilic nanoparticles were obtained by intercalation process on the oleate-capped nanoparticles with cetyltrimethylammonium bromide (CTAB, $(C_{16}H_{33})N(CH_3)_3Br$).[553] The concentration of the colloidal dispersions was 3.4±0.2 mg·mL^{-1} for all samples normalized for the active phase. The heating curves are reported in Figure 52.

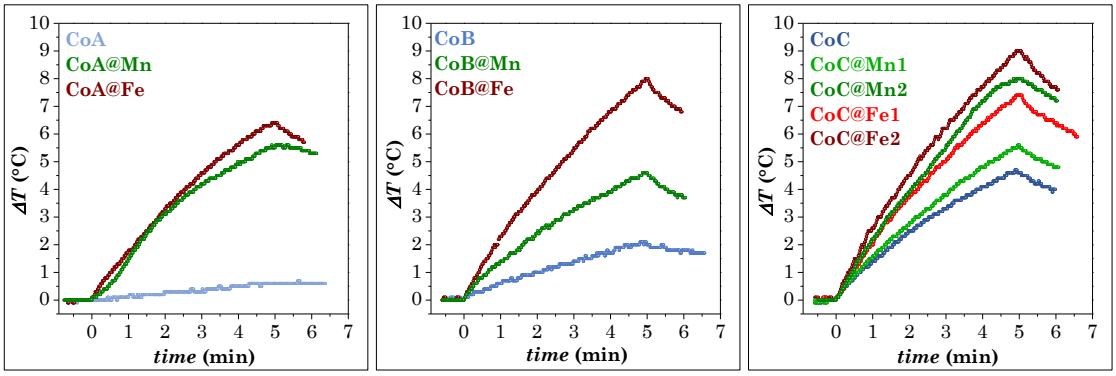

Figure 52. Heating curves obtained on aqueous colloidal dispersions of the core-shell samples (3.4±0.2 mg·mL^{-1}) and respective cores at 30 °C and under a magnetic field of f = 183 kHz and H_0 = 17 kA/m.

Table 32. Magnetic size (<D_{MAG}>), crystallite size (<D_{XRD}>), particle size (<D_{TEM}>), coercive field at 10 K (H_c^{10}), saturation magnetization at 300 K (M_s^{300}), Néel relaxation time (τ_N), specific adsorption rate (SAR), and intrinsic loss power (ILP) values of the samples. SAR and ILP are given as watt per gram of spinel ferrite phase

Sample	<D_{MAG}> (nm)	<D_{XRD}> (nm)	<D_{TEM}> (nm)	H_c^{10} (T)	M_s^{300} (Am²/kg)	τ_N (s)	SAR (W/g$_{ox}$)	ILP (nH·m²·kg$_{ox}^{-1}$)
CoA	4.7	5.5	5.4	1.28	73	9·10^{-8}	0*	0*
CoA@Mn	6.6	8.0	9.4	0.92	75	2·10^{-7}	20(1)	0.38(2)
CoA@Fe	7.6	10.7	10.5	0.76	83	1·10^{-5}	42(2)	0.80(4)
CoB	5.0	6.7	7.1	1.32	74	6·10^{-8}	21(1)	0.39(1)
CoB@Mn	6.9	9.6	12.7	0.81	75	1·10^{-3}	27(2)	0.52(4)
CoB@Fe	6.7	10.1	12.2	1.02	81	5·10^{-3}	48(1)	0.92(2)
CoC	5.6	7.9	8.5	1.54	77	1·10^{-6}	32(2)	0.60(4)
CoC@Mn1	6.7	9.3	12.6	0.56	70	2·10^{-5}	43(3)	0.81(6)
CoC@Mn2	8.1	10.8	14.4	0.60	71	2·10^{-3}	47(2)	0.89(4)
CoC@Fe1	7.4	10.8	11.1	0.60	77	1·10^{-6}	46(4)	0.88(8)
CoC@Fe2	8.7	11.8	12.1	0.83	79	2·10^{-3}	59(2)	1.12(4)

***This has to be intended as negligible heat release**

As reported in chapter 2.4, CoA sample, due its small size, did not heat up, while the larger CoB and CoC samples were responsible for a heat release corresponding to a SAR value of 21 and 32 W/g$_{ox}$ respectively. This is the expected trend for cobalt ferrite in this size range. In agreement with previous works, in all core-shell systems, a remarkable increase of SAR values with

respect to the cores were revealed. The improvement on the heating abilities in core-shell systems, as already observed (paragraph 3.3.7), can be ascribed to the magnetic coupling phenomena between the two ferrimagnetic phases in the core-shell nanostructures, as reported in the literature (Table 33).[409,623]

Table 33. Bimagnetic spinel-ferrite core-shell nanoparticles for magnetic heat induction. Size of the core (D_{CORE}) and of the entire core-shell NP (D_{NP}), effective anisotropy constant (K_{eff}), saturation magnetization at 300 K (M_s), coercive field at 5 K (H_c) or at 300 K for blocked NPs, frequency (f) and amplitude (H_0) of the applied alternate magnetic field, specific adsorption rate (SAR), and intrinsic loss power (ILP). Superparamagnetic and blocked NPs are separated by a black line.

System	D_{CORE} (nm)	D_{NP} (nm)	K_{eff} (J/m³)·10⁴	M_s (Am²/kg)	H_c (T)	f (kHz)	H_0 (kA/m)	SAR (w/g)	ILP (nH·m²kg⁻¹)	#
$CoFe_2O_4$@$MnFe_2O_4$	9#	15#	1.5	110	0.25	500	37.3	2280	3.28	409
$CoFe_2O_4$@Fe_3O_4	9#	15#	2	105	~0.25	500	37.3	1120	1.60	
$MnFe_2O_4$@$CoFe_2O_4$	9#	15#	1.7	108	~0.8	500	37.3	3034	4.36	
Fe_3O_4@$CoFe_2O_4$	9#	15#	1.8	104	~1	500	37.3	2795	4.02	
$Zn_{0.4}Co_{0.6}Fe_2O_4$@ $Zn_{0.4}Mn_{0.6}Fe_2O_4$	9#	15#	-	150	-	500	37.3	3886	5.59	
γ-Fe_2O_3@$CoFe_2O_4$	3.9§	4.3§	-	50	0.66	300	7.7	5.1	0.29	556
γ-Fe_2O_3@$CoFe_2O_4$	3.9§	7.1§	-	30	0.63	300	7.7	3.3	0.19	
γ-Fe_2O_3@$CoFe_2O_4$	3.9§	10§	-	-	-	300	7.7	1.3	0.07	
$CoFe_2O_4$@$MnFe_2O_4$	6.5#	12.2#	-	60	-	200	60	139	0.19	555
$MnFe_2O_4$@Fe_3O_4	8.7#	11.9#	-	60	0.2	765	23.9	40	0.09	416
$CoFe_2O_4$@Fe_3O_4	7.2#	12.2#	-	73	1.1	765	23.9	450	1.03	
$Zn_{0.4}Co_{0.6}Fe_2O_4$@ $Zn_{0.4}Mn_{0.6}Fe_2O_4$	7.6#	11#	-	69	-	200	60.6	1343	1.83	622
$Zn_{0.2}Co_{0.8}Fe_2O_4$@$MnFe_2O_4$	-	9.3§	-	54	-	1955	-	380	-	413
$Zn_{0.4}Co_{0.6}Fe_2O_4$@$MnFe_2O_4$	-	10.1§	-	62	-	1955	-	420	-	
$Zn_{0.6}Co_{0.4}Fe_2O_4$@$MnFe_2O_4$	-	11§	-	52	-	1955	-	470	-	
$Zn_{0.8}Co_{0.2}Fe_2O_4$@$MnFe_2O_4$	-	12§	-	47	-	1955	-	520	-	
$CoFe_2O_4$@$MnFe_2O_4$	6.7#	12.9#	3.9	87	0.5	412.5	22.4	553	2.67	415
$MnFe_2O_4$@$CoFe_2O_4$	10.2#	14.3#	5.3	84	1.3	412.5	22.4	302	1.46	
$MnFe_2O_4$@$CoFe_2O_4$	7.3#	13.8#	8.5	82	2.2	412.5	22.4	291	1.41	
Fe_3O_4@$CoFe_2O_4$	6.4§	8.2§	-	67	-	310	63.7	208	0.17	417
Fe_3O_4@$CoFe_2O_4$	7.8§	9.6§	-	68	-	310	63.7	199	0.16	
$Zn_{0.4}Fe_{2.6}O_4$@$CoFe_2O_4$	50#	70#	-	140	0.19*	500	37.7	10600	14.92	623
$CoFe_2O_4$@$MnFe_2O_4$	-	14§	-	79	0.02*	50	19.9	-	-	624
$CoFe_2O_4$@$MnFe_2O_4$	15#	26#	-	33	0.17*	765	28	73	0.12	202
$MnFe_2O_4$@$CoFe_2O_4$	10#	16#	-	26	0.28*	765	28	160	0.27	
$CoFe_2O_4$@$MnFe_2O_4$	-	8.2§	-	45	0.2*	1955	-	300	-	413
Fe_3O_4@$CoFe_2O_4$	7.8§	12§	-	83	0.01*	310	63.7	461	0.37	417
Fe_3O_4@ $CoFe_2O_4$	7.8§	16.6§	-	68	0.05*	310	63.7	129	0.10	
Fe_3O_4@$CoFe_2O_4$	9.6§	12.4§	-	76	0.03*	310	63.7	174	0.14	

***Measured at 300 K. #<D_{XRD}>. §<D_{XRD}>.**

Indeed, magnetic coupling induce unique magnetic feature, such as enhanced saturation magnetization at 300 K and reduced magnetic anisotropy with respect to cobalt ferrite. Lee *et al.*[409] found an improvement in heating abilities in core-shell systems up to 5 times the original cobalt ferrite core for manganese ferrite coating, and twice for the magnetite one. They explained

these results considering the anisotropy and magnetization tuning of the core-shell samples. Also Zhang and co-workers[415] ascribed to magnetic anisotropy, that is mostly determined by the relative cobalt ferrite fraction, the optimized heat generation on $CoFe_2O_4$@$MnFe_2O_4$ core-shell nanoparticles more than in $MnFe_2O_4$@$CoFe_2O_4$ ones. $CoFe_2O_4$@$MnFe_2O_4$ NPs have also been investigated by Angelakeris *et al.*,[412] who highlighted the importance of the interface flatness to enhance the magnetic coupling interactions between the hard and the soft phases and therefore to improve heating performances. A further confirmation of this effect comes from Liébana-Viñas and co-authors[416] who found a considerable increase (24 times) in $CoFe_2O_4$@Fe_3O_4 nanoparticles with respect to single cobalt ferrite one. Despite a discrete number of studies on this kind of systems, a systematic comparison among different soft ferrimagnetic shell phases, hard core sizes, and shell thickness is still lacking, and the correlation between the magnetic properties and the hyperthermic abilities of these materials is not trivial.

Despite the complexity of the system, the experimental data collected on three different core-shell series (CoA, CoB, and CoC, Table 32) reveal some general aspects:

1. Core-shell samples heat up more than respective cores;
2. In all sets, spinel iron oxide coated core-shell NPs feature better performances if compared to manganese ferrite-coated ones;
3. In the CoC series, both systems (CoC@Fe1/CoC@Fe2 and CoC@Mn1/CoC@Mn2) show that the increase of the shell thickness induces an improvement on the heating abilities.

The higher efficiency of spinel iron oxide-coated core-shell NPs with respect to manganese ferrite-coated ones is apparently in contrast with results reported in the literature for similar systems, where the increased heating abilities of the core-shell NPs have been attributed mainly to the tuning of anisotropy and maximization of saturation magnetization.[409]

In our systems, the SAR trend within each series can be justified primarily on terms of saturation magnetization. Indeed, the M_s^{300} of the Cox@Fe samples is always higher than that of the Cox@Mn ones in all sets (CoA@Fe shows M_s^{300} of 83 $Am^2 \cdot Kg^{-1}$ while CoA@Mn has M_s^{300} of 75 $Am^2 \cdot Kg^{-1}$, CoB@Fe shows M_s^{300} of 81 $Am^2 \cdot Kg^{-1}$ while CoB@Mn has M_s^{300} of 75 $Am^2 \cdot Kg^{-1}$, CoC@Fe1/Fe2 show M_s^{300} of 77-79 $Am^2 \cdot Kg^{-1}$ while CoC@Mn1/Mn2 has M_s^{300} of 70-71 $Am^2 \cdot Kg^{-1}$), and it seems therefore that saturation magnetization plays the central role on the heating abilities.

The reasons behind the different results with respect to the literature could be found on the differences in the stoichiometry of the compounds, in the chemical state of the metals, in the inversion degree or in the spin canting phenomena, that are known to strongly influence M_s and the other magnetic properties and, consequently, the SAR values. Indeed, differences on the

synthetic approaches, as well as on the post-synthesis treatments, can induce significant differences on the final material features. To understand the opposite results obtained in the literature these features were studied on some selected samples by ICP-OES (paragraph 3.3.2), RT and LT ^{57}Fe Mössbauer spectroscopy (paragraph 3.3.5) in the absence and the presence of magnetic field (6T), and XPS (paragraph 2.3.7). In our case, in the cores, cobalt is present only as Co^{II} and iron as Fe^{III}; the stoichiometry is $Co:Fe_{core}$ = 0.50±0.05 and $Mn:Fe_{shell}$ = 0.43±0.02; the inversion degree is $\gamma(CoFe_2O_{4core})$ = 0.70±0.05 and $\gamma(MnFe_2O_{4shell})$ = 0.45± 0.01; spin canting phenomena are not revealed. Furthermore, the iron-oxide coated samples show the co-presence of magnetite and maghemite due to size-dependent oxidation phenomena of Fe^{II} to Fe^{III}. Therefore, differences on all these characteristics, that often are not studied, can explain the discrepancy of the results obtained in the literature.

Certainly, saturation magnetization is not the only parameter responsible for the heat release, and this is evident when samples with different cores or shell thicknesses are compared. For instance:

1. CoA@Mn and CoB@Mn feature the same M_s^{300} (75 $Am^2 \cdot Kg^{-1}$) and different SAR values (20 *vs* 27 W/g_{ox});
2. CoC@Mn1 and CoC@Mn2 feature similar M_s^{300} (70 *vs* 71 $Am^2 \cdot Kg^{-1}$) and different SAR values (43 *vs* 47 W/g_{ox});
3. CoC@Fe1 and CoC@Fe2 feature similar M_s^{300} (77 *vs* 79 $Am^2 \cdot Kg^{-1}$) and very different SAR values (46 *vs* 59 W/g_{ox}).

In this regard, also the NPs' size ($\langle D_{MAG} \rangle$, $\langle D_{XRD} \rangle$, and $\langle D_{XRD} \rangle$) seems to play an important role: generally, SAR values increase with the size (Table 32). To find a possible correlation, NPs sizes were plotted *vs* SAR values. It was possible to find a certain correlation between the SAR and the $\langle D_{XRD} \rangle$ or $\langle D_{MAG} \rangle$ (R^2 = 0.84) (Figure 53) while a low correlation was observed for $\langle D_{XRD} \rangle$ (R^2 = 0.59). As expected, this rough comparison that ignores the chemical nature of the NPs, despite highlighting the importance of the NPs' size, did not explain the different SAR for various samples with similar magnetic, crystallite, or particle size. For example:

1. CoB@Fe and CoB@Mn: they have the same core and the same shell thickness, confirmed by $\langle D_{MAG} \rangle$, $\langle D_{XRD} \rangle$ and $\langle D_{XRD} \rangle$ within the experimental error. In this case a remarkable increase from 27 to 48 W/g_{ox} was found, clearly evidencing the effect of the chemical nature of the shell beyond the NPs' size and the shell thickness. In theory, magnetite and manganese ferrite have different anisotropy constant in the bulk ($1.3 \cdot 10^4$ *vs* $3 \cdot 10^3$ $J \cdot m^{-3}$) and this could also be a further reason behind the different behaviour. Nevertheless, the calculated effective anisotropy constants (Table 30), as well as the Néel relaxation times ($1 \cdot 10^{-3}$ *vs* $5 \cdot 10^{-3}$ s), did not reveal significant differences, as instead the

saturation magnetization, being higher for CoB@Fe (83 $Am^2 \cdot Kg^{-1}$) with respect to CoB@Mn (75 $Am^2 \cdot Kg^{-1}$). The mismatch between the anisotropy constants of the bulk and the calculated for the core-shell NPs can be since *K* is size-dependent and to the presence of a certain percentage of maghemite that features different anisotropy constant ($5 \cdot 10^3$ $J \cdot m^{-3}$) if compared to magnetite but similar to manganese ferrite.

2. CoA@Mn and CoC (Figure 53, A): they have the same crystallite size (7.9 *vs* 8.0 nm) and different particle (9.4 *vs* 8.5 nm) and magnetic size (6.6 *vs* 5.6 nm) but CoC heat more than CoA@Mn (32 *vs* 20 W/g_{ox}). Being equal the saturation magnetization, the reason behind this behaviour can be ascribed to the higher anisotropy of the cobalt ferrite sample, that in this range of size have its maximum efficiency, as also demonstrated by the Néel relaxation time of CoC ($1 \cdot 10^{-6}$ s) that is closer to the applied frequency ($8.7 \cdot 10^{-7}$ s) and therefore more effective than CoA@Mn ($2 \cdot 10^{-7}$ s).
3. CoB@Mn and CoC@Mn1 (Figure 53, B): they have similar crystallite (9.6 *vs* 9.3 nm), particle (12.7 *vs* 12.6 nm), and magnetic size (6.9 *vs* 6.7 nm), but heat up differently (27 *vs* 43 W/g_{ox}). In this case, the higher SAR value is reached when core diameter is larger. Even if no big difference are found regarding magnetic parameters (M_s^{300}, M_r, K_1, K_2, K_3) able to define this picture, Néel relaxation times may be helpful. Indeed, τ_N of CoB@Mn is $1 \cdot 10^{-3}$ s, much slower than that of CoC@Mn1 ($2 \cdot 10^{-5}$ s), and this could be the reason of the higher SAR values.

Other samples have similar NPs' size and SAR values, and their comparison permits to highlight further interesting magnetic parameters:

1. CoA@Fe and CoC@Fe1 (Figure 53, C): they have similar crystallite (10.7 *vs* 10.8 nm), particle (10.5 *vs* 11.1 nm), and magnetic size (7.6 *vs* 7.4 nm), but heat up only slightly differently (42 *vs* 46 W/g_{ox}). This behaviour can be explained if both Néel relaxation times and saturation magnetization are considered. Indeed, while CoC@Fe1 has τ_N faster and closer to the applied frequency than CoA@Fe ($1 \cdot 10^{-6}$ s *vs* $1 \cdot 10^{-5}$ s), the behaviour of saturation magnetization is opposite, being higher for CoA@Fe (83 $Am^2 \cdot Kg^{-1}$) with respect to CoC@Fe1 (77 $Am^2 \cdot Kg^{-1}$).
2. CoC@Mn2 with CoC@Fe1 (Figure 53, D): they have similar crystallite (10.8 *vs* 10.8 nm) and quite different particle (14.4 vs 11.1 nm) and magnetic (8.1 *vs* 7.4 nm) sizes but heat similarly (47 *vs* 46 W/g_{ox}). This is another confirmation of the higher performances of spinel iron oxide-coated core-shell NPs with respect to manganese ferrite ones: even though the particle and the magnetic size are smaller, M_S^{300} is higher and τ_N more effective.

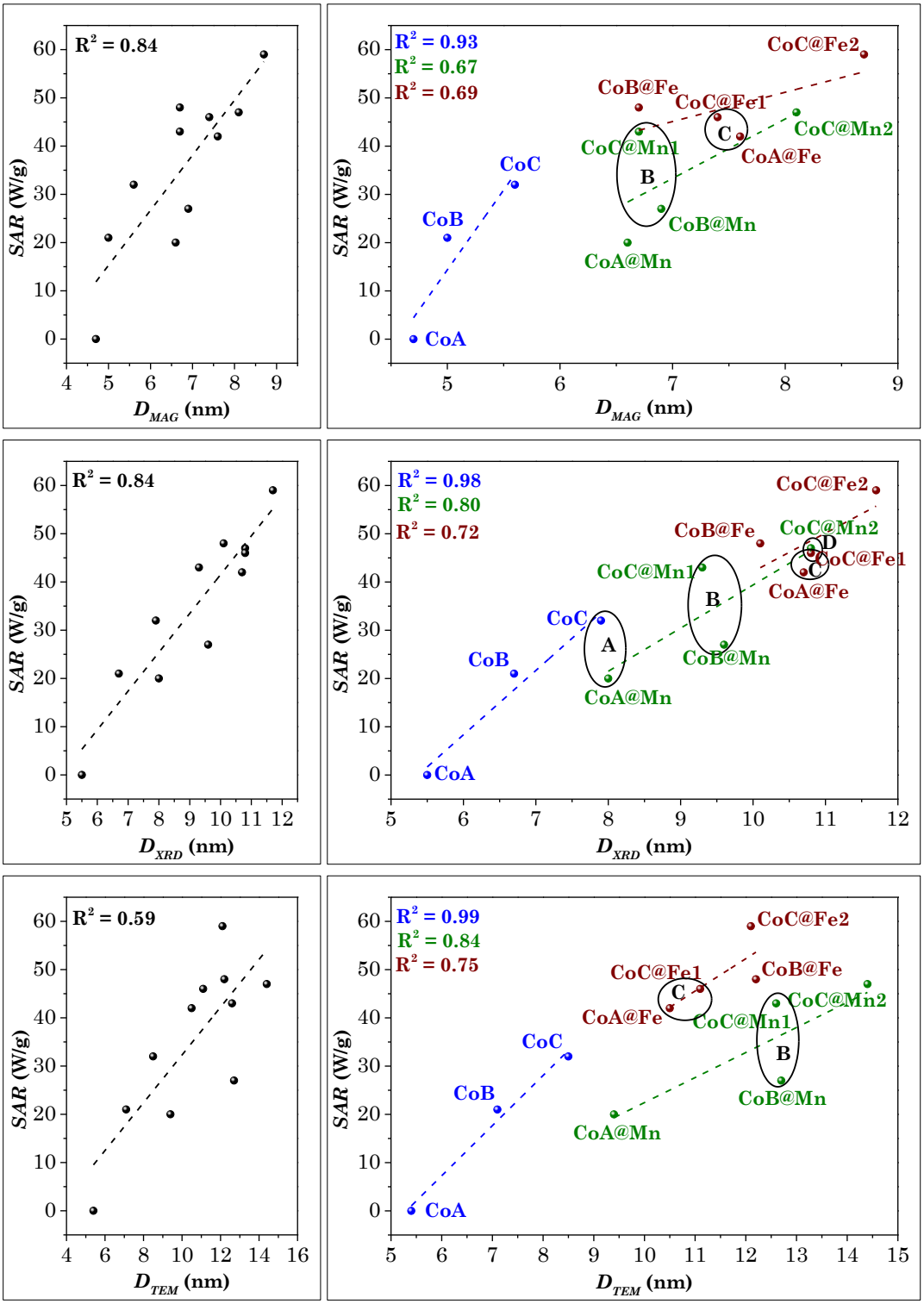

Figure 53. Evolution of SAR with <D_{MAG}>, <D_{XRD}>, and <D_{TEM}> of the samples.

All the above findings seem to depict a more complex scenario behind the heating abilities of bimagnetic core-shell systems than simple relationships with single magnetic or microstructural parameters. Herein, the importance of multitechnique analysis emerges, which can help to understand the hyperthermic properties based on the correlation of numerous parameters. Probably, effect of the size of crystalline and magnetic ordered regions, the saturation magnetization and anisotropy, and the role of the inter-particle

interactions act at the same time in systems of a such complexity. Moreover, general magnetic peculiarities of the spinel iron oxide coated samples were observed and may play a role in giving more efficient systems. The first one is related to the faster answer to the applied magnetic field of the @Fe systems in comparison to the Cox@Mn ones, showing higher magnetization values at low magnetic field in the *M vs H* curves at 300 K. Moreover, the FC curves of Cox@Fe samples have shown a temperature independent behaviour (flat curves) suggesting more interacting particles in comparison with those of the Cox@Mn ones and indicating a more efficient magnetic coupling of cobalt ferrite with spinel iron oxide than manganese ferrite.

In spite of the complex properties of these systems, it is clear that bimagnetic core-shell NHs permit an increase in the hyperthermic performances and spinel iron oxide coating seems to maximize the magnetic coupling with the hard cobalt ferrite, as demonstrated by the three different set of samples here shown, making this system the most promising for magnetic heat induction. Considered the biocompatibility of the iron oxides and their crystallinity, together with the possibility to properly tune the shell thickness and to use a biocompatible molecular coating rendering the particles dispersible in biological fluids (paragraph 2.4.1) that should hamper the release of the inner toxic cations (Co^{II}), the systems Cox@Fe could constitute very promising materials.

3.5 Conclusions

A simple, low-cost seed-mediated growth strategy in solvothermal condition were proposed to synthesize hydrophobic bimagnetic spinel ferrite core-shell nanoparticles. Conventional techniques (XRD, TEM, HRTEM/HRSTEM, TGA, FT-IR, ICP) showed for all the samples a single crystal domain, spherical shape, low dispersity and a monolayer of oleate molecules as the nanoparticles' capping agent. Larger particle size and lower dispersity than the core are indirect clues of the homogeneous growing of the shell around the pre-formed seeds. Direct proof of the core-shell structure formation was successfully provided by chemical mapping at the nanoscale, by the combination of STEM-EELS, STEM-EDX and STEM-EDX tomography. In particular, STEM-EDX is a powerful technique to obtain high-quality compositional maps and 3D reconstructions of the core-shell heterostructure with sub-nanometer spatial resolution. ^{57}Fe Mössbauer spectroscopy permitted to calculate spin canting and site occupancy of the systems, whereas DC Magnetometry demonstrated the magnetic coupling between the hard and the soft phases, that results in higher saturation magnetization at 300 K and lower coercive field and anisotropy constant, as well as higher magnetic volume. These features were exploited for magnetic heat induction under 183 kHz and 17 kA·m^{-1} alternate magnetic field. In all cases, core-shell nanoparticles showed better performances in comparison with the respective cores alone, with particular emphasis on the spinel iron oxide coated systems, thanks to the highest saturation magnetization, particle size, and appropriate tuning of magnetic anisotropy.

4 *Chemical and physical mixtures of cobalt and manganese ferrites*

Abstract

An indirect approach was applied to compare spinel ferrite-based core-shell nanoheterostructures with mixed Co-Mn ferrites ($Co_xMn_yFe_zO_4$, chemical mixtures) and mixture of $CoFe_2O_4$ and $MnFe_2O_4$ (physical mixtures). Indeed, multitechnique analysis, and in particular ^{57}Fe Mössbauer, may serve as a powerful method for the understanding of structural and magnetic properties (*e.g.* magnetic coupling) of iron containing compounds by comparing *ad-hoc* mixtures. In this context, the oleate-based solvothermal approach was employed to produce pure $CoFe_2O_4$ and $MnFe_2O_4$ and mixed Co-Mn ferrites having a manganese content in the range 0.13-0.65 and crystallite size in the range 8.3-8.8 nm. The structural and magnetic properties, studied by powder X-ray diffraction, room temperature ^{57}Fe Mössbauer spectroscopy, and DC Magnetometry, have allowed to ascertain the formation of a single spinel phase in which cobalt and manganese are present and to determine the cation distribution and the correlated magnetic properties. The comparison among the chemical mixtures, the core-shell heterostructures and physical mixtures of cobalt and manganese ferrites gives clear evidences on the heterostructures formation and the magnetic coupling.

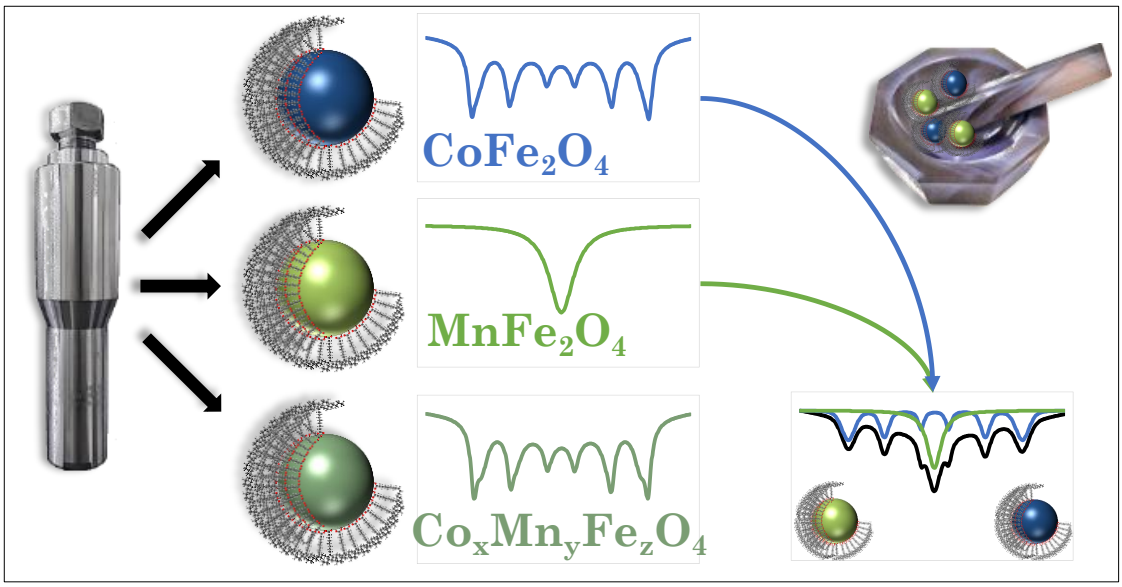

4.1 Introduction

In the previous chapters, it was highlighted that the understanding of the core-shell heterostructures is not trivial. Indeed, the direct proof of the actual architecture of the heterostructures can be obtained only by nanoscale chemical mapping, that is mandatory for this type of systems, but not always available in a research facility. Nonetheless, indirect analyses and multitechnique approaches can be useful to examine the system from different points of view confirming that the desired heterostructure was obtained. This approach is based on the differences between the divalent cations in the spinel structure that strongly affects the magnetic properties of the material, such as magnetisation and anisotropy. As previously described, manganese and cobalt ferrites differ for their magnetic behaviour and site occupancy,[70] However, as already demonstrated, the control of magnetite NPs is not trivial due to the oxidation of Fe^{II} ions. Consequently, mixed Co-Mn ferrites are an ideal system to study because of the higher stability in comparison with Co-Fe ferrites, the easiness of their characterization (*e.g.* ICP-OES to determine Co^{II}:Mn^{II} ratio), the different chemical and physical properties with respect to the single phases (cobalt and manganese ferrites), and are widely employed in many applications, from magnetic recording[30,481,505] to catalysis[39,644,645] and biomedicine.[18,224,409,646,647]
In this chapter, the oleate-based solvothermal method was applied to synthesize cobalt ferrite, manganese ferrite and mixed Co-Mn ferrite nanoparticles. The samples were characterized by means of inductively coupled plasma atomic emission spectrometry (ICP-OES), powder X-ray diffraction (XRD), and room temperature (RT) ^{57}Fe Mössbauer spectroscopy, to study their composition, structure and magnetic properties. A physical mixture of cobalt ferrite and manganese ferrite underwent RT ^{57}Fe Mössbauer spectroscopy analysis and was then compared with the pure and chemically mixed ferrites.

4.2 Synthesis

Chemically mixed Co-Mn spinel ferrites were synthesized starting from mixed Co-Fe and Mn-Fe oleates, as described in paragraph 2.2.1.[288,561] A certain amount of Co-Fe oleate and Mn-Fe oleate were added into a teflon liner, together with 1-pentanol, toluene and water, as listed in Table 34. The liner was then flushed with nitrogen, enclosed in a stainless-steel autoclave (Berghof DAB-2), briefly shaken and put into a pre-heated oven (220 °C) in vertical position for 10h. The washing step is the same described in paragraph 2.2.2.[288]

Table 34. Synthesis conditions of the chemically mixed ferrite samples. The first column lists the actual composition obtained from ICP-OES analyses.

Sample	n Co-Fe_2 Oleate (mmol)	n Mn-Fe_2 Oleate (mmol)	1-pentanol (mL)	Toluene (mL)	Water (mL)
$Co_{0.98}Fe_{2.01}O_4$	6	0	20	-	5
$Co_{0.77}Mn_{0.13}Fe_{2.07}O_4$	4.8	1.2	10	10	5
$Co_{0.66}Mn_{0.23}Fe_{2.07}O_4$	4	2	10	10	5
$Co_{0.49}Mn_{0.34}Fe_{2.11}O_4$	3	3	10	10	5
$Co_{0.31}Mn_{0.52}Fe_{2.11}O_4$	2	4	10	10	5
$Co_{0.19}Mn_{0.65}Fe_{2.11}O_4$	1.2	4.8	10	10	5
$Mn_{0.80}Fe_{2.14}O_4$	0	6	10	10	5

Physical mixtures of cobalt and manganese ferrites were prepared by manually mixing the cobalt and manganese ferrite samples reported in the previous paragraph (4.2) in a ratio $CoFe_2O_4$:$MnFe_2O_4$ = 4:1, 1:1, 1:4 for the sample PhysMix1, PhysMix2, and PhysMix3, respectively.

4.3 Characterization

4.3.1 Powder X-ray Diffraction (XRD)

XRD patterns of the chemically mixed samples (Figure 54) show the typical reflections of a spinel phase and the extracted parameters (crystallite size and lattice parameter) are reported in Table 35.

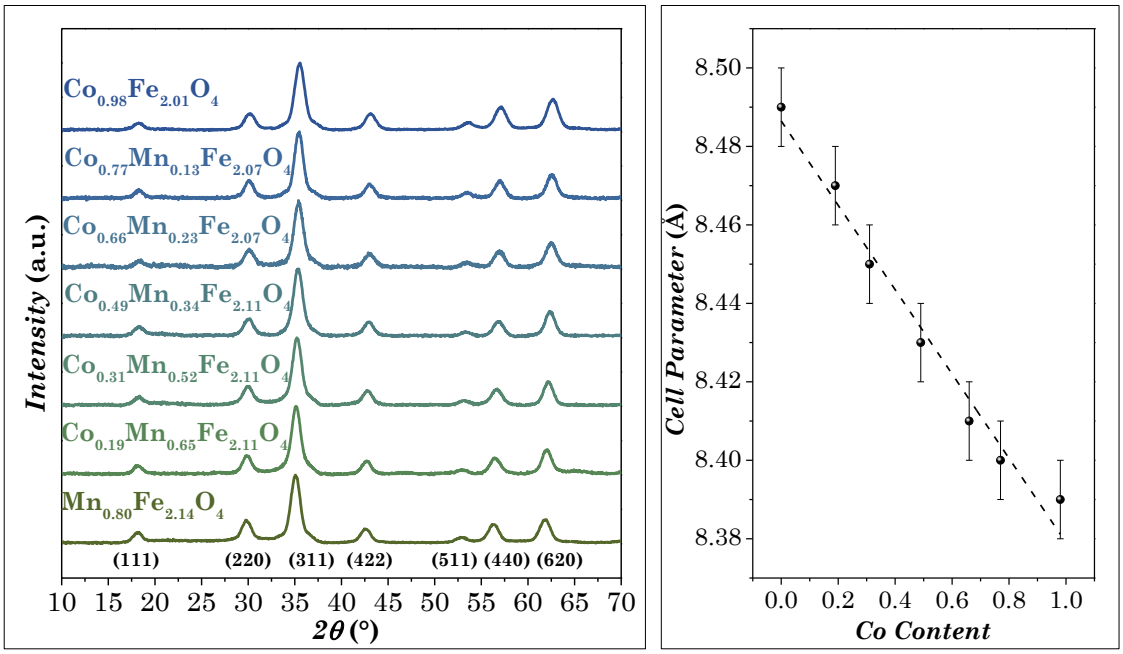

Figure 54. XRD patterns of the pure and chemically mixed Co-Mn ferrite samples (left). Trend of the lattice parameter of the Co-Mn ferrite samples as a function of the actual cobalt content determined by ICP-OES (right, linear fit: y = 8.48 - 0.11·x; R^2 = 0.98).

Table 35. Experimental composition determined by ICP-OES, crystallite size, cell parameter, and particle size of the samples.

Theoretical composition	Experimental composition (ICP-OES)	*a* (Å)	<D_{XRD}> (nm)	<D_{TEM}> (nm)	σ <D_{TEM}> (%)
$CoFe_2O_4$	$Co_{0.98}Fe_{2.01}O_4$	8.37 (1)	8.4 (2)	8.7	14
$Co_{0.8}Mn_{0.2}Fe_2O4$	$Co_{0.77}Mn_{0.13}Fe_{2.07}O_4$	8.40 (1)	8.8 (3)	9.2	14
$Co_{0.66}Mn_{0.33}Fe_2O4$	$Co_{0.66}Mn_{0.23}Fe_{2.07}O_4$	8.40 (1)	8.4 (6)	9.0	13
$Co_{0.5}Mn_{0.5}Fe_2O4$	$Co_{0.49}Mn_{0.34}Fe_{2.11}O_4$	8.42 (1)	8.6 (5)	9.7	14
$Co_{0.33}Mn_{0.66}Fe_2O4$	$Co_{0.31}Mn_{0.52}Fe_{2.11}O_4$	8.44 (1)	8.3 (6)	10.9	14
$Co_{0.2}Mn_{0.8}Fe_2O4$	$Co_{0.19}Mn_{0.65}Fe_{2.11}O_4$	8.46 (1)	8.5 (2)	10.3	16
$MnFe_2O_4$	$Mn_{0.80}Fe_{2.14}O_4$	8.48 (1)	8.7 (3)	9.8	14

The average crystallite size calculated from the profile analysis is in the range 8.3-8.7 nm, with no trend as a function of the chemical composition. The lattice parameters, *a*, for the pure ferrites are in good agreement with those reported in the literature (8.3919 Å, PDF Card: 022-1086 for cobalt ferrite and 8.4990 Å, PDF Card: 010-0319 for manganese ferrite) and, as expected, decrease linearly with the increase of the actual cobalt content, determined by ICP-OES (Figure 54), in agreement with the Vegard's law.[648] This result can be explained considering the smaller ionic radius of Co^{II} (82 pm) compared

to Mn^{II} (90 pm),[649] that causes a contraction of the structure. It can be pointed out that quasi-stoichiometric cobalt ferrite was obtained while a certain percentage of manganese did not take part into the mixed spinel structure formation, as also seen in chapter 2 for the synthesis of manganese ferrite NPs. These results highlight the importance of determining the actual chemical composition in the studies that correlate physical properties with composition.

4.3.2 Transmission Electron Microscopy (TEM)

TEM measurements was carried out to study the morphology and the particle size of the samples. TEM bright field images of the samples (Figure 55) show well-separated spheroidal nanoparticles with particle size slightly higher to crystallite size, especially for the high manganese content samples (Table 35). Size distributions are unimodal and ranges from 13 to 16%.

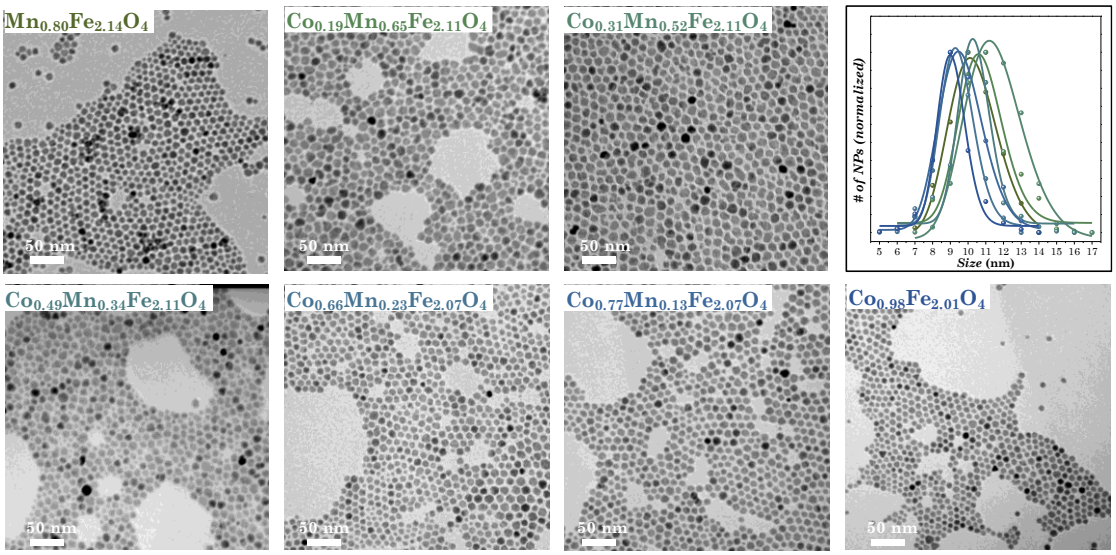

Figure 55. TEM bright field images of the samples and particle size distribution.

4.3.3 Room-Temperature ^{57}Fe Mössbauer Spectroscopy

4.3.3.1 Mössbauer spectra of chemically mixed ferrites

RT ^{57}Fe Mössbauer spectroscopy measurements were performed on all the samples. The spectra of all the samples, except $Mn_{0.80}Fe_{2.14}O_4$, show a sextet, associated to nanoparticles in the blocked state, while the singlet of the manganese ferrite sample indicates the presence of nanoparticles in the superparamagnetic state. The spectra of the blocked nanoparticles were initially fitted with one sextet (Figure 54), accounting for Fe^{III} in both octahedral and tetrahedral sites of the spinel ferrite structure (Table 36) and one broad singlet ascribed to NPs with relaxation time close to the measurement time scale (not reported in the table).

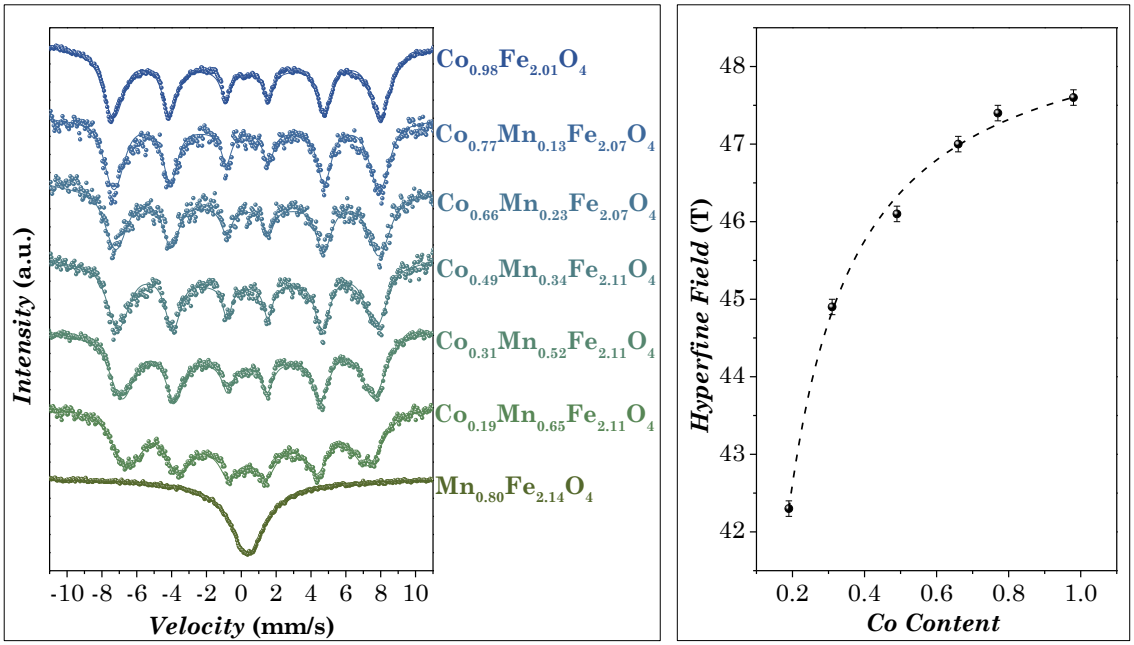

Figure 56. RT ^{57}Fe Mössbauer spectra of the chemically mixed ferrite samples fitted with one sextet (left). Evolution of B_{hf} of sextet accounting for both octahedral and tetrahedral sites as a function of Co content per formula unit (right, $Co_xMn_yFe_zO_4$).

Table 36. RT ^{57}Fe Mössbauer parameters of chemically mixed samples fitted by using one sextet for the blocked nanoparticles: values of the isomer shift (δ), quadrupole splitting (ΔE_Q), hyperfine field (B_{hf}), full width at half maximum (FWHM).

Sample	Signal	δ (mm/s)	ΔE_Q (mm/s)	B_{hf} (T)	FWHM (mm/s)
$Co_{0.98}Fe_{2.01}O_4$	Sextet	0.32(1)	-0.02(1)	47.6(1)	0.7(1)
$Co_{0.77}Mn_{0.13}Fe_{2.07}O_4$	Sextet	0.33(1)	-0.03(1)	47.4(1)	0.7(1)
$Co_{0.66}Mn_{0.23}Fe_{2.07}O_4$	Sextet	0.35(1)	-0.01(1)	47.0(0)	0.8(1)
$Co_{0.49}Mn_{0.34}Fe_{2.11}O_4$	Sextet	0.35(1)	-0.03(1)	46.1(2)	0.6(1)
$Co_{0.31}Mn_{0.52}Fe_{2.11}O_4$	Sextet	0.36(1)	0.01(1)	44.9(1)	0.7
$Co_{0.19}Mn_{0.65}Fe_{2.11}O_4$	Sextet	0.34(1)	-0.01(1)	42.8(1)	1.1(1)
$Mn_{0.80}Fe_{2.14}O_4$	Singlet	0.38(1)	-	-	2.1(1)

The quadrupole splitting values (ΔE_Q) for all the samples are almost zero, indicating a cubic symmetry and the isomer shift values (δ) for both sites are in the 0.32-0.38 mm/s range typical for Fe^{III},[577] excluding the presence of Fe^{II}. The role of Co^{II} in the spinel structure can be clarified by comparing the hyperfine field values in the mixed cobalt-manganese ferrite samples and the pure cobalt ferrite. The hyperfine field value of the sextet in the pure cobalt ferrite sample ($Co_{0.98}Fe_{2.01}O_4$) is equal to 47.6 T. This value gradually decreases when Co^{II} is replaced by Mn^{II}, due to the lower single ion magnetocrystalline anisotropy of Mn^{II} (Figure 56). These data were fitted by using Eq. 39, obtained from CME model.[578–580] Keeping constant temperature and volume of the nanoparticles, the hyperfine field depends on the anisotropy constant, that is strongly related to the cobalt and the manganese content.[650] The fitted curve produced satisfactory results as indicated by the adjusted R^2 equal to 0.99.

Then, an attempt to fit the spectra of the blocked NPs was made by using two sextets,[574] corresponding to Fe^{III} in octahedral and tetrahedral sites of the spinel ferrite (Figure 57). To this aim, the area of the sextet associated to octahedral sites were fixed to double of the tetrahedral sites area. The fit gave satisfactory results and physically acceptable hyperfine parameters (Table 37).

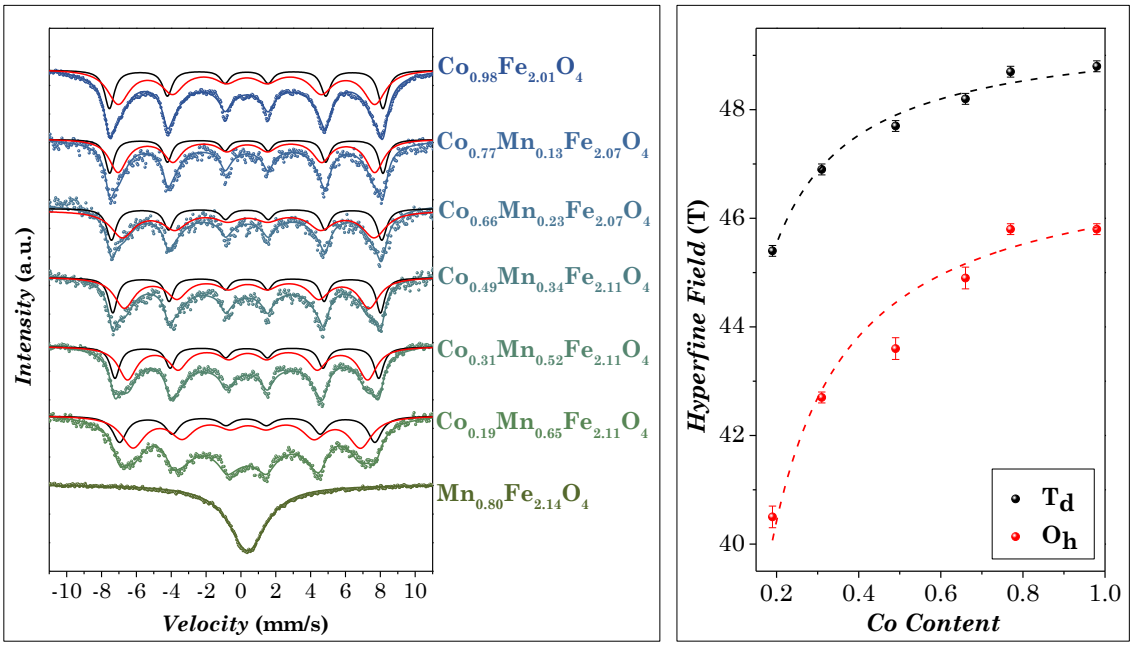

Figure 57. RT ^{57}Fe Mössbauer spectra of the chemically mixed ferrite samples fitted with two sextet (left). Evolution of B_{hf} in octahedral (red) and tetrahedral (black) sites as a function of Co content per formula unit (right, $Co_xMn_yFe_zO_4$).

Table 37. RT ^{57}Fe Mössbauer parameters of the blocked chemically mixed samples fitted by using two sextets: values of the isomer shift (δ), quadrupole splitting (ΔE_Q), hyperfine field (B_{hf}), full width at half maximum (FWHM).

Sample	δ (mm/s)	ΔE_Q (mm/s)	B_{hf} (T)	FWHM (mm/s)	Attribution
$Co_{0.98}Fe_{2.01}O_4$	0.33(1)	-0.02(1)	45.8(1)	1.5(1)	Fe^{III} in O_h sites
	0.31(1)	-0.03(1)	48.8(1)	0.7(1)	Fe^{III} in T_d sites
$Co_{0.77}Mn_{0.13}Fe_{2.07}O_4$	0.34(1)	-0.05(1)	45.8(1)	1.2(1)	Fe^{III} in O_h sites
	0.32(1)	-0.01(1)	48.7(1)	0.6(1)	Fe^{III} in T_d sites
$Co_{0.66}Mn_{0.23}Fe_{2.07}O_4$	0.41(1)	0.03(1)	44.9(2)	1.6(1)	Fe^{III} in O_h sites
	0.34(1)	-0.02(1)	48.2(1)	0.7(1)	Fe^{III} in T_d sites
$Co_{0.49}Mn_{0.34}Fe_{2.11}O_4$	0.36(1)	-0.07(1)	43.6(2)	1.4(1)	Fe^{III} in O_h sites
	0.33(1)	-0.01(1)	47.7(1)	0.6(1)	Fe^{III} in T_d sites
$Co_{0.31}Mn_{0.52}Fe_{2.11}O_4$	0.38(1)	-0.01(1)	42.7(1)	1.3(1)	Fe^{III} in O_h sites
	0.33(1)	0.02(1)	46.9(1)	0.7(1)	Fe^{III} in T_d sites
$Co_{0.19}Mn_{0.65}Fe_{2.11}O_4$	0.37(1)	-0.08(1)	40.5(1)	1.6(1)	Fe^{III} in O_h sites
	0.33(1)	0.06(1)	45.4(1)	0.9(1)	Fe^{III} in T_d sites

Tetrahedral sites, due to the higher covalent character, show lower isomer shift values compared to the octahedral ones.[574] The full width at half maximum values (FWHM) of the octahedral sites of all the samples are on average higher compared to tetrahedral sites, because of two non-equivalent

octahedral sites. Indeed, below T_{SR} (spin-reorientation transition temperature; 90 K for cobalt ferrite,[651] 225 K for manganese ferrite[652]) all Fe ions in octahedral sites are magnetically equivalent. Above T_{SR}, two non-equivalent positions in octahedral sites occur: in the first position, the axis of local trigonal distortion is parallel to the magnetization, while, in the second one, trigonal distortion and magnetization axes point along different body diagonals.[575] Consequently, a broadening of the sextet associated with the octahedral sites is observed. The full width at half maximum values of the octahedral sites of all the samples are on average higher compared to tetrahedral sites, because of the two non-equivalent octahedral sites.

The fitting by using two sextets gave us additional information about the role of Co^{II} and Mn^{II} in the spinel structure. As for the fitting by using one sextet, the hyperfine field values in the mixed cobalt-manganese ferrite samples gradually decrease when Co^{II} is replaced by Mn^{II} in both O_h and T_d sites, due to the lower single ion magnetocrystalline anisotropy of Mn^{II} (Figure 57), as previously discussed. The decrease is more consistent for O_h sites with respect to T_d ones. This behaviour can be attributed to the site occupancies of Co^{II} and Mn^{II}. In fact, the inversion degree (γ) of cobalt ferrite nanoparticles is usually around 0.7 (see 2.3.6.2),[553,561] *i.e.* 70% of Co^{II} and 30% are in octahedral and tetrahedral positions, respectively. Considering that octahedral sites are twice as much as tetrahedral sites, the site occupancy of Co^{II} can be regarded as random. Nanosized manganese ferrite shows an inversion degree around 0.5,[653] (as also reported for MnA sample in paragraph 2.3.6.2) which means that Mn^{II} demonstrates preference for tetrahedral sites. Since O_h-T_d exchange interactions (J_{AB}) are stronger than T_d-T_d (J_{AA}) or O_h-O_h (J_{AB}),[654] the hyperfine field of octahedral sites are more affected by Mn^{II} present in tetrahedral sites, causing a higher decrease in the hyperfine field values with respect to the tetrahedral sublattice.[654] Tetrahedral sites are also affected by a reduction in hyperfine field (Figure 57, Table 37), in contrast with other studies carried out on bulk ferrites.[574,655] This different behaviour can be explained by the fact that bulk materials show different site occupancies compared to nanostructured materials: in fact, bulk cobalt ferrite is totally inversed ($\gamma = 1$) while bulk manganese ferrite has almost normal spinel structure ($\gamma = 0.2$). In the study above,[574] as Mn^{II} substitutes Co^{II}, Fe^{III} ions move from tetrahedral sites to octahedral ones, leading to a $Co^{II}[O_h]/Fe^{III}(T_d)$ ratio almost constant while the $Co^{II}(T_d)/Fe^{III}[O_h]$ ratio decreases rapidly. This trend is reflected in the hyperfine field values. The data reported in Figure 57 were also fitted with Eq. 39, giving satisfactory results as indicated by the adjusted R^2 equal to 0.98 and 0.96 for octahedral and tetrahedral sites, respectively.

4.3.3.2 ^{57}Fe Mössbauer spectra of physically mixed ferrites.

As seen so far, ^{57}Fe Mössbauer spectroscopy represents a powerful tool for the understanding of both structural and magnetic properties of iron-containing materials. An additional interesting comparison can be drawn by analysing physical mixtures (PhysMix1-3) of cobalt ferrite and manganese ferrite having different $CoFe_2O_4$:$MnFe_2O_4$ ratios (Figure 58).

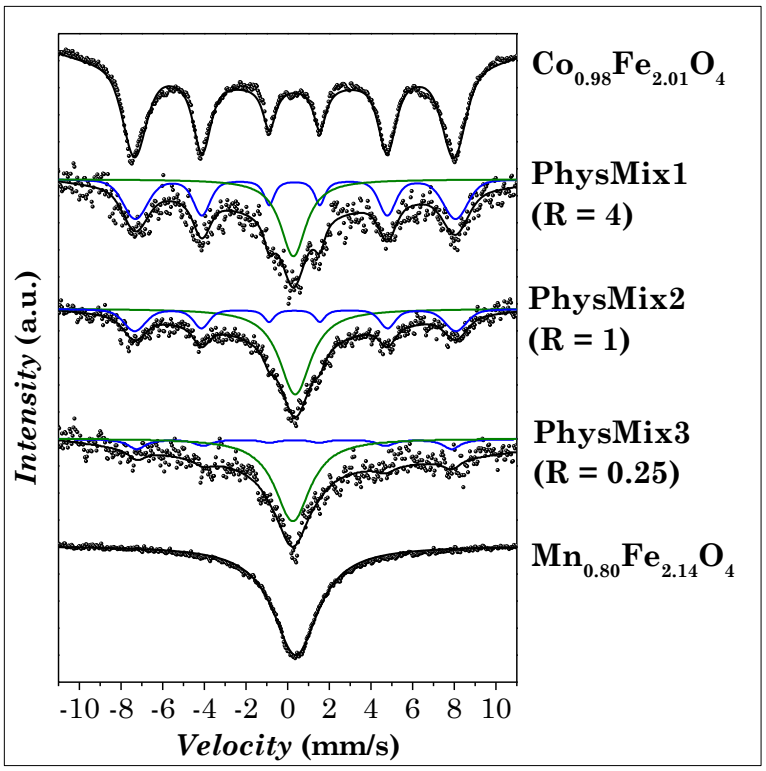

Figure 58. RT ^{57}Fe Mössbauer spectra of the physically mixed ferrite samples with cobalt and manganese ferrites.

Table 38. RT ^{57}Fe Mössbauer parameters physically mixed samples and pure cobalt and manganese ferrites (R = $CoFe_2O_4$:$MnFe_2O_4$ ratio): values of the isomer shift (δ), quadrupole splitting (ΔE_Q), hyperfine field (B_{hf}), full width at half maximum (FWHM).

Sample	R	Signal	δ (mm/s)	ΔE_Q (mm/s)	B_{hf} (T)	FWHM (mm/s)
$Co_{0.98}Fe_{2.01}O_4$	-	Sextet	0.32(1)	-0.02(1)	47.6(1)	0.7(1)
PhysMix1	4	Sextet	0.33(1)	-0.02(1)	47.7(1)	1.1(1)
		Singlet	0.33(1)	-	-	2.6(1)
PhysMix2	1	Sextet	0.35(1)	0.05(1)	47.8(1)	0.6(1)
		Singlet	0.36(1)	-	-	1.9(1)
PhysMix3	0.25	Sextet	0.35(1)	0.04(1)	47.5(1)	0.9(1)
		Singlet	0.44(1)	-	-	2.7(1)
$Mn_{0.80}Fe_{2.14}O_4$	-	Singlet	0.38(1)	-	-	2.1(1)

The spectra of the physical mixtures result in the superposition of the signals of cobalt and manganese ferrites. Indeed, they were fitted by using one sextet, ascribable to the blocked nanoparticles of cobalt ferrite, and one singlet, associated to superparamagnetic nanoparticles mostly present in manganese ferrite. The signals in the physical mixtures have similar Mössbauer

parameters found for the single phases (Table 38), indicating no influence of one phase on the other. Unfortunately, due to the broad singlets always present in each sample, it is difficult to quantitatively estimate the areas of the different components in the physical mixtures. The spectra of the mixtures were fitted by using two subspectra (one sextet and one singlet) considering that the sum of the individual three singlets (found in cobalt and manganese ferrite) could result in just one singlet representing a distribution of hyperfine field of both samples. Nevertheless, it is clear from Figure 58 how the relative areas of the sextet and the singlet change with different $CoFe_2O_4$:$MnFe_2O_4$ ratio.

4.3.4 DC Magnetometry: Magnetism

DC Magnetometry measurements, *i.e.* magnetization isotherms at 10 and 300 K and ZFC-FC protocols were carried out on some selected chemical mixtures (with middle compositions) and PhysMix2 and PhysMix3. Figure 59 and Table 39 report the results for the chemical mixtures.

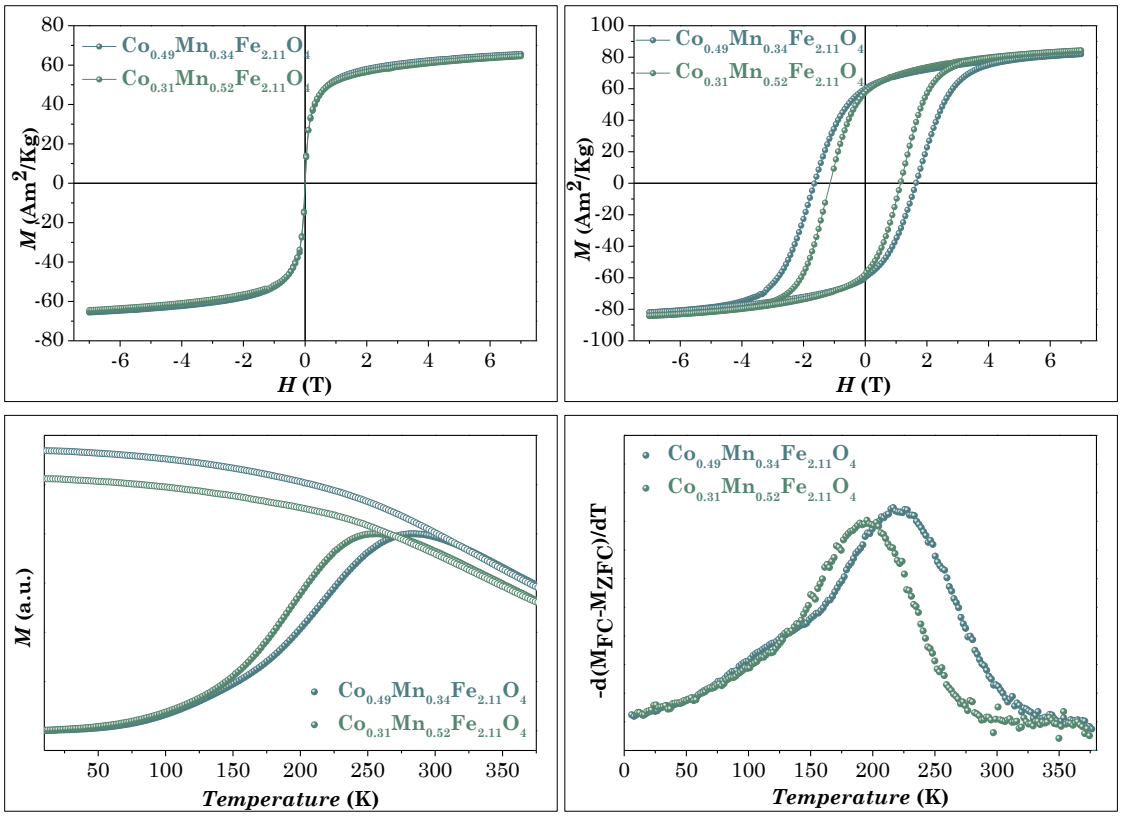

Figure 59. Magnetization isotherms of selected chemical mixtures recorded at 10 K (top). ZFC (full circles) and FC (empty circles) curves recorded at low external magnetic field (10 mT) (bottom left); anisotropy energy barrier distributions estimated by the first derivative $-d(M_{FC}-M_{ZFC})/dT$ (bottom right).

Table 39. Basic parameters determined from the ZFC curves and magnetization isotherms of cobalt and manganese ferrite, chemical mixtures, and CoA@Mn. T_{max}, T_{diff}, and T_b correspond to the maximum, furcation point of the ZFC curve (2%), and blocking temperature; H_c^{10}, H_K^{10} (2%), M_7^{10}, M_s^{10}, M_s^{300}, and M_r^{10} correspond to the coercivity, anisotropy field, magnetization at 7 T, saturation magnetization values at 10 K and 300 K, and remanent magnetization, respectively.

Sample	T_{max} (K)	T_{diff} (K)	T_b (K)	H_c^{10} (T)	H_K^{10} (T)	M_s^{300} (Am²/kg)	M_7^{10} (Am²/kg)	M_s^{10} (Am²/kg)	M_r^{10} (Am²/kg)	M_r/M_s
$Co_{0.98}Fe_{2.01}O_4$	307	336	221	1.53	4.2	77	86	91	63	0.69
$Mn_{0.80}Fe_{2.14}O_4$	79	81	18	0.01	0.01	-	83	83	6	0.07
$Co_{0.49}Mn_{0.34}Fe_{2.11}O_4$	286	303	219	1.65	4.0	67	83	91	60	0.66
$Co_{0.31}Mn_{0.52}Fe_{2.11}O_4$	259	280	194	1.15	3.2	64	84	92	58	0.63
PhysMix2	64 262	314	37 200	0.07	-	-	82	84	38	0.45
PhysMix3	-	-	-	0.02	-	-	79	79	9	0.11

All the chemical mixture samples display single-magnet behaviour in both field- and temperature-dependent magnetization. The sample with the highest cobalt content exhibits higher T_{max}, T_{diff}, T_b, H_c, and H_K values than those of the other chemical mixture, due to the lower single ion anisotropy constant of Mn with respect to Co.[243,656] On the contrary, similar values are found for remanent and saturation magnetizations at both 10 and 300 K and the difference T_{diff}-T_{max}. Interestingly, $Co_{0.49}Mn_{0.34}Fe_{2.11}O_4$ displays a coercive field slightly higher than that of cobalt ferrite samples with similar crystallite sizes (Table 39 and Table 28), that can be ascribed to the higher magnetic size (6.0 nm *vs* 5.6 nm) or the different chemical composition. Indeed, studies on Mn-[243] and Fe-substituted[582] cobalt ferrites reveal an initial increase of the coercive filed with the Mn or Fe content until a maximum is reached and then a subsequent decrease. However, other works where different cations (Mg^{II}, Zn^{II})[553,657–659] substitute Co^{II} in cobalt ferrites show a reduction of the coercivity instead, suggesting the critical role of the substituting cation. Further magnetic studies on the other chemical mixtures and therefore needed to have a complete scenario.

Figure 60 shows the results of the physical mixtures. Contrary to the chemical mixtures, the physical ones show a two-stage loop in the field-dependent magnetization, due to weak magnetic coupling between the hard cobalt ferrite phase and the soft manganese ferrite phase. The temperature-dependent magnetization of PhysMix2 shows two peaks that can be easily ascribed to the blocking temperature of $CoFe_2O_4$ and $MnFe_2O_4$, as can also be seen in the first derivative $-d(M_{FC}-M_{ZFC})/dT$, where two distributions are present. In addition, it is possible to observe a small shift in the position of the two distributions in opposite directions: the manganese ferrite maximum appears at slightly higher temperature suggesting an influence of the presence of the more anisotropic cobalt ferrite nanoparticles, and *vice-versa*.

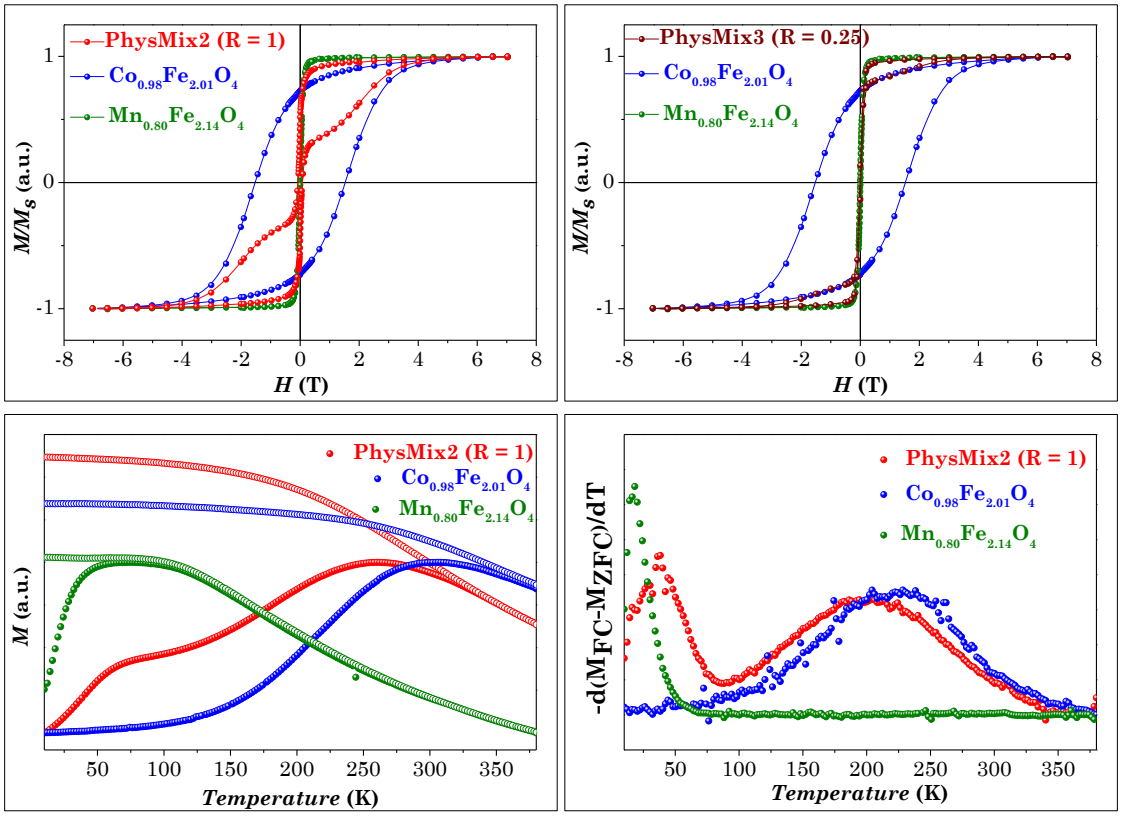

Figure 60. Magnetization isotherms of physical mixtures PhysMix2 (R = 1) and PhysMix3 (R = 0.25), manganese ferrite and cobalt ferrite recorded at 10 K (top). ZFC (full circles) and FC (empty circles) curves of PhysMix2, manganese ferrite and cobalt ferrite recorded at low external magnetic field (10 mT) (bottom left); anisotropy energy barrier distributions estimated by the first derivative *-d(M_{FC}-M_{ZFC})/dT* (bottom right).

4.4 Comparison among core-shell, chemical, and physical mixtures.

The ^{57}Fe Mössbauer spectra and DC magnetic data of physical and chemical mixtures are now compared with the core-shell made by cobalt and manganese ferrite. The core-shell sample that were chosen for the comparison is the CoA@Mn one, having crystallite size of 8.0(2) nm, similar to both the chemical and physical mixtures. Indeed, it is worth noting that the magnetic parameters can be compared thanks to the similar crystallite size of all samples, since magnetic properties strongly depend on particle volume. Since ICP-OES analyses revealed, for the sample CoA@Mn, a Mn:Co ratio equal to 1.2, it was decided to use for the comparison the physical mixture PhysMix2 (ratio = 1) and the chemical mixtures $Co_{0.49}Mn_{0.34}Fe_{2.11}O_4$ (ratio = 0.7) and $Co_{0.31}Mn_{0.52}Fe_{2.11}O_4$ (ratio = 1.6). The Mössbauer and DC magnetic spectra are shown in Figure 61 and the parameters in Table 40.

For the comparison, Mössbauer spectra where blocked NPs are present were fitted with two sextets, to use the same fitting approach for all the samples. The physical mixture, as described in the previous paragraph, presents the signals with hyperfine paraments ascribable to the single cobalt ferrite (sextet) and manganese ferrite (singlet). On the contrary, the core-shell sample shows no sharp singlet that could be associated to superparamagnetic nanoparticles, but two sextets with hyperfine field values lower than both the cobalt ferrite and the mixed Co-Mn ferrites.
Concerning the DC magnetometry analysis, the core-shell sample significantly differs from the physical mixture of cobalt and manganese ferrite, which displays two-stage loop, and from the chemical mixture, which despite showing a single-magnet behaviour, presents very different magnetic properties (Table 39). Indeed, the core-shell sample features lower blocking temperature, coercive and anisotropy field, while it has higher saturation magnetization both at 300 and 10 K and M_r/M_s, due to hard-soft magnetic coupling. Therefore, these comparisons suggest that, in the core-shell sample, the two counterparts, that is the soft manganese ferrite phase and the hard cobalt ferrite phase, are in contact and magnetically coupled, and behave like a single an individual system.

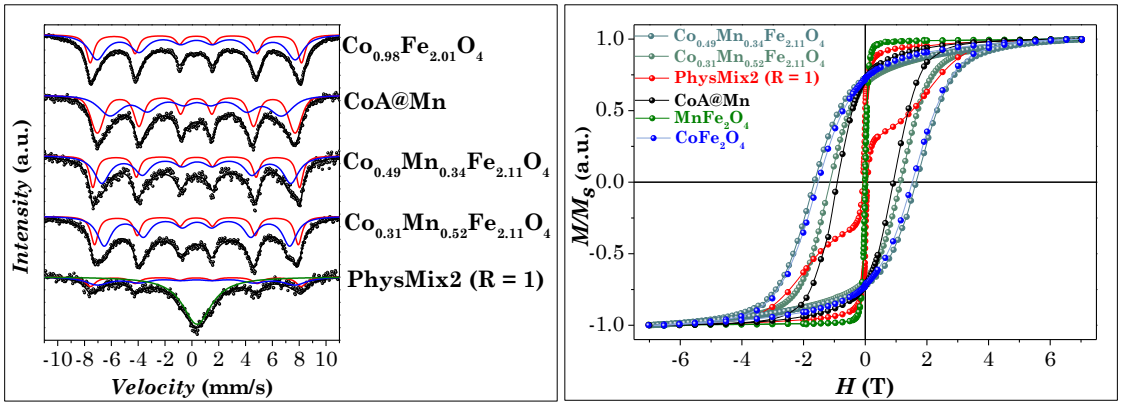

Figure 61. RT ^{57}Fe Mössbauer spectra and *M vs H* curves of the samples $Co_{0.98}Fe_{2.01}O_4$, $Mn_{0.80}Fe_{2.14}O_4$, CoA@Mn, $Co_{0.49}Mn_{0.34}Fe_{2.11}O_4$, $Co_{0.31}Mn_{0.52}Fe_{2.11}O_4$, and PhysMix2.

Table 40. RT ^{57}Fe Mössbauer and magnetic parameters of the samples $Co_{0.98}Fe_{2.01}O_4$, $Mn_{0.80}Fe_{2.14}O_4$, CoA@Mn, $Co_{0.49}Mn_{0.34}Fe_{2.11}O_4$, $Co_{0.31}Mn_{0.52}Fe_{2.11}O_4$, and PhysMix2: multiplicity of the subspectra (sub), values of the isomer shift (δ), quadrupole splitting (ΔE_Q), hyperfine field (B_{hf}), full width at half maximum (FWHM). T_b, H_c^{10}, H_K^{10} (2%), M_7^{10}, M_s^{10}, M_s^{300}, and M_r^{10} are the blocking temperature, coercivity, anisotropy field, magnetization at 7 T, saturation magnetization at 10 K and 300 K, and remanent magnetization, respectively.

	RT ^{57}Fe Mössbauer				DC Magnetometry					
Sample	**Sub**	**δ (mm/s)**	**B_{hf} (T)**	**FWHM (mm/s)**	**T_b (K)**	**H_c^{10} (T)**	**H_K^{10} (T)**	**M_s^{10} (Am²/kg)**	**M_r^{10} (Am²/kg)**	**M_r/M_s**
$Co_{0.98}Fe_{2.01}O_4$	6	0.33	45.8	1.5	206	1.54	4.1	91	63	0.69
	6	0.31	48.8	0.7						
$Mn_{0.80}Fe_{2.14}O_4$	1	0.38	-	2.1	18	0.01	0	83	6	0.07
CoA@Mn	6	0.34	39.7	1.6	185	0.92	2.6	93	67	0.72
	6	0.32	45.8	0.7						
$Co_{0.49}Mn_{0.34}Fe_{2.11}O_4$	6	0.36	43.6	1.4	219	1.65	4.0	91	60	0.66
	6	0.33	47.7	0.6						
$Co_{0.31}Mn_{0.52}Fe_{2.11}O_4$	6	0.38	42.7	1.3	194	1.15	3.2	92	58	0.63
	6	0.33	46.9	0.7						
PhysMix2	6	0.33	45.7	1.5	37	0.07	-	84	38	0.45
	6	0.31	48.8	0.7						
	1	0.39	-	2.6	200					

4.5 Conclusions

Cobalt, manganese, and Co-Mn mixed ferrites with similar crystallite size (8.3-8.8 nm) were prepared by the oleate-based solvothermal method, also used for the synthesis of spinel ferrite NPs in chapters 2 and 3. The linear increase in the lattice parameter with the manganese content is a first indication of the actual substitution of cobalt with manganese in the spinel structure. RT ^{57}Fe Mössbauer spectroscopy allowed to gather information on both the structure and the magnetic properties of the samples. Manganese ferrite is in superparamagnetic state, while all the other samples are in the blocked state, due to the presence of Co^{II}, which features a higher anisotropy constant. The hyperfine field values for both octahedral and tetrahedral sites decrease with the increase of manganese content, demonstrating the effective substitution of Co^{II} with Mn^{II} in the spinel structure, in agreement with the CME model. A more pronounced decrease of hyperfine field for octahedral sites with respect to tetrahedral sites is due to the preference of Mn^{II} for tetrahedral sites. A further confirmation of the formation of Mn-Co ferrites results from the comparison with a physical mixture of pure cobalt ferrite and manganese ferrite of similar size. DC magnetic measurements also confirmed the production of mixed ferrites with single magnetic phase response and magnetic properties different from both the cobalt and manganese ferrites and the physical mixtures. Another useful comparison was drawn between the core-shell architectures of cobalt and manganese ferrites with the chemical and physical mixtures. Both RT ^{57}Fe Mössbauer spectroscopy and DC magnetometry measurements highlighted the presence of magnetic coupling in the core-shell sample, with different properties with respect to a chemical mixture. From the findings above, the oleate-based solvothermal method results to be a promising method due to its versatility in producing different spinel-ferrite based systems, also chemically mixed. Moreover, the comparison of the physical and structural properties based on RT ^{57}Fe Mössbauer spectroscopy and DC magnetometry can be considered a useful indirect tool to discriminate among physical, chemical mixtures, and core-shell architectures besides studying microstructural and magnetic properties, even though evidences from direct chemical mapping techniques and other indirect techniques are always required.

5 *Design of Silver-Spinel Ferrite Heterostructures: Synthesis and Characterization*

Abstract

A solvothermal method was developed to prepare silver-spinel ferrite nanoheterostructures, starting both from silver and spinel ferrite nanoparticles as seeds. The first strategy, consisting in a seed-mediated growth approach, was conducted in the presence of spinel ferrite NPs by using silver nitrate or silver oleate as Ag precursor. Spinel ferrite NPs were used oleate-capped or after an exchange ligand procedure with molecules having thiol groups (dimercapto succinic acid or mercaptoundecanoic acid), able to bind silver. Concerning the second strategy, silver NPs were synthesized by thermal reduction of silver oleate and used as seeds for the growth of spinel ferrite domains (cobalt ferrite, manganese ferrite, spinel iron oxide) on their surface, using metal oleates as precursors under solvothermal conditions. The characterization was performed through XRD, TEM-HRTEM, UV-Vis, and DC Magnetometry.

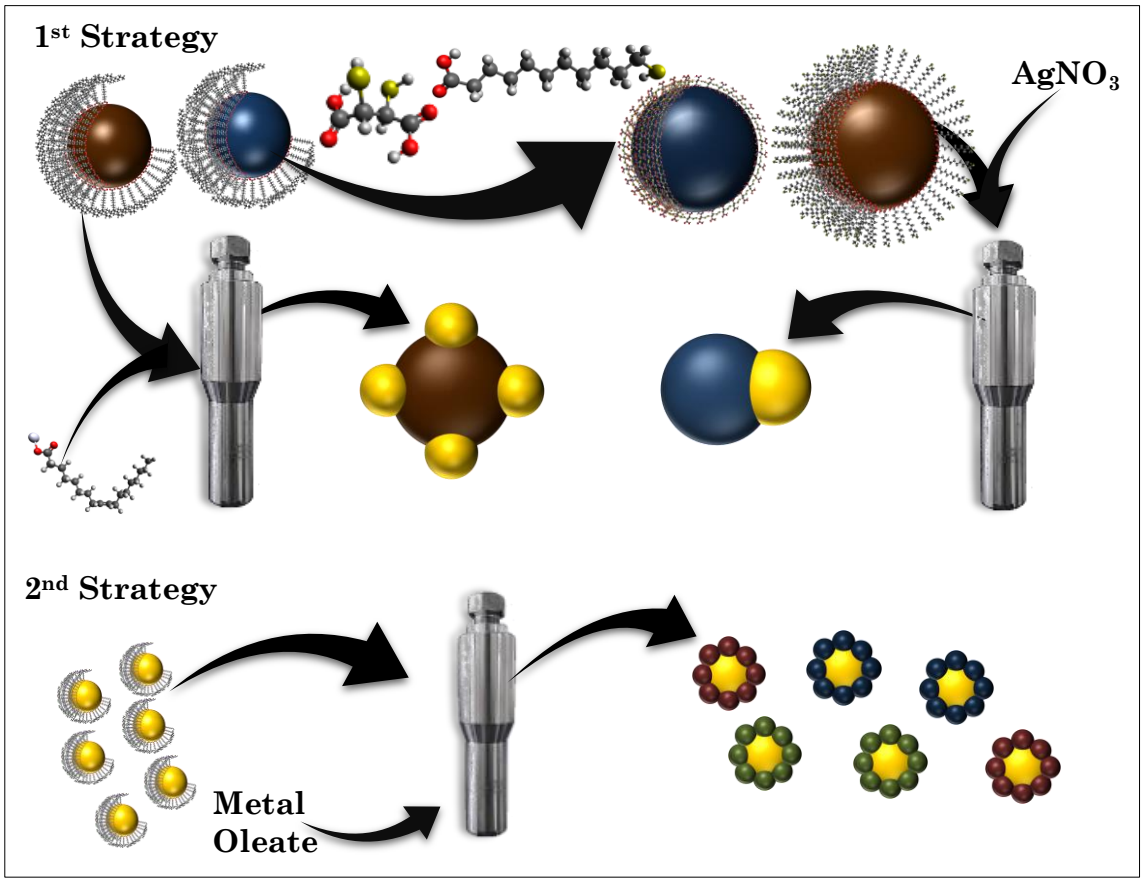

5.1 Introduction

Spinel ferrite-based nanoheterostructures (NHs) have attracted great interest in the last decades, thanks to the possibility to join in a single material different features. In this context, noble metals have been widely studied for the numerous properties (optic, catalytic, antibacterial, *etc.*) and applications that can offer, such as catalysis, material characterization, biomedicine, *etc.* The combination with magnetic materials opens new horizons of possibilities, merging magnetic and optical properties and leading to the emergence of a novel area of research: magnetoplasmonics. Silver-ferrite NHs are used for example as catalysts for purification of dye effluents,[452,496] exploiting the catalytic activities of silver and the magnetic separation of spinel ferrite. Again, these kinds of HNs are employed as substrates for surface enhanced Raman spectroscopy (SERS), thanks to the high surface resonance effect of silver.[452,477,479] Electromagnetic enhancement, caused by the construction of "hot-spots" in aggregated HNs, can contribute to optimize the SERS performances. In this context, magnetic-silver NHs represent an excellent material for SERS activity, since small superparamagnetic domains can induce magnetic aggregation without interfere with the silver localized surface plasmon resonance effect. Moreover, noble metal-spinel ferrite NHs have been employed for combined photothermal and magnetic heating, exploiting the localized surface plasmon resonance effect of the noble metal part and the magnetic behaviour of the spinel ferrite.[660–662]

Many architectures and synthesis method have been proposed in the literature, from core-shell with silver core[465,466] and *vice-versa*, to dimers[436–440,465,466] and flower-like,[431,448,452,453,477–479] prepared *via* one-pot[477–479] or two-pot syntheses (*e.g.* seed-mediated growth,[431,436–440] surface reduction[448,452,453] or oxidation,[465,466] Table 4). For example, Fe_3O_4@Ag flower-like NHs have been synthesized by a seed-mediated growth approach in organic solvents starting from magnetite NPs with silver nitrate or silver oleate as Ag precursor.[431] Janus Ag-ferrite NHs have also been synthesized by various authors,[436–440] through thermal decomposition of iron acetylacetonates or oleates in the presence of silver NPs (seed-mediated growth). Surface reduction silver nitrate in the presence of a reducing agent (*e.g.* glucose, oleylamine, *etc.*) and spinel ferrite NPs has permitted to produce dimer and flower-like NHs,[448,452,453] while surface oxidation of Ag@Fe core-shell NPs in air lead to the production of core-shell (or flower-like) NHs having silver core and magnetite/maghemite shell.[465,466] Less common approaches involve one-pot syntheses of flower-like silver-spinel iron oxide by various methods, either in solvothermal condition or *via* thermal decomposition.[477–479]

In spite of the discrete number of the above cited works, the solvothermal method has not been extensively studied for the synthesis of silver-spinel

ferrite NHs, despite its many advantages, such as the use of low-boiling organic solvents and mild temperatures, repeatability, high crystallinity, size control, and low dispersity of the products (paragraph 1.3.3).
In the previous chapters, bimagnetic spinel ferrite core-shell heterostructures were studied. The coupling between hard and soft ferrimagnetic materials induces unique magnetic properties exploitable in many applications, such as in the magnetic fluid hyperthermia. The use of isostructural materials enables the epitaxial growth of one phase to another, making possible the formation of core-shell architecture. On the contrary, when materials with different structure and cell parameter are used, the growth of the second phase is not regular, and different architectures can be obtained. In this chapter, an attempt to synthesize silver-spinel ferrite heterostructures is presented. In detail, the seed-mediated growth approach in solvothermal method were exploited for the synthesis of Ag-$M^{II}Fe_2O_4$ NHs (M^{II} = Co^{II}, Fe^{II}, Mn^{II}) by attempting various strategies, starting from (i) oleate-capped spinel ferrite NPs (or subsequent to an exchange ligand procedure) by using silver oleate or silver nitrate as Ag precursor; (ii) Ag NPs synthesized by thermal reduction treatment using metal oleate as ferrite precursor. Sample characterization were conducted through powder XRD, TEM, HRTEM, UV-Vis spectroscopy and DC magnetometry to study the structural, morphological, optical and magnetic properties.

5.2 Synthesis

The synthesis of silver-spinel ferrite heterostructures was achieved by using either spinel ferrite NPs or silver NPs as seeds for the seed-mediated growth in solvothermal conditions.

5.2.1 Synthesis Starting from Spinel Ferrite Seeds

5.2.1.1 Seed-Mediated Growth from Spinel Iron Oxide

Oleate-coated magnetite NPs synthesized as described in paragraph 2.2 (analogues to FeC) were used as seeds for the growth of silver domains, using silver nitrate or silver oleate as precursor.
Silver oleate was prepared as following. 10 mmol of NaOH were dissolved in 5 mL of distilled H_2O, followed by the addition of 5 mL of ethanol, 10 mmol of oleic acid, and 25 mL of water. The so-prepared sodium oleate in hydroalcoholic solution (35 mL) was placed under vigorous stirring (700 rpm) and of 50 mL of an aqueous solution of 0.2 M $AgNO_3$ were slowly added. The white precipitate was filtered and dried at 30 °C for two days.
Fe@Ag1 was prepared in a similar manner of the core-shell heterostructured NPs described in chapter 3, using metal oleate as shell precursor in a mixture of organic solvents and water in solvothermal conditions. In detail, around 10 mg of spinel iron oxide NPs were placed in a teflon liner together with 0.4 mmol of silver oleate, 0.4 mmol of oleylamine as reducing agent, 6 mL of toluene, 6 mL of pentanol and 3 mL of water. The total volume of the reacting mixture was 15 mL. The liner was enclosed in a stainless-steel autoclave (Berghof DAB-2), briefly shaken and placed vertically into a pre-heated (160 °C) oven for 10 hours. Fe@Ag2 was also prepared in the same manner of Fe@Ag1, using $AgNO_3$ as silver precursor, 10 mmol of oleylamine, 9.6 mmol of oleic acid, and 8.4 mL of ethanol. Table 41 summarises the synthesis conditions for these samples.

Table 41. Synthesis condition for the samples Fe@Ag1 and Fe@Ag2.

Sample	Ferrite seed (mmol)	Ag Precursor (mmol)	Oleylamine (mmol)	Oleic Acid (mmol)	Solvents (mL)	Temperature (°C)	Time (h)
Fe@Ag1	0.04	0.4 Ag-Oleate	0.4	-	6T–6P–3W	160	10
Fe@Ag2	0.04	0.4 $AgNO_3$	10	9.6	8.4E	160	10

5.2.1.2 Exchange Ligand Procedure: DMSA and MUA

A sample of oleate-coated spinel iron oxide and cobalt ferrite (similar to FeC and CoE, described in paragraph 2.2) underwent an exchange ligand procedure with 11-mercaptoundecanoic acid (MUA) and dimercaptosuccinic acid (DMSA), respectively (labelled as Fe_MUA and Co_DMSA), to introduce

thiol groups on the surface of the ferrite with the aim of binding Ag, in principle favouring the obtainment of the heterostructure.
Exchange ligand procedures were carried out according to a method retrieved in the literature.[449] In detail, around 25 mg of ferrite NPs were dispersed in 25 mL of toluene, followed by addition of 5 mL dimethyl sulfoxide (DMSO) solution containing 90 mg of DMSA (or MUA). The mixture was sonicated for 5 minutes and mechanically stirred for 48 h at room temperature. Them the precipitated NPs were recovered, washed three times with acetone and dispersed in ethanol.

5.2.1.3 Solvothermal Treatment of DMSA- or MUA-Coated Spinel Ferrite NPs in the presence of Silver Nitrate

Fe_MUA and Co_DMSA samples were used as seeds for the growth of a silver domain. The desired ethanol dispersion containing around 10 mg of MUA-or DMSA-coated ferrite NPs was placed in a teflon liner together with an ethanol solution of 0.4 mmol $AgNO_3$, and 0.4 mmol of oleylamine. The total ethanol amount was 15 mL. The liner was then enclosed in a stainless-steel autoclave (Berghof DAB-2), briefly shaken and put vertically into a pre-heated (160 °C) oven for 10 hours. Table 42 summarises the synthesis conditions for the samples.

Table 42. Synthesis condition for the samples Fe_MUA@Ag and Co_DMSA@Ag.

Sample	Ferrite seed (mmol)	Ag Precursor (mmol)	Oleylamine (mmol)	Ethanol (mL)	Temperature (°C)	Time (h)
Fe_MUA@Ag	0.04	0.4 $AgNO_3$	0.4	15	160	10
Co_DMSA@Ag	0.04	0.4 $AgNO_3$	0.4	15	160	10

5.2.2 Synthesis Starting from Silver Seeds

5.2.2.1 Silver NPs Synthesis

Silver NPs were synthesized following a reported procedure.[663] Around 2 mmol of silver oleate (synthesized as described in paragraph 5.2.1.1) were dissolved in 200 mL of oleic acid at 100 °C under nitrogen flux and vigorous stirring (700 rpm). After 15 minutes the temperature was increased to 170 °C (heating rate 4 °C/min) and allowed to react for one h, then cooled down to room temperature. The NPs have been separated by centrifugation, washed three times with hexane and ethanol, and finally stored in hexane.

5.2.2.2 Seed-Mediated Growth from Silver NPs

Ag NPs were used as seeds to prepare silver-spinel ferrite heterostructures. Around 25 mg of oleate-capped Ag NPs have been dispersed in toluene and placed into a teflon liner together with the desired amount of metal oleate

(synthesized as described in paragraph 2.2.1), 1-pentanol and water, as reported in Table 43. The liner was then enclosed in a stainless-steel autoclave (Berghof DAB-2), briefly shaken and put vertically into a pre-heated (140-220 °C) oven for 10 hours.

Table 43. Synthesis condition of silver-based spinel ferrite heterostructures. Reaction time was 10h.

Sample	Ag Seed (mmol)	n Oleate (mmol)[a]	1-pentanol (mL)	Toluene (mL)	Water (mL)	Temperature (°C)
Ag@Co1	0.2	0.5	5	5	5	220
Ag@Co2	0.2	0.5	5	5	0	140
Ag@Co3	0.2	0.25	5	5	0	140
Ag@Co4	0.2	0.125	5	5	0	140
Ag@Co5	0.2	0.125	10	10	0	140
Ag@Co6	0.2	0.125	10	10	0	180
Ag@Co7	0.2	0.125	10	10	0	200
Ag@Co8	0.2	0.125	10	10	0	220
Ag@Co9	0.2	0.125	10	10	0.1	200
Ag@Mn1	0.2	0.125	10	10	0	200
Ag@Fe1	0.2	0.125	10	10	0	200

5.3 Results and Discussion

5.3.1 Spinel ferrite-based heterostructures

The first strategy consisted on the growth of silver domains on pre-synthesized spinel ferrite nanoparticles (described in paragraph 2.2) through two central pathways: (i) direct seed-mediated growth of silver in solvothermal conditions directly on oleate-coated spinel iron oxide nanoparticles by using silver nitrate (Fe@Ag1) or silver oleate (Fe@Ag2) as silver precursor; (ii) seed-mediated growth on silver on DMSA- or MUA-coated spinel ferrite NPs by using silver nitrate as silver precursor in solvothermal conditions (Co_DMSA@Ag and Fe@MUA_Ag).
XRD and TEM data of all the samples are reported in Table 44 and Figure 62. XRD patterns were studied by both single peaks analysis (Scherrer equation for determining crystallite size and Eq. 54 to calculate the cell parameter) and Rietveld refinement (structures reported in Table 48), since two or more phases are present in the system, making semi-quantitative analysis useful for the understanding of the reactions. It is important to highlight the good agreement between the size extrapolated from Rietveld refinement and the one calculated with Scherrer formula, except for the sample Fe@Ag2, due to the strong peak overlapping of the different phases. For the comparison of crystallite sizes of the samples, Scherrer data will be adopted. On the contrary, cell parameters obtained by Rietveld method may be more accurate, due to structural refinement, compared to those calculated from single peaks analysis.

Table 44. Crystallite size, cell parameter, and quantitative analyses of spinel ferrite-based heterostructures calculated by single peaks analysis and Rietveld refinement.

Sample	Phase	Single Peaks Analysis		Rietveld Refinement			
		$\langle D_{XRD} \rangle$ (nm)	a (Å)	$\langle D_{XRD} \rangle$ (nm)	Microstrain	a (Å)	Fraction (% w/w)
Fe_3O_4	Fe_3O_4	10.1(1)	8.37(1)	16(1)	$6 \cdot 10^{-3}$	8.369(2)	-
Fe@Ag1	Fe_3O_4	10(2)	8.36(1)	13(1)	$3 \cdot 10^{-3}$	8.362(2)	69
	Ag FCC	26(3)	4.09(1)	33(2)	$1 \cdot 10^{-6}$	4.087(2)	31
Fe@Ag2	Fe_3O_4	10(3)	8.34(1)	21(2)	$8 \cdot 10^{-3}$	8.352(2)	16
	Ag FCC	6(1)	4.39(1)	7(1)	$5 \cdot 10^{-5}$	4.078(2)	38
	Ag HCP	4(1)	-	2(1)	$2 \cdot 10^{-5}$	3.017-4.700(2)	45
Fe_MUA@Ag1	Fe_3O_4	10(1)	8.33(1)	7(1)	$1 \cdot 10^{-5}$	8.360(2)	86
	Ag FCC	60(5)	4.09(1)	83(5)	$2 \cdot 10^{-4}$	4.089(2)	14
$CoFe_2O_4$		11.2(4)	8.39(1)	15(1)	$3 \cdot 10^{-3}$	8.393(2)	-
Co_DMSA@Ag1	$CoFe_2O_4$	15(2)	8.40(1)	15(1)	$8 \cdot 10^{-3}$	8.387(2)	37
	Ag FCC	40(5)	4.09(1)	40(2)	$5 \cdot 10^{-5}$	4.085(2)	62

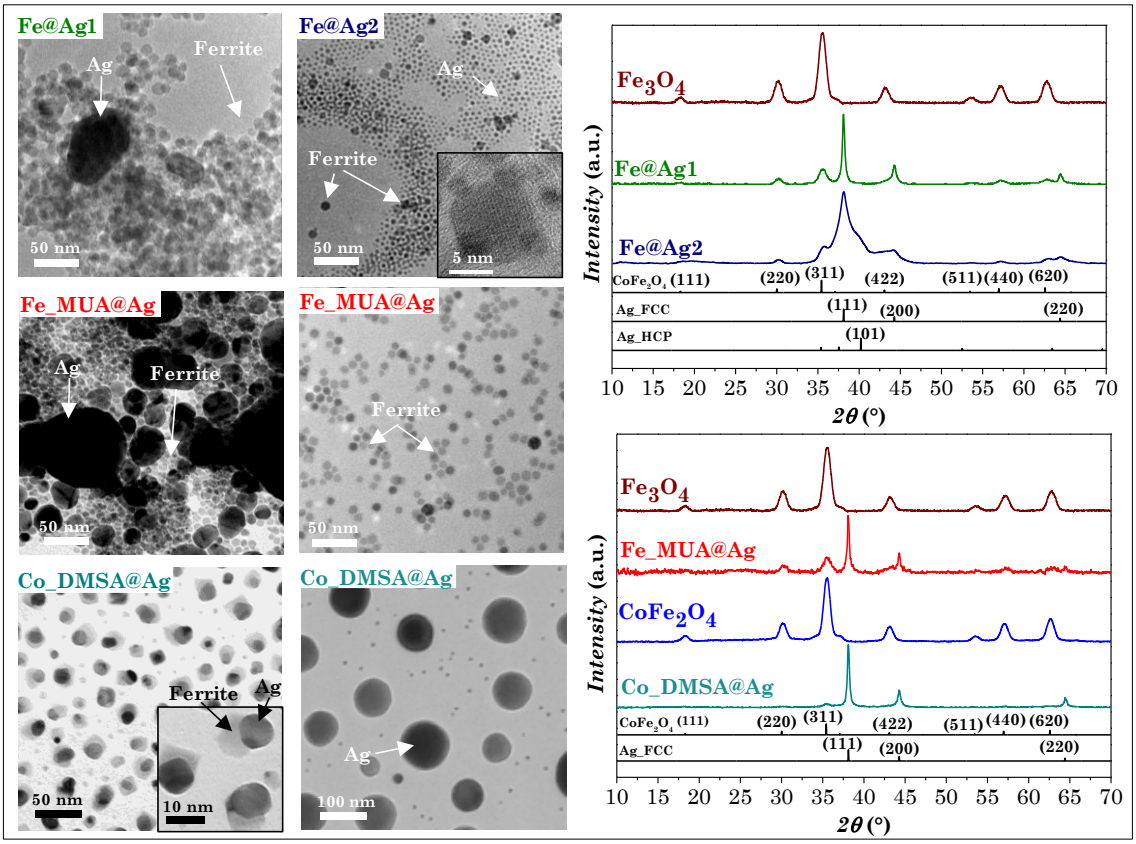

Figure 62. TEM and HRTEM images of spinel ferrite-based heterostructures (left side), and XRD patterns (right side).

As can be seen from XRD analyses (Figure 62, right side), spinel ferrite and silver phases are present in all samples. The first pathway, consisting in the use of oleate-capped spinel iron oxide NPs, conducted to different results, regarding crystalline phase, size, and morphology. Indeed, sample Fe@Ag1 (prepared with silver oleate and oleylamine as reducing agent) features spinel iron oxide NPs of the same size of the starting seeds NPs and silver NPs with crystallite size of about 30 nm (Table 44) with particle size of about 50 nm, as observed by TEM images (Figure 62, left side). Unfortunately, it seems that silver NPs did not grow on the surfaces of the ferrite seeds but formed separate NPs. This is probably due to the low solubility of silver oleate in organic solvents,[663] that could prevent the silver growth on the hydrophobic NPs' surface. To overcome this problem, Fe@Ag2 was synthesized by using $AgNO_3$ in ethanol. XRD pattern (Figure 62, right side) shows again the presence of spinel ferrite phase and very large bands ascribed to silver nanoparticles growing in both FCC and HCP phases. From Rietveld refinement analysis (Figure 63), silver was estimated to account for around 83% w/w of the whole sample, featuring a slightly prevalence of HCP phase having crystallite size of 2 nm, smaller than those found in the FCC phase ($<D_{XRD}>$ Ag_{FCC} = 7 nm). Generally, silver features a FCC structure, but in the form of ultrasmall NPs the HCP structure may be more stable, as in the case of gold.[664,665]

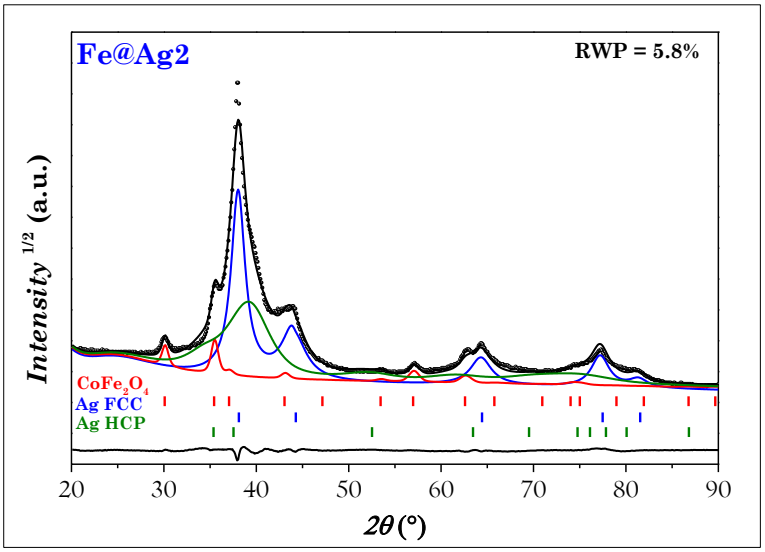

Figure 63. Rietveld refinement of the XRD pattern of sample Fe@Ag2.

TEM images (Figure 62, left side) show the presence of two populations of NPs, differing each other regarding size. The smaller are ascribable to Ag NPs while the larger ones to ferrite NPs, having particle size similar to that of the starting seeds. Nevertheless, HRTEM images reveal the formation of heterostructures, where small silver domains are attached on the surface of the ferrite NP. The careful analysis of the FFT images (Figure 64) displays the (111) Ag_{FCC} planes (2.3 Å) contiguous to the (311) ferrite planes (2.5 Å), revealing the epitaxial growth of silver. Probably, the Ag_{HCP} may have nucleated homogeneously, creating separate NPs.

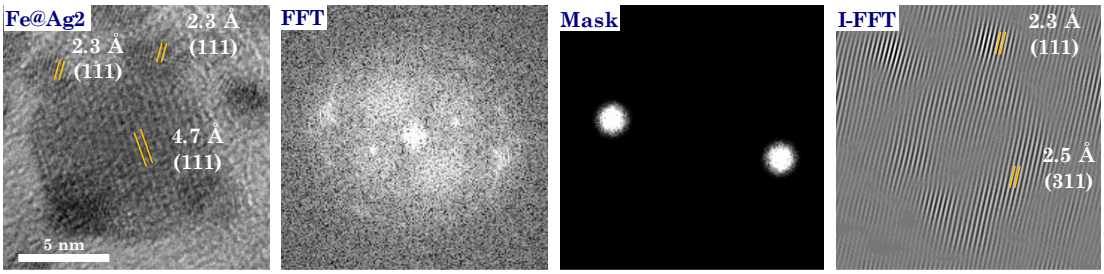

Figure 64. HRTEM, FFT, and inverse of FFT on selected spots images of Fe@Ag2

While in the case of Fe@Ag1 the ferrite seed NPs are dispersible in toluene, but the Ag-oleate is not, in the case of Fe@Ag2, $AgNO_3$ is soluble in ethanol, unlike the oleate-capped seeds spinel ferrite NPs. These non-ideal starting synthetic conditions did not lead, after the solvothermal treatment, to the desired products. For this reason, exchange ligand procedure of the capping agent of the ferrite NPs seeds with DMSA and MUA, to make them dispersible in ethanol (as $AgNO_3$), might be promising. Furthermore, thiol groups of DMSA and MUA could bind the silver precursor and facilitate the formation of heterostructure. The exchange ligand was verified with FT-IR, shown in Figure 65.

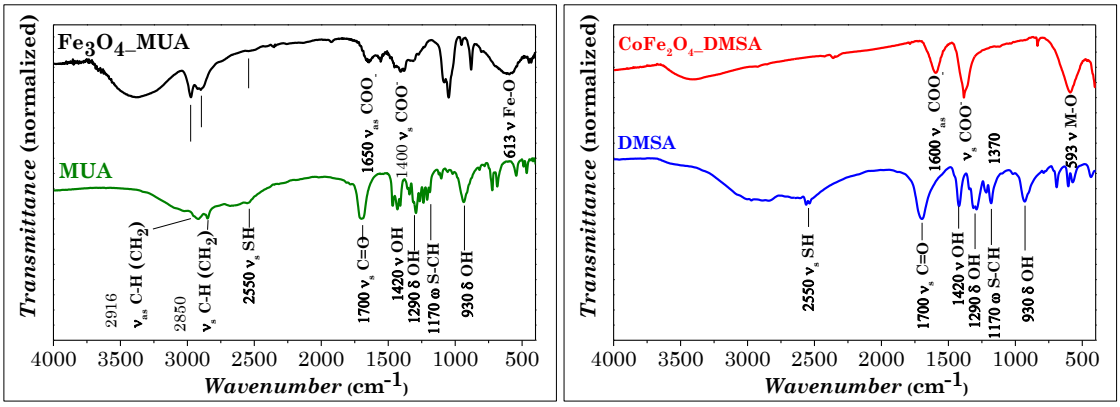

Figure 65. FTIR spectra of DMSA- and MUA-coated spinel ferrite NPs.

FT-IR spectra of pure MUA and DMSA reveal a series of adsorption bands typical for carboxylic acids (1420, 1290, and 1030 cm^{-1} for OH, 1700 cm^{-1} for C=O stretching modes) and the free thiol groups (2550 for S-H and 1290 cm^{-1} for S-CH modes). The bands related to the carbonyl groups are visible in the MUA- and DMSA- coated ferrite NPs (1650-1370 cm^{-1} region), as well as the metal-oxygen stretching mode at around 600 cm^{-1}. The thiol groups are not evident, probably due to the formation of disulfide bridges.[666] The absence of alkyl bands in Co_DMSA sample is an indication of the almost complete removal of oleate molecules, while the lack of COOH is because both carboxyl groups are linked to the surface.[666]

The corresponding silver-spinel ferrite heterostructures obtained from Fe_MUA and Co_DMSA as seeds, labelled Fe_MUA@Ag and Co_DMSA@Ag were analyzed through XRD and TEM. For both samples, XRD (Figure 62, on the right and Table 44) and TEM measurements (Figure 62, on the left) show the formation of large Ag_{FCC} crystals, only in Co_DMSA@Ag the size of ferrite NPs resulted increased. Besides the creation of separate phases due to homogeneous nucleation of silver, Co_DMSA@Ag also displays that some dimer heterostructures were successfully synthesized (Figure 62, left side). Nevertheless, the difficulties in favouring heterogeneous nucleation may be related to the not optimal dispersibility of the seeds NPs in ethanol, and the overgrowth of silver even with when eater is traces.

5.3.2 Silver-based heterostructures

Even though spinel ferrite-silver nanoheterostructures were obtained in some cases (Fe@Ag2 and Co_DMSA@Ag), to improve the homogeneity of the system, a second strategy was tested, starting from silver nanoparticles synthesised as described in paragraph 5.2.2.1. Silver oleate, insoluble in most organic solvents (as anticipated in paragraph 5.3.1), is soluble in oleic acid at 100 °C, and hence used as solvent, capping, and reducing agent.[663] Indeed, at high temperature (150-170 °C)[663] the pale-yellow solution became brown and then dark purple, due to the formation of NPs through thermal reduction of

silver oleate by oxidation of the double bond of oleic acid. The reaction must be conducted under inert atmosphere to prevent oxygen from oxidizing oleic acid. This green synthesis, (no organic solvents are employed) thanks to the high quantity of capping agent, allows to obtain very small NPs, as evidenced from XRD, TEM, and HRTEM measurements in Figure 66.

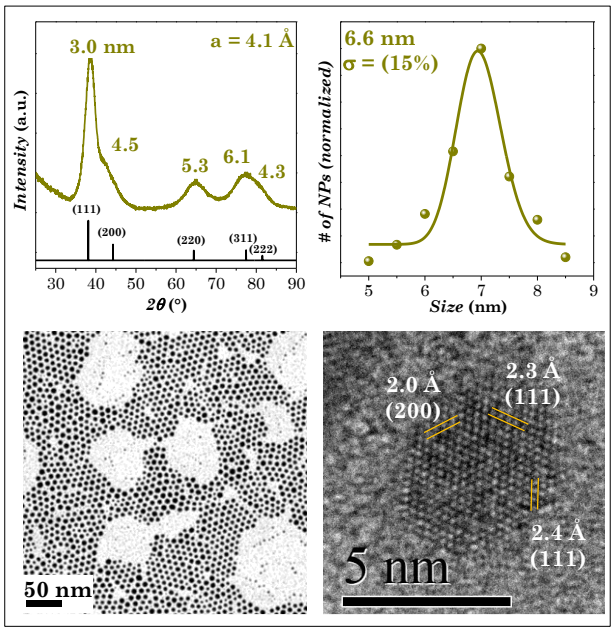

Figure 66. XRD, TEM, particle size distribution, and HRTEM of Ag NPs.

The crystallite and particle size of the sample were estimated around 3 nm and 7 nm, respectively. This discrepancy might be due to presence of stacking faults or anisotropic shaped nanoparticles. Indeed, peak broadness is not constant throughout the pattern with the (200) reflexes getting close to the (111) one. Nevertheless, the structure remains FCC (as also supported by HRTEM images), but determination of peak broadening and cell parameter is challenging. Silver-ferrite heterostructures were prepared starting from oleate-capped AgNPs as seeds and metal oleate (synthesized as described in paragraph 2.2.1) as ferrite precursor. Since both components are dispersible in the same media, the homogeneity of the synthesis should ensure an ideal starting condition for the synthesis. As first attempt, similar synthetic condition (solvents, amounts of seeds, temperature and time) of bimagnetic core-shell nanoparticles (chapter 3) were employed, starting from 25 mg of Ag NPs, 0.5 mmol of mixed Co-Fe oleate in a mixture of toluene, pentanol, and water, subjected to a solvothermal treatment at 220 °C for 10 hours (Ag@Co1). XRD and TEM analyses were carried out and the results are reported in Table 45, Figure 67, and Figure 68.

Table 45. Crystallite size, cell parameter, and quantitative analyses of silver-based heterostructures calculated by single peaks analysis and Rietveld refinement.

Sample	Phase	Single Peaks Analysis		Rietveld Refinement			
		$\langle D_{XRD} \rangle$ (nm)	a (Å)	$\langle D_{XRD} \rangle$ (nm)	Microstrain	a (Å)	Fraction (% w/w)
Ag@Co1	$CoFe_2O_4$	14(2)	8.40(1)	15(1)	$2 \cdot 10^{-3}$	8.399(2)	29
	Ag FCC	43(3)	4.09(1)	80(10)	$4 \cdot 10^{-5}$	4.089(2)	21
Ag@Co2	$CoFe_2O_4$	9(1)	8.39(1)	7(1)	$1 \cdot 10^{-3}$	8.400(2)	74
	Ag FCC	12(4)	4.08(1)	26(2)	$3 \cdot 10^{-3}$	4.083(2)	24
	AgCl	Micro	-	Micro	0	5.554(2)	2
Ag@Co3	$CoFe_2O_4$	6(1)	8.40(1)	6(1)	$8 \cdot 10^{-3}$	8.450(2)	48
	Ag FCC	5(1)	4.08(1)	15(1)	$6 \cdot 10^{-7}$	4.100(2)	52
Ag@Co4	$CoFe_2O_4$	6(1)	8.41(1)	10(1)	$1 \cdot 10^{-2}$	8.445(2)	34
	Ag FCC	7(1)	4.10(1)	9(1)	$7 \cdot 10^{-5}$	4.130(2)	66
Ag@Co5	$CoFe_2O_4$	8(3)	8.39(1)	6(1)	$2 \cdot 10^{-3}$	8.470(2)	25
	Ag FCC	6(1)	4.09(1)	22(2)	$6 \cdot 10^{-8}$	4.096(2)	75
Ag@Co6	$CoFe_2O_4$	8(2)	8.38(1)	9(1)	$5 \cdot 10^{-3}$	8.437(2)	30
	Ag FCC	9(1)	4.09(1)	24(2)	$7 \cdot 10^{-6}$	4.092(2)	70
Ag@Co7	$CoFe_2O_4$	9(2)	8.40(1)	11(1)	$6 \cdot 10^{-3}$	8.420(2)	34
	Ag FCC	10(2)	4.09(1)	29(2)	$4 \cdot 10^{-5}$	4.092(2)	66
Ag@Co8	$CoFe_2O_4$	10(2)	8.38(1)	10(1)	$3 \cdot 10^{-3}$	8.391(2)	42
	Ag FCC	26(3)	4.09(1)	80(10)	$1 \cdot 10^{-4}$	4.089(2)	58
Ag@Co9	$CoFe_2O_4$	7(1)	8.37(1)	6(1)	$7 \cdot 10^{-5}$	8.396(2)	41
	Ag FCC	>50	4.09(1)	>100	$3 \cdot 10^{-6}$	4.089(2)	59
Ag@Mn1	$MnFe_2O_4$	10(1)	8.43(1)	10(1)	$6 \cdot 10^{-3}$	8.445(2)	26
	Ag FCC	15(1)	4.04(1)	23(2)	$5 \cdot 10^{-5}$	4.092(2)	74
Ag@Fe1	$CoFe_2O_4$	7(1)	8.37(1)	10(1)	$2 \cdot 10^{-3}$	8.397(2)	32
	Ag FCC	9(2)	4.09(1)	20(2)	$1 \cdot 10^{-6}$	4.092(2)	68

XRD patterns (Figure 67) of Ag@Co1 show the formation of a spinel ferrite phase (14 nm) and the growth of silver seeds to form large NPs (from 7 nm up to 100 nm), as can also be seen from TEM images (Figure 68). In the second attempt (Ag@Co2), the temperature was decreased to 140 °C and water was removed from the solvent mixture, since it could influence the silver growth. The metal oleate hydrolysis to form ferrite NPs should be assured by the water present as impurity in the organic. The selected conditions led a sample, Ag@Co2, containing ferrite NPs having crystallite size of about 9 nm and Ag NPs of about 12 nm. XRD patterns reveals an impurity of silver chloride (around 2%) which is probably caused by the cleaning procedure of the teflon liner. Indeed, no chlorides were used in the synthesis, but since the reaction flasks and liners were washed with hydrochloric acid, causing the formation of AgCl and accidentally contaminating the final product. However, this is the only sample with high level of impurity (>1%).

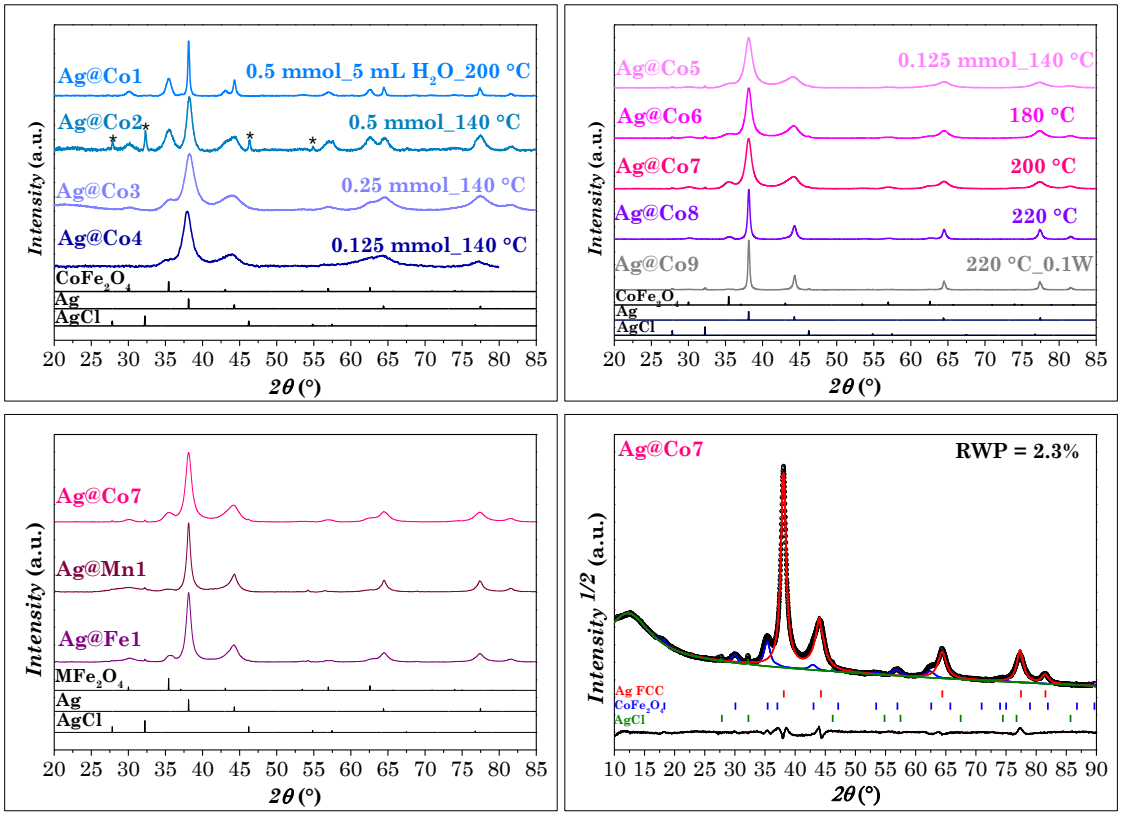

Figure 67. XRD patterns of silver-based heterostructures.

Rietveld refinement reveals that the sample is composed of around 24% w/w of silver and 74% of cobalt ferrite, close to the values obtained for Ag@Co1. TEM images (Figure 68), shows the obtainment of the flower-like silver-ferrite heterostructures featuring a dark silver core and small bright cobalt ferrite domains all around, although a fraction of isolated bare $CoFe_2O_4$ nanocrystals were formed.

To improve the homogeneity of the system, the quantity of Co-Fe oleate was progressively decreased from 0.5 to 0.25 and 0.125 mmol (Ag@Co2, Ag@Co3, and Ag@Co4, respectively), keeping the other parameters unchanged. XRD analysis shows that the crystallite sizes of the samples for both silver and spinel ferrite NPs did not change significantly, while the relative fraction of ferrite decreased from 74% w/w to 34%. The decrease in the content of cobalt ferrite NPs is evident also in TEM bright field images (Figure 68), where it is possible to observe the progressive reduction of the number of the cobalt ferrite NPs around the Ag cores, although some isolated ferrite NPs are still present.

Starting from Ag@Co4, a further step was the decrease of the reactants concentrations by increasing the solvent content (Table 43). The sample Ag@Co5 features similar crystallite size if compared with Ag@Co4, but TEM images reveal a further decrease in the number of free ferrite NPs in favour of more homogeneous silver-ferrite heterostructures. The NHs are made up of Ag core averaged surrounded by a dozen small ferrite crystallites.

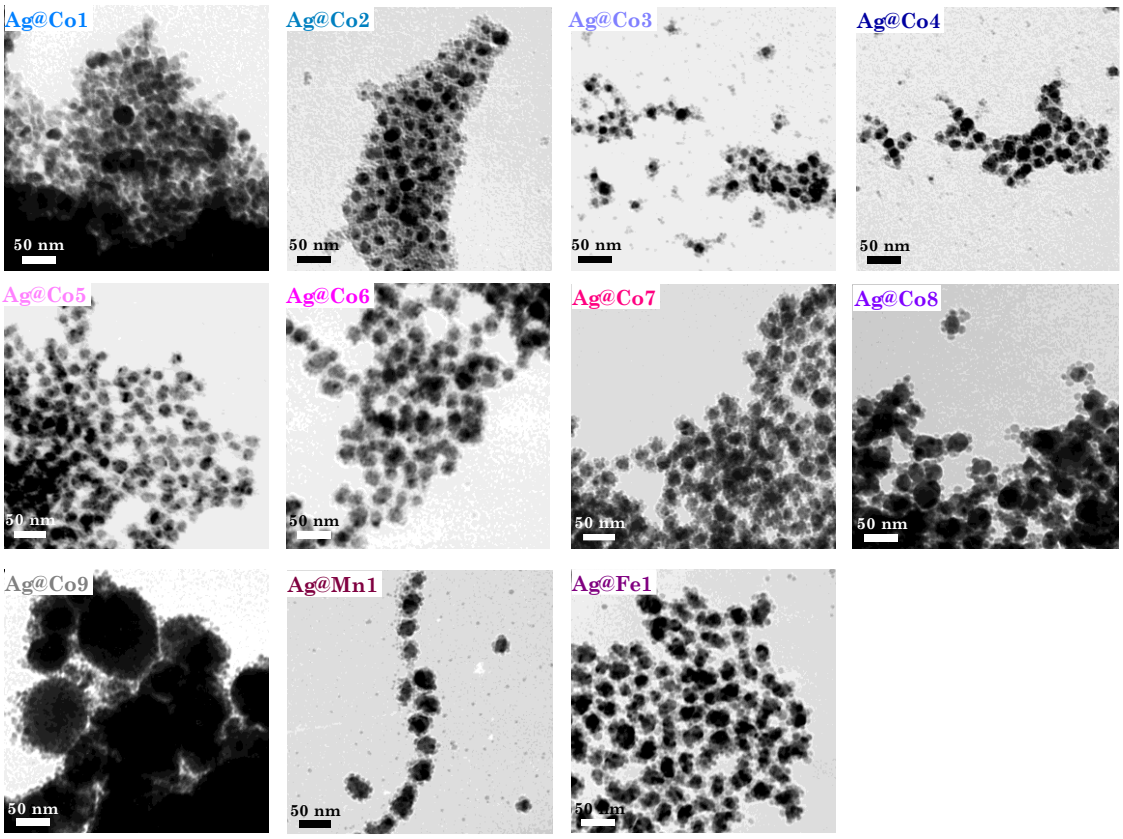

Figure 68. TEM bright field images of silver-based heterostructures

In this promising conditions, three more samples (Ag@Co6, Ag@Co7, and Ag@Co8) were prepared by increasing the reaction temperature to 180, 200, and 220 °C, respectively, to increase the spinel ferrite NPs size. The ferrite content gradually increased from 25% w/w for Ag@Co5 up to 42% for Ag@Co8. While the crystallite size of $CoFe_2O_4$ did not change appreciably (from 8 nm to 10 nm), silver crystallite size increased (from 6 nm to 26 nm), especially for Ag@Co8, synthesized at 220 °C (Table 45, Figure 68). TEM images exhibit a gradual reduction in the number of separate ferrite NPs up to the point of obtaining only silver-ferrite heterostructures (sample Ag@Co7), in which 15 nm Ag NPs are surrounded by around ten 5-6 nm $CoFe_2O_4$ NPs. The sample synthesized at 220 °C (Ag@Co8) instead shows Ag NPs of about 30 nm and 8-10 nm $CoFe_2O_4$ NPs, having overall higher size dispersity compared to the other samples.

A final attempt to further increase spinel ferrite size was made at 200 °C adding 0.1 mL of water (Ag@Co9). However, both XRD and TEM analyses reveal the obtainment of large silver particles (over 100 nm in size), surrounded by small ferrite NPs, which did not seem to be affected by the slight increase of the amount of water, contrary to silver. This is a confirmation of the detrimental effect of water on the silver NPs.

The most promising sample was Ag@Co7, prepared at 200 °C, and therefore the same conditions were adopted to prepare manganese ferrite- and spinel iron oxide-silver heterostructures, labelled Ag@Mn1 and Ag@Fe1,

respectively. XRD patterns of these three samples are very similar. Indeed, crystallite size of ferrite NPs are around 10 nm and 10-15 nm for Ag NPs. Spinel ferrite content is in the range 26-34% w/w, while cell parameters is higher for the manganese ferrite and lower for spinel iron oxide, as expected. Nonetheless, while Ag@Fe1 TEM images are similar to Ag@Co7, Ag@Mn1 shows different isolated ferrite NPs. HRTEM images of these three samples clearly show the architecture of the flower-like NHs (Figure 69). The interlayer distances in the small bright NPs confirm the presence of the spinel phase, while it is more difficult to ascribe the silver planes for the larger and darker NPs (Table 46).

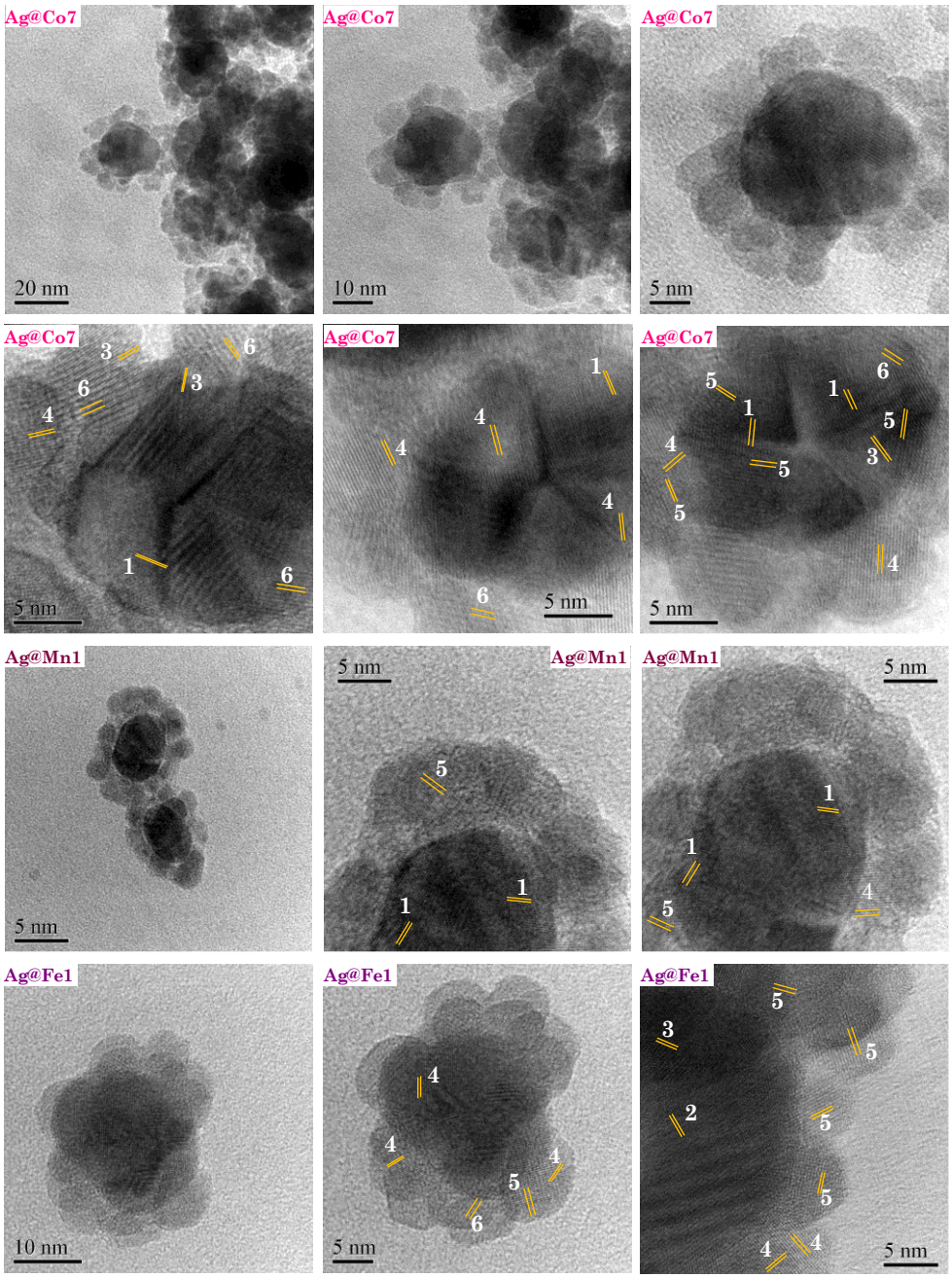

Figure 69. HRTEM images of the sample Ag@Co7 (top) and Ag@Mn1 (bottom).

Table 46. Interlayer distances and crystalline planes of HRTEM images of Figure 69.

Number	d (Å)	Phase	Structure	Miller indexes
1	2.3	Silver	FCC	111
2	2.0	Silver	FCC	200
3	2.1	Spinel ferrite	FCC	400
4	2.5	Spinel ferrite	FCC	311
5	2.9	Spinel ferrite	FCC	220
6	4.8	Spinel ferrite	FCC	111

These three samples (Ag@Co7, Ag@Mn1, and Ag@Fe1) were analysed through Vis absorption spectroscopy to study the optical properties and compared with the silver NPs (Figure 70).

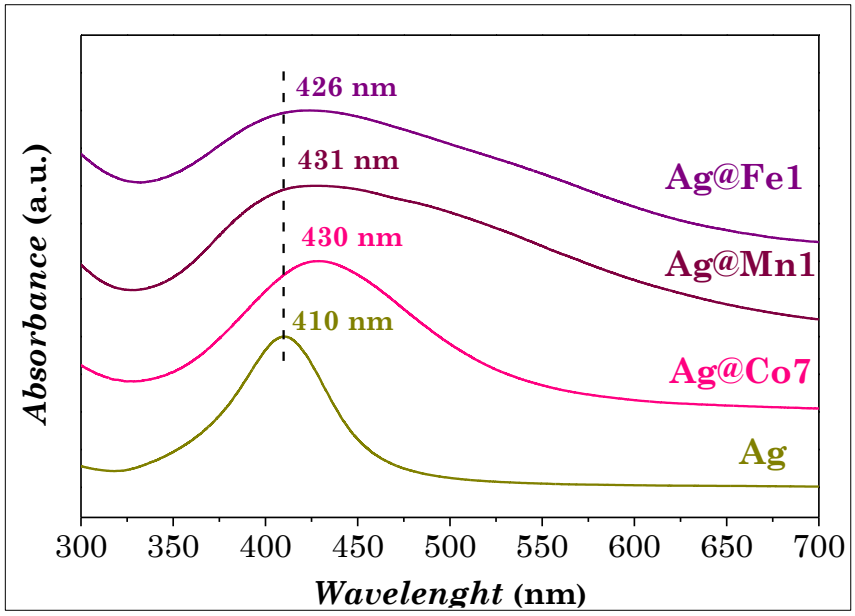

Figure 70. Vis spectra of silver NPs and silver-ferrite heterostructures.

Ag NPs used as seeds shows the presence of a sharp and well-defined plasmonic peak at about 410 nm, in line with other silver NPs of the same size.[477,663] In the ferrite-silver heterostructures, the peak is broader and shifted towards higher wavelengths (around 430 nm). The red-shift could be due to the increased size of Ag NPs, but both red-shift and the broadening of the plasmonic peak are features commonly observed in ferrite-silver heterostructures,[431,477] and can be related to the presence of the metal oxides in contact with the Ag domain. Since Ag NPs are very sensitive to the refractive index of their surroundings,[667] spinel ferrites can induce optical changes in the heterostructures, that increase as the silver surface is covered by the ferrite.

Ag@Co7 was measured with DC magnetometry (Figure 71), to study the magnetic properties of the spinel ferrite component of the heterostructure.

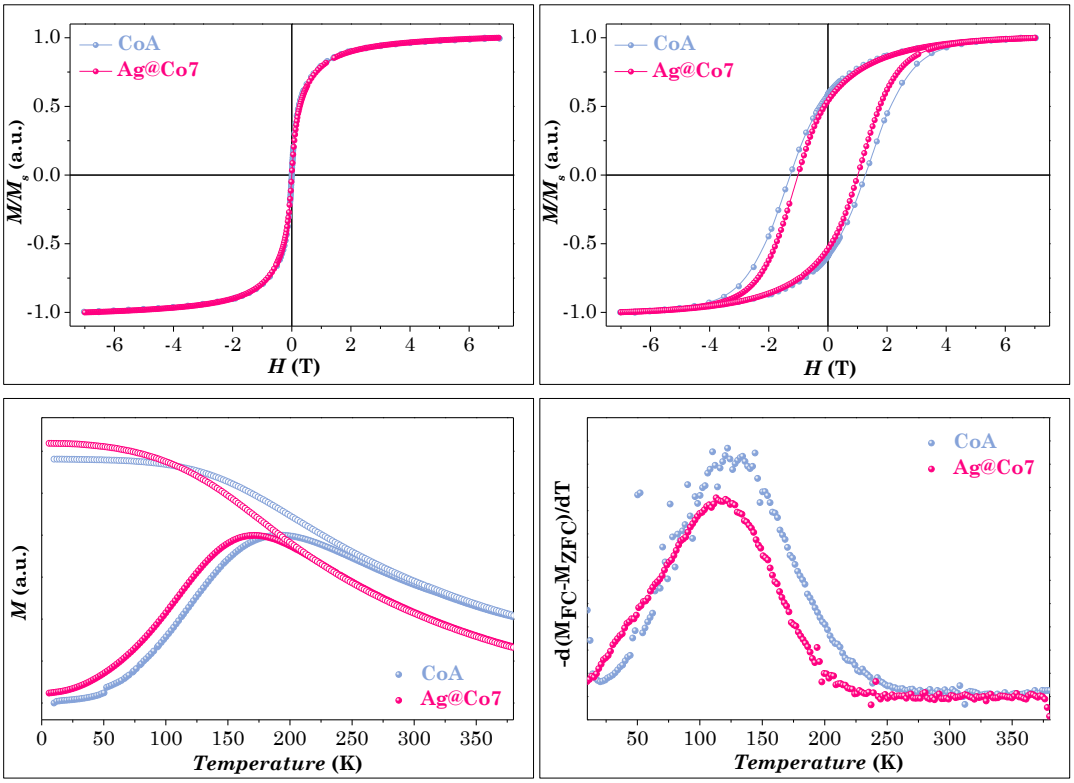

Figure 71. Magnetization isotherms at 300 K (top left) and 10 K (top right), ZFC (full circles) and FC (empty circles) curves recorded at low external magnetic field (10 mT) (bottom left), and anisotropy energy barrier distributions estimated by the first derivative $-d(M_{FC}-M_{ZFC})/dT$ (bottom right) of the samples Ag@Co7 and CoA.

The sample Ag@Co7 can be compared to the oleate-capped cobalt ferrite sample CoA, described in chapter 2, because of the same magnetic size (Table 47). The *M vs H* curves of both samples recorded at 300 K show no hysteresis, typical for NPs in the superparamagnetic state, and are superimposable. On the contrary, at 10 K the appearance of a large hysteresis occurs, characteristic of hard-magnetic behaviour of NPs in the blocked state. ZFC-FC curves of the two samples appear quite similar, as well as the energy barrier distributions. All the above findings suggest that the heterostructure retains the magnetic behaviour of cobalt ferrite, besides the optical properties of silver.

Table 47. Magnetic parameters of the sample Ag@Co7: maximum, difference, and blocking temperature (T_b). H_c^{10}, H_K^{10} (2%), M_s^{10}, M_r, and M_s^{300} correspond to the coercivity, anisotropy field, saturation and remanent magnetization values at 10 K and 300 K.

Sample	μ_m ($\mu_B \cdot 10^3$)	$\langle D_{MAG} \rangle$ (nm)	T_{max} (K)	T_{diff} (K)	T_b (K)	H_c^{10} (T)	H_K^{10} (T)	M_r/M_s
Ag@Co7	3.1	4.7	173	198	117	1.00	3.4	0.51
CoA	3.1	4.7	195	270	126	1.28	4.2	0.55

However, the samples show small differences in the magnetic parameters. Indeed, T_{max}, T_{diff}, T_b, H_c, H_K, M_r/M_s of CoA are slightly higher than those of Ag@Co7. These differences cannot be unequivocally ascribed to the formation of the heterostructure since the particles are not precisely the same of the CoA sample.

5.4 Conclusions

A seed-mediated growth approach in solvothermal conditions was developed for the synthesis of silver-spinel ferrite nanoheterostructures (NHs). Two main strategies were attempted starting from spinel ferrite or silver nanoparticles (NPs). Each strategy followed different pathways. Silver was grown on oleate-, DMSA-, or MUA-capped spinel ferrite seeds and using silver nitrate or silver oleate as Ag precursor. Spinel ferrites were grown on oleate-capped silver seeds employing as precursor metal oleates. The first strategy led to interesting results but had some drawbacks deriving from the different dispersibility of the magnetic seeds and of the precursors of the second phase that induced the formation of separate phases. To improve the homogeneity of the material, the second strategy provided ideal conditions for the dispersion of the silver seeds and the spinel ferrite precursor. Spinel ferrite NPs growth around the silver seeds creating flower-like shaped NHs, having silver core and a dozen of spinel ferrite petals around. The method was optimized to maximize the production of NHs over the separate phases. The optical properties of the heterostructures confirm the localized surface plasmon resonance effect and the comparison with the starting seeds allows to evidence the significant influence of the magnetic part on its properties. Magnetic properties of the NHs highlight the hard magnetic behaviour of $CoFe_2O_4$-Ag NHs and the comparison with a cobalt ferrite sample with the same magnetic size indicates that the silver part of the NHs does not influence much the magnetic behaviour of the NHs. Further studies will focus on the optimization of the method for the other spinel ferrites (manganese ferrite, maghemite/ magnetite) to render the comparison of the magnetic and optical properties for the three silver heterostructures possible and select the best candidate for applicative tests.

Conclusions and Perspectives

In this thesis, a solvothermal method was developed for the synthesis of bimagnetic spinel ferrite-based core-shell and silver-spinel ferrite flower-like nanoheterostructures (NHs).

Cobalt ferrite, manganese ferrite, and spinel iron oxide NPs of different sizes were firstly prepared with a solvothermal process, using *ex-situ* prepared metal oleates, in a mixture of organic solvents and water at various temperatures. The samples were characterized, with a multitechnique approach, from the compositional, structural, morphological, and magnetic point of view, by means of ICP-OES, XRD, TEM/HRTEM, FT-IR, TGA, RT and LT ^{57}Fe Mössbauer spectroscopy, XPS, and DC and AC Magnetometry. The size-dependence of the hyperthermic properties of aqueous colloidal dispersion of CTAB-coated cobalt ferrite were studied. The possibility of changing the toxic CTAB coating with the biocompatible PEG-TMS was tested, revealing the independence of the thermal response from the capping agent. Subsequently, one sample of manganese ferrite and three samples of cobalt ferrite were used as seeds for the growth of an isostructural shell of another spinel ferrite (seed-mediated growth). Direct proof of the core-shell structure formation was successfully provided by nanoscale chemical mapping, with the combined use of STEM-EELS, STEM-EDX, and STEM-EDX tomography. Magnetic coupling between hard and the soft phases, inducing unique magnetic properties, were exploited, for the cobalt ferrite core-based core shell NPs, for magnetic fluid hyperthermia applications. Despite the complex correlation between the samples' properties and their hyperthermic behaviour, it was highlighted that different parameters are involved in the heat release, such as saturation magnetization, magnetic anisotropy, NP and core size and shell thickness, Néel relaxation time, *etc.* Overall, it is evident that core-shell samples achieved higher efficiency with respect to the cores, and spinel iron oxide shells gave better performances than manganese ferrite ones. The magnetic coupling was studied and proved by DC and AC magnetic measurements. The core-shell architecture and the magnetic coupling were also demonstrated through an indirect comparison of the core-shell NHs with chemical and physical mixtures of cobalt and manganese ferrite, measured by ^{57}Fe Mössbauer spectroscopy and DC magnetometry. To summarise, some accomplishments are reported below:

1. Size-tuning of $CoFe_2O_4$ (5-17 nm), $MnFe_2O_4$ (7-12 nm), and Fe_3O_4/γ-Fe_2O_3 (8-14 nm) was achieved by varying synthetic parameters such as temperature, solvent polarity, and precursor concentration, or using a second solvothermal treatment in the presence (seed-mediated growth) or without additional metal oleate precursor.

2. The repeatability of the method was proved by preparing three replicas of CoE, MnC, and FeC, and analysing size and shape by XRD and TEM, giving similar results.
3. All samples but MnD (synthesized from MnC by seed-mediated growth) and FeE (synthesized from FeC by second solvothermal treatment without additional metal oleate precursor) have spinel structure, spherical shape, and low dispersity (σ = 10-17%), analysed by XRD and TEM.
4. All samples but MnE and FeE, (synthesized from MnC and FeC by second solvothermal treatment in the absence of further precursor) are capped by a monolayer of oleate molecules, verified by TGA and FT-IR analyses. On the contrary, MnE and FeE lost the capping agents during the second solvothermal treatment, that led to agglomeration of the particles and, in case of FeE, the formation of hematite.
5. RT ^{57}Fe Mössbauer spectroscopy allowed to assess the soft-magnetic behaviour of manganese ferrite and spinel iron oxide with respect to cobalt ferrite, which has lower critical blocking size, higher hyperfine field values that increase with increasing particle size following the CME model, higher coercive field and blocking temperature.
6. LT ^{57}Fe Mössbauer spectroscopy permitted to calculate the inversion degree, that correspond to 0.7 and 0.5 for $CoFe_2O_4$ and $MnFe_2O_4$ respectively, the absence of spin canting phenomena, and the partial oxidation of magnetite samples to maghemite.
7. XPS confirmed the inversion degree values of cobalt ferrite, as well as the stoichiometric Co:Fe ratio around 0.5 and the absence of Fe^{II} and Co^{III}.
8. Cobalt ferrite NPs, tested for magnetic fluid hyperthermia in aqueous colloidal dispersion after intercalation with CTAB, showed an improvement in the heating abilities up to 8 nm (CoC) and then a decrease, in line with the linear response theory. This results can be satisfactorily explained concerning size, anisotropy, and Néel relaxation times of the NPs, that dominates over the Brown one.
9. Magnetic fluid hyperthermia analyses on aqueous colloidal dispersion of cobalt ferrite after exchange ligand with PEG-TMS indicated the independence of the heat released from the organic coating and the possibility to use a biocompatible layer for applicative studies instead of the toxic CTAB.
10. Bimagnetic core-shell NPs were prepared *via* a seed-mediated growth method in solvothermal condition, covering MnC with spinel iron oxide or cobalt ferrite one, and CoA, CoB, and CoC with spinel iron oxide and manganese ferrite. In the case of CoC, core-shell nanoparticles with different shell thickness were prepared.

11. All core-shell NPs featured spinel structure, spherical shape, unimodal size distribution, high crystallinity with no evidences of defects, suggesting possible mismatching of the two spinel ferrites, larger size and lower dispersity than the cores, and are capped by a mono-layer of oleate molecules
12. STEM-EELS, STEM-EDX, and STEM-EDX tomography ascertained the formation of the core-shell architecture, obtaining chemical maps with sub-nanometer spatial resolution.
13. ^{57}Fe Mössbauer spectroscopy and DC magnetometry proved the magnetic coupling between the hard and the soft phase, due to the increase of hyperfine field values, magnetic diameter, blocking temperature, saturation magnetization, and the decrease of coercivity.
14. Cobalt ferrite core-based core-shell NPs tested as heat mediators for magnetic fluid hyperthermia showed better performances than the cores, with higher efficiency of the spinel iron oxide coated ones.
15. Chemical mixed cobalt-manganese ferrite were prepared *via* the same oleate-method, with manganese content in the range 0.13-0.65, crystallite size about 8-9 nm, spherical shape, and low dispersity (13-16%)
16. Hyperfine field values of both octahedral and tetrahedral sites increased with the cobalt content, in line with CME theory, as well as coercive field, anisotropy field, and blocking temperature.
17. The comparison of the RT ^{57}Fe Mössbauer spectra and DC magnetic measurements among chemical mixtures, physical mixtures of manganese and cobalt ferrite, and core-shell systems resulted to be an efficient tool on discriminating magnetic coupling through an indirect multitechnique approach between the hard and soft phases and therefore the heterostructure formation.

Despite all the above achievements, this work also opens to future perspectives. In particular, the complexity of the core-shell systems did not permit by the multitechnique characterisation described so far to ascertain the exact correlation between the chemical-physical properties and the heating abilities and some aspects need further investigation. For instance, additional magnetic measurements, through DC protocols such as IRM (isothermal remanent magnetization), DCD (direct current demagnetization), and Henkel plot, may be useful for the understanding of magnetic interparticle interactions that probably play a role in determining the better performances of the CoX@Fe systems. SAXS (small-angle X-ray scattering) and SANS (small-angle neutron scattering) are currently being performed to confirm the size (particle size, shell thickness) of the core-shell samples, being neutrons able to distinguish among the different ion type.

Regarding the second topic of the thesis, the oleate-based solvothermal method was also exploited for the synthesis of silver-spinel ferrite nanoheterostructures, starting from both silver and spinel ferrite NPs seeds (seed-mediated growth). Flower-like NHs having silver core and cobalt ferrite, manganese ferrite, or spinel iron oxide petals were successfully prepared using small silver NPs as germs. In details:

1. The synthesis with oleate-capped cobalt ferrite NPs using silver nitrate as Ag precursor, led to the production of Ag_{FCC} separately to cobalt ferrite, with no presence of heterostructure, while when silver oleate was used as Ag precursor, a mixture of Ag_{FCC} and Ag_{HCP} was obtained, together with some heterostructure having cobalt ferrite core and few small Ag_{FCC} domains on the surface.

   The synthesis with MUA-capped spinel iron oxide and DMSA-capped cobalt ferrite NPs using silver nitrate as Ag precursor led to the production of micrometric silver, while in the reaction with the DMSA-capped ferrites dimeric cobalt ferrite-silver nanoheterostructures were obtained also. The main drawback with these syntheses was ascribed to the mixtures of solvents which were unable to disperse both the seeds and the second phase precursor.
2. Silver-spinel ferrite nanoheterostructures were obtained from 5 nm Ag NPs, synthesized by thermal reduction of silver oleate in oleic acid, and metal oleates as spinel ferrite precursors (cobalt ferrite, manganese ferrite, maghemite/magnetite). The proper choice of the amounts of the seeds and the precursor of the second phase led to silver-cobalt ferrite NHs featured heterostructures with flower-like shape, having very low percentage of separate phases. In the case of silver-manganese ferrite and silver-spinel iron oxide NHs, a small amount of unbound ferrite NPs is observable. UV-Vis e DC Magnetometry show that both the optical and the magnetic properties of the individual system are well-retained in the silver-cobalt ferrite sample.

In this framework, prospects are countless. The first strategy, leading to inhomogeneous samples but interesting dimeric or oligomeric nanoheterostructures, deserves further studies and attempts. Moreover, magnetoplasmonic properties of the flower-like NHs should be further investigated studying the magnetization while the sample is illuminated with a specific wavelength or *vice-versa*, *e.g.* exploiting the Faraday or Kerr effects.[668–671] Finally, these systems may be tested as SERS-substrates, catalysts, or for combined photothermal-magnetic heating, exploiting the optical and magnetic properties of silver and spinel ferrites, respectively.

Materials and Methods

Oleic acid (>99.99%), 1-pentanol (99.89%), hexane (84.67%) and toluene (99.26%) were purchased from Lach-Ner; 1-octanol (>99.99%), 11-Mercaptoundecanoic acid (95%), $Mn(NO_3)_2 \cdot 4H_2O$ (>97.0%), acetic acid (≥99.7%), chloroform (stabilized with 1% of ethanol), dimethyil sulfoxide (≥99.5%) hexadecyltrimethylammonium bromide (CTAB, ≥98%), meso-2,3-dimercaptosuccinic acid (98%), oleylamine (≥98%), and silver nitrate (≥99%) from Sigma-Aldrich; absolute ethanol and $Co(NO_3)_2 \cdot 6H_2O$ (99.0%) from Penta; NaOH (>98.0%) from Fluka; $Fe(NO_3)_3 \cdot 9H_2O$ (98.0%) from Lachema; $FeCl_2 \cdot 4H_2O$ (99%) from Merck; Poly Ethylene Glycol Trimethoxysilane (PEG-TMS) from ABCR GmbH&Co.

Inductively Coupled Plasma – Atomic Emission Spectroscopy (ICP-OES)

The chemical composition was studied by Inductively Coupled Plasma - Atomic Emission Spectrometry (ICP-OES), at the Department of Chemical and Geological Science, University of Cagliari. The dried samples were digested by using HNO_3. The digested sample solutions were stirred at room temperature for one h, then heated up to ~50 °C for two h. The solutions were allowed to cool down, filtered and diluted by using 1% v/v HNO_3 solution. The ICP measurements were performed on a Liberty 200 ICP Varian spectrometer under the following conditions: Fe line: 259.940 nm, Co line: 238.892 nm, Mn line: 257.610 nm; Fe, Co and Mn concentration range: (0.1÷1.5) ppm; Fe detection range: (0.015÷750) ppm, Co detection range: (0.050÷2500) ppm, Mn detection range: (0.003÷150) ppm. The analyses were performed twice on different portions of the samples. The chemical formulas were calculated by assuming the absence of anions vacancies.

Powder X-ray Diffraction (XRD)

The samples were characterized by X-ray Diffraction (XRD), using a PANalytical X'Pert PRO with Cu *Ka* radiation (1.5418Å), secondary monochromator and PIXcel position sensitive detector, at the Department of Inorganic Chemistry, Charles University of Prague. Calibration of peak position and instrumental width was done using powder LaB_6 from NIST. The analyses of the XRD patterns (identification of the crystalline phase, background subtraction) were done by the PANalytical X'Pert HighScore software. The most intense X-ray peaks were fitted with Origin Software by PseudoVoigt function, using a 1:1 gaussian:lorentzian ratio ($m_u = 0.5$):

$$y = y_0 + A\left[m_u \frac{2}{\pi}\frac{w}{4(x-x_c)^2+w^2} + (1-m_u)\frac{\sqrt{4\,ln\,2}}{\sqrt{\pi}w}e^{-\frac{4\,ln\,2}{w^2}(x-x_c)^2}\right] \quad \textbf{Eq. 51}$$

In reciprocal space

$$q = \frac{2sin\theta}{\lambda} = \frac{\sqrt{h^2+k^2+l^2}}{a} \quad \textbf{Eq. 52}$$

The crystallite size (diameter) was obtained from full width at half maximum of q (denoted as Γ_q) by

$$d = \frac{1.10}{\Gamma_q}561 \quad \textbf{Eq. 53}$$

Cell parameters (a), for ferrite NPs, have been calculated by using the following formula:

$$a = \frac{\lambda}{2sin\theta}\sqrt{h^2+k^2+l^2} \quad \textbf{Eq. 54}$$

Where λ is the wavelength of the X-ray source, θ the angle of incidence, and hkl the Miller's indexes.

Refinement of the structural parameters[672] was performed by the Rietveld method using the MAUD software[673] adopting the recommended fitting procedures.[674] CIF structures used for the refinement are reported in the following table

Table 48. Structures employed for Rietveld refinement.

Formula	Structure	Space group	COD ID	Ref.
$CoFe_2O_4$	FCC	Fd-3m:2	1533163	[672]
$MnFe_2O_4$	FCC	Fd-3m:1	2300585	[675]
Fe_3O_4	FCC	Fd-3m:1	1010369	[676]
Ag	FCC	Fm-3m	1100136	[677]
Ag	HCP	P63/mmc	1509145	[677]
AgCl	FCC	Fm-3m	9011666	[678]

Transmission Electron Microscopy (TEM)

TEM images were obtained by using a JEOL 200CX operating at 160 kV, at the Department of Chemical and Geological Science, University of Cagliari. The particle size distribution was obtained by measuring in the automatic mode over 1000 particles with the aid of the software Pebbles, setting spherical shape for the elaboration.[679] The mean particle diameter was calculated as the average value and the dispersity as the percent ratio between the standard deviation and the average value.

High-Resolution Transmission Electron Microscopy (HRTEM)

HRTEM images were carried out by using JEOL JEM 2010 UHR equipped with a Gatan imaging filter (GIF) and a 794-slow scan CCD camera, at the Centro Servizi di Ateneo per la Ricerca (CeSAR), University of Cagliari.

Energy-Dispersive X-ray Spectroscopy (STEM-EDX)

EDX measurements were carried out in the STEM mode using a FEI Talos F200X with a field-emission gun operating at 200 kV equipped with a four-quadrant 0.9-sr energy dispersive X-ray spectrometer, at the Center for Functional Nanomaterials, Brookhaven National Laboratory. 3D tomography was acquired in STEM-EDX mode with tilt series from −70° to 70° and 10° intervals. The single line profiles have been calculated using the Matlab command "improfile" for different sections all over a particle (*i.e.* over 360° with a step of 0.1 and the results averaged.

Electron Energy Loss Spectroscopy (STEM-EELS)

EELS and HRSTEM measurements were carried out using an aberration-corrected scanning transmission electron microscope (Hitachi HD2700C) with a cold field emission gun operating at 200 kV equipped with a parallel EELS spectrometer (high resolution Enfina).

Fourier Transform – Infrared Spectroscopy (FT-IR)

Transform Infrared Spectroscopy (FT-IR) spectra were recorded in the region from 350 to 4000 cm^{-1} by using a Bruker Vertex 70 spectrophotometer on the colloidal dispersions using a Platinum ATR Unit A 225, (standard ATR crystal material: diamond), at the Consorzio Promozione Attività Universitarie Sulcis-Iglesiente (Consorzio AUSI).

Thermogravimetric Analysis (TGA)

TGA curves were obtained on powders by using a Mettler-Toledo TGA/SDTA 851, at the Department of Chemical and Geological Science, University of Cagliari, in the 25-1000 °C range, with a heating rate of 10 °C/min under 50 mL/min O_2 flow.

^{57}Fe Mössbauer Spectroscopy

Room temperature ^{57}Fe Mössbauer spectroscopy was performed on a Wissel spectrometer using transmission arrangement and proportional detector

LND-45431, at the Department of Inorganic Chemistry, Charles University of Prague. A α-Fe foil was used as a standard, and fitting procedure was done by NORMOS program to determine the isomer shift, quadrupole splitting, hyperfine field and full width at half maximum of the signals. The in-field measurements were done with a perpendicular arrangement of the external magnetic field with respect to the γ-beam (Figure 72) and are useful to gather information about the cationic distribution and the canting phenomena in the spinel structure.

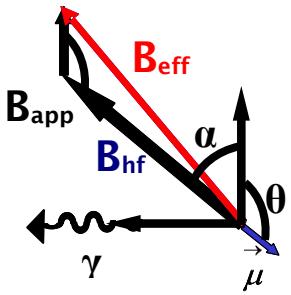

Figure 72. Arrangement of the magnetic field with the γ-beam.

Indeed, the angle θ between the magnetic moment ($\vec{\mu}$) and the applied magnetic field have been estimated thanks to the following equation:

$$B_{eff}^2 = B_{hf}^2 + B_{app}^2 - 2B_{hf}B_{app}cos\theta \qquad \text{Eq. 55}$$

Where B_{hf} is the hyperfine field (B_{hf}^{0T}), B_{eff} the total effective magnetic field at the nucleus (B_{hf}^{6T}), B_{app} the external applied magnetic field and α is the angle between B_{eff} and B_{app}.

The angle θ corresponds to the canting angle of the magnetic moment for the octahedral sites, whereas for the tetrahedral ones the canting angle is equal to π-θ. This is caused by the relative arrangement of the hyperfine and applied fields vectors that are parallel or antiparallel aligned for tetrahedral or octahedral sites, respectively.[680]

X-ray Photoelectron Spectroscopy (XPS)

XPS measurements were acquired using a Sigma2 spectrometer manufactured by Thermo Fischer Scientific Inc, in collaboration with the group of surface, electrochemical, and corrosion analysis of the University of Cagliari and ETH Zurich (Prof. A. Rossi and Dr. M. Fantauzzi). The spectrometer is equipped with an Al/Mg *Ka* twin anode source. A non-monochromatic Mg *Ka* source (1253.6 eV) operated at 200 W was used to acquire the spectra to eliminate the overlap between Fe 2p and Co Auger signal. The emitted electrons were collected by the Alpha 110 hemispherical analyser and a multichannel detector consisting of seven channeltrons was

used. The analyser operated in fixed analyser transmission mode, setting the pass energy at 25 eV with step size 0.05 eV and at 50 eV with step size of 1 eV to collect high-resolution and survey spectra, respectively. The full width at half maximum of the peak Ag $3d_{5/2}$ was 1.13 eV for Mg *Ka* and 1.28 eV for Al *Ka*. The instrument was used in large-area mode. All spectra were processed by using CasaXPS 2.3.19.

Magnetometry

The magnetic property measurements were carried out by using a SQUID magnetometer (MPMS7XL, Quantum Design) at the Cryogenics Laboratory, Charles University of Prague. The temperature dependencies of magnetization, (*M vs T*) in the zero-field cooled (ZFC) and the field cooled (FC) regime were measured as follows: first, the sample was cooled down to 10 K in the zero external magnetic field. Then, a field of 10 mT was applied, and the dependence of magnetization on temperature was measured up to 380 K. Afterwards, the sample was cooled down in the applied field of 10 mT, and the dependence of magnetization on temperature was measured again. The magnetization isotherms (*M vs H* curves) were recorded up to 7 T at selected temperatures in both the polarities of the applied magnetic field. All magnetic parameters were corrected according to the organic content. *M vs H* curves at 300 K were analysed by using MINORIM software to estimate the magnetic size ($<D_{MAG}>$).[641] Saturation magnetization (M_s) has been estimated by using the following formula:[599]

$$M = M_s\left(1 - \frac{a}{H} - \frac{b}{H^2}\right) \qquad \textbf{Eq. 56}$$

Where H is the magnetic field.

Dynamic Light Scattering (DLS)

Dynamic light scattering (DLS) measurements were performed on water colloidal dispersions at the same concentration used for the calorimetric measurements by means of a Malvern Instrument Zeta Zetasizer Ver 7.03 equipped with a He-Ne laser (λ = 633 nm, max 5 mW) and operated at a scattering angle of 173°, at the Department of Chemical and Geological Science, University of Cagliari. All measurements were performed using a refraction index value of 2.42 for the material and of 1.330 for the dispersant. In all analyses, 1 mL of particle suspensions was placed in a 12 mm × 12 mm polystyrene cuvette.

Specific Absorption Rate Measurements (SAR)

Calorimetric measurements of SAR were carried out utilizing a non-adiabatic experimental set-up built at the LAboratorio di Magnetismo Molecolare (LA.M.M), University of Florence, employing a power supply CELESs MP6/400 (FIVES CELES), a water-cooled heating station connected to the power supply and an induction coil. Heating curves were recorded under a magnetic field of 17 kA/m and 183 kHz for 300s on aqueous colloidal dispersions of the magnetic nanoparticles. The concentration of the colloidal dispersion was 3.4 mg/mL for all the samples. The temperature of the sample was monitored with an optical fibre probe (OPTOCON-FOTEMP) dipped into the solution. The samples were wrapped in polystyrene and placed in a glass Dewar, equipped by an ethylene glycol thermostat, to ensure the proper thermal isolation. The Specific Adsorption Rate (SAR), *i.e.* the thermal power per mass unit, values were estimated with a linear curve fitting in the first 20s of the heating curves (initial slope method, Eq. 38).

List of Publications

Some of the results presented in the thesis have been published in peer-reviewed journals:

1. Sanna Angotzi, M.; Musinu, A.; Mameli, V.; Ardu, A.; Cara, C.; Niznansky, D.; Xin, H. L.; Cannas, C. Spinel Ferrite Core–Shell Nanostructures by a Versatile Solvothermal Seed-Mediated Growth Approach and Study of Their Nanointerfaces. *ACS Nano* **2017**, *11* (8), 7889–7900. DOI: 10.1021/acsnano.7b02349
2. Cara, C.; Rombi, E.; Musinu, A.; Mameli, V.; Ardu, A.; Sanna Angotzi, M.; Atzori, L.; Niznansky, D.; Xin, H. L.; Cannas, C. MCM-41 Support for Ultrasmall γ-Fe_2O_3 Nanoparticles for H_2S Removal. *J. Mater. Chem. A* **2017**, *5* (41), 21688–21698. DOI: 10.1039/C7TA03652C
   Contribution: STEM-EDX and ^{57}Fe Mössbauer characterization of samples.
3. Cara, C.; Rombi, E.; Mameli, V.; Ardu, A.; Sanna Angotzi, M.; Niznansky, D.; Musinu, A.; Cannas, C. γ-Fe_2O_3-M41S Sorbents for H_2S Removal: Effect of Different Porous Structures and Silica Wall Thickness. *J. Phys. Chem. C* **2018**, *122* (23), 12231–12242. DOI: 10.1021/acs.jpcc.8b01487
   Contribution: ^{57}Fe Mössbauer characterization of samples.
4. Mameli, V.[§]; Sanna Angotzi, M. [§]; Cara, C.; Cannas, C. Liquid Phase Synthesis of Nanostructured Spinel Ferrites – A Review. *J. Nanosci. Nanotechnol.* Accepted on 18/07/2018 for publication in a special issue entitled "Nanostructured spinel ferrites: synthesis, characterization, properties and applications". DOI: 10.1166/jnn.2019.16808
   [§]These authors contributed equally to the work.
5. Sanna Angotzi, M.; Mameli, V.; Musinu, A.; Niznansky, D. ^{57}Fe Mössbauer Spectroscopy for the Study of Nanostructured Mixed Mn-Co Spinel Ferrites. *J. Nanosci. Nanotechnol.* Accepted on 27/08/2018 for publication in a special issue entitled "Nanostructured spinel ferrites: synthesis, characterization, properties and applications". DOI: 10.1166/jnn.2019.16793
6. Sanna Angotzi, M.; Mameli V.; Cara C.; Ardu A.; Niznansky D.; Musinu A. Oleate-Based Solvothermal Approach for Size Control of $M^{II}Fe^{III}_2O_4$ (M^{II} = Mn^{II}, Fe^{II}) Colloidal Nanoparticles. *J. Nanosci. Nanotechnol.* Accepted on 15/11/2018 for publication in a special issue entitled "Nanostructured spinel ferrites: synthesis, characterization, properties and applications". DOI: 10.1166/jnn.2019.16785

7. Fantauzzi M.; Secci F.; Sanna Angotzi M.; Cannas C.; Rossi A. Exploiting XPS for characterization of nanostructured spinel cobalt ferrites. Submitted.
   Contribution: synthesis of samples, tuning of the crystallite size and XRD characterization.
8. Sanna Angotzi M.; Musinu A.; Mameli V.; Sangregorio C.; Niznansky D.; Xin H. L.; Vejpravova J.; Cannas C. Heat release from water dispersions of bimagnetic core-shell spinel ferrite nanoparticles, In Preparation.
9. Sanna Angotzi M.; Musinu A.; Mameli V.; Ardu A., Cara C., Niznansky D., Cannas C. Solvothermal Approach for the Synthesis of Flower-Like Silver-Spinel Ferrite Nanoheterostructures, In Preparation.

Bibliography

(1) West, A. R. *Solid State Chemistry and Its Applications.*; Sons, J. W. &, Inc., Eds.; 1984.

(2) Krishnan, K. M. Biomedical Nanomagnetics: A Spin Through Possibilities in Imaging, Diagnostics, and Therapy. *IEEE Trans. Magn.* **2010**, *46* (7), 2523–2558.

(3) Laurent, S.; Forge, D.; Port, M.; Roch, A.; Robic, C.; Vander Elst, L.; Muller, R. N. Magnetic Iron Oxide Nanoparticles: Synthesis, Stabilization, Vectorization, Physicochemical Characterizations, and Biological Applications. *Chem. Rev.* **2008**, *108* (6), 2064–2110.

(4) Koh, I.; Josephson, L. Magnetic Nanoparticle Sensors. *Sensors* **2009**, *9* (10), 8130–8145.

(5) Sun, S.-N.; Wei, C.; Zhu, Z.-Z.; Hou, Y.-L.; Venkatraman, S. S.; Xu, Z.-C. Magnetic Iron Oxide Nanoparticles: Synthesis and Surface Coating Techniques for Biomedical Applications. *Chinese Phys. B* **2014**, *23* (3), 037503.

(6) Lima-Tenório, M. K.; Gómez Pineda, E. A.; Ahmad, N. M.; Fessi, H.; Elaissari, A. Magnetic Nanoparticles: In Vivo Cancer Diagnosis and Therapy. *Int. J. Pharm.* **2015**, *493* (1–2), 313–327.

(7) Joshi, H. M.; Lin, Y. P.; Aslam, M.; Prasad, P. V.; Schultz-Sikma, E. a.; Edelman, R.; Meade, T.; Dravid, V. P. Effects of Shape and Size of Cobalt Ferrite Nanostructures on Their MRI Contrast and Thermal Activation. *J. Phys. Chem. C* **2009**, *113* (41), 17761–17767.

(8) Hergt, R.; Dutz, S.; Müller, R.; Zeisberger, M. Magnetic Particle Hyperthermia: Nanoparticle Magnetism and Materials Development for Cancer Therapy. *J. Phys. Condens. Matter* **2006**, *18* (38), S2919–S2934.

(9) Liu, T. Y.; Hu, S. H.; Liu, D. M.; Chen, S. Y.; Chen, I. W. Biomedical Nanoparticle Carriers with Combined Thermal and Magnetic Responses. *Nano Today* **2009**, *4* (1), 52–65.

(10) Fortin, J. P.; Wilhelm, C.; Servais, J.; Ménager, C.; Bacri, J. C.; Gazeau, F. Size-Sorted Anionic Iron Oxide Nanomagnets as Colloidal Mediators for Magnetic Hyperthermia. *J. Am. Chem. Soc.* **2007**, *129* (9), 2628–2635.

(11) Roca, A. G.; Costo, R.; Rebolledo, A. F.; Veintemillas-Verdaguer, S.; Tartaj, P.; González-Carreño, T.; Morales, M. P.; Serna, C. J. Progress in the Preparation of Magnetic Nanoparticles for Applications in Biomedicine. *J. Phys. D. Appl. Phys.* **2009**, *42* (22), 224002.

(12) Di Corato, R.; Quarta, A.; Piacenza, P.; Ragusa, A.; Figuerola, A.; Buonsanti, R.; Cingolani, R.; Manna, L.; Pellegrino, T. Water Solubilization of Hydrophobic Nanocrystals by Means of Poly(Maleic Anhydride-Alt-1-Octadecene). *J. Mater. Chem.* **2008**, *18* (17), 1991.

(13) Guardia, P.; Riedinger, A.; Nitti, S.; Pugliese, G.; Marras, S.; Genovese, A.; Materia, M. E.; Lefevre, C.; Manna, L.; Pellegrino, T. One Pot Synthesis of Monodisperse Water Soluble Iron Oxide Nanocrystals with High Values of the Specific Absorption Rate: ESI. *J. Mater. Chem. B* **2014**, *2* (28), 4426.

(14) Al, L. E. E. E. T. Magnetic Nanoparticles for Ultrafast Mechanical Control of Inner Ear Hair Cells. **2014**, No. 7, 6590–6598.

(15) Covaliu, C. I.; Jitaru, I.; Paraschiv, G.; Vasile, E.; Biriş, S. Ş.; Diamandescu, L.; Ionita, V.; Iovu, H. Core-Shell Hybrid Nanomaterials Based on CoFe2O4 Particles Coated with PVP or PEG Biopolymers for Applications in Biomedicine. *Powder Technol.* **2013**, *237*, 415–426.

(16) Sperling, R. A.; Pellegrino, T.; Li, J. K.; Chang, W. H.; Parak, W. J. Electrophoretic Separation of Nanoparticles with a Discrete Number of Functional Groups. *Adv. Funct. Mater.* **2006**, *16* (7), 943–948.

(17) De Palma, R.; Peeters, S.; Van Bael, M. J.; Van den Rul, H.; Bonroy, K.; Laureyn, W.; Mullens, J.; Borghs, G.; Maes, G. Silane Ligand Exchange to Make Hydrophobic Superparamagnetic Nanoparticles Water-Dispersible. *Chem. Mater.* **2007**, *19* (7), 1821–1831.

(18) Guardia, P.; Di Corato, R.; Lartigue, L.; Wilhelm, C.; Espinosa, A.; Garcia-Hernandez, M.; Gazeau, F.; Manna, L.; Pellegrino, T. Water-Soluble Iron Oxide Nanocubes with High Values of Specific Absorption Rate for Cancer Cell Hyperthermia Treatment. *ACS Nano* **2012**, *6* (4), 3080–3091.

(19) Magnacca, G.; Allera, A.; Montoneri, E.; Celi, L.; Benito, D. E.; Gagliardi, L. G.; Gonzalez, M. C.; Mártire, D. O.; Carlos, L. Novel Magnetite Nanoparticles Coated with Waste-Sourced Biobased Substances as Sustainable and Renewable Adsorbing Materials. *ACS Sustain. Chem. Eng.* **2014**, *2* (6), 1518–1524.

(20) Chandra, V.; Park, J.; Chun, Y.; Lee, J. W.; Hwang, I. C.; Kim, K. S. Water-Dispersible Magnetite-Reduced Graphene Oxide Composites for Arsenic Removal. *ACS Nano* **2010**, *4* (7), 3979–3986.

(21) Ali, I. New Generation Adsorbents for Water Treatment. *Chem. Rev.* **2012**, *112* (10), 5073–5091.

(22) Singh, S.; Yadav, B. C.; Prakash, R.; Bajaj, B.; Lee, J. R. Synthesis of Nanorods and Mixed Shaped Copper Ferrite and Their Applications as Liquefied Petroleum Gas Sensor. *Appl. Surf.*

Sci. **2011**, *257* (24), 10763–10770.
(23) Satyanarayana, L.; Reddy, K. M.; Manorama, S. V. Nanosized Spinel NiFe2O4: A Novel Material for the Detection of Liquefied Petroleum Gas in Air. *Mater. Chem. Phys.* **2003**, *82* (1), 21–26.
(24) Darshane, S. L.; Suryavanshi, S. S.; Mulla, I. S. Nanostructured Nickel Ferrite: A Liquid Petroleum Gas Sensor. *Ceram. Int.* **2009**, *35* (5), 1793–1797.
(25) Kamble, R. B.; Mathe, V. L. Nanocrystalline Nickel Ferrite Thick Film as an Efficient Gas Sensor at Room Temperature. *Sensors Actuators, B Chem.* **2008**, *131* (1), 205–209.
(26) Wang, Z.; Liu, X.; Lv, M.; Chai, P.; Liu, Y.; Meng, J. Preparation of Ferrite MFe 2 O 4 (M) Co , Ni) Ribbons with Nanoporous Structure and Their Magnetic Properties. *J. Phys. Chem. B* **2008**, *4* (3), 11292–11297.
(27) Ghoshal, T.; Maity, T.; Senthamaraikannan, R.; Shaw, M. T.; Carolan, P.; Holmes, J. D.; Roy, S.; Morris, M. a. Size and Space Controlled Hexagonal Arrays of Superparamagnetic Iron Oxide Nanodots: Magnetic Studies and Application. *Sci. Rep.* **2013**, *3*, 2772.
(28) Nguyen, T. N. A.; Fang, Y.; Fallahi, V.; Benatmane, N.; Mohseni, S. M.; Dumas, R. K.; Åkerman, J. [Co/Pd]-NiFe Exchange Springs with Tunable Magnetization Tilt Angle. *Appl. Phys. Lett.* **2011**, *98* (17), 1–4.
(29) Wang, J. P.; Shen, W.; Hong, S. Y. Fabrication and Characterization of Exchange Coupled Composite Media. *Magn. IEEE Trans.* **2007**, *43* (2), 682–686.
(30) Dai, Q.; Berman, D.; Virwani, K.; Frommer, J.; Jubert, P. O.; Lam, M.; Topuria, T.; Imaino, W.; Nelson, A. Self-Assembled Ferrimagnet-Polymer Composites for Magnetic Recording Media. *Nano Lett.* **2010**, *10* (8), 3216–3221.
(31) Takahashi, F.; Sakai, Y.; Mizutani, Y. Immobilized Enzyme Reaction Controlled by Magnetic Heating: γ-Fe2O3-Loaded Thermosensitive Polymer Gels Consisting of N-Isopropylacrylamide and Acrylamide. *J. Ferment. Bioeng.* **1997**, *83* (2), 152–156.
(32) Kato, N.; Oishi, A.; Takahashi, F. Enzyme Reaction Controlled by Magnetic Heating Due to the Hysteresis Loss of γ-Fe2O3 in Thermosensitive Polymer Gels Immobilized β-Galactosidase. *Mater. Sci. Eng. C* **1998**, *6* (4), 291–296.
(33) Feng, X.; Mao, G. Y.; Bu, F. X.; Cheng, X. L.; Jiang, D. M.; Jiang, J. S. Controlled Synthesis of Monodisperse CoFe2O4 Nanoparticles by the Phase Transfer Method and Their Catalytic Activity on Methylene Blue Discoloration with H2O2. *J. Magn. Magn. Mater.* **2013**, *343*, 126–132.
(34) Baig, R. B. N.; Varma, R. S. Magnetically Retrievable Catalysts for Organic Synthesis. *Chem. Commun.* **2013**, *49* (8), 752–770.
(35) Miyamura, H.; Min, H.; Soulé, J.-F.; Kobayashi, S. Size of Gold Nanoparticles Driving Selective Amide Synthesis through Aerobic Condensation of Aldehydes and Amines. *Angew. Chemie Int. Ed.* **2015**, *54* (26), 7564–7567.
(36) Mattisson, T.; Johansson, M.; Lyngfelt, A. Multicycle Reduction and Oxidation of Different Types of Iron Oxide Particles-Application to Chemical-Looping Combustion. *Energy & Fuels* **2004**, *18* (3), 628–637.
(37) Ceylan, S.; Friese, C.; Lammel, C.; Mazac, K.; Kirschning, A. Inductive Heating for Organic Synthesis by Using Functionalized Magnetic Nanoparticles inside Microreactors. *Angew. Chemie - Int. Ed.* **2008**, *47* (46), 8950–8953.
(38) Zhao, N.; Ma, W.; Cui, Z.; Song, W.; Xu, C.; Gao, M. Polyhedral Maghemite Nanocrystals Prepared by a Flame Synthetic Method: Preparations, Characterizations, and Catalytic Properties. *ACS Nano* **2009**, *3* (7), 1775–1780.
(39) Shylesh, S.; Schünemann, V.; Thiel, W. R. Magnetically Separable Nanocatalysts: Bridges between Homogeneous and Heterogeneous Catalysis. *Angew. Chemie - Int. Ed.* **2010**, *49* (20), 3428–3459.
(40) Polshettiwar, V.; Luque, R.; Fihri, A.; Zhu, H.; Bouhrara, M.; Basset, J. M. Magnetically Recoverable Nanocatalysts. *Chem. Rev.* **2011**, *111* (5), 3036–3075.
(41) Zhang, D.; Zhou, C.; Sun, Z.; Wu, L.-Z.; Tung, C.-H.; Zhang, T. Magnetically Recyclable Nanocatalysts (MRNCs): A Versatile Integration of High Catalytic Activity and Facile Recovery. *Nanoscale* **2012**, *4*, 6244.
(42) Kirschning, A.; Kupracz, L.; Hartwig, J. New Synthetic Opportunities in Miniaturized Flow Reactors with Inductive Heating. *Chem. Lett.* **2012**, *41* (6), 562–570.
(43) Ghosh, P.; Mandal, A.; Subba, R. γ-Maghemite-Silica Nanocomposite: A Green Catalyst for Diverse Aromatic N-Heterocycles. *Catal. Commun.* **2013**, *41*, 146–152.
(44) Dormann, J. L. Le Phénomène de Superparamagnétisme. *Rev. Phys. Appliquée* **1981**, *16* (6), 275–301.
(45) Dormann, J. L.; Fiorani, D.; Tholence, J. L.; Sella, C. Dynamical Properties of Small Particles; Comparison with Spin Glass Behaviour. *J. Magn. Magn. Mater.* **1983**, *35* (1–3), 117–120.
(46) Roduner, E. Size Matters: Why Nanomaterials Are Different. *Chem. Soc. Rev.* **2006**, *35* (7), 583.
(47) Jun, Y. W.; Seo, J. W.; Cheon, J. Nanoscaling Laws of Magnetic Nanoparticles and Their

Applicabilities in Biomedical Sciences. *Acc. Chem. Res.* **2008**, *41* (2), 179–189.
(48) Jun, Y.; Seo, J.; Cheon, J. Nanoscaling Laws of Magnetic Nanoparticles and Their Applicabilities in Biomedical Sciences. *Acc. Chem. Res.* **2008**, *41* (2), 179–189.
(49) Bedanta, S.; Kleemann, W. Supermagnetism. *J. Phys. D. Appl. Phys.* **2009**, *42* (1), 013001.
(50) Bhushan, B. Biomimetics: Lessons from Nature--an Overview. *Philos. Trans. A. Math. Phys. Eng. Sci.* **2009**, *367* (1893), 1445–1486.
(51) Brus, L. E. Electron-Electron and Electron-Hole Interactions in Small Semiconductor Crystallites: The Size Dependence of the Lowest Excited Electronic State. *J. Chem. Phys.* **1984**, *80* (9), 4403–4409.
(52) Kroto, H. W.; Heath, J. R.; O'Brien, S. C.; Curl, R. F.; Smalley, R. E. C60: Buckminsterfullerene. *Nature* **1985**, *318* (6042), 162–163.
(53) Iijima, S. Helical Microtubules of Graphitic Carbon. *Nature* **1991**, *354* (6348), 56–58.
(54) Iijima, S.; Ichihashi, T. Single-Shell Carbon Nanotubes of 1-Nm Diameter. *Nature* **1993**, *363* (6430), 603–605.
(55) Edelstein, A. S.; Murday, J. S.; Rath, B. B. Challenges in Nanomaterials Design. *Prog. Mater. Sci.* **1997**, *42* (1–4), 5–21.
(56) Gusev, A. I. Effects of the Nanocrystalline State in Solids. *Physics-Uspekhi* **1998**, *41* (1), 49–76.
(57) Moriarty, P. Nanostructured Materials. *Reports Prog. Phys.* **2001**, *64* (3), 297–381.
(58) Tjong, S. C.; Chen, H. Nanocrystalline Materials and Coatings. *Mater. Sci. Eng. R Reports* **2004**, *45* (1–2), 1–88.
(59) Hyeon, T.; Chung, Y.; Park, J.; Lee, S. S.; Kim, Y. W.; Park, B. H. Synthesis of Highly Crystalline and Monodisperse Cobalt Ferrite Nanocrystals. *J. Phys. Chem. B* **2002**, *106* (27), 6831–6833.
(60) Rockenberger, J.; Scher, E. C.; Alivisatos, A. P. A New Nonhydrolytic Single-Precursor Approach to Surfactant-Capped Nanocrystals of Transition Metal Oxides. *J. Am. Chem. Soc.* **1999**, *121* (49), 11595–11596.
(61) Park, S.-J.; Kim, S.; Lee, S.; Khim, Z. G.; Char, K.; Hyeon, T. Synthesis and Magnetic Studies of Uniform Iron Nanorods and Nanospheres. *J. Am. Chem. Soc.* **2000**, *122* (35), 8581–8582.
(62) Sun, S.; Zeng, H. Size-Controlled Synthesis of Magnetite Nanoparticles. *J. Am. Chem. Soc.* **2002**, *124* (28), 8204–8205.
(63) Hyeon, T.; Su Seong Lee; Park, J.; Chung, Y.; Hyon Bin Na. Synthesis of Highly Crystalline and Monodisperse Maghemite Nanocrystallites without a Size-Selection Process. *J. Am. Chem. Soc.* **2001**, *123* (51), 12798–12801.
(64) Mathew, D. S.; Juang, R. S. An Overview of the Structure and Magnetism of Spinel Ferrite Nanoparticles and Their Synthesis in Microemulsion.. *Chem. Eng. J.* **2007**, *129*, 51–65.
(65) Shouheng Sun, Hao Zeng, David B. Robinson, Simone Raoux, Philip M. Rice, Shan X. Wang, and G. L. Controlled Synthesis of MFe2O4 (M = Mn, Fe, Co, Ni and Zn) Nanoparticles. *J.Am.Chem.Soc.* **2004**, *126*, 273–279.
(66) Momma, K.; Izumi, F. {\it VESTA3} for Three-Dimensional Visualization of Crystal, Volumetric and Morphology Data. *J. Appl. Crystallogr.* **2011**, *44* (6), 1272–1276.
(67) Momma, K.; Izumi, F. {\it VESTA}: A Three-Dimensional Visualization System for Electronic and Structural Analysis. *J. Appl. Crystallogr.* **2008**, *41* (3), 653–658.
(68) Anhøj, T. A.; Bilenberg, B.; Thomsen, B.; Damsgaard, C. D.; Rasmussen, H. K.; Jacobsen, C. S.; Mygind, J.; Mørup, S. Spin Canting and Magnetic Relaxation Phenomena in Mn0.25Zn0.75Fe2O4. *J. Magn. Magn. Mater. 260*, 115–30.
(69) Liu, C.; Zou, B.; Rondinone; A.J.; Zhang, Z. J. Chemical Control of Superparamagnetic Properties of Magnesium and Cobalt Spinel Ferrite Nanoparticles through Atomic Level Magnetic Couplings. *J. Am. Chem. Soc.* **2000**, *122*, 6263–7.
(70) Coey, J. M. D. *Magnetism and Magnetic Materials*; 2009; Vol. 12.
(71) Cullity, B. D.; Graham, C.; D. *Introduction to Magnetic Materials*; 2009; Vol. 12.
(72) Cannas, C.; Musinu, A.; Piccaluga, G.; Fiorani, D.; Peddis, D.; Rasmussen, H. K.; Morup, S. Magnetic Properties of Cobalt Ferrite – Silica Nanocomposites Prepared by a Sol-Gel Autocombustion Technique. *J. Chem. Phys.* **2006**, *125*, 164711.
(73) Bedanta, S.; Kleemann, W. Supermagnetism. *J. Phys. D. Appl. Phys.* **2009**, *42* (1), 013001.
(74) Cannas, C.; Peddis, D. Design of Magnetic Spinel Oxide Nanoarchitectures. *La Chim. e l'industria* **2012**, 109–117.
(75) Blundell, S. *Magnetism in Condensed Matter*; Oxford Master Series in Physics, Ed.; Oxford, 2001.
(76) NEEL; L. Theorie Du Trainage Magnetique Des Ferromagnetiques En Grains Fins Avec Applications Aux Terres Cuites. *Ann. Geophys.* **1949**, *5*, 99–136.
(77) Mameli, V.; Sanna Angotzi, M.; Cara, C.; Cannas, C. Liquid Phase Synthesis of Nanostructured Spinel Ferrites – A Review. *J. Nanosci. Nanotechnol.* **2018**, Just Accepted.
(78) Sugimoto, T.; Matijević, E. Formation of Uniform Spherical Magnetite Particles by Crystallization from Ferrous Hydroxide Gels. *J. Colloid Interface Sci.* **1980**, *74* (1), 227–243.

(79) Massart, R. Preparation of Aqueous Magnetic Liquids in Alkaline and Acidic Media. *IEEE Trans. Magn.* **1981**, *17* (2), 1247–1248.
(80) Blaskov, V.; Petkov, V.; Rusanov, V.; Martinez, L. M.; Martinez, B.; Muñoz, J. S.; Mikhov, M. Magnetic Properties of Nanophase CoFe2O4 Particles. *J. Magn. Magn. Mater.* **1996**, *162* (2–3), 331–337.
(81) Feltin, N.; Pileni, M. P. New Technique for Synthesizing Iron Ferrite Magnetic Nanosized Particles. *Langmuir* **1997**, *13* (12), 3927–3933.
(82) Vayssières, L.; Chanéac, C.; Tronc, E.; Jolivet, J. P. Size Tailoring of Magnetite Particles Formed by Aqueous Precipitation: An Example of Thermodynamic Stability of Nanometric Oxide Particles. *J. Colloid Interface Sci.* **1998**, *205* (2), 205–212.
(83) Babes, L.; Denizot, B.; Tanguy, G.; Le Jeune, J. J.; Jallet, P. Synthesis of Iron Oxide Nanoparticles Used as MRI Contrast Agents: A Parametric Study. *J. Colloid Interface Sci.* **1999**, *212* (2), 474–482.
(84) Shi, Y.; Ding, J.; Liu, X.; Wang, J. NiFe2O4 Ultrafine Particles Prepared by Co-Precipitation/Mechanical Alloying. *J. Magn. Magn. Mater.* **1999**, *205* (2), 249–254.
(85) Rajendran, M.; Pullar, R. C.; Bhattacharya, A. K.; Das, D.; Chintalapudi, S. N.; Majumdar, C. K. Magnetic Properties of Nanocrystalline CoFe2O4 Powders Prepared at Room Temperature: Variation with Crystallite Size. *J. Magn. Magn. Mater.* **2001**, *232* (1–2), 71–83.
(86) Jolivet, J. P.; Tronc, É.; Chanéac, C. Synthesis of Iron Oxide-Based Magnetic Nanomaterials and Composites. *Comptes Rendus Chim.* **2002**, *5* (10), 659–664.
(87) Kim, Y. Il; Kim, D.; Lee, C. S. Synthesis and Characterization of CoFe2O4 Magnetic Nanoparticles Prepared by Temperature-Controlled Coprecipitation Method. *Phys. B Condens. Matter* **2003**, *337* (1–4), 42–51.
(88) Jolivet, J.-P.; Froidefond, C.; Pottier, A.; Chanéac, C.; Cassaignon, S.; Tronc, E.; Euzen, P. Size Tailoring of Oxide Nanoparticles by Precipitation in Aqueous Medium. A Semi-Quantitative Modelling. *J. Mater. Chem.* **2004**, *14* (21), 3281.
(89) Jiang, W.; Yang, H. C.; Yang, S. Y.; Horng, H. E.; Hung, J. C.; Chen, Y. C.; Hong, C. Y. Preparation and Properties of Superparamagnetic Nanoparticles with Narrow Size Distribution and Biocompatible. *J. Magn. Magn. Mater.* **2004**, *283* (2–3), 210–214.
(90) Molday, R. S.; Mackenzie, D. Immunospecific Ferromagnetic Iron-Dextran Reagents for the Labeling and Magnetic Separation of Cells. *J. Immunol. Methods* **1982**, *52* (3), 353–367.
(91) Arulmurugan, R.; Jeyadevan, B.; Vaidyanathan, G.; Sendhilnathan, S. Effect of Zinc Substitution on Co-Zn and Mn-Zn Ferrite Nanoparticles Prepared by Co-Precipitation. *J. Magn. Magn. Mater.* **2005**, *288*, 470–477.
(92) Qu, Y.; Yang, H.; Yang, N.; Fan, Y.; Zhu, H.; Zou, G. The Effect of Reaction Temperature on the Particle Size, Structure and Magnetic Properties of Coprecipitated CoFe2O4 Nanoparticles. *Mater. Lett.* **2006**, *60* (29–30), 3548–3552.
(93) Wu, J.-H.; Ko, S. P.; Liu, H.-L.; Kim, S.; Ju, J.-S.; Kim, Y. K. Sub 5 Nm Magnetite Nanoparticles: Synthesis, Microstructure, and Magnetic Properties. *Mater. Lett.* **2007**, *61* (14–15), 3124–3129.
(94) Gul, I. H.; Abbasi, A. Z.; Amin, F.; Anis-ur-Rehman, M.; Maqsood, A. Structural, Magnetic and Electrical Properties of Co1-XZnxFe2O4 Synthesized by Co-Precipitation Method. *J. Magn. Magn. Mater.* **2007**, *311* (2), 494–499.
(95) Andrés Vergés, M.; Costo, R.; Roca, A. G.; Marco, J. F.; Goya, G. F.; Serna, C. J.; Morales, M. P.; Vergés, M. A.; Costo, R.; Roca, A. G.; et al. Uniform and Water Stable Magnetite Nanoparticles with Diameters around the Monodomain–multidomain Limit. *J. Phys. D. Appl. Phys.* **2008**, *41* (13), 134003.
(96) Li, Z.; Tan, B.; Allix, M.; Cooper, A. I.; Rosseinsky, M. J. Direct Coprecipitation Route to Monodisperse Dual-Functionalized Magnetic Iron Oxide Nanocrystals Without Size Selection. *Small* **2008**, *4* (2), 231–239.
(97) Cannas, C.; Ardu, A.; Musinu, A.; Peddis, D.; Piccaluga, G. Spherical Nanoporous Assemblies of Iso-Oriented Cobalt Ferrite Nanoparticles: Synthesis, Microstructure, and Magnetic Properties. *Chem. Mater.* **2008**, *20* (20), 6364–6371.
(98) Gul, I. H.; Ahmed, W.; Maqsood, A. Electrical and Magnetic Characterization of Nanocrystalline Ni-Zn Ferrite Synthesis by Co-Precipitation Route. *J. Magn. Magn. Mater.* **2008**, *320* (3–4), 270–275.
(99) Maaz, K.; Karim, S.; Mumtaz, A.; Hasanain, S. K.; Liu, J.; Duan, J. L. Synthesis and Magnetic Characterization of Nickel Ferrite Nanoparticles Prepared by Co-Precipitation Route. *J. Magn. Magn. Mater.* **2009**, *321* (12), 1838–1842.
(100) Cannas, C.; Ardu, A.; Peddis, D.; Sangregorio, C.; Piccaluga, G.; Musinu, A. Surfactant-Assisted Route to Fabricate CoFe2O4 Individual Nanoparticles and Spherical Assemblies. *J. Colloid Interface Sci.* **2010**, *343* (2), 415–422.
(101) Massart, R.; Cabuil, V. Synthèse En Milieu Alcalin de Magnétite Colloïdale : Contrôle Du Rendement et de La Taille Des Particules. *J. Chim. Phys.* **1987**, *84* (7), 967–973.
(102) Jolivet, J. P.; Cassaignon, S.; Chanéac, C.; Chiche, D.; Durupthy, O.; Portehault, D. Design of

Metal Oxide Nanoparticles: Control of Size, Shape, Crystalline Structure and Functionalization by Aqueous Chemistry. *Comptes Rendus Chim.* **2010**, *13* (1–2), 40–51.
(103) Veintemillas-Verdaguer, S.; del Puerto Morales, M.; Serna, C. J.; Andrés-Vergés, M.; Ruiz-Cabello, J.; Herranz, F. Uniform Magnetite Nanoparticles Larger Than 20 Nm Synthesized by an Aqueous Route; Springer Science and Business Media, LLC, 2012; Vol. 140, pp 379–379.
(104) Sharifi, I.; Shokrollahi, H. Structural, Magnetic and M??Ssbauer Evaluation of Mn Substituted Co-Zn Ferrite Nanoparticles Synthesized by Co-Precipitation. *J. Magn. Magn. Mater.* **2013**, *334*, 36–40.
(105) Shen, L.; Qiao, Y.; Guo, Y.; Meng, S.; Yang, G.; Wu, M.; Zhao, J. Facile Co-Precipitation Synthesis of Shape-Controlled Magnetite Nanoparticles. *Ceram. Int.* **2014**, *40* (1 PART B), 1519–1524.
(106) Houshiar, M.; Zebhi, F.; Razi, Z. J.; Alidoust, A.; Askari, Z. Synthesis of Cobalt Ferrite (CoFe2O4) Nanoparticles Using Combustion, Coprecipitation, and Precipitation Methods: A Comparison Study of Size, Structural, and Magnetic Properties. *J. Magn. Magn. Mater.* **2014**, *371*, 43–48.
(107) Cannas, C.; Ardu, A.; Musinu, A.; Suber, L.; Ciasca, G.; Amenitsch, H.; Campi, G. Hierarchical Formation Mechanism of CoFe2O4 Mesoporous Assemblies. *ACS Nano* **2015**, *9* (7), 7277–7286.
(108) Aphesteguy, J. C.; Kurlyandskaya, G. V.; De Celis, J. P.; Safronov, A. P.; Schegoleva, N. N. Magnetite Nanoparticles Prepared by Co-Precipitation Method in Different Conditions. *Mater. Chem. Phys.* **2015**, *161*, 243–249.
(109) Rani, S.; Varma, G. D. Superparamagnetism and Metamagnetic Transition in Fe3O4 Nanoparticles Synthesized via Co-Precipitation Method at Different PH. *Phys. B Condens. Matter* **2015**, *472*, 66–77.
(110) Yazdani, F.; Seddigh, M. Magnetite Nanoparticles Synthesized by Co-Precipitation Method: The Effects of Various Iron Anions on Specifications. *Mater. Chem. Phys.* **2016**, *184*, 318–323.
(111) Huang, X.; Zhang, J.; Wang, W.; Sang, T.; Song, B.; Zhu, H.; Rao, W.; Wong, C. Effect of PH Value on Electromagnetic Loss Properties of Co-Zn Ferrite Prepared via Coprecipitation Method. *J. Magn. Magn. Mater.* **2016**, *405*, 36–41.
(112) Bacri, J. C.; Perzynski, R.; Salin, D.; Cabuil, V.; Massart, R. Ionic Ferrofluids: A Crossing of Chemistry and Physics. *J. Magn. Magn. Mater.* **1990**, *85* (1–3), 27–32.
(113) Rashid, Z.; Soleimani, M.; Ghahremanzadeh, R.; Vossoughi, M.; Esmaeili, E. Effective Surface Modification of MnFe 2 O 4 @SiO 2 @PMIDA Magnetic Nanoparticles for Rapid and High-Density Antibody Immobilization. *Appl. Surf. Sci.* **2017**, *426*, 1023–1029.
(114) Mirzaee, S.; Shayesteh, S. F. Ultrasound Induced Strain in Ultrasmall CoFe 2 O 4 @polyvinyl Alcohol Nanocomposites. *Ultrason. Sonochem.* **2018**, *40* (April 2017), 583–586.
(115) Davies, K. J.; Wells, S.; Upadhyay, R. V.; Charles, S. W.; O'Grady, K.; El Hilo, M.; Meaz, T.; Mørup, S. The Observation of Multi-Axial Anisotropy in Ultrafine Cobalt Ferrite Particles Used in Magnetic Fluids. *J. Magn. Magn. Mater.* **1995**, *149* (1–2), 14–18.
(116) Davies, K. J.; Wells, S.; Charles, S. W. The Effect of Temperature and Oleate Adsorption on the Growth of Maghemite Particles. *J. Magn. Magn. Mater.* **1993**, *122* (1–3), 24–28.
(117) Prabhakaran, T.; Mangalaraja, R. V.; Denardin, J. C. Controlling the Size and Magnetic Properties of Nano CoFe<inf>2</Inf>O<inf>4</Inf>by Microwave Assisted Co-Precipitation Method. *Mater. Res. Express* **2018**, *5* (2).
(118) Gribanov, N. M.; Bibik, E. E.; Buzunov, O. V.; Naumov, V. N. Physico-Chemical Regularities of Obtaining Highly Dispersed Magnetite by the Method of Chemical Condensation. *J. Magn. Magn. Mater.* **1990**, *85* (1–3), 7–10.
(119) Jolivet, J. P.; Belleville, P.; Tronc, E.; Livage, J. Influence of Fe(II) on the Formation of the Spinel Iron Oxide in Alkaline Medium. *Clays Clay Miner.* **1992**, *40* (5), 531–539.
(120) Tronc, E.; Belleville, P.; Jolivet, J. P.; Livage, J. Transformation of Ferric Hydroxide into Spinel by Iron(II) Adsorption. *Langmuir* **1992**, *8* (1), 313–319.
(121) Uzunova, E.; Klissurski, D.; Mitov, I.; Stefanov, P. Cobalt-Iron Hydroxide Carbonate as a Precursor for the Synthesis of High-Dispersity Spinel Mixed Oxides. *Chem. Mater.* **1993**, *5* (4), 576–582.
(122) Jolivet, J. P.; Vayssieres, L.; Chaneac, C.; Tronc, E. Precipitation of Spinel Iron Oxide : Nanoparticle Size Control. *MRS Proc.* **1996**, *432*, 145.
(123) Atif, M.; Hasanain, S. K. K.; Nadeem, M. Magnetization of Sol-Gel Prepared Zinc Ferrite Nanoparticles: Effects of Inversion and Particle Size. *Solid State Commun.* **2006**, *138* (8), 416–421.
(124) Bentivegna, F.; Ferré, J.; Nývlt, M.; Jamet, J. P.; Imhoff, D.; Canva, M.; Brun, A.; Veillet, P.; Višňovský, Š.; Chaput, F.; et al. Magnetically Textured γ-Fe2O3 Nanoparticles in a Silica Gel Matrix: Structural and Magnetic Properties. *J. Appl. Phys.* **1998**, *83* (12), 7776–7788.
(125) Wu, S.; Sun, A.; Xu, W.; Zhang, Q.; Zhai, F.; Logan, P.; Volinsky, A. A. Iron-Based Soft Magnetic Composites with Mn–Zn Ferrite Nanoparticles Coating Obtained by Sol–gel Method. *J. Magn. Magn. Mater.* **2012**, *324* (22), 3899–3905.

(126) Xiong, G.; Mai, Z. H.; Wang, C. Y.; Ni, Y. M.; Zhao, Z. X.; Xu, M.; Liu, C. X.; Luo, G. M. Characterization of CoCrFeO4 Nanocrystals Prepared by a Sol-Gel Method. *Chinese Phys. Lett.* **2001**, *18* (5), 692–694.
(127) Xu, X. L.; Guo, J. D.; Wang, Y. Z. A Novel Technique by the Citrate Pyrolysis for Preparation of Iron Oxide Nanoparticles. *Mater. Sci. Eng. B* **2000**, *77* (2), 207–209.
(128) Yan, S.; Geng, J.; Yin, L.; Zhou, E. Preparation of Nanocrystalline NiZnCu Ferrite Particles by Sol–gel Method and Their Magnetic Properties. *J. Magn. Magn. Mater.* **2004**, *277* (1–2), 84–89.
(129) Yue, Z.; Guo, W.; Zhou, J.; Gui, Z.; Li, L. Synthesis of Nanocrystilline Ferrites by Sol-Gel Combustion Process: The Influence of PH Value of Solution. *J. Magn. Magn. Mater.* **2004**, *270* (1–2), 216–223.
(130) Yue, Z.; Zhou, J.; Li, L.; Zhang, H.; Gui, Z. Synthesis of Nanocrystalline NiCuZn Ferrite Powders by Sol-Gel Auto-Combustion Method. *J. Magn. Magn. Mater.* **2000**, *208* (1), 55–60.
(131) Salunkhe, A. B.; Khot, V. M.; Phadatare, M. R.; Pawar, S. H. Combustion Synthesis of Cobalt Ferrite Nanoparticles—Influence of Fuel to Oxidizer Ratio. *J. Alloys Compd.* **2012**, *514*, 91–96.
(132) Hwang, C.-C.; Tsai, J.-S.; Huang, T.-H. Combustion Synthesis of Ni–Zn Ferrite by Using Glycine and Metal Nitrates—investigations of Precursor Homogeneity, Product Reproducibility, and Reaction Mechanism. *Mater. Chem. Phys.* **2005**, *93* (2–3), 330–336.
(133) Yan, C.-H.; Xu, Z.-G.; Cheng, F.-X.; Wang, Z.-M.; Sun, L.-D.; Liao, C.-S.; Jia, J.-T. Nanophased CoFe2O4 Prepared by Combustion Method. *Solid State Commun.* **1999**, *111* (5), 287–291.
(134) Kikukawa, N.; Takemori, M.; Nagano, Y.; Sugasawa, M.; Kobayashi, S. Synthesis and Magnetic Properties of Nanostructured Spinel Ferrites Using a Glycine–nitrate Process. *J. Magn. Magn. Mater.* **2004**, *284*, 206–214.
(135) Cannas, C.; Ardu, A.; Niznansky, D.; Peddis, D.; Piccaluga, G.; Musinu, A. Simple and Fast Preparation of Pure Maghemite Nanopowders through Sol-Gel Self-Combustion. *J. Sol-Gel Sci. Technol.* **2011**, *60* (3), 266–274.
(136) Hwang, C.-C.; Wu, T.-Y.; Wan, J.; Tsai, J.-S. Development of a Novel Combustion Synthesis Method for Synthesizing of Ceramic Oxide Powders. *Mater. Sci. Eng. B* **2004**, *111* (1), 49–56.
(137) Bentivegna, F.; Nyvlt, M.; Ferré, J.; Jamet, J. P.; Brun, A.; Višňovsky, S.; Urban, R. Magnetically Textured γ-Fe2O3 Nanoparticles in a Silica Gel Matrix: Optical and Magneto-Optical Properties. *J. Appl. Phys.* **1999**, *85* (4), 2270–2278.
(138) del Monte, F.; Morales, M. P.; Levy, D.; Fernandez, A.; Ocaña, M.; Roig, A.; Molins, E.; O'Grady, K.; Serna, C. J. Formation of γ-Fe 2 O 3 Isolated Nanoparticles in a Silica Matrix. *Langmuir* **1997**, *13* (14), 3627–3634.
(139) Niznansky, D.; Viart, N.; Rehspringer, J. L. Nanocomposites Fe2O3/SiO2-Preparation by Sol-Gel Method and Physical Properties. *J. Sol-Gel Sci. Technol.* **1997**, *8* (1–3), 615–618.
(140) Petrache, C.; Jitianu, A.; Zaharescu, M.; Predoi, D.; Kuncser, V.; Filoti, G.; Academy, R. Sol-Gel FexOy-SiO2 Nanocomposites. *Rom. Journ. Phys* **2005**, *50* (5–6), 595–606.
(141) Raileanu, M.; Crisan, M.; Petrache, C.; Crisan, D.; Zaharescu, M. Fe 2 O 3 -SiO 2 NANOCOMPOSITES OBTAINED BY DIFFERENT SOL-GEL ROUTES. *J. Optoelectron. Adv. Mater.* **2003**, *5* (3), 693–698.
(142) Solinas, S.; Piccaluga, G.; Morales, M. P.; Serna, C. J. Sol-Gel Formation of γ-Fe2O3/SiO2 Nanocomposites. *Acta Mater.* **2001**, *49* (14), 2805–2811.
(143) Sutka, A.; Mezinskis, G. Sol-Gel Auto-Combustion Synthesis of Spinel-Type Ferrite Nanomaterials. *Front. Mater. Sci.* **2012**, *6* (2), 128–141.
(144) Li, L.; Li, G.; Smith, R. L.; Inomata, H. Microstructural Evolution and Magnetic Properties of NiFe2O4 Nanocrystals Dispersed in Amorphous Silica. *Chem. Mater.* **2000**, *12* (12), 3705–3714.
(145) Chatterjee, A.; Das, D.; Pradhan, S. K. K.; Chakravorty, D. Synthesis of Nanocrystalline Nickel-Zinc Ferrite by the Sol-Gel Method. *J. Magn. Magn. Mater.* **1993**, *127* (1–2), 214–218.
(146) Cannas, C.; Falqui, A.; Musinu, A.; Peddis, D.; Piccaluga, G. CoFe2O4 Nanocrystalline Powders Prepared by Citrate-Gel Methods: Synthesis, Structure and Magnetic Properties. *J. Nanoparticle Res.* **2006**, *8* (2), 255–267.
(147) Cannas, C.; Musinu, A.; Peddis, D.; Piccaluga, G. New Synthesis of Ferrite–Silica Nanocomposites by a Sol–Gel Auto-Combustion. *J. Nanoparticle Res.* **2004**, *6* (2), 223–232.
(148) Hutlova, A.; Niznansky, D.; Rehspringer, J.-L.; Estournès, C.; Kurmoo, M. High Coercive Field for Nanoparticles of CoFe2O4 in Amorphous Silica Sol–Gel. *Adv. Mater.* **2003**, *15* (19), 1622–1625.
(149) Concas, G.; Spano, G.; Cannas, C.; Musinu, A.; Peddis, D.; Piccaluga, G. Inversion Degree and Saturation Magnetization of Different Nanocrystalline Cobalt Ferrites. *J. Magn. Magn. Mater.* **2009**, *321* (12), 1893–1897.
(150) Cannas, C.; Musinu, A.; Peddis, D.; Piccaluga, G. Synthesis and Characterization of CoFe 2 O 4 Nanoparticles Dispersed in a Silica Matrix by a Sol−Gel Autocombustion Method. *Chem. Mater.* **2006**, *18* (16), 3835–3842.

(151) Cannas, C.; Gatteschi, D.; Musinu, A.; Piccaluga, G.; Sangregorio, C. Structural and Magnetic Properties of Fe2O3 Nanoparticles Dispersed over a Silica Matrix. *J. Phys. Chem. B* **1998**, *102* (98), 7721–7726.
(152) Chanéac, C.; Tronc, E.; Jolivet, J. P.; Chancac, C.; Tronc, E.; Jolivet, J. P. Magnetic Iron Oxide–silica Nanocomposites. Synthesis and Characterization. *J. Mater. Chem.* **1996**, *6* (12), 1905–1911.
(153) George, M.; Mary John, A.; Nair, S. S.; Joy, P. A.; Anantharaman, M. R. Finite Size Effects on the Structural and Magnetic Properties of Sol-Gel Synthesized NiFe2O4 Powders. *J. Magn. Magn. Mater.* **2006**, *302* (1), 190–195.
(154) Lavela, P.; Tirado, J. L. L. CoFe2O4 and NiFe2O4 Synthesized by Sol-Gel Procedures for Their Use as Anode Materials for Li Ion Batteries. *J. Power Sources* **2007**, *172* (1), 379–387.
(155) Srivastava, M.; Ojha, A. K.; Chaubey, S.; Sharma, P. K.; Pandey, A. C. Influence of PH on Structural Morphology and Magnetic Properties of Ordered Phase Cobalt Doped Lithium Ferrites Nanoparticles Synthesized by Sol-Gel Method. *Mater. Sci. Eng. B Solid-State Mater. Adv. Technol.* **2010**, *175* (1), 14–21.
(156) Horner, O.; Neveu, S.; De Montredon, S.; Siaugue, J. M.; Cabuil, V. Hydrothermal Synthesis of Large Maghemite Nanoparticles: Influence of the PH on the Particle Size. *J. Nanoparticle Res.* **2009**, *11* (5), 1247–1250.
(157) Kolen'Ko, Y. V.; Bañobre-López, M.; Rodríguez-Abreu, C.; Carbó-Argibay, E.; Sailsman, A.; Piñeiro-Redondo, Y.; Cerqueira, M. F.; Petrovykh, D. Y.; Kovnir, K.; Lebedev, O. I.; et al. Large-Scale Synthesis of Colloidal Fe3O4 Nanoparticles Exhibiting High Heating Efficiency in Magnetic Hyperthermia. *J. Phys. Chem. C* **2014**, *118* (16), 8691–8701.
(158) Kim, C. K.; Lee, J. H.; Katoh, S.; Murakami, R.; Yoshimura, M. Synthesis of Co-, Co-Zn and Ni-Zn Ferrite Powders by the Microwave-Hydrothermal Method. *Mater. Res. Bull.* **2001**, *36* (12), 2241–2250.
(159) Köseoğlu, Y. Structural and Magnetic Properties of Cr Doped NiZn-Ferrite Nanoparticles Prepared by Surfactant Assisted Hydrothermal Technique. *Ceram. Int.* **2015**, *41* (5), 6417–6423.
(160) Baykal, A.; Kasapoğlu, N.; Köseoğlu, Y.; Toprak, M. S.; Bayrakdar, H. CTAB-Assisted Hydrothermal Synthesis of NiFe2O4 and Its Magnetic Characterization. *J. Alloys Compd.* **2008**, *464* (1–2), 514–518.
(161) Verma, S.; Joy, P. A.; Khollam, Y. B.; Potdar, H. S.; Deshpande, S. B. Synthesis of Nanosized MgFe2O4 Powders by Microwave Hydrothermal Method. *Mater. Lett.* **2004**, *58* (6), 1092–1095.
(162) Wu, X.; Wang, W.; Li, F.; Khaimanov, S.; Tsidaeva, N.; Lahoubi, M. PEG-Assisted Hydrothermal Synthesis of CoFe2O4 Nanoparticles with Enhanced Selective Adsorption Properties for Different Dyes. *Appl. Surf. Sci.* **2016**, *389*, 1003–1011.
(163) Lee, J. H.; Kim, C. K.; Katoh, S.; Murakami, R. Microwave-Hydrothermal versus Conventional Hydrothermal Preparation of Ni- and Zn-Ferrite Powders. *J. Alloys Compd.* **2001**, *325* (1–2), 276–280.
(164) Melo, R. S.; Silva, F. C.; Moura, K. R. M.; De Menezes, A. S.; Sinfrônio, F. S. M. Magnetic Ferrites Synthesised Using the Microwave-Hydrothermal Method. *J. Magn. Magn. Mater.* **2015**, *381*, 109–115.
(165) Sertkol, M.; Köseoğlu, Y.; Baykal, A.; Kavas, H.; Basaran, A. C. Synthesis and Magnetic Characterization of Zn0.7Ni0.3Fe2O4 Nanoparticles via Microwave-Assisted Combustion Route. *J. Magn. Magn. Mater.* **2010**, *322* (7), 866–871.
(166) Shan, A. X.; Wu, X.; Lu, J.; Chen, C. P.; Wang, R. M. Phase Formations and Magnetic Properties of Single Crystal Nickel Ferrite (NiFe2O4) with Different Morphologies. *Crystengcomm* **2015**, *17* (7), 1603–1608.
(167) Nejati, K.; Zabihi, R. Preparation and Magnetic Properties of Nano Size Nickel Ferrite Particles Using Hydrothermal Method. *Chem. Cent. J.* **2012**, *6* (1), 23.
(168) Sun, X.; Zheng, C.; Zhang, F.; Yang, Y.; Wu, G.; Yu, A.; Guan, N. Size-Controlled Synthesis of Magnetite (Fe 3 O 4) Nanoparticles Coated with Glucose and Gluconic Acid from a Single Fe(III) Precursor by a Sucrose Bifunctional Hydrothermal Method. *J. Phys. Chem. C* **2009**, *113* (36), 16002–16008.
(169) Fan, G.; Gu, Z.; Yang, L.; Li, F. Nanocrystalline Zinc Ferrite Photocatalysts Formed Using the Colloid Mill and Hydrothermal Technique. *Chem. Eng. J.* **2009**, *155* (1–2), 534–541.
(170) Wang, J.; Zeng, C.; Peng, Z.; Chen, Q. Synthesis and Magnetic Properties of Zn1−xMnxFe2O4 Nanoparticles. *Phys. B Condens. Matter* **2004**, *349* (1–4), 124–128.
(171) Chen, Z.; Gao, L. Synthesis and Magnetic Properties of CoFe2O4 Nanoparticles by Using PEG as Surfactant Additive. *Mater. Sci. Eng. B Solid-State Mater. Adv. Technol.* **2007**, *141* (1–2), 82–86.
(172) Rozman, M.; Drofenik, M. Hydrothermal Synthesis of Manganese Zinc Ferrites. *J. Am. Ceram. Soc.* **1995**, *78* (9), 2449–2455.
(173) Chen, D.; Chen, D.; Jiao, X.; Zhao, Y.; He, M. Hydrothermal Synthesis and Characterization of Octahedral Nickel Ferrite Particles. *Powder Technol.* **2003**, *133* (1–3), 247–250.

(174) Köseoğlu, Y.; Alan, F.; Tan, M.; Yilgin, R.; Öztürk, M. Low Temperature Hydrothermal Synthesis and Characterization of Mn Doped Cobalt Ferrite Nanoparticles. *Ceram. Int.* **2012**, *38* (5), 3625–3634.
(175) Zhao, L.; Zhang, H.; Xing, Y.; Song, S.; Yu, S.; Shi, W.; Guo, X.; Yang, J.; Lei, Y.; Cao, F. Studies on the Magnetism of Cobalt Ferrite Nanocrystals Synthesized by Hydrothermal Method. *J. Solid State Chem.* **2008**, *181* (2), 245–252.
(176) Komarneni, S.; D'Arrigo, M. C.; Leonelli, C.; Pellacani, G. C.; Katsuki, H. Microwave-Hydrothermal Synthesis of Nanophase Ferrites. *J. Am. Ceram. Soc.* **2005**, *81* (11), 3041–3043.
(177) Georgiadou, V.; Dendrinou-Samara, C. Impact of the Presence of Octadecylamine on the Properties of Hydrothermally Prepared CoFe 2 O 4 Nanoparticles. *Eur. J. Inorg. Chem.* **2014**, *2014* (23), 3645–3656.
(178) Xu, C.; Teja, A. S. Continuous Hydrothermal Synthesis of Iron Oxide and PVA-Protected Iron Oxide Nanoparticles. *J. Supercrit. Fluids* **2008**, *44* (1), 85–91.
(179) Ahmadi, R.; Masoudi, A.; Madaah Hosseini, H. R.; Gu, N. Kinetics of Magnetite Nanoparticles Formation in a One Step Low Temperature Hydrothermal Process. *Ceram. Int.* **2013**, *39* (5), 4999–5005.
(180) Sue, K.; Aoki, M.; Sato, T.; Nishio-Hamane, D.; Kawasaki, S. I.; Hakuta, Y.; Takebayashi, Y.; Yoda, S.; Furuya, T.; Sato, T.; et al. Continuous Hydrothermal Synthesis of Nickel Ferrite Nanoparticles Using a Central Collision-Type Micromixer: Effects of Temperature, Residence Time, Metal Salt Molality, and Naoh Addition on Conversion, Particle Size, and Crystal Phase. *Ind. Eng. Chem. Res.* **2011**, *50* (16), 9625–9631.
(181) Sasaki, T.; Ohara, S.; Naka, T.; Vejpravova, J.; Sechovsky, V.; Umetsu, M.; Takami, S.; Jeyadevan, B.; Adschiri, T. Continuous Synthesis of Fine MgFe2O4nanoparticles by Supercritical Hydrothermal Reaction. *J. Supercrit. Fluids* **2010**, *53* (1–3), 92–94.
(182) Matson, D. W.; Linehan, J. C.; Darab, J. G.; Buehler, M. F. Nanophase Iron-Based Liquefaction Catalysts: Synthesis, Characterization, and Model Compound Reactivity. *Energy & Fuels* **1994**, *8*, 10–18.
(183) Millot, N.; Xin, B.; Pighini, C.; Aymes, D. Hydrothermal Synthesis of Nanostructured Inorganic Powders by a Continuous Process under Supercritical Conditions. *J. Eur. Ceram. Soc.* **2005**, *25* (12 SPEC. ISS.), 2013–2016.
(184) Matson, D. W.; Linehan, J. C.; Bean, R. M. Ultrafine Iron-Oxide Powders Generated Using a Flow-through Hydrothermal Process. *Mater. Lett.* **1992**, *14* (4), 222–226.
(185) Darr, J. A.; Zhang, J.; Makwana, N. M.; Weng, X. Continuous Hydrothermal Synthesis of Inorganic Nanoparticles: Applications and Future Directions. *Chem. Rev.* **2017**, *117* (17), 11125–11238.
(186) Darab, J. G.; Matson, D. W. Continuous Hydrothermal Processing of Nano-Crystalline Particulates for Chemical-Mechanical Planarization. *J. Electron. Mater.* **1998**, *27* (10), 1068–1072.
(187) Cabañas, A.; Poliakoff, M. The Continuous Hydrothermal Synthesis of Nano-Particulate Ferrites in near Critical and Supercritical Water. *J. Mater. Chem.* **2001**, *11* (5), 1408–1416.
(188) Aimable, A.; Muhr, H.; Gentric, C.; Bernard, F.; Le Cras, F.; Aymes, D. Continuous Hydrothermal Synthesis of Inorganic Nanopowders in Supercritical Water: Towards a Better Control of the Process. *Powder Technol.* **2009**, *190* (1–2), 99–106.
(189) Adschiri, T.; Kanazawa, K.; Arai, K. Rapid and Continuous Hydrothermal Crystallization of Metal Oxide Particles in Supercritical Water. *J. Am. Ceram. Soc.* **1992**, *75* (4), 1019–1022.
(190) Jensen, K. M. Ø.; Andersen, H. L.; Tyrsted, C.; Bøjesen, E. D.; Dippel, A. C.; Lock, N.; Billinge, S. J. L.; Iversen, B. B.; Christensen, M. Mechanisms for Iron Oxide Formation under Hydrothermal Conditions: An in Situ Total Scattering Study. *ACS Nano* **2014**, *8* (10), 10704–10714.
(191) Xu, J.; Yang, H.; Fu, W.; Du, K.; Sui, Y.; Chen, J.; Zeng, Y.; Li, M.; Zou, G. Preparation and Magnetic Properties of Magnetite Nanoparticles by Sol-Gel Method. *J. Magn. Magn. Mater.* **2007**, *309* (2), 307–311.
(192) Köseoğlu, Y.; Bay, M.; Tan, M.; Baykal, A.; Sözeri, H.; Topkaya, R.; Akdoğan, N. Magnetic and Dielectric Properties of Mn0.2Ni0.8Fe2O4 Nanoparticles Synthesized by PEG-Assisted Hydrothermal Method. *J. Nanoparticle Res.* **2011**, *13* (5), 2235–2244.
(193) Taniguchi, T.; Nakagawa, K.; Watanabe, T.; Matsushita, N.; Yoshimura, M. Hydrothermal Growth of Fatty Acid Stabilized Iron Oxide Nanocrystals. *J. Phys. Chem. C* **2009**, *113* (3), 839–843.
(194) Adschiri, T.; Hakuta, Y.; Arai, K. Hydrothermal Synthesis of Metal Oxide Fine Particles at Supercritical Conditions. *Ind. Eng. Chem. Res.* **2000**, *39* (12), 4901–4907.
(195) Rizzuti, A.; Dassisti, M.; Mastrorilli, P.; Sportelli, M. C.; Cioffi, N.; Picca, R. A.; Agostinelli, E.; Varvaro, G.; Caliandro, R. Shape-Control by Microwave-Assisted Hydrothermal Method for the Synthesis of Magnetite Nanoparticles Using Organic Additives. *J. Nanoparticle Res.* **2015**, *17* (10), 1–16.
(196) Daou, T. J.; Pourroy, G.; Bégin-Colin, S.; Grenèche, J. M.; Ulhaq-Bouillet, C.; Legaré, P.;

Bernhardt, P.; Leuvrey, C.; Rogez, G. Hydrothermal Synthesis of Monodisperse Magnetite Nanoparticles. *Chem. Mater.* **2006**, *18* (18), 4399–4404.
(197) Santoyo Salazar, J.; Perez, L.; De Abril, O.; Truong Phuoc, L.; Ihiawakrim, D.; Vazquez, M.; Greneche, J. M.; Begin-Colin, S.; Pourroy, G. Magnetic Iron Oxide Nanoparticles in 10-40 Nm Range: Composition in Terms of Magnetite/Maghemite Ratio and Effect on the Magnetic Properties. *Chem. Mater.* **2011**, *23* (6), 1379–1386.
(198) Kennedy, G. C. Pressure-Volume-Temperature Relations in Water at Elevated Temperatures and Pressures. *Am. J. Sci.* **1950**, *248* (8), 540–564.
(199) Zhao, D.; Wu, X.; Guan, H.; Han, E. Study on Supercritical Hydrothermal Synthesis of CoFe2O4 Nanoparticles. *J. Supercrit. Fluids* **2007**, *42* (2), 226–233.
(200) Cannas, C.; Musinu, A.; Ardu, A.; Orrù, F.; Peddis, D.; Casu, M.; Sanna, R.; Angius, F.; Diaz, G.; Piccaluga, G. CoFe 2 O 4 and CoFe 2 O 4 /SiO 2 Core/Shell Nanoparticles: Magnetic and Spectroscopic Study. *Chem. Mater.* **2010**, *22* (11), 3353–3361.
(201) Cheng, H.-W.; Li, J.; Wong, S.; Zhong, C.-J. Assessment of Aggregative Growth of MnZn Ferrite Nanoparticles. *Nanoscale* **2016**, *8* (46), 19359–19367.
(202) Angelakeris, M.; Li, Z.-A.; Hilgendorff, M.; Simeonidis, K.; Sakellari, D.; Filippousi, M.; Tian, H.; Van Tendeloo, G.; Spasova, M.; Acet, M.; et al. Enhanced Biomedical Heat-Triggered Carriers via Nanomagnetism Tuning in Ferrite-Based Nanoparticles. *J. Magn. Magn. Mater.* **2015**, *381*, 179–187.
(203) Cheon, J.; Kang, N.-J.; Lee, S.-M.; Lee, J.-H.; Yoon, J.-H.; Oh, S. J. Shape Evolution of Single-Crystalline Iron Oxide Nanocrystals. *J. Am. Chem. Soc.* **2004**, *126* (7), 1950–1951.
(204) Davis, R.; Schultz, H. P. Studies of Thermal Decarboxylation of Iron Carboxylates. I. Preparation of Symmetrical Aliphatic Ketones. *J. Org. Chem.* **1962**, *27* (3), 854–857.
(205) De-León-Prado, L. E.; Cortés-Hernández, D. A.; Almanza-Robles, J. M.; Escobedo-Bocardo, J. C.; Sánchez, J.; Reyes-Rdz, P. Y.; Jasso-Terán, R. A.; Hurtado-López, G. F. Synthesis and Characterization of Nanosized MgxMn1−xFe2O4 Ferrites by Both Sol-Gel and Thermal Decomposition Methods. *J. Magn. Magn. Mater.* **2017**, *427* (June 2016), 230–234.
(206) Demortière, A.; Panissod, P.; Pichon, B. P.; Pourroy, G.; Guillon, D.; Donnio, B.; Bégin-Colin, S. Size-Dependent Properties of Magnetic Iron Oxidenanocrystals. *Nanoscale* **2011**, *3* (1), 225–232.
(207) Fantechi, E.; Innocenti, C.; Albino, M.; Lottini, E.; Sangregorio, C. Influence of Cobalt Doping on the Hyperthermic Efficiency of Magnetite Nanoparticles. *J. Magn. Magn. Mater.* **2015**, *380*, 365–371.
(208) Gavrilov-Isaac, V.; Neveu, S.; Dupuis, V.; Taverna, D.; Gloter, A.; Cabuil, V. Synthesis of Trimagnetic Multishell MnFe2O4@CoFe2O4@NiFe2O4 Nanoparticles. *Small* **2015**, *11* (22), 2614–2618.
(209) Guardia, P.; Batlle-Brugal, B.; Roca, A. G.; Iglesias, O.; Morales, M. P.; Serna, C. J.; Labarta, A.; Batlle, X. Surfactant Effects in Magnetite Nanoparticles of Controlled Size. *J. Magn. Magn. Mater.* **2007**, *316* (2 SPEC. ISS.), 756–759.
(210) Gyergyek, S.; Makovec, D.; Kodre, A.; Arčon, I.; Jagodič, M.; Drofenik, M. Influence of Synthesis Method on Structural and Magnetic Properties of Cobalt Ferrite Nanoparticles. *J. Nanoparticle Res.* **2010**, *12* (4), 1263–1273.
(211) Hu, F.; Wei, L.; Zhou, Z.; Ran, Y.; Li, Z.; Gao, M. Preparation of Biocompatible Magnetite Nanocrystals for in Vivo Magnetic Resonance Detection of Cancer. *Adv. Mater.* **2006**, *18* (19), 2553–2556.
(212) Jana, N. R.; Chen, Y.; Peng, X. Size- and Shape-Controlled Magnetic (Cr, Mn, Fe, Co, Ni) Oxide Nanocrystals via a Simple and General Approach. *Chem. Mater.* **2004**, *16* (20), 3931–3935.
(213) Jeun, M.; Moon, S. J.; Kobayashi, H.; Shin, H. Y.; Tomitaka, A.; Kim, Y. J.; Takemura, Y.; Paek, S. H.; Park, K. H.; Chung, K. W.; et al. Effects of Mn Concentration on the Ac Magnetically Induced Heating Characteristics of Superparamagnetic MnxZn1-XFe 2O4 Nanoparticles for Hyperthermia. *Appl. Phys. Lett.* **2010**, *96* (20), 6–9.
(214) Jeun, M.; Park, S.; Jang, G. H.; Lee, K. H. Tailoring MgxMn1-XFe2O4 Superparamagnetic Nanoferrites for Magnetic Fluid Hyperthermia Applications. *ACS Appl. Mater. Interfaces* **2014**, *6* (19), 16487–16492.
(215) Kang, E.; Park, J.; Hwang, Y.; Kang, M.; Park, J. G.; Hyeon, T. Direct Synthesis of Highly Crystalline and Monodisperse Manganese Ferrite Nanocrystals. *J. Phys. Chem. B* **2004**, *108* (37), 13932–13935.
(216) Lasheras, X.; Insausti, M.; Gil de Muro, I.; Garaio, E.; Plazaola, F.; Moros, M.; De Matteis, L.; M. de la Fuente, J.; Lezama, L. Chemical Synthesis and Magnetic Properties of Monodisperse Nickel Ferrite Nanoparticles for Biomedical Applications. *J. Phys. Chem. C* **2016**, *120* (6), 3492–3500.
(217) Lassenberger, A.; Grünewald, T. A.; Van Oostrum, P. D. J.; Rennhofer, H.; Amenitsch, H.; Zirbs, R.; Lichtenegger, H. C.; Reimhult, E. Monodisperse Iron Oxide Nanoparticles by Thermal Decomposition: Elucidating Particle Formation by Second-Resolved in Situ Small-

Angle X-Ray Scattering. *Chem. Mater.* **2017**, *29* (10), 4511–4522.
(218) Lee, J.-H. H.; Jang, J.-T. T.; Choi, J.-S. S.; Moon, S. H.; Noh, S.-H. H.; Kim, J.-G. W. G. J.-W.; Kim, I.-S. S.; Park, K. I.; Cheon, J.; Kim, J.-G. W. G. J.-W.; et al. Exchange-Coupled Magnetic Nanoparticles for Efficient Heat Induction. *Nat. Nanotechnol.* **2011**, *6* (7), 418–422.
(219) Li, D.; Yun, H.; Diroll, B. T.; Doan-Nguyen, V. V. T.; Kikkawa, J. M.; Murray, C. B. Synthesis and Size-Selective Precipitation of Monodisperse Nonstoichiometric MxFe3-XO4 (M = Mn, Co) Nanocrystals and Their DC and AC Magnetic Properties. *Chem. Mater.* **2016**, *28* (2), 480–489.
(220) Li, Y.; Afzaal, M.; O'Brien, P. The Synthesis of Amine-Capped Magnetic (Fe, Mn, Co, Ni) Oxide Nanocrystals and Their Surface Modification for Aqueous Dispersibility. *J. Mater. Chem.* **2006**, *16* (22), 2175.
(221) Li, Z.; Chen, H.; Bao, H.; Gao, M. One-Pot Reaction to Synthesize Water-Soluble Magnetite Nanocrystals. *Chem. Mater.* **2004**, *16* (8), 1391–1393.
(222) Li, Z.; Sun, Q.; Gao, M. Preparation of Water-Soluble Magnetite Nanocrystals from Hydrated Ferric Salts in 2-Pyrrolidone: Mechanism Leading to Fe3O4. *Angew. Chemie - Int. Ed.* **2004**, *44* (1), 123–126.
(223) Lu, L. T.; Dung, N. T.; Tung, L. D.; Thanh, C. T.; Quy, O. K.; Chuc, N. V.; Maenosono, S.; Thanh, N. T. K. Synthesis of Magnetic Cobalt Ferrite Nanoparticles with Controlled Morphology, Monodispersity and Composition: The Influence of Solvent, Surfactant, Reductant and Synthetic Conditions. *Nanoscale* **2015**, *7* (46), 19596–19610.
(224) Mameli, V.; Musinu, A.; Ardu, A.; Ennas, G.; Peddis, D.; Niznansky, D.; Sangregorio, C.; Innocenti, C.; Thanh, N. T. K.; Cannas, C. Studying the Effect of Zn-Substitution on the Magnetic and Hyperthermic Properties of Cobalt Ferrite Nanoparticles. *Nanoscale* **2016**, *8* (19), 10124–10137.
(225) Masala, O.; Hoffman, D.; Sundaram, N.; Page, K.; Proffen, T.; Lawes, G.; Seshadri, R. Preparation of Magnetic Spinel Ferrite Core/Shell Nanoparticles: Soft Ferrites on Hard Ferrites and Vice Versa. *Solid State Sci.* **2006**, *8* (9), 1015–1022.
(226) Masala, O.; Seshadri, R. Magnetic Properties of Capped, Soluble MnFe2O4 Nanoparticles. *Chem. Phys. Lett.* **2005**, *402* (December 2004), 160–164.
(227) Mathur, S.; Cavelius, C.; Moh, K.; Shen, H.; Bauer, J. Cobalt Ferrite Nanoparticles from Single and Multi-Component Precursor Systems. *Zeitschrift fur Anorg. und Allg. Chemie* **2009**, *635* (6–7), 898–902.
(228) Moriya, M.; Ito, M.; Sakamoto, W.; Yogo, T. One-Pot Synthesis and Morphology Control of Spinel Ferrite (MFe 2 O 4 , M = Mn, Fe, and Co) Nanocrystals from Homo- and Heterotrimetallic Clusters. *Cryst. Growth Des.* **2009**, *9* (4), 1889–1893.
(229) Muscas, G.; Concas, G.; Cannas, C.; Musinu, A.; Ardu, A.; Orrù, F.; Fiorani, D.; Laureti, S.; Rinaldi, D.; Piccaluga, G.; et al. Magnetic Properties of Small Magnetite Nanocrystals. *J. Phys. Chem. C* **2013**, *117* (44), 23378–23384.
(230) Nakhjavan, B.; Tahir, M. N.; Panthöfer, M.; Gao, H.; Schladt, T. D.; Gasi, T.; Ksenofontov, V.; Branscheid, R.; Weber, S.; Kolb, U.; et al. Synthesis, Characterization and Functionalization of Nearly Mono-Disperse Copper Ferrite CuxFe3−xO4 Nanoparticles. *J. Mater. Chem.* **2011**, *21* (19), 6909.
(231) Noh, S.; Na, W.; Jang, J.; Lee, J.-H.; Lee, E. J.; Moon, S. H.; Lim, Y.; Shin, J.-S.; Cheon, J. Nanoscale Magnetism Control via Surface and Exchange Anisotropy for Optimized Ferrimagnetic Hysteresis. *Nano Lett.* **2012**, *12* (7), 3716–3721.
(232) Park, J.; An, K.; Hwang, Y.; Park, J.-G.; Noh, H.-J.; Kim, J.-Y.; Park, J.-H.; Hwang, N.-M.; Hyeon, T. Ultra-Large-Scale Syntheses of Monodisperse Nanocrystals. *Nat. Mater.* **2004**, *3* (12), 891–895.
(233) Park, J.; Lee, E.; Hwang, N.-M.; Kang, M.; Kim, S. C.; Hwang, Y.; Park, J.-G.; Noh, H.-J.; Kim, J.-Y.; Park, J.-H.; et al. One-Nanometer-Scale Size-Controlled Synthesis of Monodisperse Magnetic Iron Oxide Nanoparticles. *Angew. Chemie Int. Ed.* **2005**, *44* (19), 2872–2877.
(234) Peddis, D.; Cannas, C.; Musinu, A.; Ardu, A.; Orrù, F.; Fiorani, D.; Laureti, S.; Rinaldi, D.; Muscas, G.; Concas, G.; et al. Beyond the Effect of Particle Size: Influence of CoFe 2 O 4 Nanoparticle Arrangements on Magnetic Properties. *Chem. Mater.* **2013**, *25* (10), 2005–2013.
(235) Peddis, D.; Orrù, F.; Ardu, A.; Cannas, C.; Musinu, A.; Piccaluga, G. Interparticle Interactions and Magnetic Anisotropy in Cobalt Ferrite Nanoparticles: Influence of Molecular Coating. *Chem. Mater.* **2012**, *24* (6), 1062–1071.
(236) Redl, F. X.; Black, C. T.; Papaefthymiou, G. C.; Sandstrom, R. L.; Yin, M.; Zeng, H.; Murray, C. B.; O'Brien, S. P. Magnetic, Electronic, and Structural Characterization of Nonstoichiometric Iron Oxides at the Nanoscale. *J. Am. Chem. Soc.* **2004**, *126* (44), 14583–14599.
(237) Roca, A. G.; Morales, M. P.; O'Grady, K.; Serna, C. J. Structural and Magnetic Properties of Uniform Magnetite Nanoparticles Prepared by High Temperature Decomposition of Organic Precursors. *Nanotechnology* **2006**, *17* (11), 2783–2788.
(238) Sathya, A.; Guardia, P.; Brescia, R.; Silvestri, N.; Pugliese, G.; Nitti, S.; Manna, L.; Pellegrino, T. Co x Fe 3– x O 4 Nanocubes for Theranostic Applications: Effect of Cobalt Content and

Particle Size. *Chem. Mater.* **2016**, *28* (6), 1769–1780.
(239) Song, L.; Yan, C.; Zhang, W.; Wu, H.; Jia, Z.; Ma, M.; Xie, J.; Gu, N.; Zhang, Y. Influence of Reaction Solvent on Crystallinity and Magnetic Properties of MnFe 2 O 4 Nanoparticles Synthesized by Thermal Decomposition. *J. Nanomater.* **2016**, *2016*, 1–8.
(240) Abdulwahab, K. O.; Malik, M. A.; O'Brien, P.; Timco, G. A.; Tuna, F.; Muryn, C. A.; Winpenny, R. E. P.; Pattrick, R. A. D.; Coker, V. S.; Arenholz, E. A One-Pot Synthesis of Monodispersed Iron Cobalt Oxide and Iron Manganese Oxide Nanoparticles from Bimetallic Pivalate Clusters. *Chem. Mater.* **2014**, *26* (2), 999–1013.
(241) Song, Q.; Ding, Y.; Wang, Z. L.; Zhang, Z. J. Tuning the Thermal Stability of Molecular Precursors for the Nonhydrolytic Synthesis of Magnetic MnFe 2 O 4 Spinel Nanocrystals. *Chem. Mater.* **2007**, *19* (19), 4633–4638.
(242) Song, Q.; Zhang, Z. J. Shape Control and Associated Magnetic Properties of Spinel Cobalt Ferrite Nanocrystals. *J. Am. Chem. Soc.* **2004**, *126* (19), 6164–6168.
(243) Song, Q.; Zhang, Z. J. Controlled Synthesis and Magnetic Properties of Bimagnetic Spinel Ferrite CoFe2O4 and MnFe2O4 Nanocrystals with Core-Shell Architecture. *J. Am. Chem. Soc.* **2012**, *134* (24), 10182–10190.
(244) Soon, G. K.; Piao, Y.; Park, J.; Angappane, S.; Jo, Y.; Hwang, N. M.; Park, J. G.; Hyeon, T. Kinetics of Monodisperse Iron Oxide Nanocrystal Formation by "Heating-up" Process. *J. Am. Chem. Soc.* **2007**, *129* (41), 12571–12584.
(245) Virumbrales-del Olmo, M.; Delgado-Cabello, A.; Andrada-Chacón, A.; Sánchez-Benítez, J.; Urones-Garrote, E.; Blanco-Gutiérrez, V.; Torralvo, M. J.; Sáez-Puche, R. Effect of Composition and Coating on the Interparticle Interactions and Magnetic Hardness of MFe_2O_4 (M = Fe, Co, Zn) Nanoparticles. *Phys. Chem. Chem. Phys.* **2017**, *19* (12), 8363–8372.
(246) Wang, L.; Yan, Y.; Wang, M.; Yang, H.; Zhou, Z.; Peng, C.; Yang, S. An Integrated Nanoplatform for Theranostics via Multifunctional Core-Shell Ferrite Nanocubes. *J. Mater. Chem. B* **2016**, *4* (10), 1908–1914.
(247) Woo, K.; Hong, J.; Choi, S.; Lee, H.-W.; Ahn, J.-P.; Kim, C. S.; Lee, S. W. Easy Synthesis and Magnetic Properties of Iron Oxide Nanoparticles. *Chem. Mater.* **2004**, *16* (14), 2814–2818.
(248) Xie, J.; Yan, C.; Zhang, Y.; Gu, N. Shape Evolution of "Multibranched" Mn–Zn Ferrite Nanostructures with High Performance: A Transformation of Nanocrystals into Nanoclusters. *Chem. Mater.* **2013**, *25* (18), 3702–3709.
(249) Yang, W.; Yu, Y.; Wang, L.; Yang, C.; Li, H. Controlled Synthesis and Assembly into Anisotropic Arrays of Magnetic Cobalt-Substituted Magnetite Nanocubes. *Nanoscale* **2015**, *7* (7), 2877–2882.
(250) Yao, C.; Zeng, Q.; Goya, G. F.; Torres, T.; Liu, J.; Wu, H.; Ge, M.; Zeng, Y.; Wang, Y.; Jiang, J. Z. ZnFe2O4 Nanocrystals: Synthesis and Magnetic Properties. *J. Phys. Chem. C* **2007**, *111* (33), 12274–12278.
(251) Sun, S.; Zeng, H.; Robinson, D. B.; Raoux, S.; Rice, P. M.; Wang, S. X.; Li, G. Monodisperse MFe2O4 (M = Fe, Co, Mn) Nanoparticles. *J. Am. Chem. Soc.* **2004**, *126* (1), 273–279.
(252) Yu, W. W.; Falkner, J. C.; Yavuz, C. T.; Colvin, V. L. Synthesis of Monodisperse Iron Oxide Nanocrystals by Thermal Decomposition of Iron Carboxylate Salts. *Chem. Commun.* **2004**, No. 20, 2306.
(253) Yun, H.; Kim, J.; Paik, T.; Meng, L.; Jo, P. S.; Kikkawa, J. M.; Kagan, C. R.; Allen, M. G.; Murray, C. B. Alternate Current Magnetic Property Characterization of Nonstoichiometric Zinc Ferrite Nanocrystals for Inductor Fabrication via a Solution Based Process. *J. Appl. Phys.* **2016**, *119* (11).
(254) Zeng, H.; Rice, P. M.; Wang, S. X.; Sun, S. Shape-Controlled Synthesis and Shape-Induced Texture of MnFe 2 O 4 Nanoparticles. *J. Am. Chem. Soc.* **2004**, *126* (37), 11458–11459.
(255) Vestal, C. R.; Song, Q.; Zhang, Z. J. Effects of Interparticle Interactions upon the Magnetic Properties of $CoFe_2O_4$ and $MnFe_2O_4$ Nanocrystals. *J. Phys. Chem. B* **2004**, *108* (47), 18222–18227.
(256) Monfared, A. H.; Zamanian, A.; Beygzadeh, M.; Sharifi, I.; Mozafari, M. A Rapid and Efficient Thermal Decomposition Approach for the Synthesis of Manganese-Zinc/Oleylamine Core/Shell Ferrite Nanoparticles. *J. Alloys Compd.* **2017**, *693*, 1090–1095.
(257) Kim, D.; Lee, N.; Park, M.; Kim, B. H.; An, K.; Hyeon, T. Synthesis of Uniform Ferrimagnetic Magnetite Nanocubes. *J. Am. Chem. Soc.* **2009**, *131* (2), 454–455.
(258) Li, Z.; Wei, L.; Gao, M. Y.; Lei, H. One-Pot Reaction to Synthesize Biocompatible Magnetite Nanoparticles. *Adv. Mater.* **2005**, *17* (8), 1001–1005.
(259) Hyun, S. W.; Kim, H. J.; Park, C. S.; Kang, K.-S.; Kim, C. S. Synthesis and Size Dependent Properties of Magnesium Ferrites. *IEEE Trans. Magn.* **2009**, *45* (6), 2551–2553.
(260) Bao, N.; Shen, L.; An, W.; Padhan, P.; Heath Turner, C.; Gupta, A. Formation Mechanism and Shape Control of Monodisperse Magnetic CoFe 2 O 4 Nanocrystals. *Chem. Mater.* **2009**, *21* (14), 3458–3468.
(261) Bao, N.; Shen, L.; Wang, Y.; Padhan, P.; Gupta, A. A Facile Thermolysis Route to Monodisperse Ferrite Nanocrystals. *J. Am. Chem. Soc.* **2007**, *129* (41), 12374–12375.

(262) Cabrera, L. I.; Somoza, Á.; Marco, J. F.; Serna, C. J.; Puerto Morales, M. Synthesis and Surface Modification of Uniform MFe 2O 4 (M = Fe, Mn, and Co) Nanoparticles with Tunable Sizes and Functionalities. *J. Nanoparticle Res.* **2012**, *14* (6).
(263) Pinna, N.; Grancharov, S.; Beato, P.; Bonville, P.; Antonietti, M.; Niederberger, M. Magnetite Nanocrystals: Nonaqueous Synthesis, Characterization, and Solubility. *Chem. Mater.* **2005**, *17* (11), 3044–3049.
(264) Masthoff, I. C.; Kraken, M.; Mauch, D.; Menzel, D.; Munevar, J. A.; Baggio Saitovitch, E.; Litterst, F. J.; Garnweitner, G. Study of the Growth Process of Magnetic Nanoparticles Obtained via the Non-Aqueous Sol-Gel Method. *J. Mater. Sci.* **2014**, *49* (14), 4705–4714.
(265) Yáñez-Vilar, S.; Sánchez-Andújar, M.; Gómez-Aguirre, C.; Mira, J.; Señarís-Rodríguez, M. A.; Castro-García, S. A Simple Solvothermal Synthesis of MFe2O4 (M=Mn, Co and Ni) Nanoparticles. *J. Solid State Chem.* **2009**, *182* (10), 2685–2690.
(266) Bilecka, I.; Djerdj, I.; Niederberger, M. One-Minute Synthesis of Crystalline Binary and Ternary Metal Oxide Nanoparticles. *Chem. Commun.* **2008**, No. 7, 886–888.
(267) Kubli, M.; Luo, L.; Bilecka, I.; Niederberger, M. Microwave-Assisted Nonaqueous Sol–Gel Deposition of Different Spinel Ferrites and Barium Titanate Perovskite Thin Films. *Chim. Int. J. Chem.* **2010**, *64* (3), 170–172.
(268) Bilecka, I.; Kubli, M.; Amstad, E.; Niederberger, M. Simultaneous Formation of Ferrite Nanocrystals and Deposition of Thin Films via a Microwave-Assisted Nonaqueous Sol–gel Process. *J. Sol-Gel Sci. Technol.* **2011**, *57* (3), 313–322.
(269) Baek, S.; Yu, S.-H.; Park, S.-K.; Pucci, A.; Marichy, C.; Lee, D.-C.; Sung, Y.-E.; Piao, Y.; Pinna, N. A One-Pot Microwave-Assisted Non-Aqueous Sol–gel Approach to Metal Oxide/Graphene Nanocomposites for Li-Ion Batteries. *RSC Adv.* **2011**, *1* (9), 1687.
(270) Erdem, D.; Bingham, N. S.; Heiligtag, F. J.; Pilet, N.; Warnicke, P.; Heyderman, L. J.; Niederberger, M. CoFe2O4 and CoFe2O4-SiO2 Nanoparticle Thin Films with Perpendicular Magnetic Anisotropy for Magnetic and Magneto-Optical Applications. *Adv. Funct. Mater.* **2016**, *26* (12), 1954–1963.
(271) Sciancalepore, C.; Rosa, R.; Barrera, G.; Tiberto, P.; Allia, P.; Bondioli, F. Microwave-Assisted Nonaqueous Sol e Gel Synthesis of Highly Crystalline Magnetite Nanocrystals. *Mater. Chem. Phys.* **2014**, *148* (1–2), 117–124.
(272) Ooi, F.; Duchene, J. S.; Qiu, J.; Graham, J. O.; Engelhard, M. H.; Cao, G.; Gai, Z.; Wei, W. D. A Facile Solvothermal Synthesis of Octahedral Fe3O4nanoparticles. *Small* **2015**, *11* (22), 2649–2653.
(273) Tian, Y.; Yu, B.; Li, X.; Li, K. Facile Solvothermal Synthesis of Monodisperse Fe3O4 Nanocrystals with Precise Size Control of One Nanometre as Potential MRI Contrast Agents. *J. Mater. Chem.* **2011**, *21* (8), 2476.
(274) Qi, M.; Zhang, K.; Li, S.; Wu, J.; Pham-Huy, C.; Diao, X.; Xiao, D.; He, H. Superparamagnetic Fe $_3$ O $_4$ Nanoparticles: Synthesis by a Solvothermal Process and Functionalization for a Magnetic Targeted Curcumin Delivery System. *New J. Chem.* **2016**, *40* (5), 4480–4491.
(275) Blanco-Gutierrez, V.; Climent-Pascual, E.; Torralvo-Fernandez, M. J.; Saez-Puche, R.; Fernandez-Diaz, M. T. Neutron Diffraction Study and Superparamagnetic Behavior of ZnFe 2O4 Nanoparticles Obtained with Different Conditions. *J. Solid State Chem.* **2011**, *184* (7), 1608–1613.
(276) Li, X. H.; Xu, C. L.; Han, X. H.; Qiao, L.; Wang, T.; Li, F. S. Synthesis and Magnetic Properties of Nearly Monodisperse CoFe 2O 4 Nanoparticles through a Simple Hydrothermal Condition. *Nanoscale Res. Lett.* **2010**, *5* (6), 1039–1044.
(277) Ma, J.; Hou, Y.; Ji, T.; Zhao, J.; Zhang, S. Preparation of MnFe $_2$ O $_4$ Nanoparticles *Via* a Facile Water-Glycol Solvothermal Approach. *Synth. React. Inorganic, Met. Nano-Metal Chem.* **2016**, *46* (10), 1513–1518.
(278) Jia, X.; Chen, D.; Jiao, X.; He, T.; Wang, H.; Jiang, W. Monodispersed Co , Ni-Ferrite Nanoparticles with Tunable Sizes: Controlled Synthesis, Magnetic Properties, and Surface Modification. *J. Phys. Chem. C* **2008**, *112* (4), 911–917.
(279) Munjal, S.; Khare, N.; Nehate, C.; Koul, V. Water Dispersible CoFe2O4 Nanoparticles with Improved Colloidal Stability for Biomedical Applications. *J. Magn. Magn. Mater.* **2016**, *404*, 166–169.
(280) Li, S.; Zhang, T.; Tang, R.; Qiu, H.; Wang, C.; Zhou, Z. Solvothermal Synthesis and Characterization of Monodisperse Superparamagnetic Iron Oxide Nanoparticles. *J. Magn. Magn. Mater.* **2015**, *379*, 226–231.
(281) Stoia, M.; Muntean, E.; Păcurariu, C.; Mihali, C. Thermal Behavior of MnFe2O4 and MnFe2O4 /C Nanocomposite Synthesized by a Solvothermal Method. *Thermochim. Acta* **2017**, *652*, 1–8.
(282) Hou, C.; Yu, H.; Zhang, Q.; Li, Y.; Wang, H. Preparation and Magnetic Property Analysis of Monodisperse Co-Zn Ferrite Nanospheres. *J. Alloys Compd.* **2010**, *491* (1–2), 431–435.
(283) Wang, J.; Ren, F.; Yi, R.; Yan, A.; Qiu, G.; Liu, X. Solvothermal Synthesis and Magnetic Properties of Size-Controlled Nickel Ferrite Nanoparticles. *J. Alloys Compd.* **2009**, *479* (1–2),

791–796.
(284) Blanco-Gutiérrez, V.; Torralvo-Fernandez, M. J.; Saez-Puche, R. Innovative Study of Superparamagnetism in 3 Nm CoFe2O4 Particles. *RSC Adv.* **2016**, *6*, 87995–88000.
(285) Vázquez-Vázquez, C.; López-Quintela, M. A.; Buján-Núñez, M. C.; Rivas, J. Finite Size and Surface Effects on the Magnetic Properties of Cobalt Ferrite Nanoparticles. *J. Nanoparticle Res.* **2011**, *13* (4), 1663–1676.
(286) Stoia, M.; Păcurariu, C.; Muntean, E. C. Thermal Stability of the Solvothermal-Synthesized MnFe2O4 Nanopowder. *J. Therm. Anal. Calorim.* **2017**, *127* (1), 155–162.
(287) Bi, Y.; Ren, Y.; Bi, F.; He, T. Water-Assisted and Surfactant-Free Synthesis of Cobalt Ferrite Nanospheres via Solvothermal Method. *J. Alloys Compd.* **2015**, *646*, 827–832.
(288) Sanna Angotzi, M.; Musinu, A.; Mameli, V.; Ardu, A.; Cara, C.; Niznansky, D.; Xin, H. L.; Cannas, C. Spinel Ferrite Core–Shell Nanostructures by a Versatile Solvothermal Seed-Mediated Growth Approach and Study of Their Nanointerfaces. *ACS Nano* **2017**, *11* (8), 7889–7900.
(289) Repko, A.; Nižňanský, D.; Matulková, I.; Kalbáč, M.; Vejpravová, J. Hydrothermal Preparation of Hydrophobic and Hydrophilic Nanoparticles of Iron Oxide and a Modification with CM-Dextran. *J. Nanoparticle Res.* **2013**, *15* (7), 1–9.
(290) Wang, X.; Zhuang, J.; Peng, Q.; Li, Y. A General Strategy for Nanocrystal Synthesis. *Nature* **2005**, *437* (7055), 121–124.
(291) Repko, A.; Vejpravová, J.; Vacková, T.; Zákutná, D.; Nižňanský, D. Oleate-Based Hydrothermal Preparation of CoFe2O4 Nanoparticles, and Their Magnetic Properties with Respect to Particle Size and Surface Coating. *J. Magn. Magn. Mater.* **2015**, *390*, 142–151.
(292) Pinna, N.; Garnweitner, G.; Antonietti, M.; Niederberger, M. A General Nonaqueous Route to Binary Metal Oxide Nanocrystals Involving a C-C Bond Cleavage. *J. Am. Chem. Soc.* **2005**, *127* (15), 5608–5612.
(293) Repko, A.; Nižňanský, D.; Poltierová-Vejpravová, J. A Study of Oleic Acid-Based Hydrothermal Preparation of CoFe 2O4 Nanoparticles. *J. Nanoparticle Res.* **2011**, *13* (10), 5021–5031.
(294) Cara, C.; Musinu, A.; Mameli, V.; Ardu, A.; Niznansky, D.; Bursik, J.; Scorciapino, M. A.; Manzo, G.; Cannas, C. Dialkylamide as Both Capping Agent and Surfactant in a Direct Solvothermal Synthesis of Magnetite and Titania Nanoparticles. *Cryst. Growth Des.* **2015**, *15* (5), 2364–2372.
(295) Li, C.; Wei, Y.; Liivat, A.; Zhu, Y.; Zhu, J. Microwave-Solvothermal Synthesis of Fe 3 O 4 Magnetic Nanoparticles. *Mater. Lett.* **2013**, *107* (3), 23–26.
(296) Feng, X.; Mao, G. Y. Y.; Bu, F. X. X.; Cheng, X. L. L.; Jiang, D. M. M.; Jiang, J. S. S. Controlled Synthesis of Monodisperse CoFe2O4 Nanoparticles by the Phase Transfer Method and Their Catalytic Activity on Methylene Blue Discoloration with H2O2. *J. Magn. Magn. Mater.* **2013**, *343* (18), 126–132.
(297) Li, Z.; Godsell, J. F.; O'Byrne, J. P.; Petkov, N.; Morris, M. A.; Roy, S.; Holmes, J. D. Supercritical Fluid Synthesis of Magnetic Hexagonal Nanoplatelets of Magnetite. *J. Am. Chem. Soc.* **2010**, *132* (36), 12540–12541.
(298) Rangappa, D.; Sone, K.; Ichihara, M.; Kudo, T.; Honma, I. Rapid One-Pot Synthesis of LiMPO4 (M = Fe, Mn) Colloidal Nanocrystals by Supercritical Ethanol Process. *Chem. Commun.* **2010**, *46* (40), 7548–7550.
(299) Pascu, O.; Marre, S.; Aymonier, C.; Roig, A. Ultrafast and Continuous Synthesis of Crystalline Ferrite Nanoparticles in Supercritical Ethanol. *Nanoscale* **2013**, *5* (5), 2126.
(300) Pahari, S. K.; Adschiri, T.; Panda, A. B. Synthesis of Monodispersed Nanocrystalline Materials in Supercritical Ethanol: A Generalized Approach. *J. Mater. Chem.* **2011**, *21* (28), 10377.
(301) Veriansyah, B.; Kim, J. D.; Min, B. K.; Kim, J. Continuous Synthesis of Magnetite Nanoparticles in Supercritical Methanol. *Mater. Lett.* **2010**, *64* (20), 2197–2200.
(302) Vázquez-Vázquez, C.; Lovelle, M.; Mateo, C.; López-Quintela, M. A.; Buján-Núñez, M. C.; Serantes, D.; Baldomir, D.; Rivas, J. Magnetocaloric Effect and Size-Dependent Study of the Magnetic Properties of Cobalt Ferrite Nanoparticles Prepared by Solvothermal Synthesis. *Phys. status solidi* **2008**, *205* (6), 1358–1362.
(303) Fang, J.; Shama, N.; Tung, D. Le; Shin, E. Y.; O'Connor, C. J.; Stokes, K. L.; Caruntu, G.; Wiley, J. B.; Spinu, L.; Tang, J. Ultrafine NiFe2O4 Powder Fabricated from Reverse Microemulsion Process. *J. Appl. Phys.* **2003**, *93* (10), 7483–7485.
(304) Kale, A.; Gubbala, S.; Misra, R. D. K. Magnetic Behavior of Nanocrystalline Nickel Ferrite Synthesized by the Reverse Micelle Technique. *J. Magn. Magn. Mater.* **2004**, *277* (3), 350–358.
(305) Reddy, K. M.; Satyanarayana, L.; Manorama, S. V.; Misra, R. D. K. A Comparative Study of the Gas Sensing Behavior of Nanostructured Nickel Ferrite Synthesized by Hydrothermal and Reverse Micelle Techniques. *Mater. Res. Bull.* **2004**, *39* (10), 1491–1498.
(306) Karimi, A.; Sadatlu, M. A. A.; Saberi, B.; Shariatmadar, H.; Ashjaee, M. Experimental Investigation on Thermal Conductivity of Water Based Nickel Ferrite Nanofluids. *Adv.*

Powder Technol. **2015**, *26* (6), 1529–1536.
(307) Carpenter, E. E.; O'Connor, C. J.; Harris, V. G. Atomic Structure and Magnetic Properties of MnFe2O4 Nanoparticles Produced by Reverse Micelle Synthesis. *J. Appl. Phys.* **1999**, *85* (8 II A), 5175–5177.
(308) Liu, C.; Zou, B.; Rondinone, A. J.; Zhang, Z. J. Reverse Micelle Synthesis and Characterization of Superparamagnetic MnFe 2 O 4 Spinel Ferrite Nanocrystallites. *J. Phys. Chem. B* **2000**, *104* (6), 1141–1145.
(309) Liu, C.; Zhang, Z. J. Size-Dependent Superparamagnetic Properties of Mn Spinel Ferrite Nanoparticles Synthesized from Reverse Micelles. *Chem. Mater.* **2001**, *13* (14), 2092–2096.
(310) Bellusci, M.; Canepari, S.; Ennas, G.; La Barbera, A.; Padella, F.; Santini, A.; Scano, A.; Seralessandri, L.; Varsano, F. Phase Evolution in Synthesis of Manganese Ferrite Nanoparticles. *J. Am. Ceram. Soc.* **2007**, *90* (12), 3977–3983.
(311) Scano, A.; Ennas, G.; Frongia, F.; La Barbera, A.; López-Quintela, M. A.; Marongiu, G.; Paschina, G.; Peddis, D.; Pilloni, M.; Vázquez-Vázquez, C. Mn-Ferrite Nanoparticles via Reverse Microemulsions: Synthesis and Characterization. *J. Nanoparticle Res.* **2011**, *13* (7), 3063–3073.
(312) Hochepied, J. F.; Bonville, P.; Pileni, M. P. Nonstoichiometric Zinc Ferrite Nanocrystals: Syntheses and Unusual Magnetic Properties. *J. Phys. Chem. B* **2000**, *104* (5), 905–912.
(313) Makovec, D.; Košak, A.; Žnidaršič, A.; Drofenik, M. The Synthesis of Spinel–ferrite Nanoparticles Using Precipitation in Microemulsions for Ferrofluid Applications. *J. Magn. Magn. Mater.* **2005**, *289*, 32–35.
(314) Wang, J.; Chong, P. F.; Ng, S. C.; Gan, L. M. Microemulsion Processing of Manganese Zinc Ferrites. *Mater. Lett.* **1997**, *30* (2–3), 217–221.
(315) Gubbala, S.; Nathani, H.; Koizol, K.; Misra, R. D. K. Magnetic Properties of Nanocrystalline Ni-Zn, Zn-Mn, and Ni-Mn Ferrites Synthesized by Reverse Micelle Technique. *Phys. B Condens. Matter* **2004**, *348* (1–4), 317–328.
(316) Košak, A.; Makovec, D.; Žnidaršič, A.; Drofenik, M. Preparation of MnZn-Ferrite with Microemulsion Technique. *J. Eur. Ceram. Soc.* **2004**, *24* (6), 959–962.
(317) Morrison, S. A.; Cahill, C. L.; Carpenter, E. E.; Calvin, S.; Swaminathan, R.; McHenry, M. E.; Harris, V. G. Magnetic and Structural Properties of Nickel Zinc Ferrite Nanoparticles Synthesized at Room Temperature. *J. Appl. Phys.* **2004**, *95* (11), 6392–6395.
(318) Uskoković, V.; Drofenik, M.; Ban, I. The Characterization of Nanosized Nickel-Zinc Ferrites Synthesized within Reverse Micelles of CTAB/1-Hexanol/Water Microemulsion. *J. Magn. Magn. Mater.* **2004**, *284* (1–3), 294–302.
(319) Thakur, S.; Katyal, S. C.; Singh, M. Structural and Magnetic Properties of Nano Nickel-Zinc Ferrite Synthesized by Reverse Micelle Technique. *J. Magn. Magn. Mater.* **2009**, *321* (1), 1–7.
(320) Singh, C.; Jauhar, S.; Kumar, V.; Singh, J.; Singhal, S. Synthesis of Zinc Substituted Cobalt Ferrites via Reverse Micelle Technique Involving in Situ Template Formation: A Study on Their Structural, Magnetic, Optical and Catalytic Properties. *Mater. Chem. Phys.* **2015**, *156*, 188–197.
(321) Ebrahimi, H. R.; Parish, M.; Amiri, G. R.; Bahraminejad, B.; Fatahian, S. Synthesis, Characterization and Gas Sensitivity Investigation of Ni0.5Zn0.5Fe2O4 Nanoparticles. *J. Magn. Magn. Mater.* **2016**, *414*, 55–58.
(322) Lee, Y.; Lee, J.; Bae, C. J.; Park, J.-H. J.-G.; Noh, H.-J.; Park, J.-H. J.-G.; Hyeon, T. Large-Scale Synthesis of Uniform and Crystalline Magnetite Nanoparticles Using Reverse Micelles as Nanoreactors under Reflux Conditions. *Adv. Funct. Mater.* **2005**, *15* (3), 503–509.
(323) Chen, J. P.; Lee, K. M.; Sorensen, C. M.; Klabunde, K. J.; Hadjipanayis, G. C. Magnetic Properties of Microemulsion Synthesized Cobalt Fine Particles. *J. Appl. Phys.* **1994**, *75* (10), 5876–5878.
(324) Moumen, N.; Veillet, P.; Pileni, M. P. Controlled Preparation of Nanosize Cobalt Ferrite Magnetic Particles. *J. Magn. Magn. Mater.* **1995**, *149* (1–2), 67–71.
(325) Moumen, N.; Pileni, M. P. Control of the Size of Cobalt Ferrite Magnetic Fluid. *J. Phys. Chem.* **1996**, *100* (5), 1867–1873.
(326) Moumen, N.; Pileni, M. P. New Syntheses of Cobalt Ferrite Particles in the Range 2−5 Nm: Comparison of the Magnetic Properties of the Nanosized Particles in Dispersed Fluid or in Powder Form. *Chem. Mater.* **1996**, *8* (5), 1128–1134.
(327) Pillai, V.; Shah, D. O. Synthesis of High-Coercivity Cobalt Ferrite Particles Using Water-in-Oil Microemulsions. *J. Magn. Magn. Mater.* **1996**, *163* (1–2), 243–248.
(328) Rondinone, A. J.; Samia, A. C. S.; Zhang, Z. J. Superparamagnetic Relaxation and Magnetic Anisotropy Energy Distribution in CoFe2O4 Spinel Ferrite Nanocrystallites. *J. Phys. Chem. B* **1999**, *103* (33), 6876–6880.
(329) Tago, T.; Hatsuta, T.; Miyajima, K.; Kishida, M.; Tashiro, S.; Wakabayashi, K. Novel Synthesis of Silica-Coated Ferrite Nanoparticles Prepared Using Water-in-Oil Microemulsion. *J. Am. Ceram. Soc.* **2002**, *85* (9), 2188–2194.

(330) Ibrahim, A. M.; El-Latif, M. M. A.; Mahmoud, M. M. Synthesis and Characterization of Nano-Sized Cobalt Ferrite Prepared via Polyol Method Using Conventional and Microwave Heating Techniques. *J. Alloys Compd.* **2010**, *506* (1), 201–204.
(331) Wang, J.; Wan, J.; Chen, K. Facile Synthesis of Superparamagnetic Fe-Doped ZnO Nanoparticles in Liquid Polyols. *Mater. Lett.* **2010**, *64* (21), 2373–2375.
(332) Wu, H.; Zhang, N.; Mao, L.; Li, T.; Xia, L. Controlled Synthesis and Magnetic Properties of Monodisperse Ni1−xZnxFe2O4/MWCNT Nanocomposites via Microwave-Assisted Polyol Process. *J. Alloys Compd.* **2013**, *554*, 132–137.
(333) Abbas, M.; Parvatheeswara Rao, B.; Naga, S. M.; Takahashi, M.; Kim, C. Synthesis of High Magnetization Hydrophilic Magnetite (Fe3O 4) Nanoparticles in Single Reaction - Surfactantless Polyol Process. *Ceram. Int.* **2013**, *39* (7), 7605–7611.
(334) Parsons, P.; Duncan, K.; Giri, A. K.; Xiao, J. Q.; Karna, S. P. Electromagnetic Properties of NiZn Ferrite Nanoparticles and Their Polymer Composites. *J. Appl. Phys.* **2014**, *115* (17).
(335) Abbas, M.; Parvatheeswara Rao, B.; Kim, C. Shape and Size-Controlled Synthesis of Ni Zn Ferrite Nanoparticles by Two Different Routes. *Mater. Chem. Phys.* **2014**, *147* (3), 443–451.
(336) Kostopoulou, a; Brintakis, K.; Vasilakaki, M.; Trohidou, K. N.; Douvalis, a P.; Lascialfari, a; Manna, L.; Lappas, a. Assembly-Mediated Interplay of Dipolar Interactions and Surface Spin Disorder in Colloidal Maghemite Nanoclusters. *Nanoscale* **2014**, *6* (7), 3764–3776.
(337) Palchoudhury, S.; Lead, J. R. A Facile and Cost-Effective Method for Separation of Oil-Water Mixtures Using Polymer-Coated Iron Oxide Nanoparticles. *Environ. Sci. Technol.* **2014**, *48* (24), 14558–14563.
(338) Gaudisson, T.; Beji, Z.; Herbst, F.; Nowak, S.; Ammar, S.; Valenzuela, R. Ultrafine Grained High Density Manganese Zinc Ferrite Produced Using Polyol Process Assisted by Spark Plasma Sintering. *J. Magn. Magn. Mater.* **2015**, *387*, 90–95.
(339) Khot, V. M.; Salunkhe, A. B.; Ruso, J. M.; Pawar, S. H. Improved Magnetic Induction Heating of Nanoferrites for Hyperthermia Applications: Correlation with Colloidal Stability and Magneto-Structural Properties. *J. Magn. Magn. Mater.* **2015**, *384*, 335–343.
(340) Flores-Arias, Y.; Vázquez-Victorio, G.; Ortega-Zempoalteca, R.; Acevedo-Salas, U.; Ammar, S.; Valenzuela, R. Magnetic Phase Transitions in Ferrite Nanoparticles Characterized by Electron Spin Resonance. *J. Appl. Phys.* **2015**, *117* (17), 2013–2016.
(341) Beji, Z.; Sun, M.; Smiri, L. S.; Herbst, F.; Mangeney, C.; Ammar, S. Polyol Synthesis of Non-Stoichiometric Mn–Zn Ferrite Nanocrystals: Structural /Microstructural Characterization and Catalytic Application. *RSC Adv.* **2015**, *5* (80), 65010–65022.
(342) Töpfer, J.; Angermann, A. Nanocrystalline Magnetite and Mn-Zn Ferrite Particles via the Polyol Process: Synthesis and Magnetic Properties. *Mater. Chem. Phys.* **2011**, *129* (1–2), 337–342.
(343) Sabale, S.; Jadhav, V.; Khot, V.; Zhu, X.; Xin, M.; Chen, H. Superparamagnetic MFe2O 4 (M = Ni, Co, Zn, Mn) Nanoparticles: Synthesis, Characterization, Induction Heating and Cell Viability Studies for Cancer Hyperthermia Applications. *J. Mater. Sci. Mater. Med.* **2015**, *26* (3), 127.
(344) Piraux, H.; Hai, J.; Gaudisson, T.; Ammar, S.; Gazeau, F.; El Hage Chahine, J. M.; Hémadi, M. Transferrin-Bearing Maghemite Nano-Constructs for Biomedical Applications. *J. Appl. Phys.* **2015**, *117* (17).
(345) Amir, M.; Sertkol, M.; Baykal, A.; Sözeri, H. Magnetic and Catalytic Properties of Cu x Fe1−x Fe2O4 Nanoparticles. *J. Supercond. Nov. Magn.* **2015**, *28* (8), 2447–2454.
(346) Emadi, H.; Kharat, A. N. Synthesis and Characterization of Ultrafine and Mesoporous Structure of Cobalt Ferrite. *J. Ind. Eng. Chem.* **2015**, *21*, 951–956.
(347) Solano, E.; Yáñez, R.; Ricart, S.; Ros, J. Journal of Magnetism and Magnetic Materials New Approach towards the Polyol Route to Fabricate MFe 2 O 4 Magnetic Nanoparticles : The Use of MCl 2 and Fe (Acac) 3 as Chemical Precursors. *J. Magn. Magn. Mater.* **2015**, *382*, 1–6.
(348) Sathish, S.; Balakumar, S. Influence of Physicochemical Interactions of Capping Agent on Magnetic Properties of Magnetite Nanoparticles. *Mater. Chem. Phys.* **2016**, *173*, 364–371.
(349) Haddad, P. S.; Santos, M. C.; de Guzzi Cassago, C. A.; Bernardes, J. S.; de Jesus, M. B.; Seabra, A. B. Synthesis, Characterization, and Cytotoxicity of Glutathione-PEG-Iron Oxide Magnetic Nanoparticles. *J. Nanoparticle Res.* **2016**, *18* (12).
(350) Hanini, A.; Massoudi, M. El; Gavard, J.; Kacem, K.; Ammar, S.; Souilem, O. Nanotoxicological Study of Polyol-Made Cobalt-Zinc Ferrite Nanoparticles in Rabbit. *Environ. Toxicol. Pharmacol.* **2016**, *45*, 321–327.
(351) Wagle, D. V.; Rondinone, A. J.; Woodward, J. D.; Baker, G. A. Polyol Synthesis of Magnetite Nanocrystals in a Thermostable Ionic Liquid. *Cryst. Growth Des.* **2017**, *17* (4), 1558–1567.
(352) Pavithradevi, S.; Suriyanarayanan, N.; Boobalan, T.; Velumani, S.; Chandramohan, M.; Manivel Raja, M. Synthesis and Characterization of Polyol-Assisted Nano Cu0.2Ni0.2Sn0.2Ba0.4 Fe2O4 by a Wet Hydroxyl Route. *J. Electron. Mater.* **2017**, *46* (8), 4835–4841.
(353) Imine, S.; Schoenstein, F.; Mercone, S.; Zaghrioui, M.; Bettahar, N.; Jouini, N. Bottom-up and

New Compaction Processes: A Way to Tunable Properties of Nanostructured Cobalt Ferrite Ceramics. *J. Eur. Ceram. Soc.* **2011**, *31* (15), 2943–2955.
(354) Pavithradevi, S.; Suriyanarayanan, N.; Boobalan, T. Synthesis, Structural, Dielectric and Magnetic Properties of Polyol Assisted Copper Ferrite Nano Particles. *J. Magn. Magn. Mater.* **2017**, *426* (March 2016), 137–143.
(355) Wang, W.-W. Microwave-Induced Polyol-Process Synthesis of MIIFe2O4 (M = Mn, Co) Nanoparticles and Magnetic Property. *Mater. Chem. Phys.* **2008**, *108* (2–3), 227–231.
(356) Muscas, G.; Yaacoub, N.; Concas, G.; Sayed, F.; Sayed Hassan, R.; Greneche, J. M.; Cannas, C.; Musinu, A.; Foglietti, V.; Casciardi, S.; et al. Evolution of the Magnetic Structure with Chemical Composition in Spinel Iron Oxide Nanoparticles. *Nanoscale* **2015**, *7* (32), 13576–13585.
(357) Wan, J.; Jiang, X.; Li, H.; Chen, K. Facile Synthesis of Zinc Ferrite Nanoparticles as Non-Lanthanide T1 MRI Contrast Agents. *J. Mater. Chem.* **2012**, *22* (27), 13500.
(358) Ballot, N.; Schoenstein, F.; Mercone, S.; Chauveau, T.; Brinza, O.; Jouini, N. Reduction under Hydrogen of Ferrite MFe2O4 (M: Fe, Co, Ni) Nanoparticles Obtained by Hydrolysis in Polyol Medium: A Novel Route to Elaborate CoFe2, Fe and Ni3Fe Nanoparticles. *J. Alloys Compd.* **2012**, *536*, S381–S385.
(359) Xiao, W.; Gu, H.; Li, D.; Chen, D.; Deng, X.; Jiao, Z.; Lin, J. Microwave-Assisted Synthesis of Magnetite Nanoparticles for MR Blood Pool Contrast Agents. *J. Magn. Magn. Mater.* **2012**, *324* (4), 488–494.
(360) Ben Tahar, L.; Basti, H.; Herbst, F.; Smiri, L. S.; Quisefit, J. P.; Yaacoub, N.; Greneche, J. M.; Ammar, S. Co1-XZnxFe2O4 (0 <= x <= 1) Nanocrystalline Solid Solution Prepared by the Polyol Method: Characterization and Magnetic Properties. *Mater. Res. Bull.* **2012**, *47* (9), 2590–2598.
(361) Valenzuela, R.; Herbst, F.; Ammar, S. Ferromagnetic Resonance in Ni-Zn Ferrite Nanoparticles in Different Aggregation States. *J. Magn. Magn. Mater.* **2012**, *324* (21), 3398–3401.
(362) Sudalai Muthu, K.; Lakshminarasimhan, N. Impedance Spectroscopic Studies on NiFe2O4 with Different Morphologies: Microstructure vs. Dielectric Properties. *Ceram. Int.* **2013**, *39* (3), 2309–2315.
(363) Romero, V.; Costas-Mora, I.; Lavilla, I.; Bendicho, C. Insitu Ultrasound-Assisted Synthesis of Fe3O4 Nanoparticles with Simultaneous Ion Co-Precipitation for Multielemental Analysis of Natural Waters by Total Reflection X-Ray Fluorescence Spectrometry. *J. Anal. At. Spectrom.* **2013**, *28* (6), 923.
(364) Abbas, M.; Torati, S. R.; Rao, B. P.; Abdel-Hamed, M. O.; Kim, C. Size Controlled Sonochemical Synthesis of Highly Crystalline Superparamagnetic Mn–Zn Ferrite Nanoparticles in Aqueous Medium. *J. Alloys Compd.* **2015**, *644*, 774–782.
(365) Dang, F.; Enomoto, N.; Hojo, J.; Enpuku, K. Sonochemical Synthesis of Monodispersed Magnetite Nanoparticles by Using an Ethanol-Water Mixed Solvent. *Ultrason. Sonochem.* **2009**, *16* (5), 649–654.
(366) Mizukoshi, Y.; Shuto, T.; Masahashi, N.; Tanabe, S. Preparation of Superparamagnetic Magnetite Nanoparticles by Reverse Precipitation Method: Contribution of Sonochemically Generated Oxidants. *Ultrason. Sonochem.* **2009**, *16* (4), 525–531.
(367) Abbas, M.; Parvatheeswara Rao, B.; Nazrul Islam, M.; Kim, K. W.; Naga, S. M.; Takahashi, M.; Kim, C. Size-Controlled High Magnetization CoFe2O4 Nanospheres and Nanocubes Using Rapid One-Pot Sonochemical Technique. *Ceram. Int.* **2014**, *40* (2), 3269–3276.
(368) Kim, E. H.; Lee, H. S.; Kwak, B. K.; Kim, B. K. Synthesis of Ferrofluid with Magnetic Nanoparticles by Sonochemical Method for MRI Contrast Agent. *J. Magn. Magn. Mater.* **2005**, *289*, 328–330.
(369) Lv, W.; Liu, B.; Luo, Z.; Ren, X.; Zhang, P. XRD Studies on the Nanosized Copper Ferrite Powders Synthesized by Sonochemical Method. *J. Alloys Compd.* **2008**, *465* (1–2), 261–264.
(370) Lukashova, N. V.; Savchenko, A. G.; Yagodkin, Y. D.; Muradova, A. G.; Yurtov, E. V. Investigation of Structure and Magnetic Properties of Nanocrystalline Iron Oxide Powders for Use in Magnetic Fluids. *J. Alloys Compd.* **2014**, *586*, S298–S300.
(371) Wang, Y.; Nkurikiyimfura, I.; Pan, Z. Sonochemical Synthesis of Magnetic Nanoparticles. *Chem. Eng. Commun.* **2015**, *202* (5), 616–621.
(372) Abbas, M.; Islam, M. N.; Rao, B. P.; Abou Aitah, K. E.; Kim, C. Facile Approach for Synthesis of High Moment Fe/Ferrite and FeCo/Ferrite Core/Shell Nanostructures. *Mater. Lett.* **2015**, *139*, 161–164.
(373) Zhu, S.; Guo, J.; Dong, J.; Cui, Z.; Lu, T.; Zhu, C.; Zhang, D.; Ma, J. Sonochemical Fabrication of Fe3O4 Nanoparticles on Reduced Graphene Oxide for Biosensors. *Ultrason. Sonochem.* **2013**, *20* (3), 872–880.
(374) Goswami, P. P.; Choudhury, H. a; Chakma, S.; Moholkar, V. S. Sonochemical Synthesis of Cobalt Ferrite Nanoparticles. *Int. J. Chem. Eng.* **2013**, *2013*, 1–6.
(375) Dorniani, D.; Hussein, M. Z. Bin; Kura, A. U.; Fakurazi, S.; Shaari, A. H.; Ahmad, Z.

Preparation of Fe_3O_4 Magnetic Nanoparticles Coated with Gallic Acid for Drug Delivery. *Int. J. Nanomedicine* **2012**, *7*, 5745–5756.
(376) Abu-Much, R.; Gedanken, A. Sonochemical Synthesis under a Magnetic Field: Structuring Magnetite Nanoparticles and the Destabilization of a Colloidal Magnetic Aqueous Solution under a Magnetic Field. *J. Phys. Chem. C* **2008**, *112* (1), 35–42.
(377) Shafi, K. V. P. M.; Koltypin, Y.; Gedanken, A.; Lendvai, J.; Felner, I. Sonochemical Preparation of Nanosized Amorphous NiFe 2 O 4 Particles. *J. Phys. Chem. B* **1997**, *5647* (97), 6409–6414.
(378) Cheng, J. P.; Ma, R.; Chen, X.; Shi, D.; Liu, F.; Zhang, X. B. Effect of Ferric Ions on the Morphology and Size of Magnetite Nanocrystals Synthesized by Ultrasonic Irradiation. *Cryst. Res. Technol.* **2011**, *46* (7), 723–730.
(379) Sivakumar, M.; Takami, T.; Ikuta, H.; Towata, A.; Yasui, K.; Tuziuti, T.; Kozuka, T.; Bhattacharya, D.; Iida, Y. Fabrication of Zinc Ferrite Nanocrystals by Sonochemical Emulsification and Evaporation: Observation of Magnetization and Its Relaxation at Low Temperature. *J. Phys. Chem. B* **2006**, *110* (31), 15234–15243.
(380) Choudhury, H. A.; Choudhary, A.; Sivakumar, M.; Moholkar, V. S. Mechanistic Investigation of the Sonochemical Synthesis of Zinc Ferrite. *Ultrason. Sonochem.* **2013**, *20* (1), 294–302.
(381) Senapati, K. K.; Borgohain, C.; Phukan, P. Synthesis of Highly Stable CoFe2O4 Nanoparticles and Their Use as Magnetically Separable Catalyst for Knoevenagel Reaction in Aqueous Medium. *J. Mol. Catal. A Chem.* **2011**, *339* (1–2), 24–31.
(382) Abbas, M.; Takahashi, M.; Kim, C. Facile Sonochemical Synthesis of High-Moment Magnetite (Fe 3O4) Nanocube. *J. Nanoparticle Res.* **2013**, *15* (1).
(383) Wang, N.; Zhu, L.; Wang, D.; Wang, M.; Lin, Z.; Tang, H. Sono-Assisted Preparation of Highly-Efficient Peroxidase-like Fe3O4 Magnetic Nanoparticles for Catalytic Removal of Organic Pollutants with H2O2. *Ultrason. Sonochem.* **2010**, *17* (3), 526–533.
(384) Marchegiani, G.; Imperatori, P.; Mari, A.; Pilloni, L.; Chiolerio, A.; Allia, P.; Tiberto, P.; Suber, L. Sonochemical Synthesis of Versatile Hydrophilic Magnetite Nanoparticles. *Ultrason. Sonochem.* **2012**, *19* (4), 877–882.
(385) Suber, L.; Peddis, D. *Approaches to Synthesis and Characterization of Spherical and Anisometric Metal Oxide Magnetic Nanomaterials*; 2010; Vol. 4.
(386) Niederberger, M.; Pinna, N. *Metal Oxide Nanoparticles in Organic Solvents. Synthesis, Formation, Assembly and Application*; Springer, 2009.
(387) Brinker, C. J.; Scherer, G. W. *Sol-Gel Science*; 1990.
(388) Livage, J.; Henry, M.; Sanchez, C. Sol-Gel Chemistry of Transition Metal Oxides. *Prog. Solid State Chem.* **1988**, *18* (4), 259–341.
(389) LaMer, V. K.; Dinegar, R. H. Theory, Production and Mechanism of Formation of Monodispersed Hydrosols. *J. Am. Chem. Soc.* **1950**, *72* (11), 4847–4854.
(390) Ho, C.-H.; Tsai, C.-P.; Chung, C.-C.; Tsai, C.-Y.; Chen, F.-R.; Lin, H.-J.; Lai, C.-H. Shape-Controlled Growth and Shape-Dependent Cation Site Occupancy of Monodisperse Fe 3 O 4 Nanoparticles. *Chem. Mater.* **2011**, *23* (7), 1753–1760.
(391) Kwon, S. G.; Hyeon, T. Formation Mechanisms of Uniform Nanocrystals via Hot-Injection and Heat-up Methods. *Small* **2011**, *7* (19), 2685–2702.
(392) Bilecka, I.; Niederberger, M. New Developments in the Nonaqueous and/or Non-Hydrolytic Sol–gel Synthesis of Inorganic Nanoparticles. *Electrochim. Acta* **2010**, *55* (26), 7717–7725.
(393) Niederberger, M.; Garnweitner, G. Organic Reaction Pathways in the Nonaqueous Synthesis of Metal Oxide Nanoparticles. *Chem. - A Eur. J.* **2006**, *12* (28), 7282–7302.
(394) Slomkowski, S.; Alemán, J. V.; Gilbert, R. G.; Hess, M.; Horie, K.; Jones, R. G.; Kubisa, P.; Meisel, I.; Mormann, W.; Penczek, S.; et al. Terminology of Polymers and Polymerization Processes in Dispersed Systems (IUPAC Recommendations 2011). *Pure Appl. Chem.* **2011**, *83* (12), 2229–2259.
(395) Kwon, S. G.; Hyeon, T.; Soon, G. K.; Hyeon, T. Colloidal Chemical Synthesis and Formation Kinetics of Uniformly Sized Nanocrystals of Metals, Oxides, and Chalcogenides. *Acc. Chem. Res.* **2008**, *41* (12), 1696–1709.
(396) Hyeon, T. Chemical Synthesis of Magnetic Nanoparticles. *Chem. Commun.* **2003**, *9* (8), 927–934.
(397) Teja, A. S.; Koh, P. Y. Synthesis, Properties, and Applications of Magnetic Iron Oxide Nanoparticles. *Prog. Cryst. Growth Charact. Mater.* **2009**, *55* (1–2), 22–45.
(398) West, A. R. *Solid State Chemistry*; 2013.
(399) Feng, S.; Xu, R. New Materials in Hydrothermal Synthesis. *Acc. Chem. Res.* **2001**, *34* (3), 239–247.
(400) Aliofkhazraei, M. *Handbook of Nanoparticles*; Aliofkhazraei, M., Ed.; Springer International Publishing: Cham, 2015.
(401) Dinh, C.; Nguyen, T.; Kleitz, F.; Do, T. Shape-Controlled Synthesis of Highly Crystalline Titania Nanocrystals. *ACS Nano* **2009**, *3* (11), 3737–3743.
(402) Bilecka, I.; Niederberger, M. Microwave Chemistry for Inorganic Nanomaterials Synthesis.

Nanoscale **2010**, *2* (8), 1358.
(403) Scarfiello, R.; Nobile, C.; Cozzoli, P. D. Colloidal Magnetic Heterostructured Nanocrystals with Asymmetric Topologies: Seeded-Growth Synthetic Routes and Formation Mechanisms. *Front. Mater.* **2016**, *3* (December), 1–29.
(404) Carbone, L.; Cozzoli, P. D. Colloidal Heterostructured Nanocrystals: Synthesis and Growth Mechanisms. *Nano Today* **2010**, *5* (5), 449–493.
(405) Almeida, T. P.; Moro, F.; Fay, M. W.; Zhu, Y.; Brown, P. D. Tuneable Magnetic Properties of Hydrothermally Synthesised Core/Shell CoFe2O4/NiFe2O4 and NiFe2O4/CoFe2O4 Nanoparticles. *J. Nanoparticle Res.* **2014**, *16* (5), 1–13.
(406) Sattar, A. A.; EL-Sayed, H. M.; ALsuqia, I. Structural and Magnetic Properties of CoFe2O4/NiFe2O4 Core/Shell Nanocomposite Prepared by the Hydrothermal Method. *J. Magn. Magn. Mater.* **2015**, *395* (3), 89–96.
(407) Yu, L. Q.; Wen, Y. H.; Yan, M. Exchange Bias of MnFe2O4@γFe2O3 and CoFe2O4@γFe2O3 Core/Shell Nanoparticles. **2004**, *283* (2--3), 353–356.
(408) Gomes, J. a.; Azevedo, G. M.; Depeyrot, J.; Mestnik-Filho, J.; Paula, F. L. O.; Tourinho, F. a.; Perzynski, R. Structural, Chemical, and Magnetic Investigations of Core–Shell Zinc Ferrite Nanoparticles. *J. Phys. Chem. C* **2012**, *116* (45), 24281–24291.
(409) Lee, J.-H.; Jang, J.-T.; Choi, J.-S.; Moon, S. H.; Noh, S.-H.; Kim, J.-G. J.-W. J.-G. J.-W.; Kim, J.-G. J.-W. J.-G. J.-W.; Kim, I.-S.; Park, K. I.; Cheon, J. Exchange-Coupled Magnetic Nanoparticles for Efficient Heat Induction. *Nat. Nanotechnol.* **2011**, *6* (7), 418–422.
(410) Wang, J.; Zhou, Z.; Wang, L.; Wei, J.; Yang, H.; Yang, S.; Zhao, J. CoFe2O4@MnFe2O4/Polypyrrole Nanocomposites for in Vitro Photothermal/Magnetothermal Combined Therapy. *RSC Adv.* **2014**, *5* (10), 2–4.
(411) Zhang, Q.; Yin, T.; Gao, G.; Shapter, J. G.; Lai, W.; Huang, P.; Qi, W.; Song, J.; Cui, D. Multifunctional Core@Shell Magnetic Nanoprobes for Enhancing Targeted Magnetic Resonance Imaging and Fluorescent Labeling in Vitro and in Vivo. *ACS Appl. Mater. Interfaces* **2017**, *9* (21), 17777–17785.
(412) Angelakeris, M.; Li, Z. A.; Hilgendorff, M.; Simeonidis, K.; Sakellari, D.; Filippousi, M.; Tian, H.; Van Tendeloo, G.; Spasova, M.; Acet, M.; et al. Enhanced Biomedical Heat-Triggered Carriers via Nanomagnetism Tuning in Ferrite-Based Nanoparticles. *J. Magn. Magn. Mater.* **2015**, *381*, 179–187.
(413) Hammad, M.; Nica, V.; Hempelmann, R. Synthesis and Characterization of Bi-Magnetic Core/Shell Nanoparticles for Hyperthermia Applications. *IEEE Trans. Magn.* **2017**, *53* (4).
(414) Kim, M.; Kim, C. S.; Kim, H. J.; Yoo, K.-H.; Hahn, E. Effect Hyperthermia in CoFe2O4@MnFe2O4 Nanoparticles Studied by Using Field-Induced Mössbauer Spectroscopy. *J. Korean Phys. Soc.* **2013**, *63* (11), 2175–2178.
(415) Zhang, Q.; Castellanos-Rubio, I.; Munshi, R.; Orue, I.; Pelaz, B.; Gries, K. I.; Parak, W. J.; Del Pino, P.; Pralle, A. Model Driven Optimization of Magnetic Anisotropy of Exchange-Coupled Core-Shell Ferrite Nanoparticles for Maximal Hysteretic Loss. *Chem. Mater.* **2015**, *27* (21), 7380–7387.
(416) Liébana-Viñas, S.; Simeonidis, K.; Wiedwald, U.; Li, Z.-A.; Ma, Z.; Myrovali, E.; Makridis, A.; Sakellari, D.; Vourlias, G.; Spasova, M.; et al. Optimum Nanoscale Design in Ferrite Based Nanoparticles for Magnetic Particle Hyperthermia. *RSC Adv.* **2016**, *6* (77), 72918–72925.
(417) Robles, J.; Das, R.; Glassell, M.; Phan, M. H.; Srikanth, H. Exchange-Coupled Fe<inf>3</Inf>O<inf>4</Inf>/CoFe<inf>2</Inf>O<inf>4</Inf>nanoparticles for Advanced Magnetic Hyperthermia. *AIP Adv.* **2018**, *8* (5), 2–8.
(418) Sathya, A.; Guardia, P.; Brescia, R.; Silvestri, N.; Pugliese, G.; Nitti, S.; Manna, L.; Pellegrino, T. CoxFe3-XO4Nanocubes for Theranostic Applications: Effect of Cobalt Content and Particle Size. *Chem. Mater.* **2016**, *28* (6), 1769–1780.
(419) Wang, L.; Wang, X.; Luo, J.; Wanjala, B. N.; Wang, C.; Chernova, N. a.; Engelhard, M. H.; Liu, Y.; Bae, I. T.; Zhong, C. J. Core-Shell-Structured Magnetic Ternary Nanocubes. *J. Am. Chem. Soc.* **2010**, *132* (50), 17686–17689.
(420) Oberdick, S. D.; Abdelgawad, A.; Moya, C.; Mesbahi-Vasey, S.; Kepaptsoglou, D.; Lazarov, V. K.; Evans, R. F. L.; Meilak, D.; Skoropata, E.; Van Lierop, J.; et al. Spin Canting across Core/Shell Fe3O4/MnxFe3-XO4nanoparticles. *Sci. Rep.* **2018**, *8* (1), 1–12.
(421) Jiang, M.; Peng, X. Anisotropic Fe_3O_4/Mn_3O_4 Hybrid Nanocrystals with Unique Magnetic Properties. *Nano Lett.* **2017**, *17* (6), 3570–3575.
(422) López-Ortega, A.; Estrader, M.; Salazar-Alvarez, G.; Estradé, S.; Golosovsky, I. V; Dumas, R. K.; Keavney, D. J.; Vasilakaki, M.; Trohidou, K. N.; Sort, J.; et al. Strongly Exchange Coupled Inverse Ferrimagnetic Soft/Hard, Mn(x)Fe(3-x)O4/Fe(x)Mn(3-x)O4, Core/Shell Heterostructured Nanoparticles. *Nanoscale* **2012**, *4* (16), 5138–5147.
(423) Noh, S. H.; Na, W.; Jang, J. T.; Lee, J. H.; Lee, E. J.; Moon, S. H.; Lim, Y.; Shin, J. S.; Cheon, J. Nanoscale Magnetism Control via Surface and Exchange Anisotropy for Optimized Ferrimagnetic Hysteresis. *Nano Lett.* **2012**, *12* (7), 3716–3721.
(424) Estrader, M.; López-Ortega, A.; Estradé, S.; Golosovsky, I. V.; Salazar-Alvarez, G.; Vasilakaki,

M.; Trohidou, K. N.; Varela, M.; Stanley, D. C.; Sinko, M.; et al. Robust Antiferromagnetic Coupling in Hard-Soft Bi-Magnetic Core/Shell Nanoparticles. *Nat. Commun.* **2013**, *4*, 2960.
(425) Torruella, P.; Ruiz-Caridad, A.; Walls, M.; Gomez Roca, A. G.; López-Ortega, A.; Blanco-Portals, J.; Lopez-Conesa, L.; Nogues, J.; Peiró, F.; Estrade, S. Atomic Scale Determination of Cation Inversion in Spinel-Based Oxide Nanoparticles. *Nano Lett.* **2018**, acs.nanolett.8b02524.
(426) Zeng, H.; Li, J.; Wang, Z. L.; Liu, J. P.; Sun, S. Bimagnetic Core/Shell FePt/Fe_3O_4 Nanoparticles. *Nano Lett.* **2004**, *4* (1), 187–190.
(427) Liu, X.; Pichon, B. P.; Ulhaq, C.; Lefèvre, C.; Grenèche, J.-M.; Bégin, D.; Bégin-Colin, S. Systematic Study of Exchange Coupling in Core–Shell Fe $_{3-\delta}$ O $_4$ @CoO Nanoparticles. *Chem. Mater.* **2015**, *27* (11), 4073–4081.
(428) Masala, O.; Seshadri, R. Spinel Ferrite/MnO Core/Shell Nanoparticles: Chemical Synthesis of All-Oxide Exchange Biased Architectures. *J. Am. Chem. Soc.* **2005**, *127* (26), 9354–9355.
(429) Troitiño, N. F.; Rivas-Murias, B.; Rodríguez-González, B.; Salgueiriño, V. Exchange Bias Effect in CoO@Fe3O4 Core−Shell Octahedron-Shaped Nanoparticles. *Chem. Mater.* **2014**, *26*, 5566–5575.
(430) Salazar-Alvarez, G.; Lidbaum, H.; López-Ortega, A.; Estrader, M.; Leifer, K.; Sort, J.; Suriñach, S.; Baró, M. D.; Nogués, J. Two-, Three-, and Four-Component Magnetic Multilayer Onion Nanoparticles Based on Iron Oxides and Manganese Oxides. *J. Am. Chem. Soc.* **2011**, *133* (42), 16738–16741.
(431) Mao, Y.; Yi, P.; Deng, Z.; Ge, J. Fe3O4–Ag Heterostructure Nanocrystals with Tunable Ag Domains and Magnetic Properties. *CrystEngComm* **2013**, *15* (18), 3575.
(432) Robinson, I.; Tung, L. D.; Maenosono, S.; Wälti, C.; Thanh, N. T. K. Synthesis of Core-Shell Gold Coated Magnetic Nanoparticles and Their Interaction with Thiolated DNA. *Nanoscale* **2010**, *2*, 2624–2630.
(433) Wang, L.; Luo, J.; Fan, Q.; Suzuki, M.; Suzuki, I. S.; Engelhard, M. H.; Lin, Y.; Kim, N.; Wang, J. Q.; Zhong, C.-J. Monodispersed Core-Shell Fe3O4@Au Nanoparticles. *J. Phys. Chem. B* **2005**, *109* (46), 21593–21601.
(434) Fantechi, E.; Roca, A. G.; Sepúlveda, B.; Torruella, P.; Estradé, S.; Peiró, F.; Coy, E.; Jurga, S.; Bastús, N. G.; Nogués, J.; et al. Seeded Growth Synthesis of Au–Fe 3 O 4 Heterostructured Nanocrystals: Rational Design and Mechanistic Insights. *Chem. Mater.* **2017**, *29* (9), 4022–4035.
(435) Zang, W.; Li, G.; Wang, L.; Zhang, X. Catalytic Hydrogenation by Noble-Metal Nanocrystals with Well-Defined Facets: A Review. *Catal. Sci. Technol.* **2015**, *5* (5), 2532–2553.
(436) Lin, F.; Chen, W.; Liao, Y.-H.; Doong, R.; Li, Y. Effective Approach for the Synthesis of Monodisperse Magnetic Nanocrystals and M-Fe3O4 (M = Ag, Au, Pt, Pd) Heterostructures. *Nano Res.* **2011**, *4* (12), 1223–1232.
(437) Moscoso-Lodoño, O.; Muraca, D.; Tancredi, P.; Cosio-Castañeda, C.; Pirota, K. R.; Socolovsky, L. M. Physicochemical Studies of Complex Silver − Magnetite Nanoheterodimers with Controlled Morphology. *J. Phys. Chem. C* **2014**, *118*, 13168–13176.
(438) Brollo, M. E. F.; López-Ruiz, R.; Muraca, D.; Figueroa, S. J. A.; Pirota, K. R.; Knobel, M. Compact Ag@Fe3O4 Core-Shell Nanoparticles by Means of Single-Step Thermal Decomposition Reaction. *Sci. Rep.* **2015**, *4* (1), 6839.
(439) Tancredi, P.; Moscoso Londoño, O.; Rivas Rojas, P. C.; Wolff, U.; Socolovsky, L. M.; Knobel, M.; Muraca, D. Strategies to Tailor the Architecture of Dual Ag/Fe-Oxide Nano-Heterocrystals - Interfacial and Morphology Effects on the Magnetic Behavior. *J. Phys. D. Appl. Phys.* **2018**, *51* (29).
(440) Lai, C.-H.; Wu, T.-F.; Lan, M.-D. Synthesis and Properties of Core-Shell Ag@Fe3O4 Nanoparticles. *IEEE Trans. Magn.* **2005**, *41* (10), 3397–3399.
(441) Huang, J.; Guo, M.; Ke, H.; Zong, C.; Ren, B.; Liu, G.; Shen, H.; Ma, Y.; Wang, X.; Zhang, H.; et al. Rational Design and Synthesis of ΓFe2O3@Au Magnetic Gold Nanoflowers for Efficient Cancer Theranostics. *Adv. Mater.* **2015**, n/a--n/a.
(442) Yeo, K. M.; Shin, J.; Lee, I. S. Reductive Dissolution of Fe $_3$ O $_4$ Facilitated by the Au Domain of an Fe $_3$ O $_4$ /Au Hybrid Nanocrystal: Formation of a Nanorattle Structure Composed of a Hollow Porous Silicananoshell and Entrapped Aunanocrystal. *Chem. Commun.* **2010**, *46* (1), 64–66.
(443) Jin, C.; Qu, Y.; Wang, M.; Han, J.; Hu, Y.; Guo, R. Aqueous Solution-Based Fe3O4Seed-Mediated Route to Hydrophilic Fe3O4-Au Janus Nanoparticles. *Langmuir* **2016**, *32* (18), 4595–4601.
(444) Wang, L.; Park, H.-Y.; Lim, S. I.-I.; Schadt, M. J.; Mott, D.; Luo, J.; Wang, X.; Zhong, C.-J. Core@shell Nanomaterials: Gold-Coated Magnetic Oxide Nanoparticles. *J. Mater. Chem.* **2008**, *18* (23), 2629.
(445) Odio, O. F.; Martínez, R.; Reguera, E. Supporting Information for Sorption of Gold by Naked and Thiol Capped Magnetite Nanoparticles : An XPS. **2014**, No. Iii.
(446) Silvestri, A.; Mondini, S.; Marelli, M.; Pifferi, V.; Falciola, L.; Ponti, A.; Ferretti, A. M.; Polito,

L. Synthesis of Water Dispersible and Catalytically Active Gold-Decorated Cobalt Ferrite Nanoparticles. *Langmuir* **2016**, *32* (28), 7117–7126.
(447) Hui, W.; Shi, F.; Yan, K.; Peng, M.; Cheng, X.; Luo, Y.; Chen, X.; Roy, V. A. L.; Cui, Y.; Wang, Z. Fe $_3$ O $_4$ /Au/Fe $_3$ O $_4$ Nanoflowers Exhibiting Tunable Saturation Magnetization and Enhanced Bioconjugation. *Nanoscale* **2012**, *4* (3), 747–751.
(448) Xu, Z.; Hou, Y.; Sun, S. Magnetic Core/Shell Fe 3 O 4 /Au and Fe 3 O 4 /Au/Ag Nanoparticles with Tunable Plasmonic Properties. *J. Am. Chem. Soc.* **2007**, *129* (28), 8698–8699.
(449) Carlà, F.; Campo, G.; Sangregorio, C.; Caneschi, A.; de Julián Fernández, C.; Cabrera, L. I. Electrochemical Characterization of Core@shell CoFe2O4/Au Composite. *J. Nanoparticle Res.* **2013**, *15* (8), 1813.
(450) Mikalauskaitė, A.; Kondrotas, R.; Niaura, G.; Jagminas, A. Gold-Coated Cobalt Ferrite Nanoparticles via Methionine-Induced Reduction. *J. Phys. Chem. C* **2015**, *119* (30), 17398–17407.
(451) Pita, M.; Abad, J. M.; Vaz-Dominguez, C.; Briones, C.; Mateo-Mart??, E.; Mart??n-Gago, J. A.; del Puerto Morales, M.; Fern??ndez, V. M. Synthesis of Cobalt Ferrite Core/Metallic Shell Nanoparticles for the Development of a Specific PNA/DNA Biosensor. *J. Colloid Interface Sci.* **2008**, *321* (2), 484–492.
(452) Kaloti, M.; Kumar, A. Synthesis of Chitosan-Mediated Silver Coated ??-Fe2O3 (Ag-??-Fe2O3@Cs) Superparamagnetic Binary Nanohybrids for Multifunctional Applications. *J. Phys. Chem. C* **2016**, *120* (31), 17627–17644.
(453) Gu, H.; Yang, Z.; Gao, J.; Chang, C. K.; Xu, B. Heterodimers of Nanoparticles: Formation at a Liquid-Liquid Interface and Particle-Specific Surface Modification by Functional Molecules. *J. Am. Chem. Soc.* **2005**, *127* (1), 34–35.
(454) Sytnyk, M.; Kirchschlager, R.; Bodnarchuk, M. I.; Primetzhofer, D.; Kriegner, D.; Ennser, H.; Stangl, J.; Bauer, P.; Voith, M.; Hassel, A.; et al. Tuning the Magnetic Properties of Metal-Oxide Nanocrystal Heterostructures by Cation Exchange. *Nano Lett.* **2013**, 1–13.
(455) Jiang, G.; Huang, Y.; Zhang, S.; Zhu, H.; Wu, Z.; Sun, S.; Talapin, D. V.; Lee, J. S.; Kovalenko, M. V.; Shevchenko, E. V.; et al. Controlled Synthesis of Au–Fe Heterodimer Nanoparticles and Their Conversion into Au–Fe $_3$ O $_4$ Heterostructured Nanoparticles. *Nanoscale* **2016**, *8* (41), 17947–17952.
(456) Lee, Y.; Garcia, M. A.; Frey Huls, N. A.; Sun, S. Synthetic Tuning of the Catalytic Properties of Au-Fe $_3$ O $_4$ Nanoparticles. *Angew. Chemie* **2010**, *122* (7), 1293–1296.
(457) Guardia, P.; Nitti, S.; Materia, M. E.; Pugliese, G.; Yaacoub, N.; Greneche, J. M.; Lefevre, C.; Manna, L.; Pellegrino, T. Gold-Iron Oxide Dimers for Magnetic Hyperthermia: The Key Role of Chloride Ions in the Synthesis to Boost the Heating Efficiency. *J. Mater. Chem. B* **2017**, *5* (24), 4587–4594.
(458) Yu, H.; Chen, M.; Rice, P. M.; Wang, S. X.; White, R. L.; Sun, S. Dumbbell-like Bifunctional Au-Fe3O4nanoparticles. *Nano Lett.* **2005**, *5* (2), 379–382.
(459) Xu, C.; Wang, B.; Sun, S. Dumbbell-like Au - Fe 3 O 4 Nanoparticles for Target-Specific Platin Delivery. *J. Am. Chem. Soc.* **2009**, *131*, 4216–4217.
(460) Zhang, X. F.; Clime, L.; Ly, H. Q.; Trudeau, M.; Veres, T. Multifunctional Fe 3 O 4 −Au/Porous Silica@Fluorescein Core/Shell Nanoparticles with Enhanced Fluorescence Quantum Yield. *J. Phys. Chem. C* **2010**, *114* (43), 18313–18317.
(461) Shevchenko, E. V.; Bodnarchuk, M. I.; Kovalenko, M. V.; Talapin, D. V.; Smith, R. K.; Aloni, S.; Heiss, W.; Alivisatos, A. P. Gold/Iron Oxide Core/Hollow-Shell Nanoparticles. *Adv. Mater.* **2008**, *20* (22), 4323–4329.
(462) Jishkariani, D.; Wu, Y.; Wang, D.; Liu, Y.; Van Blaaderen, A.; Murray, C. B. Preparation and Self-Assembly of Dendronized Janus Fe3O4-Pt and Fe3O4-Au Heterodimers. *ACS Nano* **2017**, *11* (8), 7958–7966.
(463) Wei, Y.; Klajn, R.; Pinchuk, A. O.; Grzybowski, B. A. Synthesis, Shape Control, and Optical Properties of Hybrid Au/Fe 3O4 "Nanoflowers." *Small* **2008**, *4* (10), 1635–1639.
(464) Wang, C.; Yin, H.; Dai, S.; Sun, S. A General Approach to Noble Metal-Metal Oxide Dumbbell Nanoparticles and Their Catalytic Application for CO Oxidation. *Chem. Mater.* **2010**, *22* (10), 3277–3282.
(465) Lu, P. A. N.; Jing, T.; Yonghong, C. Synthesis of Fe 3 O 4 , Fe 2 O 3 , Ag / Fe 3 O 4 and Ag / Fe 2 O 3 Nanoparticles and Their Electrocatalytic Properties. **2012**, *1* (8), 39–45.
(466) Peng, S.; Lei, C.; Ren, Y.; Cook, R. E.; Sun, Y. Plasmonic/Magnetic Bifunctional Nanoparticles. *Angew. Chemie - Int. Ed.* **2011**, *50* (14), 3158–3163.
(467) Hai, H. T.; Yang, H. T.; Kura, H.; Hasegawa, D.; Ogata, Y.; Takahashi, M.; Ogawa, T. Size Control and Characterization of Wustite (Core)/Spinel (Shell) Nanocubes Obtained by Decomposition of Iron Oleate Complex. *J. Colloid Interface Sci.* **2010**, *346* (1), 37–42.
(468) Pichon, B.; Gerber, O.; Lefevre, C. Microstructural and Magnetic Investigations of Wüstite-Spinel Core-Shell Cubic-Shaped Nanoparticles. *Chem. …* **2011**, *23*, 2886–2900.
(469) Wetterskog, E.; Tai, C.; Grins, J.; Bergstro, L.; Salazar-alvarez, G.; Chemistry, E. Anomalous Magnetic Properties of Nanoparticles Arising from Defect Structures: Topotaxial Oxidation of

Fe 1. **2013**, No. Xx, 7132–7144.
(470) Lottini, E.; López-Ortega, A.; Bertoni, G.; Turner, S.; Meledina, M.; Tendeloo, G. Van; De Julián Fernández, C.; Sangregorio, C. Strongly Exchange Coupled Core|Shell Nanoparticles with High Magnetic Anisotropy: A Strategy toward Rare-Earth-Free Permanent Magnets. *Chem. Mater.* **2016**, *28* (12), 4214–4222.
(471) Baaziz, W.; Pichon, B. P.; Liu, Y.; Greneche, J.-M.; Ulhaq-Bouillet, C.; Terrier, E.; Bergeard, N.; Halte, V.; Boeglin, C.; Choueikani, F.; et al. Tuning of Synthesis Conditions by Thermal Decomposition towards Core-Shell CoxFe1-XO@CoyFe3-YO4 and $CoFe_2O_4$ Nanoparticles with Spherical and Cubic Shapes. *Chem. Mater.* **2014**, *26* (17), 5063–5073.
(472) Bodnarchuk, M. I.; Kovalenko, M. V.; Groiss, H.; Resel, R.; Reissner, M.; Hesser, G.; Lechner, R. T.; Steiner, W.; Schäffler, F.; Heiss, W. Exchange-Coupled Bimagnetic Wüstite/Metal Ferrite Core/Shell Nanocrystals: Size, Shape, and Compositional Control. *Small* **2009**, *5* (20), 2247–2252.
(473) Frison, R.; Cernuto, G.; Cervellino, A.; Zaharko, O.; Colonna, G. M.; Guagliardi, A.; Masciocchi, N. Magnetite-Maghemite Nanoparticles in the 5-15 Nm Range: Correlating the Core-Shell Composition and the Surface Structure to the Magnetic Properties. A Total Scattering Study. *Chem. Mater.* **2013**, *25* (23), 4820–4827.
(474) Zuddas, E.; Lentijo-Mozo, S.; Casu, A.; Deiana, D.; Falqui, A. Building Composite Iron–Manganese Oxide Flowerlike Nanostructures: A Detailed Magnetic Study. *J. Phys. Chem. C* **2017**, *121* (31), 17005–17015.
(475) Oh, M. H.; Yu, T.; Yu, S.-H.; Lim, B.; Ko, K.-T.; Willinger, M.-G.; Seo, D.-H.; Kim, B. H.; Cho, M. G.; Park, J.-H.; et al. Galvanic Replacement Reactions in Metal Oxide Nanocrystals. *Science (80-.).* **2013**, *340* (6135), 964–968.
(476) Cheon, J.; Park, J.-I.; Choi, J.; Jun, Y.; Kim, S.; Kim, M. G.; Kim, Y.-M. J.; Kim, Y.-M. J. Magnetic Superlattices and Their Nanoscale Phase Transition Effects. *Proc. Natl. Acad. Sci. U. S. A.* **2006**, *103* (9), 3023–3027.
(477) Huang, J.; Sun, Y.; Huang, S.; Yu, K.; Zhao, Q.; Peng, F.; Yu, H.; Wang, H.; Yang, J. Crystal Engineering and SERS Properties of Ag–Fe3O4 Nanohybrids: From Heterodimer to Core–shell Nanostructures. *J. Mater. Chem.* **2011**, *21* (44), 17930.
(478) Pan, L. . b; Chen, Y. . b; Wang, F. . Synthesis of Nanostructured M/Fe 3O 4 (M = Ag, Cu) Composites Using Hexamethylentetramine and Their Electrocatalytic Properties. *Mater. Chem. Phys.* **2012**, *134* (1), 177–182.
(479) Shan, Y.; Yang, Y.; Cao, Y.; Huang, Z. Facile Solvothermal Synthesis of Ag/Fe_3O_4 Nanocomposites and Their SERS Applications in on-Line Monitoring of Pesticide Contaminated Water. *RSC Adv.* **2015**, *5* (124), 102610–102618.
(480) Weller, D.; Mosendz, O.; Parker, G.; Pisana, S.; Santos, T. S. L1 0 FePtX-Y Media for Heat-Assisted Magnetic Recording. *Phys. status solidi* **2013**, *210* (7), 1245–1260.
(481) Wu, L.; Mendoza-Garcia, A.; Li, Q.; Sun, S. Organic Phase Syntheses of Magnetic Nanoparticles and Their Applications. *Chem. Rev.* **2016**, *116* (18), 10473–10512.
(482) Wu, L.; Jubert, P.-O.; Berman, D.; Imaino, W.; Nelson, A.; Zhu, H.; Zhang, S.; Sun, S. Monolayer Assembly of Ferrimagnetic Co x Fe 3– x O 4 Nanocubes for Magnetic Recording. *Nano Lett.* **2014**, *14* (6), 3395–3399.
(483) Dai, Q.; Berman, D.; Virwani, K.; Frommer, J.; Jubert, P.-O.; Lam, M.; Topuria, T.; Imaino, W.; Nelson, A. Self-Assembled Ferrimagnet−Polymer Composites for Magnetic Recording Media. *Nano Lett.* **2010**, *10* (8), 3216–3221.
(484) Dee, R. H. Magnetic Tape for Data Storage: An Enduring Technology. *Proc. IEEE* **2008**, *96* (11), 1775–1785.
(485) Kiwi, M. Exchange Bias Theory. *J. Magn. Magn. Mater.* **2001**, *234* (3), 584–595.
(486) Nogués, J.; Schuller, I. K. Exchange Bias. *J. Magn. Magn. Mater.* **1999**, *192* (2), 203–232.
(487) Nogués, J.; Sort, J.; Langlais, V.; Skumryev, V.; Suriñach, S.; Muñoz, J. S.; Baró, M. D. Exchange Bias in Nanostructures. *Phys. Rep.* **2005**, *422* (3), 65–117.
(488) Campos, E. A.; Stockler Pinto, D. V. B.; Oliveira, J. I. S. de; Mattos, E. da C.; Dutra, R. de C. L. Synthesis, Characterization and Applications of Iron Oxide Nanoparticles - a Short Review. *J. Aerosp. Technol. Manag.* **2015**, *7* (3), 267–276.
(489) Teja, A. S.; Koh, P.-Y. Synthesis, Properties, and Applications of Magnetic Iron Oxide Nanoparticles. *Prog. Cryst. Growth Charact. Mater.* **2009**, *55* (1), 22–45.
(490) Weddemann, A.; Ennen, I.; Regtmeier, A.; Albon, C.; Wolff, A.; Eckstädt, K.; Mill, N.; Peter, M. K. H.; Mattay, J.; Plattner, C.; et al. Review and Outlook: From Single Nanoparticles to Self-Assembled Monolayers and Granular GMR Sensors. *Beilstein J. Nanotechnol.* **2010**, *1* (1), 75–93.
(491) Chaturvedi, S.; Dave, P. N.; Shah, N. K. Applications of Nano-Catalyst in New Era. *J. Saudi Chem. Soc.* **2012**, *16* (3), 307–325.
(492) Gregor, C.; Hermanek, M.; Jancik, D.; Pechousek, J.; Filip, J.; Hrbac, J.; Zboril, R. The Effect of Surface Area and Crystal Structure on the Catalytic Efficiency of Iron(III) Oxide Nanoparticles in Hydrogen Peroxide Decomposition. *Eur. J. Inorg. Chem.* **2010**, *2010* (16),

2343–2351.
(493) Cheng, Z.; Lai, A.; Tan, K.; Tao, Y.; Shan, D.; Ting, K. E.; Yin, X. J. Synthesis and Characterization of Iron Oxide Nanoparticles and Applications in the Removal of Heavy Metals from Industrial Wastewater. **2012**, *2012*.
(494) Cara, C.; Rombi, E.; Mameli, V.; Ardu, A.; Sanna Angotzi, M.; Niznansky, D.; Musinu, A.; Cannas, C. γ-Fe2O3-M41S Sorbents for H2S Removal: Effect of Different Porous Structures and Silica Wall Thickness. *J. Phys. Chem. C* **2018**, *122* (23), 12231–12242.
(495) Cara, C.; Rombi, E.; Musinu, A.; Mameli, V.; Ardu, A.; Sanna Angotzi, M.; Atzori, L.; Niznansky, D.; Xin, H. L.; Cannas, C. MCM-41 Support for Ultrasmall γ-Fe $_2$ O $_3$ Nanoparticles for H $_2$ S Removal. *J. Mater. Chem. A* **2017**, *5* (41), 21688–21698.
(496) Amarjargal, A.; Tijing, L. D.; Im, I. T.; Kim, C. S. Simultaneous Preparation of Ag/Fe3O4 Core-Shell Nanocomposites with Enhanced Magnetic Moment and Strong Antibacterial and Catalytic Properties. *Chem. Eng. J.* **2013**, *226*, 243–254.
(497) *Applied Magnetism*; Gerber, R., Wright, C. D., Asti, G., Eds.; Springer Netherlands: Dordrecht, 1994.
(498) Moeser, G. D.; Roach, K. A.; Green, W. H.; Hatton, T. A.; Laibinis, P. E. High-Gradient Magnetic Separation of Coated Magnetic Nanoparticles. *AIChE J.* **2004**, *50* (11), 2835–2848.
(499) Roca, a G.; Costo, R.; Rebolledo, a F.; Veintemillas-Verdaguer, S.; Tartaj, P.; González-Carreño, T.; Morales, M. P.; Serna, C. J.; Review, T. Progress in the Preparation of Magnetic Nanoparticles for Applications in Biomedicine. *J. Phys. D. Appl. Phys.* **2009**, *42* (22), 224002.
(500) Kumar, C. S. S. R.; Mohammad, F. Magnetic Nanomaterials for Hyperthermia-Based Therapy and Controlled Drug Delivery. *Adv. Drug Deliv. Rev.* **2011**, *63* (9), 789–808.
(501) Lim, Ekn. for T. R. A. and F. C.; Kim, T.; Paik, S.; Haam, S.; Yong-Min, H.; Lee, K. Nanomaterials for Theranostics: Recent Advances and Future Challenges. *Chem. Rev.* **2014**.
(502) Tran, N.; Webster, T. J. Magnetic Nanoparticles: Biomedical Applications and Challenges. *J. Mater. Chem.* **2010**, *20* (40), 8760.
(503) Jinhao, G. A. O.; Hongwei, G. U.; Bing, X. U. Multifunctional Magnetic Nanoparticles: Design, Synthesis, and Biomedical Applications. *Acc. Chem. Res.* **2009**, *42* (8), 1097–1107.
(504) Shubayev, V. I.; Pisanic, T. R.; Jin, S. Magnetic Nanoparticles for Theragnostics. *Adv. Drug Deliv. Rev.* **2009**, *61* (6), 467–477.
(505) López-Ortega, A.; Estrader, M.; Salazar-Alvarez, G.; Roca, A. G.; Nogués, J. Applications of Exchange Coupled Bi-Magnetic Hard/Soft and Soft/Hard Magnetic Core/Shell Nanoparticles. *Phys. Rep.* **2015**, *553*, 1–32.
(506) Lee, N.; Yoo, D.; Ling, D.; Cho, M. H.; Hyeon, T.; Cheon, J. Iron Oxide Based Nanoparticles for Multimodal Imaging and Magnetoresponsive Therapy. *Chem. Rev.* **2015**, 150807073744009.
(507) Caravan, P.; Ellison, J. J.; McMurry, T. J.; Lauffer, R. B. Gadolinium(III) Chelates as MRI Contrast Agents: Structure, Dynamics, and Applications. *Chem. Rev.* **1999**, *99* (9), 2293–2352.
(508) Sandiford, L.; Phinikaridou, A.; Protti, A.; Meszaros, L. K.; Cui, X.; Yan, Y.; Frodsham, G.; Williamson, P. A.; Gaddum, N.; Botnar, R. M.; et al. Bisphosphonate-Anchored PEGylation and Radiolabeling of Superparamagnetic Iron Oxide: Long-Circulating Nanoparticles for in Vivo Multimodal (T1 MRI-SPECT) Imaging. *ACS Nano* **2013**, *7* (1), 500–512.
(509) Tromsdorf, U. I.; Bruns, O. T.; Salmen, S. C.; Beisiegel, U.; Weller, H. A Highly Effective, Nontoxic T 1 MR Contrast Agent Based on Ultrasmall PEGylated Iron Oxide Nanoparticles. *Nano Lett.* **2009**, *9* (12), 4434–4440.
(510) Taboada, E.; Rodríguez, E.; Roig, A.; Oró, J.; Roch, A.; Muller, R. N. Relaxometric and Magnetic Characterization of Ultrasmall Iron Oxide Nanoparticles with High Magnetization. Evaluation as Potential T 1 Magnetic Resonance Imaging Contrast Agents for Molecular Imaging. *Langmuir* **2007**, *23* (8), 4583–4588.
(511) Dong, A.; Ye, X.; Chen, J.; Kang, Y.; Gordon, T.; Kikkawa, J. M.; Murray, C. B. A Generalized Ligand-Exchange Strategy Enabling Sequential Surface Functionalization of Colloidal Nanocrystals. *J. Am. Chem. Soc.* **2011**, *133* (4), 998–1006.
(512) Lee, N.; Choi, Y.; Lee, Y.; Park, M.; Moon, W. K.; Choi, S. H.; Hyeon, T. Water-Dispersible Ferrimagnetic Iron Oxide Nanocubes with Extremely High r 2 Relaxivity for Highly Sensitive in Vivo MRI of Tumors. *Nano Lett.* **2012**, *12* (6), 3127–3131.
(513) Jang, J.; Nah, H.; Lee, J.-H.; Moon, S. H.; Kim, M. G.; Cheon, J. Critical Enhancements of MRI Contrast and Hyperthermic Effects by Dopant-Controlled Magnetic Nanoparticles. *Angew. Chemie Int. Ed.* **2009**, *48* (7), 1234–1238.
(514) Lee, J.-H.; Huh, Y.-M.; Jun, Y.; Seo, J.; Jang, J.; Song, H.-T.; Kim, S.; Cho, E.-J.; Yoon, H.-G.; Suh, J.-S.; et al. Artificially Engineered Magnetic Nanoparticles for Ultra-Sensitive Molecular Imaging. *Nat. Med.* **2007**, *13* (1), 95–99.
(515) Jun, Y.; Huh, Y.-M.; Choi, J.; Lee, J.-H.; Song, H.-T.; Kim; Yoon, S.; Kim, K.-S.; Shin, J.-S.; Suh, J.-S.; et al. Nanoscale Size Effect of Magnetic Nanocrystals and Their Utilization for Cancer Diagnosis via Magnetic Resonance Imaging. *J. Am. Chem. Soc.* **2005**, *127* (16), 5732–5733.
(516) de la Presa, P.; Luengo, Y.; Multigner, M.; Costo, R.; Morales, M. P.; Rivero, G.; Hernando, A.

Study of Heating Efficiency as a Function of Concentration, Size, and Applied Field in γ-Fe2O3 Nanoparticles. *J. Phys. Chem. C* **2012**, *116* (48), 25602–25610.
(517) Rosensweig, R. E. Heating Magnetic Fluid with Alternating Magnetic Field. *J. Magn. Magn. Mater.* **2002**, *252*, 370–374.
(518) Carrey, J.; Mehdaoui, B.; Respaud, M. Simple Models for Dynamic Hysteresis Loop Calculations of Magnetic Single-Domain Nanoparticles: Application to Magnetic Hyperthermia Optimization. *J. Appl. Phys.* **2011**, *109* (8), 083921.
(519) Stauffer, P. R.; Cetas, T. C.; Fletcher, a M.; DeYoung, D. W.; Dewhirst, M. W.; Oleson, J. R.; Roemer, R. B. Observations on the Use of Ferromagnetic Implants for Inducing Hyperthermia. *IEEE Trans. Biomed. Eng.* **1984**, *31* (1), 76–90.
(520) Hergt, R.; Dutz, S. Magnetic Particle Hyperthermia—biophysical Limitations of a Visionary Tumour Therapy. *J. Magn. Magn. Mater.* **2007**, *311* (1), 187–192.
(521) Natividad, E.; Castro, M.; Mediano, A. Adiabatic vs. Non-Adiabatic Determination of Specific Absorption Rate of Ferrofluids. *J. Magn. Magn. Mater.* **2009**, *321* (10), 1497–1500.
(522) http://www.magforce.de/en/home.html.
(523) Suto, M.; Hirota, Y.; Mamiya, H.; Fujita, A.; Kasuya, R.; Tohji, K.; Jeyadevan, B. Heat Dissipation Mechanism of Magnetite Nanoparticles in Magnetic Fluid Hyperthermia. *J. Magn. Magn. Mater.* **2009**, *321* (10), 1493–1496.
(524) Kikuchi, T.; Kasuya, R.; Endo, S.; Nakamura, A.; Takai, T.; Metzler-Nolte, N.; Tohji, K.; Balachandran, J. Preparation of Magnetite Aqueous Dispersion for Magnetic Fluid Hyperthermia. *J. Magn. Magn. Mater.* **2011**, *323* (10), 1216–1222.
(525) Lartigue, L.; Innocenti, C.; Kalaivani, T.; Awwad, A.; Sanchez Duque, M. D. M.; Guari, Y.; Larionova, J.; Guérin, C.; Montero, J.-L. G.; Barragan-Montero, V.; et al. Water-Dispersible Sugar-Coated Iron Oxide Nanoparticles. An Evaluation of Their Relaxometric and Magnetic Hyperthermia Properties. *J. Am. Chem. Soc.* **2011**, *133* (27), 10459–10472.
(526) Liu, X. L.; Fan, H. M.; Yi, J. B.; Yang, Y.; Choo, E. S. G.; Xue, J. M.; Fan, D. Di; Ding, J. Optimization of Surface Coating on Fe3O4 Nanoparticles for High Performance Magnetic Hyperthermia Agents. *J. Mater. Chem.* **2012**, *22* (17), 8235.
(527) Song, M.; Zhang, Y.; Hu, S.; Song, L.; Dong, J.; Chen, Z.; Gu, N. Influence of Morphology and Surface Exchange Reaction on Magnetic Properties of Monodisperse Magnetite Nanoparticles. *Colloids Surfaces A Physicochem. Eng. Asp.* **2012**, *408*, 114–121.
(528) Jadhav, N. V; Prasad, A. I.; Kumar, A.; Mishra, R.; Dhara, S.; Babu, K. R.; Prajapat, C. L.; Misra, N. L.; Ningthoujam, R. S.; Pandey, B. N.; et al. Synthesis of Oleic Acid Functionalized Fe3O4 Magnetic Nanoparticles and Studying Their Interaction with Tumor Cells for Potential Hyperthermia Applications. *Colloids Surf. B. Biointerfaces* **2013**, *108*, 158–168.
(529) Shete, P. B.; Patil, R. M.; Thorat, N. D.; Prasad, A.; Ningthoujam, R. S.; Ghosh, S. J.; Pawar, S. H. Magnetic Chitosan Nanocomposite for Hyperthermia Therapy Application: Preparation, Characterization and in Vitro Experiments. *Appl. Surf. Sci.* **2014**, *288*, 149–157.
(530) Lv, Y.; Yang, Y.; Fang, J.; Zhang, H.; Peng, E.; Liu, X.; Xiao, W.; Ding, J. Size Dependent Magnetic Hyperthermia of Octahedral Fe 3 O 4 Nanoparticles. *RSC Adv.* **2015**, *5* (94), 76764–76771.
(531) Sasikala, A. R. K.; GhavamiNejad, A.; Unnithan, A. R.; Thomas, R. G.; Moon, M.; Jeong, Y. Y.; Park, C. H.; Kim, C. S. A Smart Magnetic Nanoplatform for Synergistic Anticancer Therapy: Manoeuvring Mussel-Inspired Functional Magnetic Nanoparticles for PH Responsive Anticancer Drug Delivery and Hyperthermia. *Nanoscale* **2015**, 18119–18128.
(532) Otero-Lorenzo, R.; Fantechi, E.; Sangregorio, C.; Salgueiriño, V. Solvothermally Driven Mn Doping and Clustering of Iron Oxide Nanoparticles for Heat Delivery Applications. *Chem. - A Eur. J.* **2016**, *22* (19), 6666–6675.
(533) Hilger, I.; Andrä, W.; Hergt, R.; Hiergeist, R.; Schubert, H.; Kaiser, W. a. Electromagnetic Heating of Breast Tumors in Interventional Radiology: In Vitro and in Vivo Studies in Human Cadavers and Mice. *Radiology* **2001**, *218* (2), 570–575.
(534) Pradhan, P.; Giri, J.; Samanta, G.; Sarma, H. D.; Mishra, K. P.; Bellare, J.; Banerjee, R.; Bahadur, D. Comparative Evaluation of Heating Ability and Biocompatibility of Different Ferrite-Based Magnetic Fluids for Hyperthermia Application. *J. Biomed. Mater. Res. Part B Appl. Biomater.* **2007**, *81B* (1), 12–22.
(535) Zhang, L.-Y.; Gu, H.-C.; Wang, X.-M. Magnetite Ferrofluid with High Specific Absorption Rate for Application in Hyperthermia. *J. Magn. Magn. Mater.* **2007**, *311* (1), 228–233.
(536) Gonzales-Weimuller, M.; Zeisberger, M.; Krishnan, K. M. Size-Dependant Heating Rates of Iron Oxide Nanoparticles for Magnetic Fluid Hyperthermia. *J. Magn. Magn. Mater.* **2009**, *321* (13), 1947–1950.
(537) Purushotham, S.; Chang, P. E. J.; Rumpel, H.; Kee, I. H. C.; Ng, R. T. H.; Chow, P. K. H.; Tan, C. K.; Ramanujan, R. V. Thermoresponsive Core-Shell Magnetic Nanoparticles for Combined Modalities of Cancer Therapy. *Nanotechnology* **2009**, *20* (30), 305101.
(538) Lacroix, L.-M.; Malaki, R. B.; Carrey, J.; Lachaize, S.; Respaud, M.; Goya, G. F.; Chaudret, B. Magnetic Hyperthermia in Single-Domain Monodisperse FeCo Nanoparticles: Evidences for

Stoner–Wohlfarth Behavior and Large Losses. *J. Appl. Phys.* **2009**, *105* (2), 023911.
(539) Mehdaoui, B.; Meffre, A.; Lacroix, L.-M.; Carrey, J.; Lachaize, S.; Gougeon, M.; Respaud, M.; Chaudret, B. Large Specific Absorption Rates in the Magnetic Hyperthermia Properties of Metallic Iron Nanocubes. *J. Magn. Magn. Mater.* **2010**, *322* (19), L49–L52.
(540) Lacroix, L.; Huls, N. F.; Ho, D.; Sun, X.; Cheng, K.; Sun, S. Stable Single-Crystalline Body Centered Cubic Fe Nanoparticles. *Nano Lett.* **2011**, *11* (4), 1641–1645.
(541) Zeisberger, M.; Dutz, S.; Müller, R.; Hergt, R.; Matoussevitch, N.; Bönnemann, H. Metallic Cobalt Nanoparticles for Heating Applications. *J. Magn. Magn. Mater.* **2007**, *311* (1), 224–227.
(542) Mehdaoui, B.; Meffre, A.; Carrey, J.; Lachaize, S.; Lacroix, L.-M.; Gougeon, M.; Chaudret, B.; Respaud, M. Optimal Size of Nanoparticles for Magnetic Hyperthermia: A Combined Theoretical and Experimental Study. *Adv. Funct. Mater.* **2011**, *21* (23), 4573–4581.
(543) Hergt, R.; Hiergeist, R.; Zeisberger, M.; Schüler, D.; Heyen, U.; Hilger, I.; Kaiser, W. a. Magnetic Properties of Bacterial Magnetosomes as Potential Diagnostic and Therapeutic Tools. *J. Magn. Magn. Mater.* **2005**, *293* (1), 80–86.
(544) Alphandéry, E.; Faure, S.; Raison, L.; Duguet, E.; Howse, P. A.; Bazylinski, D. A. Heat Production by Bacterial Magnetosomes Exposed to an Oscillating Magnetic Field. *J. Phys. Chem. C* **2011**, *115* (1), 18–22.
(545) Alphandéry, E.; Faure, S.; Seksek, O.; Guyot, F.; Chebbi, I. Chains of Magnetosomes Extracted from AMB-1 Magnetotactic Bacteria for Application in Alternative Magnetic Field Cancer Therapy. *ACS Nano* **2011**, *5* (8), 6279–6296.
(546) Kim, D.-H.; Nikles, D. E.; Johnson, D. T.; Brazel, C. S. Heat Generation of Aqueously Dispersed CoFe2O4 Nanoparticles as Heating Agents for Magnetically Activated Drug Delivery and Hyperthermia. *J. Magn. Magn. Mater.* **2008**, *320* (19), 2390–2396.
(547) Franchini, M. C.; Baldi, G.; Bonacchi, D.; Gentili, D.; Giudetti, G.; Lascialfari, A.; Corti, M.; Marmorato, P.; Ponti, J.; Micotti, E.; et al. Bovine Serum Albumin-Based Magnetic Nanocarrier for MRI Diagnosis and Hyperthermic Therapy: A Potential Theranostic Approach against Cancer. *Small* **2010**, *6* (3), 366–370.
(548) Mazario, E.; Menéndez, N.; Herrasti, P.; Cañete, M.; Connord, V.; Carrey, J. Magnetic Hyperthermia Properties of Electrosynthesized Cobalt Ferrite Nanoparticles. *J. Phys. Chem. C* **2013**, *117*, 11405–11411.
(549) Fantechi, E.; Innocenti, C.; Albino, M.; Lottini, E.; Sangregorio, C. Influence of Cobalt Doping on the Hyperthermic Efficiency of Magnetite Nanoparticles. *J. Magn. Magn. Mater.* **2015**, *380*, 365–371.
(550) Nappini, S.; Magnano, E.; Bondino, F.; Píš, I.; Barla, A.; Fantechi, E.; Pineider, F.; Sangregorio, C.; Vaccari, L.; Venturelli, L.; et al. Surface Charge and Coating of $CoFe_2O_4$ Nanoparticles: Evidence of Preserved Magnetic and Electronic Properties. *J. Phys. Chem. C* **2015**, acs.jpcc.5b04910.
(551) Nikam, D. S.; Jadhav, S. V.; Khot, V. M.; Ningthoujam, R. S.; Hong, C. K.; Mali, S. S.; Pawar, S. H. Colloidal Stability of Polyethylene Glycol Functionalized Co0.5Zn0.5Fe2O4 Nanoparticles: Effect of PH, Sample and Salt Concentration for Hyperthermia Application. *RSC Adv.* **2014**, *4* (25), 12662.
(552) Bohara, R. A.; Thorat, N. D.; Chaurasia, A. K.; Pawar, S. H. Cancer Cells Extinction through Magnetic Fluid Hyperthermia Treatment Produced by Superparamagnetic Co-Zn Ferrite Nanoparticles. *RSC Adv.* **2015**, *5*, 47225–47234.
(553) Mameli, V.; Musinu, A.; Ardu, A.; Ennas, G.; Peddis, D.; Niznansky, D.; Sangregorio, C.; Innocenti, C.; Thanh, N. T. K.; Cannas, C. Studying the Effect of Zn-Substitution on the Magnetic and Hyperthermic Properties of Cobalt Ferrite Nanoparticles. *Nanoscale* **2016**, *8* (19), 10124–10137.
(554) Lee, S. C.; Fu, C. M.; Chang, F. H. Effects of Core/Shell Structure on Magnetic Induction Heating Promotion in Fe3O4/γ-Fe2O3 Magnetic Nanoparticles for Hyperthermia. *Appl. Phys. Lett.* **2013**, *103* (16).
(555) Wang, J.; Zhou, Z.; Wang, L.; Wei, J.; Yang, H.; Yang, S.; Zhao, J. $CoFe_2O_4$@$MnFe_2O_4$/Polypyrrole Nanocomposites for in Vitro Photothermal/Magnetothermal Combined Therapy. *RSC Adv.* **2015**, *5* (10), 7349–7355.
(556) Yelenich, O. V.; Solopan, S. O.; Greneche, J. M.; Belous, A. G. Synthesis and Properties MFe<inf>2</Inf>O<inf>4</Inf> (M = Fe, Co) Nanoparticles and Core-Shell Structures. *Solid State Sci.* **2015**, *46*, 19–26.
(557) Chaudhuri, R. G.; Paria, S. Core/Shell Nanoparticles : Classes, Properties, Synthesis Mechanisms, Characterization, and Applications. *Chem. Rev.* **2012**, *112*, 2373–2433.
(558) Liu, F.; Hou, Y.; Gao, S. Exchange-Coupled Nanocomposites: Chemical Synthesis, Characterization and Applications. *Chem. Soc. Rev.* **2014**, *43* (23), 8098–8113.
(559) *Magnetic Nanoparticles: From Fabrication and Clinical Applications*, CRC Press,.; Thanh, N. T. K., Ed.; 2012.
(560) Krishnan, K. M. Biomedical Nanomagnetics: A Spin through Possibilities in Imaging, Diagnostics, and Therapy. *IEEE Trans. Magn.* **2010**, *46* (7), 2523–2558.

(561) Repko, A.; Vejpravová, J.; Vacková, T.; Zákutná, D.; Nižňanský, D. Oleate-Based Hydrothermal Preparation of CoFe2O4 Nanoparticles, and Their Magnetic Properties with Respect to Particle Size and Surface Coating. *J. Magn. Magn. Mater.* **2015**, *390*, 142–151.
(562) Repko, A.; Nižňanský, D.; Poltierová-Vejpravová, J. A Study of Oleic Acid-Based Hydrothermal Preparation of CoFe2O4 Nanoparticles. *J. Nanoparticle Res.* **2011**, *13* (10), 5021–5031.
(563) De Palma, R.; Peeters, S.; Van Bael, M. J.; Van Den Rul, H.; Bonroy, K.; Laureyn, W.; Mullens, J.; Borghs, G.; Maes, G. Silane Ligand Exchange to Make Hydrophobic Superparamagnetic Nanoparticles Water-Dispersible. *Chem. Mater.* **2007**, *19* (7), 1821–1831.
(564) Bloemen, M.; Brullot, W.; Luong, T. T.; Geukens, N.; Gils, A.; Verbiest, T. Improved Functionalization of Oleic Acid-Coated Iron Oxide Nanoparticles for Biomedical Applications. *J. Nanoparticle Res.* **2012**, *14* (9).
(565) Abuin, E. B.; Rubio, M. A.; Lissi, E. A. Solubility of Water in Water-in-Oil Microemulsions Stabilized by Cetyltrimethylammonium: Effects of the Surfactant Counterion, the Nature and Composition of the Oil, and the Salinity of the Droplets. *Journal of Colloid And Interface Science*. 1993, pp 129–132.
(566) Yang, H.; Zhou, H.; Zhang, C.; Li, X.; Hu, H.; Wu, H.; Yang, S. Water-Soluble Magnetic CoO Nanocrystals Functionalized with Surfactants as T2-Weighed MRI Contrast Agents in Vitro. *Dalt. Trans.* **2011**, *40* (14), 3616–3621.
(567) Fan, H.; Leve, E. W.; Scullin, C.; Gabaldon, J.; Tallant, D.; Bunge, S.; Boyle, T.; Wilson, M. C.; Brinker, C. J. Surfactant-Assisted Synthesis of Water-Soluble and Biocompatible Semiconductor Quantum Dot Micelles. *Nano Lett.* **2005**, *5* (4), 645–648.
(568) Jubb, A. M.; Allen, H. C. Vibrational Spectroscopic Characterization of Hematite, Maghemite, and Magnetite Thin Films Produced by Vapor Deposition. *ACS Appl. Mater. Interfaces* **2010**, *2* (10), 2804–2812.
(569) Otero-Lorenzo, R.; Ramos-Docampo, M. A.; Rodríguez-González, B.; Comesaña-Hermo, M.; Salgueiriño, V. Solvothermal Clustering of Magnetic Spinel Ferrite Nanocrystals: A Raman Perspective. *Chem. Mater.* **2017**, *29* (20), 8729–8736.
(570) Cannas, C.; Musinu, A.; Ardu, A.; Orrù, F.; Peddis, D.; Casu, M.; Sanna, R.; Angius, F.; Diaz, G.; Piccaluga, G. CoFe2O4 and CoFe2O4/SiO2 Core/Shell Nanoparticles: Magnetic and Spectroscopic Study. *Chem. Mater.* **2010**, *22* (11), 3353–3361.
(571) van Ewijk, G. A.; Vroege, G. J.; Philipse, A. P. Convenient Preparation Methods for Magnetic Colloids. *J. Magn. Magn. Mater.* **1999**, *201* (1–3), 31–33.
(572) Gnanaprakash, G.; Philip, J.; Jayakumar, T.; Raj, B. Effect of Digestion Time and Alkali Addition Rate on Physical Properties of Magnetite Nanoparticles. *J. Phys. Chem. B* **2007**, *111* (28), 7978–7986.
(573) Ayyappan, S.; Gnanaprakash, G.; Panneerselvam, G.; Antony, M. P.; Philip, J. Effect of Surfactant Monolayer on Reduction of Fe 3 O 4 Nanoparticles under Vacuum. *J. Phys. Chem. C* **2008**, *112* (47), 18376–18383.
(574) Atif, M.; Idrees, M.; Nadeem, M.; Siddique, M.; Ashraf, M. W. Investigation on the Structural, Dielectric and Impedance Analysis of Manganese Substituted Cobalt Ferrite i.e., $Co_{1-x}Mn_xFe_2O_4$ ($0.0 \leq x \leq 0.4$). *RSC Adv.* **2016**, *6* (25), 20876–20885.
(575) Kohout, J.; Gamaliy, E.; Stepankova, H.; Englich, J.; Procházka, V.; Chlan, V.; Brabers, V. A. M. NMR of 57Fe, 69Ga and 71Ga in Ga Substituted Magnetite. *J. Magn. Magn. Mater.* **2005**, *290–291 PA*, 1018–1020.
(576) da Costa, G. M.; De Grave, E.; Bowen, L. H.; de Bakker, P. M. A.; Vandenberghe, R. E. Temperature Dependence of the Hyperfine Parameters of Maghemite and Al-Substituted Maghemites. *Phys. Chem. Miner.* **1995**, *22* (3), 178–185.
(577) Duarte, J. M. G.; Campbell, S. L. M ¨ Ossbauer Spectroscopy. *Design* **2009**, *02142* (4), 3–7.
(578) Mørup, S.; Topsøe, H. Mössbauer Studies of Thermal Excitations in Magnetically Ordered Microcrystals. *Appl. Phys.* **1976**, *11* (1), 63–66.
(579) Lee, J. Y.; Oh, S. J.; Sohn, J. G.; Kwon, S. J. On the Correlation between the Hyperfine Field and the Particle Size of Fine Geothite Synthesized in Chloride Solution. *Corros. Sci.* **2001**, *43* (5), 803–808.
(580) Hoy, G. R.; Long, G. J. *Mössbauer Spectroscopy Applied to Inorganic Chemistry*; Long, G. J., Ed.; Springer US: Boston, MA, 1984; Vol. 2.
(581) Peddis, D.; Yaacoub, N.; Ferretti, M.; Martinelli, A.; Piccaluga, G.; Musinu, A.; Cannas, C.; Navarra, G.; Greneche, J. M.; Fiorani, D. Cationic Distribution and Spin Canting in CoFe2O4 Nanoparticles. *J. Phys. Condens. Matter* **2011**, *23* (42), 426004.
(582) Fantechi, E.; Campo, G.; Carta, D.; Corrias, A.; de Julián Fernández, C.; Gatteschi, D.; Innocenti, C.; Pineider, F.; Rugi, F.; Sangregorio, C. Exploring the Effect of Co Doping in Fine Maghemite Nanoparticles. *J. Phys. Chem. C* **2012**, *116* (14), 8261–8270.
(583) Carta, D.; Casula, M. F.; Falqui, a.; Loche, D.; Mountjoy, G.; Sangregorio, C.; Corrias, a. A Structural and Magnetic Investigation of the Inversion Degree in Ferrite Nanocrystals MFe 2 O 4 (M = Mn, Co, Ni). *J. Phys. Chem. C* **2009**, *113* (20), 8606–8615.

(584) Blanco-Gutiérrez, V.; Gallastegui, J. A.; Bonville, P.; Torralvo-Fernández, M. J.; Sáez-Puche, R. MFe2O4 (M: Co2+, Ni2+) Nanoparticles: Mössbauer and X-Ray Absorption Spectroscopies Studies and High-Temperature Superparamagnetic Behavior. *J. Phys. Chem. C* **2012**, *116* (45), 24331–24339.
(585) Carta, D.; Corrias, A.; Falqui, A.; Brescia, R.; Fantechi, E.; Pineider, F.; Sangregorio, C. EDS, HRTEM/STEM, and X-Ray Absorption Spectroscopy Studies of Co-Substituted Maghemite Nanoparticles. *J. Phys. Chem. C* **2013**, *117* (18), 9496–9506.
(586) Vamvakidis, K.; Katsikini, M.; Sakellari, D.; Paloura, E. C.; Kalogirou, O.; Dendrinou-Samara, C. Reducing the Inversion Degree of MnFe2O4 Nanoparticles through Synthesis to Enhance Magnetization: Evaluation of Their (1)H NMR Relaxation and Heating Efficiency. *Dalton Trans.* **2014**, *43* (33), 12754–12765.
(587) Seah, M. P.; Dench, W. A. Quantitative Electron Spectroscopy of Surfaces : *Surf. Interface Anal.* **1979**, *1* (1), 2–11.
(588) Riviere, J.; Myhra, S.; Hubbard, A. *Handbook of Surface and Interface Analysis*; Press, C., Ed.; CRC Press: Boca Raton, 2009.
(589) Revie, P. No Title. **1975**, *12* (1).
(590) Gupta, R. P.; Sen, S. K. Calculation of Multiplet Structure of Core p -Vacancy Levels. II. *Phys. Rev. B* **1975**, *12* (1), 15–19.
(591) Biesinger, M. C.; Payne, B. P.; Grosvenor, A. P.; Lau, L. W. M.; Gerson, A. R.; Smart, R. S. C. Resolving Surface Chemical States in XPS Analysis of First Row Transition Metals, Oxides and Hydroxides: Cr, Mn, Fe, Co and Ni. *Appl. Surf. Sci.* **2011**, *257* (7), 2717–2730.
(592) Fantauzzi, M.; Pacella, A.; Atzei, D.; Gianfagna, A.; Andreozzi, G. B.; Rossi, A. Combined Use of X-Ray Photoelectron and Mössbauer Spectroscopic Techniques in the Analytical Characterization of Iron Oxidation State in Amphibole Asbestos. *Anal. Bioanal. Chem.* **2010**, *396* (8), 2889–2898.
(593) Grosvenor, A. P.; Kobe, B. A.; Biesinger, M. C.; McIntyre, N. S. Investigation of Multiplet Splitting of Fe 2p XPS Spectra and Bonding in Iron Compounds. *Surf. Interface Anal.* **2004**, *36* (12), 1564–1574.
(594) Zhou, Z.; Zhang, Y.; Wang, Z.; Wei, W.; Tang, W.; Shi, J.; Xiong, R. Electronic Structure Studies of the Spinel CoFe2O4by X-Ray Photoelectron Spectroscopy. *Appl. Surf. Sci.* **2008**, *254* (21), 6972–6975.
(595) Li, M.; Mao, Y.; Yang, H.; Li, W.; Wang, C.; Liu, P.; Tong, Y. Controllable Electrochemical Synthesis of CoFe2O4 Nanostructures on FTO Substrate and Their Magnetic Properties. *New J. Chem.* **2013**, *37* (10), 3116.
(596) Aghavnian, T.; Moussy, J. B.; Stanescu, D.; Belkhou, R.; Jedrecy, N.; Magnan, H.; Ohresser, P.; Arrio, M. A.; Sainctavit, P.; Barbier, A. Determination of the Cation Site Distribution of the Spinel in Multiferroic CoFe2O4/BaTiO3layers by X-Ray Photoelectron Spectroscopy. *J. Electron Spectros. Relat. Phenomena* **2015**, *202*, 16–21.
(597) Kester, E.; Gillot, B. Cation Distribution, Thermodynamic and Kinetics Considerations in Nanoscaled Copper Ferrite Spinels. New Experimental Approach by XPS and New Results Both in the Bulk and on the Grain Boundary. *J. Phys. Chem. Solids* **1998**, *59* (8), 1259–1269.
(598) Stoner, B. E. C. A M E C H A N IS M O F M A G N E T IC H Y S T E R E S IS IN. **1948**, *826* (May).
(599) Morrish, A. H. *The Physical Principles of Magnetism*; Wiley-IEEE Press: Winnipeg, 2001.
(600) Bedanta, S.; Cobalt, C. A. G.; Nanoparticles, F. The Magnetic Properties of Single-Domain Particles with Cubic Anisotropy . I . Hysteresis Loops The Magnetic Properties of Single-Domain Particles with Cubic Anisotropy : I . Hysteresis Loops. **1993**.
(601) Peddis, D.; Rinaldi, D.; Ennas, G.; Scano, A.; Agostinelli, E.; Fiorani, D. Superparamagnetic Blocking and Superspin-Glass Freezing in Ultra Small δ-(Fe(0.67)Mn(0.33))OOH Particles. *Phys. Chem. Chem. Phys.* **2012**, *14* (9), 3162–3169.
(602) Peddis, D.; Cannas, C.; Musinu, a; Ardu, a; Orrù, F.; Fiorani, D.; Laureti, S.; Rinaldi, D.; Muscas, G.; Concas, G.; et al. Beyond the Effect of Particle Size: Influence of CoFe2O4 Nanoparticle Arrangements on Magnetic Properties. *Chem. Mater.* **2013**, *25* (10), 2–10.
(603) Hutlova, A.; Niznansky, D.; Rehspringer, J. L.; Estournes, C.; Kurmoo, M. High Coercive Field for Nanoparticles of CoFe2O4 in Amorphous Silica Sol-Gel. *Adv. Mater.* **2003**, *15* (19), 1622–+.
(604) Vejpravova, J.; Sechovsky, V.; Plocek, J.; Niznansky, D.; Hutlova, A.; Rehspringer, J. L. Magnetism of Sol-Gel Fabricated CoFe2O4/SiO2 Nanocomposites. *J. Appl. Phys.* **2005**, *97* (12).
(605) Shtrikman, S and Wohlfarth, E. P. THE THEORY OF THE VOGEL—FULCHER LAW OF SPIN GLASSES S. SHTRIKMAN a and E.P. WOHLFARTH. *Phys. Lett.* **1981**, *85* (8), 467–470.
(606) Shukla, N.; Liu, C.; Jones, P. M.; Weller, D. FTIR Study of Surfactant Bonding to FePt Nanoparticles. *J. Magn. Magn. Mater.* **2003**, *266* (1–2), 178–184.
(607) Wildeboer, R. R.; Southern, P.; Pankhurst, Q. A. On the Reliable Measurement of Specific Absorption Rates and Intrinsic Loss Parameters in Magnetic Hyperthermia Materials. *J. Phys. D. Appl. Phys.* **2014**, *47* (49), 495003.

(608) Kallumadil, M.; Tada, M.; Nakagawa, T.; Abe, M.; Southern, P.; Pankhurst, Q. a. Suitability of Commercial Colloids for Magnetic Hyperthermia. *J. Magn. Magn. Mater.* **2009**, *321* (10), 1509–1513.
(609) Reddy, L. H.; Arias, J. L.; Nicolas, J.; Couvreur, P. Magnetic Nanoparticles: Design and Characterization, Toxicity and Biocompatibility, Pharmaceutical and Biomedical Applications. *Chem. Rev.* **2012**, *112* (11), 5818–5878.
(610) Yamaura, M.; Camilo, R. L.; Sampaio, L. C.; Macêdo, M. A.; Nakamura, M.; Toma, H. E. Preparation and Characterization of (3-Aminopropyl)Triethoxysilane-Coated Magnetite Nanoparticles. *J. Magn. Magn. Mater.* **2004**, *279* (2–3), 210–217.
(611) Meiklejohn, W. H.; Bean, C. P. New Magnetic Anisotropy. *Phys. Rev.* **1957**, *105* (3), 904–913.
(612) Lo, A.; Tobia, D.; Winkler, E.; Golosovsky, I. V; Gonza, M. A.; Surin, S.; Arbiol, J.; Peiro, F.; Zysler, R. D.; Baro, M. D.; et al. Size-Dependent Passivation Shell and Magnetic Properties in Antiferromagnetic/Ferrimagnetic Core/Shell MnO Nanoparticles. *J. Am. Chem. Soc.* **2002**, *132*, 9398–9407.
(613) Kavich, D. W.; Dickerson, J. H.; Mahajan, S. V.; Hasan, S. A.; Park, J. H. Exchange Bias of Singly Inverted FeO/Fe3O4 Core-Shell Nanocrystals. *Phys. Rev. B - Condens. Matter Mater. Phys.* **2008**, *78* (17), 1–6.
(614) Winkler, E. L.; Lima, E.; Tobia, D.; Saleta, M. E.; Troiani, H. E.; Agostinelli, E.; Fiorani, D.; Zysler, R. D. Origin of Magnetic Anisotropy in ZnO/CoFe2O4 and CoO/CoFe2O4 Core/Shell Nanoparticle Systems. *Appl. Phys. Lett.* **2012**, *101* (25), 2–6.
(615) Lottini, E.; López-Ortega, A.; Bertoni, G.; Turner, S.; Meledina, M.; Van Tendeloo, G.; de Julián Fernández, C.; Sangregorio, C. Strongly Exchange Coupled Core|Shell Nanoparticles with High Magnetic Anisotropy: A Strategy toward Rare-Earth-Free Permanent Magnets. *Chem. Mater.* **2016**, *28* (12), 4214–4222.
(616) Cannas, C.; Musinu, a.; Peddis, D.; Piccaluga, G. Synthesis and Characterization of CoFe 2 O 4 Nanoparticles Dispersed in a Silica Matrix by a Sol−Gel Autocombustion Method. *Chem. Mater.* **2006**, *18* (16), 3835–3842.
(617) Sun, S.; Zeng, H.; Robinson, D. B.; Raoux, S.; Rice, P. M.; Wang, S. X.; Li, G. Monodisperse MFe2O4 (M=Fe, Co, Mn) Nanoparticles. *J. Am. Chem. Soc.* **2004**, *126*, 273–279.
(618) Cannas, C.; Ardu, A.; Peddis, D.; Sangregorio, C.; Piccaluga, G.; Musinu, A. Surfactant-Assisted Route to Fabricate CoFe2O4 Individual Nanoparticles and Spherical Assemblies. *J. Colloid Interface Sci.* **2010**, *343* (2), 415–422.
(619) Carla Cannas, Andrea Ardu Anna Musinu,Lorenza Suber, Gabriele Ciasca, Heinz Amenitsch, and G. C. Hierarchical Formation Mechanism of CoFe2O4 Mesoporous Assemblies. *ACS Nano* **2015**, *9* (7 '), 7277–7286.
(620) Thanh, N. T. K.; Maclean, N.; Mahiddine, S. Mechanisms of Nucleation and Growth of Nanoparticles in Solution. *Chem. Rev.* **2014**, *114* (15), 7610–7630.
(621) Xia, Y.; Gilroy, K. D.; Peng, H.-C.; Xia, X. Seed-Mediated Growth of Colloidal Metal Nanocrystals. *Angew. Chemie Int. Ed.* **2017**, *56* (1), 60–95.
(622) Wang, L.; Yan, Y.; Wang, M.; Yang, H.; Zhou, Z.; Peng, C.; Yang, S. An Integrated Nanoplatform for Theranostics via Multifunctional Core–shell Ferrite Nanocubes. *J. Mater. Chem. B* **2016**, *4* (10), 1908–1914.
(623) Noh, S.-H. H.; Na, W.; Jang, J.-T. T.; Lee, J.-H. H.; Lee, E. J.; Moon, S. H.; Lim, Y.; Shin, J. S.; Cheon, J. Nanoscale Magnetism Control via Surface and Exchange Anisotropy for Optimized Ferrimagnetic Hysteresis. *Nano Lett.* **2012**, *12* (7), 3716–3721.
(624) Kim, M. S.; Kim, C. S.; Kim, H. J.; Yoo, K. H.; Hahn, E. J. Effect Hyperthermia in CoFe2O4@MnFe2O4 Nanoparticles Studied by Using Field-Induced Mössbauer Spectroscopy. *J. Korean Phys. Soc.* **2013**, *63* (11), 2175–2178.
(625) Vasilakaki, M.; Trohidou, K. N.; Nogués, J. Enhanced Magnetic Properties in Antiferromagnetic-Core/Ferrimagnetic-Shell Nanoparticles. *Sci. Rep.* **2015**, *5*, 9609.
(626) White, W. B.; DeAngelis, B. a. Interpretation of the Vibrational Spectra of Spinels. *Spectrochim. Acta Part A Mol. Spectrosc.* **1967**, *23* (4), 985–995.
(627) Taylor, R. M. Maghemite in Soils and Its Origin I. PROPERTIES AND OBSERVATIONS ON SOIL MAGHEMITES. *Clay Miner.* **1974**, *10* (4), 289–298.
(628) Han, L.; Meng, Q.; Wang, D.; Zhu, Y.; Wang, J.; Du, X.; Stach, E. A.; Xin, H. L. Interrogation of Bimetallic Particle Oxidation in Three Dimensions at the Nanoscale. *Nat. Commun.* **2016**, *7*, 13335.
(629) Wang, D.; Liu, S.; Wang, J.; Lin, R.; Kawasaki, M.; Rus, E.; Silberstein, K. E.; Lowe, M. A.; Lin, F.; Nordlund, D.; et al. Spontaneous Incorporation of Gold in Palladium-Based Ternary Nanoparticles Makes Durable Electrocatalysts for Oxygen Reduction Reaction. *Nat. Commun.* **2016**, *7* (May), 11941.
(630) Wang, D.; He, H.; Han, L.; Lin, R.; Wang, J.; Wu, Z.; Liu, H.; Xin, H. L. Three-Dimensional Hollow-Structured Binary Oxide Particles as an Advanced Anode Material for High-Rate and Long Cycle Life Lithium-Ion Batteries. *Nano Energy* **2016**, *20*, 212–220.
(631) Schlossmacher, P.; Klenov, D. O.; Freitag, B.; Harrach, S. Von; Steinbach, A. Nanoscale

Chemical Compositional Analysis with an Innovative S/TEM-EDX System. *Microsc. Anal. Nanotechnol. Suppl.* **2010**, *24* (August 2010), S5–S8.
(632) Schlossmacher, P.; Klenov, D. O.; Freitag, B.; von Harrach, H. S. Enhanced Detection Sensitivity with a New Windowless XEDS System for AEM Based on Silicon Drift Detector Technology. *Micros. Today* **2010**, *18* (04), 14–20.
(633) Harrach, H. S. Von; Dona, P.; Freitag, B.; Soltau, H.; Niculae, A.; Rohde, M. An Integrated Silicon Drift Detector System for FEI Schottky Field. *Microsc. Microanal.* **2009**, *15* (Suppl 2), 8–9.
(634) Allen, L. J.; D'Alfonso, A. J.; Freitag, B.; Klenov, D. O. Chemical Mapping at Atomic Resolution Using Energy-Dispersive x-Ray Spectroscopy. *MRS Bull.* **2012**, *37* (01), 47–52.
(635) Kothleitner, G.; Neish, M. J.; Lugg, N. R.; Findlay, S. D.; Grogger, W.; Hofer, F.; Allen, L. J. Quantitative Elemental Mapping at Atomic Resolution Using X-Ray Spectroscopy. *Phys. Rev. Lett.* **2014**, *112* (8), 1–5.
(636) Gomes, J. D. a; Sousa, M. H.; Tourinho, F. a.; Aquino, R.; Da Silva, G. J.; Depeyrot, J.; Dubois, E.; Perzynski, R. Synthesis of Core-Shell Ferrite Nanoparticles for Ferrofluids: Chemical and Magnetic Analysis. *J. Phys. Chem. C* **2008**, *112* (16), 6220–6227.
(637) Chantrell, R. W.; El-Hilo, M.; O'Grady, K. Spin-Glass Behavior in a Fine Particle System. *IEEE Trans. Magn.* **1991**, *27* (4), 3570–3578.
(638) Peddis, D.; Hudl, M.; Binns, C.; Fiorani, D.; Nordblad, P. Aging Experiments in a Superspin Glass System of Co Particles in Mn Matrix. *J. Phys. Conf. Ser.* **2010**, *200* (SECTION 7).
(639) Margaris, G.; Vasilakaki, M.; Peddis, D.; Trohidou, K. N.; Laureti, S.; Binns, C.; Agostinelli, E.; Rinaldi, D.; Mathieu, R.; Fiorani, D. Superspin Glass State in a Diluted Nanoparticle System Stabilized by Interparticle Interactions Mediated by an Antiferromagnetic Matrix. *Nanotechnology* **2017**, *28* (3).
(640) Vasilakaki, M.; Trohidou, K. N.; Peddis, D.; Fiorani, D.; Mathieu, R.; Hudl, M.; Nordblad, P.; Binns, C.; Baker, S. Memory Effects on the Magnetic Behavior of Assemblies of Nanoparticles with Ferromagnetic Core/Antiferromagnetic Shell Morphology. *Phys. Rev. B - Condens. Matter Mater. Phys.* **2013**, *88* (14), 1–5.
(641) Van Rijssel, J.; Kuipers, B. W. M.; Erné, B. H. Non-Regularized Inversion Method from Light Scattering Applied to Ferrofluid Magnetization Curves for Magnetic Size Distribution Analysis. *J. Magn. Magn. Mater.* **2014**, *353*, 110–115.
(642) Boni, A.; Basini, A. M.; Capolupo, L.; Innocenti, C.; Corti, M.; Cobianchi, M.; Orsini, F.; Guerrini, A.; Sangregorio, C.; Lascialfari, A. Optimized PAMAM Coated Magnetic Nanoparticles for Simultaneous Hyperthermic Treatment and Contrast Enhanced MRI Diagnosis. *RSC Adv.* **2017**, *7* (70), 44104–44111.
(643) Muscas, G.; Yaacoub, N.; Concas, G.; Sayed, F.; Sayed Hassan, R.; Greneche, J. M.; Cannas, C.; Musinu, A.; Foglietti, V.; Casciardi, S.; et al. Evolution of the Magnetic Structure with Chemical Composition in Spinel Iron Oxide Nanoparticles. *Nanoscale* **2015**, *7* (32), 13576–13585.
(644) Gawande, M. B.; Goswami, A.; Asefa, T.; Guo, H.; Biradar, A. V; Peng, D.; Zboril, R.; Varma, R. S. Core-Shell Nanoparticles: Synthesis and Applications in Catalysis and Electrocatalysis. *Chem. Soc. Rev.* **2015**, *44* (21), 7540–7590.
(645) Luo, Y.; Lin, J. Synthesis and Characterization of Co(II) Salen Functionalized MCM-41-Type Hybrid Mesoporous Silicas and Their Applications in Catalysis for Styrene Oxidation with H2O2. *Microporous Mesoporous Mater.* **2005**, *86* (1–3), 23–30.
(646) Choi, H.; An, M.; Eom, W.; Lim, S. W.; Shim, I.-B.; Kim, C. S.; Kim, S. J. Crystallographic and Magnetic Properties of the Hyperthermia Material CoFe2O4@AlFe2O4. *J. Korean Phys. Soc.* **2017**, *70* (2), 173–176.
(647) Fantechi, E.; Innocenti, C.; Zanardelli, M.; Fittipaldi, M.; Falvo, E.; Carbo, M.; Shullani, V.; Di Cesare Mannelli, L.; Ghelardini, C.; Ferretti, A. M.; et al. A Smart Platform for Hyperthermia Application in Cancer Treatment: Cobalt-Doped Ferrite Nanoparticles Mineralized in Human Ferritin Cages. *ACS Nano* **2014**, *8* (5), 4705–4719.
(648) King, H. W.; Vegard, Y. Lo. Yon Lo Vegard. *J. Mater. Sci.* **1921**, *1* (1), 79–90.
(649) Shannon, R. D.; Prewitt, C. T. Revised Values of Effective Ionic Radii. *Acta Crystallogr. Sect. B Struct. Crystallogr. Cryst. Chem.* **1970**, *26* (7), 1046–1048.
(650) Melikhov, Y.; Snyder, J. E.; Jiles, D. C.; Ring, A. P.; Paulsen, J. A.; Lo, C. C. H.; Dennis, K. W. Temperature Dependence of Magnetic Anisotropy in Mn-Substituted Cobalt Ferrite. *J. Appl. Phys.* **2006**, *99* (8).
(651) Verwey, E. J. © 1953 Nature Publishing Group. *Nature* **1953**, 1054–1055.
(652) López Maldonado, K. L.; Vazquez Zubiate, L.; de la Presa, P.; Matutes Aquino, J. A.; Elizalde Galindo, J. T. Magneto-Resistive Coefficient Enhancement Observed around Verwey-like Transition on Spinel Ferrites XFe 2 O 4 (X = Mn, Zn). *J. Appl. Phys.* **2014**, *115* (17), 17C705.
(653) Menil, F. Systematic Trends of the 57Fe Mössbauer Isomer Shifts in (FeOn) and (FeFn) Polyhedra. Evidence of a New Correlation between the Isomer Shift and the Inductive Effect of the Competing Bond T-X (→ Fe) (Where X Is O or F and T Any Element with a Formal

Posit. *J. Phys. Chem. Solids* **1985**, *46* (7), 763–789.
(654) Zuo, X.; He, Y.; Yang, A.; Bernardo, B.; Harris, V. G.; Vittoria, C. Calculation of Exchange Constants in Spinel Ferrites with Magnetic S -State Ions. *J. Appl. Phys.* **2005**, *97* (10), 2005–2007.
(655) Hoon, D.; Seok, H.; Hyun, C.; Ahn, K.; Hong, K.; Lee, D. H.; Kim, H. S.; Yo, C. H.; Kim, K. H. The Magnetic Properties and Electrical Conduction Mechanism of Co1−xMnxFe2O4 Spinel. *Mater. Chem. Phys.* **1998**, *57* (2), 169–172.
(656) Bhame, S. D.; Joy, P. A. Magnetic and Magnetostrictive Properties of Manganese Substituted Cobalt Ferrite. *J. Phys. D. Appl. Phys.* **2007**, *40* (11), 3263–3267.
(657) Nethala, G. P.; Tadi, R.; Anupama, A. V.; Shinde, S. L.; Veeraiah, V. Correlation between Structural, Magnetic and Spectroscopic Properties of Mg Substituted CoFe2O4. *Mater. Sci. Pol.* **2018**, *36* (2), 310–319.
(658) Sharma, J.; Sharma, N.; Yadav, P.; Parashar, J.; Jadoun, P.; Saxena, V. K.; Bhatnagar, D.; Sharma, K. B. Structural and Magnetic Properties of Mg Substituted Co Nanoferrites; 2016; p 050039.
(659) Vinayak, V.; Khirade, P. P.; Birajdar, S. D.; Sable, D. B.; Jadhav, K. M. Structural, Microstructural, and Magnetic Studies on Magnesium (Mg2+)-Substituted CoFe2O4Nanoparticles. *J. Supercond. Nov. Magn.* **2016**, *29* (4), 1025–1032.
(660) Abdulla-Al-Mamun, M.; Kusumoto, Y.; Zannat, T.; Horie, Y.; Manaka, H. Au-Ultrathin Functionalized Core-Shell (Fe3O4@Au) Monodispersed Nanocubes for a Combination of Magnetic/Plasmonic Photothermal Cancer Cell Killing. *RSC Adv.* **2013**, *3* (21), 7816–7827.
(661) El-shahawy, A. Laser and Radiofrequency Induced Hyperthermia Treatment via Gold-Coated Magnetic Nanocomposites. **2013**.
(662) Espinosa, A.; Bugnet, M.; Radtke, G.; Neveu, S.; Botton, G. A.; Wilhelm, C.; Abou-Hassan, A. Can Magneto-Plasmonic Nanohybrids Efficiently Combine Photothermia with Magnetic Hyperthermia? *Nanoscale* **2015**, *7* (45), 18872–18877.
(663) Xu, Z.; Hu, G. Simple and Green Synthesis of Monodisperse Silver Nanoparticles and Surface-Enhanced Raman Scattering Activity. *RSC Adv.* **2012**, *2* (30), 11404.
(664) Fan, Z.; Huang, X.; Chen, Y.; Huang, W.; Zhang, H. Facile Synthesis of Gold Nanomaterials with Unusual Crystal Structures. *Nat. Protoc.* **2017**, *12* (11), 2367–2378.
(665) Huang, X.; Li, S.; Huang, Y.; Wu, S.; Zhou, X.; Li, S.; Gan, C. L.; Boey, F.; Mirkin, C. A.; Zhang, H. Synthesis of Hexagonal Close-Packed Gold Nanostructures. *Nat. Commun.* **2011**, *2* (1), 292–296.
(666) Chen, Z. P.; Zhang, Y.; Zhang, S.; Xia, J. G.; Liu, J. W.; Xu, K.; Gu, N. Preparation and Characterization of Water-Soluble Monodisperse Magnetic Iron Oxide Nanoparticles via Surface Double-Exchange with DMSA. *Colloids Surfaces A Physicochem. Eng. Asp.* **2008**, *316* (1–3), 210–216.
(667) Sepúlveda, B.; Angelomé, P. C.; Lechuga, L. M.; Liz-marzán, L. M. LSPR-Based Nanobiosensors. **2009**, 244–251.
(668) Wang, L.; Clavero, C.; Huba, Z.; Carroll, K. J.; Carpenter, E. E.; Gu, D.; Lukaszew, R. A. Plasmonics and Enhanced Magneto-Optics in Core-Shell Co-Ag Nanoparticles. *Nano Lett.* **2011**, *11* (3), 1237–1240.
(669) Liu, Q.; Zheng, X.; He, J.; Wang, W.; Fu, M.; Cao, Y.; Li, H.; Wu, Y.; Chen, T.; Zhang, C.; et al. Enhanced Magneto-Optical Effects in Composite Coaxial Nanowires Embedded with Ag Nanoparticles. *Sci. Rep.* **2016**, *6* (January), 4–11.
(670) Esmailzadeh, B.; Moradi, M. Enhancement of Kerr Signal in Co Thin Films Incorporating Ag Nanoparticles Surrounded by TiO2. *J. Supercond. Nov. Magn.* **2018**, *31* (5), 1483–1488.
(671) Bader, D. Weber_1999_Handb_logistik_886-899.Pdf. **1993**, *70* (7), 1006–1010.
(672) Ferreira, T. A. S.; Waerenborgh, J. C.; Mendonça, M. H. R. M.; Nunes, M. R.; Costa, F. M. Structural and Morphological Characterization of FeCo2O4and CoFe2O4spinels Prepared by a Coprecipitation Method. *Solid State Sci.* **2003**, *5* (2), 383–392.
(673) Lutterotti, L.; Scardi, P. Simultaneous Structure and Size–strain Refinement by the Rietveld Method. *J. Appl. Crystallogr.* **1990**, *23* (4), 246–252.
(674) Young, R. A.; Wiles, D. B. Profile Shape Functions in Rietveld Refinements. *J. Appl. Crystallogr.* **1982**, *15* (4), 430–438.
(675) Koenig, U.; Chol, G. Roentgenbeugungs- Und Neutronenbeugungsuntersuchungen an Ferriten Der Reihe Mnx Zn1-x Fe2 O4. *J. Appl. Crystallogr.* **1968**, *1*, 124–126.
(676) Montoro, V. Miscibilita Fra Gli Ossidi Salini Di Ferro e Di Manganese. *Gazz. Chim. Ital.* **1938**, *68*, 728–733.
(677) Novgorodovo, M. I.; Gorshkov, A. I.; Mokhov, A. V. Native Silver and Its New Structural Modifications. *Int. Geol. Rev.* **1981**, *23* (4), 485–494.
(678) Hull, S.; Keen, D. A. Pressure-Induced Phase Transitions in AgCl, AgBr, and AgI. *Phys. Rev. B* **1999**, *59* (2), 750–761.
(679) Mondini, S.; Ferretti, a. M.; Puglisi, a.; Ponti, a. Pebbles and PebbleJuggler: Software for Accurate, Unbiased, and Fast Measurement and Analysis of Nanoparticle Morphology from

Transmission Electron Microscopy (TEM) Micrographs. *Nanoscale* **2012**, *4* (17), 5356.
(680) Greneche, J.-M. Structural and Magnetic Properties of Nanostructured Oxides Investigated by 57 Fe Mössbauer Spectrometry. *Hyperfine Interact.* **2003**, *148/149*, 79–89.